

---


Electronic Theses and Dissertations, 2004-2019

---

2019

## A Theoretical Investigation of Small Organic Molecules on Transition Metal Surfaces

Walter Malone  
*University of Central Florida*

 Part of the [Atomic, Molecular and Optical Physics Commons](#)  
Find similar works at: <https://stars.library.ucf.edu/etd>  
University of Central Florida Libraries <http://library.ucf.edu>

This Doctoral Dissertation (Open Access) is brought to you for free and open access by STARS. It has been accepted for inclusion in Electronic Theses and Dissertations, 2004-2019 by an authorized administrator of STARS. For more information, please contact [STARS@ucf.edu](mailto:STARS@ucf.edu).

---

### STARS Citation

Malone, Walter, "A Theoretical Investigation of Small Organic Molecules on Transition Metal Surfaces" (2019). *Electronic Theses and Dissertations, 2004-2019*. 6344.  
<https://stars.library.ucf.edu/etd/6344>

A THEORETICAL INVESTIGATION OF SMALL ORGANIC MOLECULES ON  
TRANSITION METAL SURFACES

by  
WALTER MALONE  
B.S. University of Portland, 2014  
M.S. University of Central Florida, 2016

A dissertation submitted in partial fulfillment of the requirements  
for the degree of Doctor of Philosophy  
in the Department of Physics  
in the College of Sciences  
at the University of Central Florida  
Orlando, Florida

Spring Term  
2019

Major Professor: Abdelkader Kara

## ABSTRACT

With the ever growing number of proposed density functional theory (DFT) functionals it becomes necessary to thoroughly screen any new method to determine its merit. Especially relevant methods include a proper description of the van der Waals (vdW) interaction, which can prove vital to a correct description of a myriad of systems of technological importance. The first part of this dissertation explores the utility of several vdW-inclusive DFT functionals including optB86b-vdW, optB88-vdW, optPBE-vdW, revPBE-vdW, rPW86-vdW2, and SCAN+rVV10 by applying them to model systems of small organic molecules, pyridine and thiophene, on transition metal surfaces. Overall, we find the optB88-vdW functional gives the best, most balanced description of both thiophene and pyridine on transition metal surfaces while revPBE-vdW, rPW86-vdW2, and SCAN+rVV10 functionals perform especially poorly for these systems. In the second part of this dissertation we change our focus to potential applications of DFT. Specifically, we study the hydrodesulfurization (HDS) process and molecules that could be used in molecular electronics. The removal of sulfur containing molecules from petrochemicals through HDS is an exceptionally important process economically, and the field of molecular electronics is rapidly developing with hopes of competing with and replacing their silicon analogues. First we investigate the hydrodesulfurization of thiophene. In this dissertation we manage to map the HDS rate of thiophene in realistic reaction conditions to the charge transfer and adsorption energy of thiophene on bare transition metal surfaces in hopes of predicting ever more active HDS catalysis. Finally we look at the adsorption of polythiophenes and 5,14-dihydro-5,7,12,14-tetraazapentacene (DHTAP) on Au(111) and Cu(110). We find that

polythiophenes may dissociate of Au(111), presenting an issue for their use in molecular electronics. DHTAP, in contrast, proves to a suitable candidate for use practical devices.

Dedicated to my family

## **ACKNOWLEDGMENTS**

I would like to acknowledge the support of my adviser, Dr. Abdelkader Kara. I would like to thank him for introducing me to density functional theory and surface science, allowing me access to an abundant of computational resources both at UCF and at national lab facilities, and guiding me through my graduate school career. I truly appreciate his wisdom, guidance and support throughout my dissertation.

I would also like to acknowledge the support of my committee members, Dr. Kaden, Dr. Stolbov, and Dr. Thomas, for taking time out their busy schedules to attend my dissertation proposal and defense and providing me useful feedback

## TABLE OF CONTENTS

LIST OF FIGURES .....	xi
LIST OF TABLES .....	xix
LIST OF ACRONYMS AND ABBREVIATIONS .....	xxiv
CHAPTER ONE: INTRODUCTION.....	1
CHAPTER TWO: DENSITY FUNCTIONAL THEORY .....	5
2.1 Schrödinger's Equation: The Motivation behind DFT .....	6
2.2 Hohenberg Kohn Theorems .....	8
2.3 Kohn-Sham Equations .....	11
2.4 Modeling the Exchange-Correlation Interaction .....	14
2.4.1 The Local Density Approximation (LDA) .....	15
2.4.2 The Generalized Gradient Approximation (GGA) .....	17
2.4.3 Meta-GGA .....	18
2.5 Treating Long Range Dispersion .....	20
2.5.1 The van der Waals (vdW) Functionals .....	22
2.5.2 SCAN+rVV10 .....	24
2.6 General Computational Considerations .....	25
2.6.1 Basis Sets: The Plane Wave Basis .....	25
2.6.2 k-point Sampling.....	28

2.6.3 Pseudopotentials .....	29
2.6.4 General Algorithms for Solving the Kohn Sham equations .....	30
CHAPTER THREE: SCREENING THE VDW INCLUSIVE METHODS .....	32
3.1 Pyridine on (111) Coinage Metals .....	34
3.1.1 Computational Details .....	35
3.1.2 Stability of the Initial Adsorption Configurations .....	38
3.1.3 Adsorption Heights, Energies, and Other Structural Information .....	47
3.1.4 Electronic Structure Analysis .....	50
3.1.5 Effect of Coverage .....	53
3.1.6 Conclusions.....	61
3.2 Pyridine on (111) Reactive Metals .....	62
3.2.1 Computational Details .....	63
3.2.2 Equilibrium Adsorption Configurations .....	64
3.2.3 Adsorption Heights, Energies, and Other Structural Information .....	68
3.2.4 Electronic Structure Analysis .....	73
3.2.5 Change in Magnetization of Ni(111).....	83
3.2.6 Conclusions.....	84
3.3 Pyridine on (110) Metal Surfaces .....	86
3.3.1 Computational Details .....	87



3.3.2	Equilibrium Adsorption Configurations .....	90
3.3.3	Adsorption Heights, Energies, and Other Structural Information .....	97
3.3.4	Electronic Analysis .....	102
3.3.5	Conclusions and Brief Comparison to the (111) Metal Surfaces .....	106
3.4	Thiophene on Ni(100) and Cu(100).....	109
3.4.1	Computational Details .....	110
3.4.2	Equilibrium Adsorption Configurations .....	113
3.4.3	Adsorption Heights, Energies, and Other Structural Information .....	116
3.4.4	Electronic Analysis .....	121
3.4.5	Change in the Magnetization of Ni(100) .....	125
3.4.6	Conclusions.....	126
3.5	Thiophene on Ag, Au, Pt, Pd, and Rh(100) .....	128
3.5.1	Computational Details .....	128
3.5.2	Equilibrium Adsorption Configurations .....	129
3.5.3	Adsorption Heights, Energies, and Other Structural Information .....	132
3.5.4	Electronic Analysis .....	139
3.5.5	Conclusions.....	143
3.6	Using SCAN+rVV10 to Explore Thiophene on Ag, Rh, and Ir(100) .....	145
3.6.1	Computational Details .....	146

3.6.2	Equilibrium Adsorption Configurations .....	147
3.6.3	Adsorption Heights, Energies, and Other Structural Information .....	150
3.6.4	Electronic Analysis .....	155
3.6.5	Comparison to optB88-vdW and Conclusions .....	161
CHAPTER FOUR: OTHER APPLICATIONS OF DENSITY FUNCTIONAL THEORY .....		163
4.1	Studying the Initial Steps of Thiophene Hydrodesulfurization .....	163
4.1.1	Computational Details .....	165
4.1.2	Adsorption Energetics and Geometry .....	167
4.1.3	The Desulfurization of Thiophene as a Process Mediated by Charge Transfer Process .....	175
4.1.4	Work Function and Density of State Calculations.....	178
4.1.5	Charge Transfer & Adsorption Energy vs Periodic HDS Trends.....	181
4.1.6	Conclusions.....	183
4.2	Polythiophenes on Au(111) .....	184
4.2.1	Computational Methods.....	186
4.2.2	1T .....	189
4.2.3	2T .....	193
4.2.4	3T .....	196
4.2.5	Conclusions.....	203

4.3 DHTAP on Cu(110).....	204
4.3.1 Computational Details .....	205
4.3.2 STEM and LEED measurements.....	207
4.3.3 DFT calculations.....	212
4.3.4 Conclusions.....	217
CHAPTER FIVE: CONCLUSIONS .....	219
APPENDIX A: COPYRIGHT PERMISSION LETTERS .....	224
APPENDIX B: LIST OF PUBLICATIONS.....	232
LIST OF REFERENCES .....	234

## LIST OF FIGURES

Figure 1: General algorithm for solving the Kohn-Sham equations.....	31
Figure 2: Initial adsorption sites a) v-a, b) v-a30, c)v-b, d)v-b90, e) v-fcc, f)v-fcc30, g)v-hcp, h)v-hvp30, i)bA1, j)bA2, k)bB1, l)bB2, m)fA, n)fB1, o)fB2, p)hA, q)hB1, r)hB2, s)t1, and t)t2 for pyridine adsorbed on the fcc (111) metal surfaces. Orange atoms represent N atoms, brown atoms represent C atoms, white atoms represent H atoms, silver atoms represent the first layer substrate atoms, and teal atoms represent the second layer and lower substrate atoms. ....	38
Figure 3: Final adsorption site for pyridine adsorbed initially in v-fcc30 on Au(111) calculated using optB88-vdW.....	40
Figure 4: a) Adsorption energies and b) N-Cu distances (adsorption heights) for pyridine adsorbed on Cu(111).....	40
Figure 5: a) Adsorption energies and b) N-Ag distances (adsorption heights) for pyridine adsorbed on Ag(111).....	43
Figure 6: a) Adsorption energies and b) N-Au distances (adsorption heights) for pyridine adsorbed on Au(111).....	44
Figure 7: The adsorption energies and N-Metal distances for pyridine adsorbed on Ag(111) and Au(111) in both the 2x2 and 3x4 unit cell for the highest adsorption energy configurations. ....	57
Figure 8: The change in the surface's work function and the change in the width of the d-band of the atoms that compose the first layer of the substrate for pyridine adsorbed on Ag(111) and Au(111) in the highest adsorption energy configurations in the 2x2 and 3x4 unit cell.....	60
Figure 9: Energy difference, $\Delta E$ , between the vertical adsorption configuration (tilt angle = $90^\circ$ ) with the highest adsorption energy and the flat adsorption configuration (tilt angle $< 10^\circ$ ) with	

the highest adsorption energy. A larger  $\Delta E$  corresponds to a particular functional more strongly favoring a vertical adsorption configuration on a given surface..... 66

Figure 10: a) The adsorption energies and b) N-Metal distances (adsorption heights) for pyridine adsorbed on Pt, Pd, Rh, and Ni(111) in the highest adsorption energy configurations. .... 71

Figure 11: a) Charge transfer to the pyridine molecule for functional/metal combinations that lead to a flat equilibrium adsorption site and b) charge transfer to the pyridine molecule for functional/metal combinations that lead to a vertical equilibrium adsorption site for pyridine adsorbed on Pt, Pd, Rh, and Ni(111). .... 77

Figure 12: The d-band of the atoms that compose the first layer of the Pd(111) substrate before, black line, and after, red line, the adsorption of pyridine as calculated using the optB86b-vdW, b) optB88-vdW, c) optPBE-vdW, d) PBE, e) revPBE-vdW, and f) rPW86-vdW2 functionals ..... 82

Figure 13: Initial adsorption sites a) v-top, b) v-top90, c)v-blong, d)v-blong90, e) v-bshort, f)v-bshort90, g)v-tr, h)v-tr90, i)bridgeL1, j)bridgeL2, k)bridgeL3, l)bridgeS1, m)bridgeS2, n)bridgeS3, o)top1, p)top2, q)top3, r)trough1, s)trough2, and t)trough3 for pyridine adsorbed on the fcc (110) metal surfaces. Orange atoms represent N atoms, brown atoms represent C atoms, white atoms represent H atoms, silver atoms represent the first layer metal atoms, and teal atoms represent the second layer and lower substrate atoms. .... 89

Figure 14: The difference in adsorption energy ( $\Delta E$ ) between the vertical adsorption site v-top90 and trough3. The number by each data point corresponds to the tilt angle pyridine picks up when initially placed in trough3. Pyridine in v-top90 always remains perpendicular to the surface,  $\Theta = 90^\circ$ . Only metal/functional combinations that predict v-top90 to be the most stable adsorption site are shown..... 93

Figure 15: a) The new adsorption site that gave the highest adsorption energy for pyridine on Pt(110) as calculated by PBE, optB86b-vdW, optB88-vdW, and optPBE-vdW, and b) the trough3 adsorption site. PBE calculated these two specific adsorption geometries, but the opt-type functionals calculate nearly identical configurations..... 96

Figure 16: a) The adsorption energies and b) N-Metal distances or adsorption heights for pyridine adsorbed on Pt, Cu, Ag, and Au(110) in the highest adsorption energy configuration. 100

Figure 17: Initial adsorption sites a) v-hollow0, b) v-hollow45, c) v-bridge0, d) v-bridge90, e) v-atop0, f) v-atop45, g) hollow0, h) hollow45, i) bridge0, j) bridge45, k) atop0, and l) atop45 for thiophene adsorbed on the fcc (100) metal surfaces. Yellow atoms represent S atoms, brown atoms represent C atoms, white atoms represent H atoms, silver atoms represent substrate atoms in the first layer, and teal atoms represent substrate atoms in the second layer and lower. .... 112

Figure 18: Adsorption energies for thiophene adsorbed on Cu(100) and Ni(100) as calculated using the PBE and optB88-vdW functionals. Unstable adsorption sites are indicated with an arrow pointing from the initial adsorption site towards the final adsorption site. Note that thiophene in bridge45 on Ni(100) spontaneously broke apart..... 114

Figure 19: Thiophene broken over the bridge45 site. .... 115

Figure 20: a) Adsorption energy and b) adsorption height ( $H_s$ ) for thiophene adsorbed on Cu(100) and Ni(100). .... 119

Figure 21: Charge transfer to the thiophene molecule from the Ni(100) or the Cu(100) surface. .... 124

Figure 22: Energy difference,  $\Delta E$ , between the flat configuration (hollow45) with highest adsorption energy and the vertical adsorption configuration (tilt angle =90°) with the highest

adsorption energy. A larger  $\Delta E$  corresponds to a particular functional more strongly favoring a flat adsorption configuration on a given surface..... 132

Figure 23: Adsorption energies ( $E_{\text{ads}}$ ), and adsorption heights (H) for thiophene adsorbed on Ag, Au, Rh, Pt, and Pd(100) in the hollow45 configuration. .... 137

Figure 24: Charge transfer from the surface to the molecule for thiophene adsorbed on Ag, Au, Rh, Pt, and Pd(100) in the hollow45 configuration. .... 142

Figure 25: Adsorption energies for thiophene on a) Ag(100), b) Rh(100), and c) Ir(100) as calculated using the SCAN+rVV10 functional and the optB88-vdW functional. Unstable adsorption sites are denoted with an arrow pointing from the initial adsorption site to the final adsorption site. Unstable adsorption sites that lead to new adsorption sites are labeled with a \*. .... 148

Figure 26: Adsorption energies ( $E_{\text{ads}}$ ), and adsorption heights (H) for thiophene adsorbed in the hollow45 configuration on Ag, Rh, and Ir(100), and in the bridge45 configuration on Ir(100). Note optB88-vdW predicts thiophene to move from bridge45 to hollow45 on Ir(100), and SCAN+rVV10 predicts thiophene to break over bridge45 on Ir(100). .... 152

Figure 27: The charge transfer from the surface to the thiophene molecule ( $\Delta q$ ) for thiophene adsorbed in the hollow45 configuration on Ag, Rh, and Ir(100), and in the bridge45 configuration on Ir(100). Note optB88-vdW predicts thiophene to move from bridge45 to hollow45 on Ir(100), and SCAN+rVV10 predicts thiophene to break over bridge45 on Ir(100). .... 157

Figure 28: An illustration of any adsorption configurations that result in thiophene breaking at least one C-S bond. .... 169

Figure 29: a) The adsorption energies , and b) ( $S_z$ -Surface $_z$ ) distances and S-Metal distances of thiophene adsorbed on Al(100), Co(10-10), Ir(100), Nb(100), V(100), Cr(100), Mo(100), Ta(100), and W(100) in the adsorption site that led to the highest adsorption energy. A single dot over a bar means that thiophene broke one C-S bond in the highest adsorption energy configuration on that specific transition metal surface. A double dot over the bar means that thiophene broke two C-S bonds in the highest adsorption energy configuration on that specific transition metal surface. .... 173

Figure 30: a) The average of the two C-S distances vs. the charge transfer to the thiophene molecule, and b) the average of the two C-S distances vs. the charge transfer to the S atom for thiophene adsorbed on Ni(100), Cr(100), V(100), Ta(100), W(100), Mo(100), Nb(100), Al(100), and Co(10-10) in all the flat configuration. In b) thiophene takes only 0.4 (-e) from Ni(100), putting it in the “intact” section, yet thiophene breaks one C-S bond over Ni(100). Therefore, an arrow exists pointing from our one Ni(100) point to the single broken C-S bond section. .... 178

Figure 31: Previously reported thiophene HDS activities, taken from reference 171, plotted as a function of both adsorption energy and charge transfer to the S atom. Activities are represented using log-scaled, color-contrasted, contoured features. .... 182

Figure 32: Thiophene derivatives studied in this section. .... 187

Figure 33: a) Terthiophene with its long axis perpendicular to the surface, b) terthiophene with its long axis parallel to the surface with two S atoms pointing towards the surface, and c) terthiophene with its long axis parallel to the surface with one S atom pointing towards the surface. .... 189

Figure 34: XPS spectra with fits for 1T, 2T, and 3T on Au grown on mica. .... 190



Figure 35: XPS spectra with fits for 1T, 2T, and 3T on Au(111)..... 191

Figure 36: CLBEs for, from bottom to top, intact thiophene with an adatom, intact thiophene without an adatom, broken thiophene metallocycle, broken thiophene alkene chain, and an alkane chain. The 4x4 unit cell calculations are denoted by a 4. The  $\sqrt{7}\times\sqrt{7}$  unit cell calculations are denoted by a  $\sqrt{7}$ , and L corresponds to configurations where thiophene is flat on the surface. Each hash corresponds to the CLBE of a S atom in a molecule in a particular adsorption site. Hashes are located horizontally from the S atom they belong to ..... 193

Figure 37: CLBEs of, from bottom to top, broken bithiophene and intact bithiophene in the 4x4 unit cell. Each hash corresponds to the CLBE of a S atom in a particular adsorption site. Hashes are located horizontally from the S atom they belong to. .... 195

Figure 38: Two adsorption configurations where broken bithiophene dragged an Au atom out of the surface. .... 196

Figure 39: CLBEs for, from bottom to top, broken terthiophene, intact terthiophene with two S atoms pointing towards the surface, intact terthiophene with one S atom pointing towards the surface, and terthiophene sitting flat on the surface. Each hash corresponds to the CLBE of a S atom in a particular adsorption site. Hashes are located horizontally from the S atom they belong to. .... 202

Figure 40: Fit of the 3T XPS spectra on Au(111) taking into account the difference in CLBEs between the central S atom the side S atoms. .... 202

Figure 41: Initial adsorption configurations a) C1, b) C2, c) C3, and d) C4 for DHTAP adsorbed on Cu(110). White atoms correspond to H atoms, red atoms correspond to C atoms, orange

atoms correspond to N atoms, blue atoms correspond to Cu atoms in the first layer, and silver atoms correspond to Cu atoms in the second layer and lower. .... 206

Figure 42: a) STM image of DHTAP deposited at room temperature on Cu(110). DHTAP molecules appear as bright yellow rods. Panel b) illustrates an STM image of the atomically resolved substrate with a DHTAP trimer. The coverage for both images was 0.1 ML. Overlaid on the STM image is a ball-and-stick model of DHTAP. Tunneling parameters: a)  $I_t = 50$  pA,  $V_{\text{sample}} = +0.5$  V and b)  $I_t = 6$  nA,  $V_{\text{sample}} = -0.10$  mV. .... 208

Figure 43: STM images of DHTAP deposited on Cu(110) at room temperature at a coverage of a) 0.35 ML and b) 0.50 ML. The images in c) and d) are high-resolution zooms of the image in b), and reveal two structures that can be described by the matrices  $(7 \ 0 \ | \ 1 \ 2)$  and  $(6 \ -1 \ | \ 1 \ 2)$ , respectively. Tunneling parameters:  $I_t = 100$  pA,  $V_{\text{sample}} = +0.5$  V. .... 209

Figure 44: STM of 0.8ML of DHTAP deposited on Cu(110) at temperatures of a) 240 K, b) 330 K, and c) 430 K. Tunneling parameters:  $I_t = 100$  pA,  $V_{\text{sample}} = +0.5$  V. .... 210

Figure 45: STM of 1 ML of DHTAP deposited on Cu(110) at temperatures of a) 240 K, b) 330 K, and c) 430 K. Tunneling parameters:  $I_t = 100$  pA,  $V_{\text{sample}} = +0.5$  V. The panels d)-f) illustrate the LEED patterns of the surfaces in panels a)- c) respectively. LEED patterns were acquired using an electron beam energy of 17.6 eV. Overlaid in panels d)-f) are the simulated LEED patterns for the  $(6 \ 0 \ | \ 1 \ 2)$  and  $(6 \ -1 \ | \ 1 \ 2)$  structures. Red and blue arrows correspond to the unit cell vectors of the two mirror domains. .... 212

Figure 46: Calculated equilibrium adsorption geometries for DHTAP on Cu(110) in the, a) and d),  $(6 \ -1 \ | \ 1 \ 2)$  unit cell, b) and e), the  $(7 \ 0 \ | \ 1 \ 2)$  unit cell, c) and f), and the  $(6 \ 0 \ | \ 1 \ 2)$  unit cell. Orange atoms correspond to N atoms, red atoms correspond to C atoms, white atoms correspond

to H atoms, blue atoms correspond to first layer Cu atoms, and silver atoms correspond to second layer and lower Cu atoms. Pictures a) through c) are top views of the systems. Pictures d) through f) are side views of the systems which illustrate the buckling of the molecule. .... 213

Figure 47: The STM images of DHTAP on Cu(110) in the a)  $(6 \times 1 | 1 \times 2)$  structure, the  $(7 \times 0 | 1 \times 2)$  structure, and the  $(6 \times 0 | 1 \times 2)$  structure. Overlaid on the STM images are the calculated adsorption configurations. Tunneling parameters:  $I_t = 100 \text{ pA}$ ,  $V_{\text{sample}} = +0.5 \text{ V}$ , scale:  $(2.2 \times 4.2) \text{ nm}^2$ .

..... 216

## LIST OF TABLES

Table 1: Calculated lattice constants for Cu, Ag, and Au taken from reference 90. Experimental lattice constants taken from reference 91 are given for comparison. ....	36
Table 2: Adsorption Energy ( $E_{\text{ads}}$ ), N-Metal distance or adsorption height, N-C distance, buckling of the first layer of the substrate, and tilt angle ( $\Theta$ ) of the molecule for pyridine adsorbed on Cu, Ag, and Au(111). ....	48
Table 3: Charge transfer to the molecule, change in the width ( $\Delta W$ ) and the center ( $\Delta C$ ) of the atoms that compose the first layer of the substrate, and change in the surface's work function ( $\Delta\Phi$ ) for pyridine adsorbed on Cu, Ag, and Au(111) in the highest adsorption energy configuration. ....	51
Table 4: Adsorption energies and tilt angle away from the surface, in circle brackets, for pyridine adsorbed on Ag(111) and Au(111) in the initial v-a, v-a30, v-fcc30, and v-hcp30 configurations in the 2x2 unit cell.....	55
Table 5: Adsorption Energy ( $E_{\text{ads}}$ ), N-Metal distances, N-C bond lengths, buckling of the first layer of the substrate, and tilt angle, $\Theta$ , for pyridine adsorbed in the highest adsorption energy configurations in the 2x2 unit cell. ....	56
Table 6: Charge transfer to the molecule, change in the width ( $\Delta W$ ) and the center ( $\Delta C$ ) of the atoms that compose the first layer of the substrate, and change in the surface's work function for pyridine adsorbed on Ag(111) and Au(111) in the highest adsorption energy configuration in the 2x2 unit cell.....	60
Table 7: Calculated lattice constants for Rh, Pt, Pd and Ni taken from reference 90. Experimental lattice constants taken from reference 91 are given for comparison. ....	64

Table 8: Adsorption energies, N-Metal distances (adsorption heights), N-C distances, buckling of the first layer of the substrate, and tilt angles ( $\Theta$ ) of the molecule for pyridine adsorbed on Rh, Pt, Pd and Ni(111) in the adsorption configuration with the highest adsorption energy.....	70
Table 9: Charge transfer to the molecule, change in the work function ( $\Delta\Phi$ ), and change in the width ( $\Delta W$ ) and the center ( $\Delta C$ ) of the d-band of the atoms that compose the first layer of the substrate for pyridine adsorbed on Rh, Pt, Pd and Ni(111) in the highest adsorption energy configuration.....	76
Table 10: Change in the average magnetic moment of the atoms that compose the first layer of the Ni(100) substrate, $\Delta\mu$ , upon the adsorption of pyridine.....	84
Table 11: Adsorption energy and tilt angle away from the surface ( $\Theta$ ) for pyridine adsorbed in the adsorption site that leads to the largest adsorption energy and trough3. ....	96
Table 12: Adsorption energy ( $E_{ads}$ ), N- Metal distance (adsorption heights), buckling of the first layer of the substrate ( $B_1$ ), buckling of the second layer of the substrate ( $B_2$ ), and the tilt angle of the molecule away from the surface ( $\Theta$ ) for pyridine adsorbed on Au, Ag, Cu , and Pt(110) in the highest adsorption energy configuration.....	99
Table 13: Charge transfer to the molecule, change in the surface's work function ( $\Delta\Phi$ ) and change in the width ( $\Delta W$ ) and center ( $\Delta C$ ) of the atoms that compose the first layer of the substrate upon the adsorption of pyridine. ....	104
Table 14: The adsorption energy ( $E_{ads}$ ), adsorption height ( $H_s$ ), buckling of the first layer of the substrate, and tilt angle ( $\Theta$ ) for thiophene adsorbed on the Cu(100) and Ni(100). ....	118
Table 15: Adsorption energy ( $E_{ads}$ ) and S-Cu distances for thiophene adsorbed on Cu(100) in the hollow45 configuration. Values in circle brackets are taken from reference 151. ....	120

Table 16: Charge transfer to the molecule and change in the center ( $\Delta C$ ) and width ( $\Delta W$ ) of the atoms that compose the first layer of the substrate upon the adsorption of thiophene. ....	123
Table 17: Change in the average magnetic moment ( $\Delta\mu$ ) of the atoms that compose the first layer of the Ni(100) substrate upon the adsorption of thiophene.....	126
Table 18: Adsorption energies ( $E_{ads}$ ), adsorption heights (H), C-S bond lengths, buckling of the first layer of the substrate, and tilt angle of the molecule relative to the surface plane ( $\Theta$ ) for thiophene adsorbed on Ag, Au, Rh, Pt, and Pd(100) in the hollow45 configuration. ....	135
Table 19: Charge transfer from the surface to the thiophene molecule, and change in the center ( $\Delta C$ ) and width ( $\Delta W$ ) of the atoms that compose the first layer of the substrate for thiophene adsorbed on Ag, Au, Rh, Pt, and Pd(100) in the hollow45 configuration. ....	141
Table 20: Calculated lattice constants for Rh, Ag, and Ir using optB88-vdW and SCAN+rVV10. Experimental lattice constants are also given for comparison.....	146
Table 21: Adsorption energies ( $E_{ads}$ ), adsorption heights (H), C-S bond lengths, buckling of the first layer of the substrate, and tilt angle of the molecule relative to the surface plane ( $\Theta$ ) for thiophene adsorbed in the hollow45 configuration on Ag, Rh, and Ir(100), and in the bridge45 configuration on Ir(100). * Note optB88-vdW predicts thiophene to move from bridge45 to hollow45 on Ir(100). ** Note SCAN+rVV10 predicts thiophene to break over bridge45 on Ir(100). ....	151
Table 22: The charge transfer from the surface to the thiophene molecule ( $\Delta q$ ), the change in the width ( $\Delta W$ ) and the center ( $\Delta C$ ) of the d-band of the atoms that compose the first layer of the substrate, and the change in the surface's work function ( $\Delta\Phi$ ) for thiophene adsorbed in the hollow45 configuration on Ag, Rh, and Ir(100), and in the bridge45 configuration on Ir(100). *	

Note optB88-vdW predicts thiophene to move from bridge45 to hollow45 on Ir(100). \*\* Note SCAN+rVV10 predicts thiophene to break over bridge45 on Ir(100). ..... 156

Table 23: The induced dipole moment of thiophene perpendicular to the surface ( $\mu_{\text{mol}}$ ), the contribution to the change in the work function of the surface from the induced dipole moment of thiophene perpendicular to the surface ( $\Delta\Phi_{\text{mol}}$ ), the contribution to the change in the work function of the surface from the charge transfer to the thiophene molecule and the “pushback” effect ( $\Delta\Phi_{\text{chg}}$ ), and the total change in the surface’s work function ( $\Delta\Phi$ ) for thiophene adsorbed in the hollow45 configuration on Ag, Rh, and Ir(100) ..... 161

Table 24: Calculated lattice constants for Al, Ir, W, Mo, Cr, Ta, Nb, V, and Co using the optB88-vdW functional. Experimental lattice constants, taken from reference 91, 182, or 183, are given for comparison. .... 166

Table 25: Adsorption energy ( $E_{\text{ads}}$ ), S-Metal distances, the z-coordinate of the S atom minus the average of the z-coordinates of the atoms that compose the first layer of the substrate ( $S_z$ -Surface $_z$ ), and the buckling of the first layer of the substrate for each configuration that broke at least one C-S bond and the hollow45 configuration on each transition metal surface. .... 171

Table 26: The charge transfer to the thiophene molecule ( $\Delta q_{\text{mol}}$ ), and the charge transfer to the S atom ( $\Delta q_{\text{s}}$ ) for thiophene on Cr(100), V(100), Ta(100), W(100), Mo(100), Nb(100), Al(100), and Co(10-10) in the highest adsorption energy configuration and in the hollow45 configuration.. 177

Table 27: Change in the width ( $\Delta W$ ), and center ( $\Delta C$ ) of the d-band (p-band for Al(100)) of the atoms that compose the first layer of the substrate, and the change in the work function ( $\Delta\Phi$ ) for thiophene on Cr(100), V(100), Ta(100), W(100), Mo(100), Nb(100), Al(100), and Co(10-10) in the highest adsorption energy configuration and in the hollow45 configuration. .... 180

Table 28: Adsorption energy ( $E_{\text{ads}}$ ), S2p Binding Energy, and S-Au distances for intact thiophene, broken thiophene, and an alkane chain adsorbed on Au(100) in the 4x4 and $\sqrt{7}\times\sqrt{7}$ unit cell.....	192
Table 29 Adsorption energy ( $E_{\text{ads}}$ ), S2p binding energies for each S atom in the molecule, and S-Au distances for each S atom in the molecule for intact bithiophene and broken bithiophene on Au(111) in a 4x4 unit cell. ....	195
Table 30: Adsorption energy ( $E_{\text{ads}}$ ), S2p Binding Energies for each S atom in the molecule, and S-Au distances for each S atom in the molecule for intact terthiophene and broken terthiophene on Au(111) in the 5x5 and 2x6 unit cell. In these configurations terthiophene has its long axis parallel to the surface. ....	199
Table 31: Adsorption energy ( $E_{\text{ads}}$ ), S2p Binding Energies for each S atom in the molecule, and S-Au distances for each S atom in the molecule for intact terthiophene with its long axis perpendicular to Au(111) in the 5x5 and 2x6 unit cell. ....	201
Table 32: Adsorption energy ( $E_{\text{ads}}$ ), surface adsorption energy (Surface $E_{\text{ads}}$ ), adsorption height ( $H_{\text{ads}}$ ), N-Cu distances, buckling of the first layer of the substrate ( $B_s$ ), buckling of the molecule ( $B_m$ ), and charge transfer to the DHTAP molecule ( $\Delta q$ ) for DHTAP adsorbed on Cu(110) in the (7 0   1 2), (6 -1   1 2), and ( 6 0   1 2) unit cells. ....	215



## LIST OF ACRONYMS AND ABBREVIATIONS

ACFD: adiabatic-connection fluctuation dissipation theorem

BCC: body-centered cubic

BJ: Becke-Johnson

BZ: Brillouin zone

CG: conjugate gradient

CLBE: core level binding energy

DFT: density functional theory

DHTAP: 5,14-dihydro-5,7,12,14-tetraazapentacene

DH4T:  $\alpha$ ,  $\omega$ -diquaterthiophene

DH6T: dihexylsexithiophene

FCC: face-centered cubic

GGA: generalized gradient approximation

HCP: hexagonal close packed

HDS: hydrodesulfurization

HEG: homogenous electron gas

LDA: local density approximation

LEED: low-energy electron diffraction

LSDA: local spin density approximation

LUMO: lowest unoccupied molecular orbital

OFET: organic field-effect transistor

OLED: organic light emitting diode

OTFT: organic thin film transistor

O-LEFT: organic light-emitting film transistor

PAW: projector augmented wave

PBE: Perdew-Burke-Ernzerhof

RPA: Random-Phase Approximation

SCAN: Strongly Constrained and Appropriately Normed

STM: scanning tunneling microscopy

VASP: Vienna Ab initio Simulation Package

vdW: van der Waals

XPS: X-ray photoelectron spectroscopy

## CHAPTER ONE: INTRODUCTION

This dissertation aims to complete two main goals. First this work compares the accuracy of several new and promising quantum mechanical modeling methods with already well-established ones. The second part of this dissertation applies the method the first part of this dissertation found most accurate to systems of technological interest.

Quantum mechanical modeling, often utilized in tandem with experiments, has become an ever more popular tool for investigating both the electronic and geometric properties of materials. Density functional theory (DFT) [1], one specific quantum mechanical modeling scheme, in particular achieved a substantial amount of success in the past few decades due to its accuracy, often low computational cost, and the wide variety of both free and commercially available DFT codes. The basic idea of DFT is to model systems on the atomic scale using electron density. The total energy of a system in DFT formalism then becomes a functional of electron density. Despite its success, DFT research is a never ending affair as researchers strive to push the method's overall accuracy to new limits. While this continual advancement is beneficial to an increased understanding of matter, each time a new improvement to DFT is proposed, it must be rigorously tested against both experimental data and high accuracy quantum chemical calculations. This is done as a safeguard to ensure that any step forward in DFT's evolution is a correct one.

While **chapter 2** serves as a basic introduction to density functional theory, **chapter 3** of this dissertation undertakes the necessary task of screening several new DFT methods. The methods targeted in this work attempt to accurately describe the long range van der Waals (vdW) forces.

Throughout a good portion of DFT's long history the method, in its standard implementation, failed to accurately describe long range dispersion. This becomes problematic as the long range vdW forces appear to be key to describing a myriad of systems [2-11]. Researchers made a number of attempts to rectify this problem [12-20]. The vdW-DF [2,17-18] and the vdW-DF2[19] methods in particular stand out among recent attempts to correctly describe the vdW interaction. These methods work at the level of approximation of the generalized gradient approximation (GGA) [21-23], and offer a seamless self-consistent treatment of the vdW forces that adds little computational cost beyond the cost of a standard GGA functional. Meta-GGA [24-28] functionals, the next natural step beyond GGA functionals, add substantially more computational cost than GGA type functional, but are expected to be more accurate. Promising among recently developed meta-GGA functionals that seek to incorporate the long range vdW forces is the SCAN+rVV10 functional [29]. It combines the SCAN [30] meta-GGA functional with the rVV10 [12] correlation functional which tackles, self-consistently, the long range vdW interactions. In this dissertation we will screen the vdW-DF, vdW-DF2, and SCAN+rVV10 methods by exploring systems where the vdW interaction is thought to play an important role. Specifically we explore the adsorption of two small organic molecules, pyridine ( $\text{NC}_5\text{H}_5$ ) and thiophene ( $\text{SC}_4\text{H}_4$ ), on various transition metal surfaces. Notably we study the adsorption of pyridine on Rh, Pt, Pd, Ni, Ag, Au, and Cu(111), pyridine on Cu, Ag, Au, and Pt (110), and thiophene on Rh, Pt, Pd, Ni, Ir, Cu, Ag, and Au (100). For these systems we present a detailed analysis of both the geometric and electronic structure of the calculated equilibrium adsorption geometry with a thorough comparison to the available experimental results.

Improving DFT is meaningless without target applications. Thus the next chapter of this dissertation centers on applying the method found in the previous chapter of this dissertation that gave the best, most balanced results, vdW-DF, to systems of technological interest. These calculations were completed in tandem with experiments performed by our collaborators, and we specifically target systems that may be useful in the creation of organic electronics.

Lately, many research proposals have focused on organic electronics. These devices tend to be cheaper and more flexible than their inorganic counterparts. Recent studies have demonstrated the potential impact of devices such as organic light emitting diodes [31,32] (OLED), organic light-emitting film transistors (O-LEFT) [33], organic field-effect transistors (OFET) [34], and organic thin film transistors (OTFT) [35]. Currently their relatively low performance limits these organic devices' ability to replace their inorganic counterparts. The physics of the interface of a semiconducting organic material with a metal substrate, specifically the charge transfer across and along this boundary, often determines the capability of these organic devices. Therefore, crucial to the advancement of these novel organic electronics is an improved understanding of how organic molecules interact with metal substrates. To this end, in **chapter 4** of this dissertation, we study the adsorption of polythiophene molecules on Au(111) and 5,14-dihydro-5,7,12,14-tetraazapentacene (DHTAP) on Cu(110) using the vdW-DF method. Each one of these systems has the potential to be quite useful in molecular electronic devices, making each one of these molecule/substrate systems a great candidate to explore with DFT.

Another practical use of DFT tackled in **chapter 4** of this dissertation is the study of catalysts. With increasing government regulations focusing on environmental protection, petrochemical

companies have been forced to produce less and less poisonous fuels. Sulfur (S) containing compounds are often the first molecules targeted for removal from fuels as the burning of S containing compounds causes smog and acid rain [36]. These S containing compounds are removed from petrochemicals with the aid of a catalyst through a process known as hydrodesulfurization (HDS). Thiophene, a small S containing organic molecule previously mentioned in this work, is frequently the subject of HDS studies as it is one of the simplest S containing compounds but also one of the hardest to desulfurize due the stability of its aromatic ring [37]. In this dissertation we not only, in the third chapter, study thiophene on transition metals as a model to screen various computational methods but we also study, in the fourth chapter, thiophene on metals commonly used in commercially available catalysts, along with some other metal surfaces for comparison, with the goal of modeling and improving the understanding of the HDS process. We expressly chose to study thiophene on Al(100), Nb(100), Cr(100), V(100), Ta(100), W(100), Co(10-10), and Mo (100) in **chapter 4** of this dissertation.

Finally, in **chapter 5** of this dissertation, we present the conclusions of our work. We present an in depth comparison of the vdW-DF, vdW-DF2, and SCAN+rVV10 methods with a heavy focus on how well each method reproduces the available experimental results. We then go through the systems we studied with one method, vdW-DF, in conjunction with our experimental collaborators. We will then discuss the potential each system has for use in future commercially available devices with a focus on how DFT can supplement and illuminate experimental results. We will also analyze how well DFT can reproduce what is already known experimentally about these systems in order to further our discussion about the merits of the vdW-DF method.

## CHAPTER TWO: DENSITY FUNCTIONAL THEORY

As mentioned density functional theory is a quantum mechanical theory that models systems at the atomic scale as a continuous electron density. It is a versatile tool that one may use to calculate the properties of any atomic system. In this work we limit ourselves to use it to calculate the equilibrium adsorption geometry, adsorption energy, change in the work function and density of states of the surface, core-level shifts, and charge transfer of small organic molecules on transition metal surfaces. DFT, however, can also be used to calculate HOMO-LUMO gaps, elastic constants, piezoelectric tensors, and much more.

In this chapter we present a brief but thorough introduction to DFT from the ground up. The introduction assumes the reader possesses basic knowledge of quantum mechanics and calculus of variations. In section 1, we start with the reasons DFT exists by looking at the many-body Schrödinger equation. In the next section we touch on the two theorems that DFT sprung out of: the Hohenberg-Kohn theorems. In section 3 we delve into how the Hohenberg-Kohn theorems give rise to the Kohn-Sham equations, and demonstrate how these equations form the bedrock of DFT. In section 4, we explain how one can model the exchange-correlation interaction and its importance within the theory. This section is further broken up into three subsections which each cover a different approximation to the exchange-correlation energy. These approximations, in order of their appearance in this dissertation, are the local density approximation (LDA), the generalized gradient approximation (GGA), and the meta-GGA approximation. Moving forward, section 5 of this chapter is devoted to the vdW inclusive functionals as most of calculations presented in this dissertation are carried out using vdW inclusive functionals.

Specifically we discuss the vdW-DF and vdW-DF2 methods in subsection 2.5.1, and the SCAN+rVV10 method in subsection 2.5.2. Finally in section 6 we go over some of the general computational parameters one must take into consideration when performing any DFT calculation including choosing a basis set, k-point sampling, and pseudopotentials. We also cover the general algorithms all DFT codes perform to solve the Kohn-Sham equations in this section. The introduction presented in this dissertation is fairly broad and thus it is by no means exhaustive. Many textbooks and review articles have been solely devoted to DFT and are available to the curious reader [1,38-41].

### **2.1 Schrödinger's Equation: The Motivation behind DFT**

To describe a system at the quantum level one must solve Schrödinger's equation, which, from basic quantum mechanics, for a system with N nuclei and M electrons looks like:

$$H\Psi(\mathbf{R}_1, \mathbf{R}_2, \dots, \mathbf{R}_N; \mathbf{r}_1, \mathbf{r}_2, \dots, \mathbf{r}_M) = E\Psi(\mathbf{R}_1, \mathbf{R}_2, \dots, \mathbf{R}_N; \mathbf{r}_1, \mathbf{r}_2, \dots, \mathbf{r}_M) \quad (1)$$

In this equation the Hamiltonian operator is denoted by H, the total energy of system is denoted by E, and the wave function of the system is denoted by  $\psi$ . The wave function of the system includes all the information that can ever be known about the system. For this equation and the rest of the equations that appear in this dissertation, vectors will be **bolded** and operators will be *italicized*. The wave function is a function of the N-position coordinates of the nuclei and the M-position coordinates of the electrons. Furthermore, the Hamiltonian operator can be further broken down into several parts: the kinetic energy of the electrons ( $T_e$ ), the kinetic energy of the nuclei ( $T_n$ ), the electron-electron interactions ( $V_{e-e}$ ), the nuclei-nuclei interactions ( $V_{n-n}$ ), and the



nuclei-electron interactions ( $V_{n-e}$ ). If one were to write out each individual term one would get the following equations:

$$T_e = - \sum_{i=1}^M \frac{\hbar^2 \nabla_i^2}{2m_e} \quad (2)$$

$$T_n = - \sum_{k=1}^N \frac{\hbar^2 \nabla_k^2}{2m_n} \quad (3)$$

$$V_{e-e} = \sum_{i=1}^M \sum_{j>i}^M \frac{e^2}{4\pi\epsilon_0 |\mathbf{r}_i - \mathbf{r}_j|} \quad (4)$$

$$V_{n-n} = \sum_{k=1}^N \sum_{l>k}^N \frac{e^2 Z_k Z_l}{4\pi\epsilon_0 |\mathbf{R}_k - \mathbf{R}_l|} \quad (5)$$

$$V_{n-e} = - \sum_{k=1}^N \sum_{i=1}^M \frac{e^2 Z_k}{4\pi\epsilon_0 |\mathbf{R}_k - \mathbf{r}_i|} \quad (6)$$

Now as one may remember, the exact solution to this equation is only known for a few simple systems, notably the H atom. More complex systems cannot even be solved numerically let alone exactly as the wave function is a function of  $3(n+m)$  variables, three position variables for each nucleus and electron. Even for a simple molecule like thiophene, for example, the wave function would have 159 variables. Solving for a wave function with this many variables would require an enormous amount of calculations and an unattainable amount of computational time. Therefore, to solve for the ground state of a quantum system one must make approximations. As the nuclei are much more massive than the electrons, a single proton is over 1800 times more massive than an electron, one can first assume that the nuclei are stationary, which eliminates the nucleus kinetic energy term from the Hamiltonian (equation 3), makes the nucleus-nucleus interaction a constant (equation 5), and eliminates  $3n$  coordinates from the wave function. This

approximation is known as the Born–Oppenheimer approximation. While the Born–Oppenheimer approximation greatly simplify our problem, it is still not enough. Using thiophene again as example, even with the Born–Oppenheimer approximation the wave function would possess 132 coordinates, yielding a problem still way beyond the limits of computational physics. Thus the motivation for DFT is simply to reduce the intractable problem of having a wave function with many independent variables into a tractable problem with fewer variables. DFT accomplishes this by assuming the total energy of any system is a functional, a function of a function, of electron density. We can then write the total energy, using the Born–Oppenheimer approximation, as:

$$E[n] = T[n] + V_{\text{ext}}[n] + V_{\text{ee}}[n] \quad (7)$$

In the above equation  $T$  is the kinetic energy of the electrons,  $V_{\text{ext}}$  is the interaction of the electrons with the field created by the stationary nuclei which we will, from now on, call the external potential, and  $V_{\text{ee}}$  is the electron-electron interaction. If one can justify equation 7 then DFT successfully reduces the number of variables involved in modeling a quantum system from  $3m$  position variables down to a single variable, the electron density. Justification can be found through the Hohenberg-Kohn theorems.

## **2.2 Hohenberg Kohn Theorems**

The Hohenberg Kohn theorems are two theorems used as the basis and justification of DFT. In this section will briefly go over their derivation and significance. The first Hohenberg-Kohn theorem simply states that the external potential is a unique functional of the electron density within a trivial additive constant [42], or in other words there is a one to one correspondence

between the external potential and the electron density. The proof proceeds via a *reductio ad absurdum*. Let  $V_{\text{ext1}}(\mathbf{r})$  be an external potential with a ground state  $\psi_1$  that leads to a density  $n(\mathbf{r})$ . Now assume there is some second external potential,  $V_{\text{ext2}}(\mathbf{r})$ , with a ground state wave function  $\psi_2$  leads to the same charge density  $n(\mathbf{r})$ . From this hypothetical situation one will first notice that  $\psi_1$  and  $\psi_2$  cannot be equal to one another, unless  $V_{\text{ext1}}(\mathbf{r}) - V_{\text{ext2}}(\mathbf{r}) = \text{constant}$ , since they are solutions to different Schrödinger's equation. Remember that  $H_1$  and  $H_2$ , the Hamiltonian's for our two systems, must be different as they both include a different external potential and the same kinetic energy and electron-electron interaction terms.

$$H_1 = T + V_{\text{ee}} + V_{\text{ext1}} \quad (8)$$

$$H_2 = T + V_{\text{ee}} + V_{\text{ext2}} \quad (9)$$

It follows from basic quantum mechanics that:

$$E_2 = \langle \psi_2 | H_2 | \psi_2 \rangle \quad (10)$$

$$E_1 = \langle \psi_1 | H_1 | \psi_1 \rangle \quad (11)$$

From the variational principle and quantum mechanics, we know that the ground state wave functions  $\psi_1$  and  $\psi_2$  minimize the energy for the systems represented by Hamiltonian  $H_1$  and  $H_2$  respectively. Therefore, if we swap out  $\psi_2$  in equation 10 for  $\psi_1$  we will get:

$$E_2 = \langle \psi_2 | H_2 | \psi_2 \rangle < \langle \psi_1 | H_2 | \psi_1 \rangle = \langle \psi_1 | H_1 - V_{\text{ext1}} + V_{\text{ext2}} | \psi_1 \rangle \quad (12)$$

Which we can simplify down to:

$$E_2 < E_1 + \int n(\mathbf{r}) [V_{\text{ext2}}(\mathbf{r}) - V_{\text{ext1}}(\mathbf{r})] d^3r \quad (13)$$

We can then write  $E_1$  in the same fashion and simplify appropriately.

$$E_1 = \langle \psi_1 | H_1 | \psi_1 \rangle < \langle \psi_2 | H_1 | \psi_2 \rangle = \langle \psi_2 | H_2 - V_{\text{ext}2} + V_{\text{ext}1} | \psi_2 \rangle \quad (14)$$

$$E_1 < E_2 + \int n(\mathbf{r}) [V_{\text{ext}1}(\mathbf{r}) - V_{\text{ext}2}(\mathbf{r})] d^3\mathbf{r} \quad (15)$$

For the next step in the proof we will add equation 13 and 15 which results in equations 16:

$$E_1 + E_2 < E_2 + E_1 \quad (16)$$

Clearly this cannot be true. Therefore our initial assumption must be incorrect. The external potential must be a unique functional of electron density. In other words a one to one correspondence must exist between the electron density and the external potential. This is a huge leap forward in being able to model quantum systems using electron density. However, an astute observer may ask how do we know an electron density is really the ground state electron density. The second Hohenberg-Kohn theorem answers this question. It states that a functional of electron density yields the ground state energy if and only if the input electron density is the ground state electron density[42]. This theorem can handily be proved using the variational principle. First, however, sticking to Hohenberg and Kohn's derivation we first introduce a universal functional  $F[n]$ :

$$F[n] = \langle \Psi[n] | T + V_{\text{ee}} | \Psi[n] \rangle \quad (17)$$

This universal function is valid for any external potential, meaning it does not depend on the atomic structure or the number of particles. With this universal function defined, we can write the total energy of any system as:

$$E[n] = \int V_{\text{ext}}(\mathbf{r})n(\mathbf{r})d^3r + F[n] \quad (18)$$

Now we simply insert a trial wave function,  $\Psi'$ , with its own charge density  $n'(\mathbf{r})$ , its own external potential  $V'_{\text{ext}}$ , and its own Hamiltonian  $H'$  into equation 18.

$$E[n'] = \langle \Psi' | H' | \Psi' \rangle = F[n'] + \int V_{\text{ext}}(\mathbf{r})n(\mathbf{r})d^3r \quad (19)$$

We know through the variational principle that since this wave function is not the ground state wave function,  $\psi$ , its energy when operated on by the Hamiltonian must be higher than the ground state energy.

$$\langle \Psi' | H | \Psi' \rangle = E[n'] > E[n] = \langle \Psi | H | \Psi \rangle \quad (20)$$

Thus we have proven the second Hohenberg-Kohn theorem which states that a functional of electron density yields the ground state energy if and only if the input electron density is the ground state electron density. With the proofs out of the way we may now move on to how to make practical use of these two theorems.

### **2.3 Kohn-Sham Equations**

The Kohn-Sham equations are a set of equations that aim to utilize the Hohenberg-Kohn theorems [43]. Kohn and Sham devised these equations roughly a year after the ground breaking paper in which the Hohenberg-Kohn theorems appeared. Recall from the previous section that if we know the universal function,  $F[n]$ , we could easily minimize the total energy of the system, hence finding the ground state. However, this turns out to be impossible as we only know the form of classical electron-electron interaction exactly. To remedy this situation, Kohn and Sham

had the clever idea to build a reference system of non-interacting electrons that delivers the same ground state electron density such that

$$n(\mathbf{r}) = \sum_{i=1}^N |\varphi_i|^2 \quad (21)$$

In this equation we introduce the Kohn-Sham orbitals,  $\varphi_i$ . Summing the moduli squared of these orbitals leads to the correct electron density connecting our fictitious system of non-interacting electrons to the real system we are interested in. The benefit of using a system of non-interacting electrons is that we know the kinetic energy of a system of non-interacting electrons.

$$T_{KS} = -\frac{1}{2} \sum_{i=1}^N \langle \varphi_i | \nabla^2 | \varphi_i \rangle = -\frac{1}{2} \sum_{i=1}^N \int \varphi_i^*(\mathbf{r}) \nabla^2 \varphi_i(\mathbf{r}) d^3r \quad (22)$$

In this equation, and the ones following, we will work in natural units;  $e$ ,  $\hbar$ ,  $(1/4\pi\epsilon_0)$  and  $m$  all equal 1. First note that the kinetic energy of our fictitious systems is of course not equal to the kinetic energy of our real system. Kohn and Sham accounted for this by modifying the universal function,  $F[n]$ , to include the error introduced by using a system of non-interacting electrons.

$$F[n] = T_{KS}[n] + J[n] + E_{xc}[n] \quad (23)$$

In this updated universal function  $T_{KS}$  is of course the kinetic energy of our system of non-interacting electrons,  $J$  is the classical electron-electron interaction, and  $E_{xc}$  is the newly introduced exchange-correlation energy. This term can be further broken apart into:

$$E_{xc}[n] = T_c[n] + E_{xcl}[n] \quad (24)$$

In this equation  $T_c$  is the kinetic energy correlation term. It includes the error in the kinetic energy by assuming our electrons are non-interacting.  $E_{xcl}$ , on the other hand, is the electron-

electron exchange-correlation term.  $E_{xc}[n]$  not only contains electron-electron correlation energy but also the exchange energy of the electrons (electrons are fermions and cannot occupy the same quantum state at the same time), and also any electron self-interaction error.

Altogether, the exchange-correlation term contains all the information we do not know exactly.

We can now write the total energy of any system by combining equation 23 and 18:

$$E[n] = T_{KS}[n] + J[n] + E_{xc}[n] + \int V_{ext}(\mathbf{r})n(\mathbf{r})d^3r \quad (25)$$

To find the ground energy we can apply the variational principle to this equation:

$$\frac{\delta E[n]}{\delta n(\mathbf{r})} = \frac{\delta T_{KS}[n]}{\delta n(\mathbf{r})} + \frac{\delta J[n]}{\delta n(\mathbf{r})} + \frac{\delta E_{xc}[n]}{\delta n(\mathbf{r})} + V_{ext} = \frac{\delta T_{KS}[n]}{\delta n(\mathbf{r})} + V_{ee} + V_{xc} + V_{ext} = \frac{\delta T_{KS}[n]}{\delta n(\mathbf{r})} + V_{eff} \quad (26)$$

As we can see from equation 26 we have successfully reduced down our original problem down to the problem of a system of non-interacting electrons interacting with a single effective potential  $V_{eff}$ . This problem can be solved by using the single particle Schrödinger's equation:

$$\varphi_i \left( \frac{-\nabla^2}{2} + V_{eff} \right) = \varepsilon_i \quad (27)$$

Equation 27 or rather all of the equations denoted by the subscript (i) are the Kohn-Sham equations. In these equations we see the reappearance of the Kohn-Sham orbitals and a new quantity,  $\varepsilon_i$ , the Kohn-Sham eigenvalues or energies associated with each one of the Kohn-Sham orbitals. With the Kohn-Sham equations we have successfully simplified modeling a quantum system down to one variable, electron density. This is orders of magnitudes simpler than the many-body Schrödinger's equation covered in the first section of this chapter. Furthermore, this theory is indeed exact if one knows the form of the exchange-correlation interaction. This is,

however, where an approximation must be made. In contrast to the kinetic energy, the classical electron-electron interaction, and the external potential, the exact form of the exchange-correlation term is unknown. In the next section we will cover some of the popular treatments of the exchange-correlation interaction.

## **2.4 Modeling the Exchange-Correlation Interaction**

In the previous sections we demonstrated how one can model the ground state of any quantum mechanical system. We covered the formalism of Kohn-sham DFT and illustrated that DFT is exact if we know the exact form of the exchange-correlation functional. Unfortunately, no one knows its exact form. However, there are some features of the exact exchange-correlation functional we are aware of. In fact there are 17 known exact constraints an exchange-correlation functional should fulfill [30]. Along with these constraints, researchers often design their exchange-correlation functionals to satisfy appropriate norms. They design their functionals to correctly describe systems that a functional can be expected to describe exactly or very accurately.

Despite appropriate norms and the 17 constraints an exchange-correlation functional should fulfill, one still must make approximations when designing an exchange-correlation functional. The most basic approximation is the local density approximation (LDA) where one assumes the exchange-correlation functional depends only on the electron density at each point in space. The next natural step one can take to increase an exchange-correlation functional's accuracy is to let it depend not only on the electron density but also on the gradient of the electron density at each point in space. This approximation is known as the generalized gradient approximation (GGA). One can go even further than the GGA and let the exchange-correlation functional depend on the



electron density, the gradient of the electron density, and the Laplacian of the electron density at each point in space. Functionals that take into account the Laplacian of the electron density are known as meta-GGA functionals. Both meta-GGA and GGA functionals are classified as semi-local functionals as they go beyond only taking into account the electron density at each point in space. They are not classified as nonlocal because in a truly nonlocal functional the exchange-correlation energy at a single point in space would depend on the electron density at every other point in space. In this section we focus on local and semi-local DFT starting with LDA and working our way to more complex levels of approximation.

#### 2.4.1 The Local Density Approximation (LDA)

The simplest approximation one can make when constructing an exchange-correlation functional is to assume that the functional at each point in space only depends on the electron density at that point in space. This approximation is called the local density approximation (LDA) or the local spin density approximation (LSDA) when working with spin-polarized calculations [44-48]. Kohm and Sham theorized that the LDA should provide a good description of systems in which the electron density slowly varies. If we write out the exchange-correlation energy in the LDA approximation we get the following:

$$E_{xc}^{LDA}[n] = \int \epsilon_{xc}[n(\mathbf{r})]n(\mathbf{r})d^3r \quad (28)$$

In the above equation  $\epsilon_{xc}$  is the exchange-correlation energy per electron at  $\mathbf{r}$ . In theory one can design  $\epsilon_{xc}$  as one wishes. In practice one makes an approximation to  $\epsilon_{xc}$  derived from the homogenous electron gas (HEG) model. These expressions for  $\epsilon_{xc}$  based upon the HEG model

have achieved a great deal of success. In the HEG model the exchange energy per electron is known analytically:

$$\epsilon_x[n(\mathbf{r})] = -\frac{3}{4} \left( \frac{3n(\mathbf{r})}{\pi} \right)^{\frac{1}{3}} \quad (29)$$

There are not any analytical solutions for the correlation energy per electron, however researchers tend to use the results from Monte Carlo simulations conducted by Ceperly and Alder [50]. These calculations suggest the correlation energy per electron in the low density limit behaves as:

$$\epsilon_c[n(\mathbf{r})] = \frac{\gamma}{1 + \beta_1 \sqrt{r_s} + \beta_2 r_s} \quad (30)$$

And in the high density limit the correlation energy per electron behaves as:

$$\epsilon_c[n(\mathbf{r})] = A \ln r_s + B + C \ln r_s + D r_s \quad (31)$$

Where  $r_s$ , the Wigner-Seitz parameter, is a dimensionless quantity related to the electron density:

$$r_s = [3/(4\pi n)]^{1/3} \quad (32)$$

As the LDA approximation in this form has achieved a large degree of unexpected success, LDA functionals have become popular tools for analyzing a wide array of systems at the atomic scale.

It should be noted, however, that LDA functionals tend to underestimate lattice constants and overestimate the bonding of small molecules.

### 2.4.2 The Generalized Gradient Approximation (GGA)

The Generalized Gradient Approximation [21-23,50-53] (GGA) goes beyond the LDA approximation by assuming the exchange-correlation functional depends not only on the electron density but also the gradient of the electron density. GGA functionals, like LDA functionals, can also handle spin polarized calculations when the density of spin up and spin electrons are unequal. For the case when the spin up and spin down electron densities are equal we can write the exchange-correlation energy in the GGA as:

$$\epsilon_{xc}^{GGA} = \int \epsilon_{xc}[n(\mathbf{r}), \nabla n(\mathbf{r})] n(\mathbf{r}) d^3 r \quad (33)$$

The parameter  $\epsilon_{xc}$ , as with the LDA, is the exchange-correlation energy per electron which now depends on both the electron density and the gradient of the electron density. Unlike with the LDA, there are many parameterizations of  $\epsilon_{xc}$ . One exceedingly popular GGA functional, used frequently in the dissertation, is the Perdew-Burke-Ernzerhof (PBE) functional [51]. PBE models the exchange interaction, for the case when spin is not polarized, as:

$$E_X^{GGA}[n] = \int d^3 r n \epsilon_X^{LDA}(n) F_X(s) \quad (34)$$

This equation combines the LDA exchange energy per electron with a new quantity  $F_X$ , the so-called exchange enhancement factor, which depends on a dimensionless gradient,  $s$ :

$$s = \frac{|\nabla n|}{2(3\pi^2)^{1/3} n^{4/3}} \quad (35)$$

The exact form of PBE's exchange enhancement factors looks like

$$F_X(s) = 1 + \kappa - \frac{\kappa}{(1 + \mu s^2 / \kappa)} \quad (36)$$

with  $\kappa$  being set at 0.804 and  $\mu$  being set at 0.21951. The correlation part of the PBE exchange-correlation interaction is a fair bit more complicated than the exchange part so we will not go into too much detail. However at its basic level it is the LDA correlation with an added correction.

$$E_c^{\text{GGA}}[n] = \int n[\epsilon_c^{\text{LDA}}(n) + H(r_s, t)]d^3r \quad (37)$$

The added correction,  $H$ , depends on both  $r_s$ , the Wigner-Seitz parameter, and  $t$ , which is just another dimensionless gradient. For a detailed derivation of PBE's correlation term see the original paper by Perdew, Burke, and Ernzerhof [51].

Overall, GGA type functionals, like PBE, are expected to be more accurate than LDA type functionals, meaning a GGA functional should give better results for a larger array of systems than a LDA functional. A LDA functional may perform better than a GGA functional for a particular system or a particular group of systems, but overall a GGA functional should give better result than a LDA functional.

### 2.4.3 Meta-GGA

Going further, meta-GGA functionals [24-28,30] cost even more computational time than LDA or GGA functionals. This increase in computational cost is believed to be rewarded with an increase in accuracy. The reason why meta-GGA functionals cost more than GGA functionals is because they are more mathematically complex than GGA functionals. Meta-GGA functionals, in contrast to all the functionals discussed previously, allow the exchange-correlation interaction to depend on the electron density, the gradient of the electron density, and the Laplacian of the electron density:

$$E_{xc} = \int n \varepsilon_{xc}[n, \nabla n, \nabla^2 n] d^3r \quad (38)$$

As with GGA functionals, there are many different parameterizations of  $\varepsilon_{xc}$ . In this dissertation we focus on the SCAN (Strongly Constrained and Appropriately Normed) functional [30]. As with PBE, SCAN's  $\varepsilon_{xc}$  can be divided further into an exchange and correlation energy per electron. SCAN's exchange energy per electron is exceedingly complicated and possesses a large amount of parameters. Its general form however is:

$$E_x = \int n \varepsilon_x^{LDA}(n) F_x(s, \alpha) d^3r \quad (39)$$

From our discussion of the PBE functional we are familiar with all the terms in the above equation except  $\alpha$ , which is a dimensionless Laplacian of the electron density.

$$\alpha = \frac{\tau - \tau_w}{\tau_{unif}} > 0 \quad (40)$$

Where  $\tau$  is the Laplacian of the electron density,  $\tau_w$  is the single-orbit limit of  $\tau$ , and  $\tau_{unif}$  is  $\tau$  in the uniform-density limit. With these definitions  $\tau = \tau_w$  or  $\alpha = 0$  corresponds to the single-orbit limit or the limit of a single covalent bond, and  $(\tau - \tau_w) = \tau_{unif}$  or  $\alpha = 1$  corresponds to the uniform-density limit or the metallic limit. SCAN's exchange energy per unit electron was constructed as an interpolation between  $\alpha = 0$  and  $\alpha = 1$ , and an extrapolation to  $\alpha = \infty$ . Explicitly,  $\tau_w$  and  $\tau_{unif}$  are:

$$\tau_w = |\nabla n|^2 / (8n) \quad (41)$$

$$\tau_{unif} = (3/10)(3\pi^2)^{2/3} (n)^{5/3} \quad (42)$$

The expression for SCAN's correlation energy possesses an even more complicated form than SCAN's exchange energy so we will omit it here. We will mention though, like the exchange

energy, the correlation energy is a functional of the dimensionless Laplacian of electron density,  $\tau$ , and that it was constructed as an interpolation between single-orbit limit,  $\alpha=0$ , and the uniform density limit,  $\alpha=1$ , and as an extrapolation to  $\alpha=\infty$ . The interested readers will find the correlation energy along with the rest of the derivation of SCAN in Sun's original paper [30].

As mentioned earlier in this chapter, 17 exact constraints are known which the exact exchange-correlation should fulfill. SCAN was designed to fulfill all 17 constraints in addition to being appropriately normed on systems for which one can expect a semilocal functional to perform exceedingly well on [30], making SCAN a very promising functional and a great candidate for thorough testing. The very initial testing of SCAN demonstrated that it captures the intermediate vdW forces quite well. Nonetheless, SCAN, like many other semilocal functionals, fails to appropriately account for the long range vdW interactions. This can become especially problematic for the numerous systems where the long range vdW forces are thought to be important [2-11].

## **2.5 Treating Long Range Dispersion**

Several groups with varying degrees of success have tried to compensate for semilocal DFT's failure to appropriately model long range dispersion by adding a correction term to the correlation energy [12-20]. It is useful to group these so-called vdW inclusive functionals by how they incorporate long range dispersion. Klimeš et al. [5] give a convenient way to classify methods based on how well they treat long range dispersion interactions utilizing the well-known "Jacob's Ladder". Each method lies on a specific rung of the ladder. The higher we go up on the ladder the better the methods describe the underlying physical properties that govern dispersion, and usually the more computationally expensive the methods are. On the ground

rung of the ladder we have methods that do not give the correct  $1/r^6$  asymptotic behavior for molecules in the gas phase [5]. Standard LDA, GGA, and meta-GGA methods lie on this rung. One rung higher we have methods, like DFT-D2 [13], that give the correct  $1/r^6$  asymptotic behavior for molecules in the gas phase by adding a dispersion energy of the form [5]:

$$E_{\text{dis}} = \sum_{A,B} \frac{C_6^{AB}}{r_{AB}^6} \quad (43)$$

Immediately one may notice a problem with this type of correction. The  $C_6$  parameters are completely predetermined and independent of the environment of the atom. Methods on rung two try to rectify this problem by including  $C_6$  coefficients that vary with the environment of the atom. Examples of these methods include the DFT-D3 [14], vdW(TS) [16], and the Becke-Johnson (BJ) [15] model. While these methods have had their fair share of success, the coefficients in these models, while being able to change in response to the environment of the atom, are still predetermined or require predetermined input such as atomic polarizabilities. Methods one rung further avoid requiring predetermined input by adding a nonlocal component to the local or semi-local correlation functional such that the exchange-correlation energy reads [5]:

$$E_{\text{XC}} = E_{\text{xc}}^0 + E_{\text{C}}^{\text{nl}} \quad (44)$$

Where, from left to right, we have some semilocal exchange-correlation energy paired with a non-local correlation energy. By adding this nonlocal correlation one can compute the long range dispersion interactions directly from the electron density. Examples of this type of method include the vdW-DF [2,17-18], vdW-DF2 [19], vv10[20], and rVV10[12] methods. Despite the

improvements introduced by the methods on level three of the ladder, all the methods so far have been pairwise additive. They fail to consider the medium that separates atoms and by treating the atoms separately ignore any possibility of collective excitations [5]. Any method that tries to treat these shortcomings by going beyond pairwise addition lies on the fourth and final rung of the ladder [5]. As an example of a method that lies on the fourth rung of the ladder we give the Random-Phase Approximation (RPA) treated within the framework of the adiabatic-connection fluctuation dissipation theorem (ACFD) [54-56]. Methods, like RPA, that lie on the fourth rung of the ladder are usually computationally prohibitive for even modestly sized systems. For that reason we focus on methods that lie on the third rung of the ladder: vdW-DF, vdW-DF2, and SCAN+rVV10. We also run calculations using PBE, a method on the ground rung of the ladder, for comparison.

### 2.5.1 The van der Waals (vdW) Functionals

The first two methods we focus on in this dissertation are the vdW-DF and vdW-DF2 methods. Both methods have an exchange-correlation interaction of the form:

$$E_{XC} = E_X^{GGA} + E_C^{LDA} + E_C^{nl} \quad (45)$$

They combine a GGA exchange term, the first term, with the LDA correlation term, the second term, and a nonlocal correlation term, the last term. In this dissertation we study four different flavors of the vdW-DF method: optB86b-vdW [2], optB88-vdW [17], optPBE-vdW [17], and revPBE-vdW [18,57]. We also look at one flavor of the vdW-DF2 method, rPW86-vdW2 [19,58]. While all of these methods contain the LDA correlation functional they differ on which



exchange functional, denoted by the first name of the method, and/or nonlocal correlation functional, denoted by the second name of the method, they include.

Going into the details of both methods, the mathematical form of both vdW-DF and vdW-DF2's nonlocal correlation functional can generally be written as,

$$E_c^{nl} = \frac{1}{2} \int d^3r d^3r' n(\mathbf{r})n(\mathbf{r}')\varphi(\mathbf{r}, \mathbf{r}') \quad [46]$$

where  $\varphi$  is the correlation kernel.  $\Phi$  for both the vdW-DF and vdW-DF2 methods is quite complex, but can be found in reference 18 and 19 respectively [18,19]. Note that the nonlocal nature of this functional enters this expression through the two radial vectors,  $r$  and  $r'$ , which express the distance between two different points in the electron density.

The exchange functional for these methods, on the other hand, is semilocal and much less mathematically complex than the correlation kernel. The exchange functional is actually of the exact same form as the PBE exchange functional with different enhancement factors. The exact form of the enhancement factors for optB86, optB88, optPBE, revPBE, and rPW86 are given below in equations 47-51 respectively:

$$F_x(s) = 1 + \frac{\mu s^2}{(1+\mu s^2)^{4/5}}, \mu = 0.1234 \quad (47)$$

$$F_x(s) = 1 + \frac{\mu s^2}{[1+\beta s \operatorname{arcsinh}(cs)]^{4/5}}, \mu = 0.1234, \beta = 0.1576, c = 7.7956 \quad (48)$$

$$F_x(s) = 1 + \kappa - \frac{\kappa}{(1+\mu s^2/\kappa)}, \mu = 0.175519, \kappa = 1.04804 \quad (49)$$

$$F_x(s) = 1 + \kappa - \frac{\kappa}{(1+\mu s^2/\kappa)}, \mu = 0.21951, \kappa = 1.245 \quad (50)$$

$$F_x(s) = (1 + 15as^2 + bs^4 + cs^6)^{1/15}, a = 0.0864, b = 14, c = 0.2 \quad (51)$$

### 2.5.2 SCAN+rVV10

Besides pairing a nonlocal correlation correction with a GGA type functional one can also pair a nonlocal correlation correction with a meta-GGA type functional. We already mentioned that the SCAN functional, which was designed to fulfill all 17 constraints a semilocal functional should fulfill, demonstrated a lot of promise. Naturally one would want to explore the possibility of pairing SCAN with a nonlocal correlation functional to further improve its accuracy. To date, SCAN often is paired with the rVV10 nonlocal correlation functional creating the SCAN+rVV10 [29] functional. The rVV10 functional is nothing more than a slightly revised version of the VV10 functional. SCAN+rVV10 takes the semilocal exchange and correlation terms provided by SCAN (see section 2.3.3) and tacks on the rVV10 correlation, which has a very similar form to the vdW-DF and vdW-DF2 correlation:

$$E_c^{nl} = \frac{1}{2} \int d^3r d^3r' n(\mathbf{r})n(\mathbf{r}')\varphi(\mathbf{r}, \mathbf{r}') + \beta \quad (52)$$

In this expression a new parameter,  $\beta$ , is needed to ensure that the nonlocal correlation energy goes to zero in the limit of a uniform electron gas. Besides  $\beta$  we note the reappearance of the correlation kernel,  $\varphi$ . The rVV10's correlation kernel contains two empirical parameters C and b which grant the rVV10 method more flexibility than either the vdW-DF or vdW-DF2 methods. The first parameter, C, is chosen to give accurate vdW interactions at long range. The second parameter, b, controls the damping of this interaction at short ranges. Peng et al. fits b to an Ar dimer curve calculated using the CCSD(T) method. They found b=15.7 minimized error. They left the C at its original value, 0.0093 [29], for SCAN+rVV10. We will briefly mention the

original C and b values for rVV10 are  $C=0.0093$  and  $b=6.3$  and for VV10 are  $C=0.0093$  and  $b=5.9$ .

Initial testing of this method involved calculating the interaction energies for the S22 set of molecular complexes, calculating the atomization energy and lattice volume for 50 solid systems, calculating the adsorption height and energy of benzene on coinage metals, and calculating the lattice constants and inter-layer binding energy for 28 layered materials [29]. This initial testing revealed this functional to be a promising candidate to describe a wide range of system, making it an appealing candidate for further screening.

## **2.6 General Computational Considerations**

Now that we have covered some of the important theoretical aspects of DFT, we will now move on to some of the more technical aspects of running DFT calculations. All of our technical discussion will be geared towards running calculations in the Vienna Ab initio Simulation Package (VASP) as that was the software package used to produce the results for this dissertation. Nonetheless, a great deal of our analysis will apply well to any DFT software package. In this section we will start our discourse by examining the plane wave basis sets for approximating wave functions. We will then move on to discussing the k-point sampling of the Brillouin zone. We then go over pseudopotentials and finish our discussion with the general algorithm for solving the Kohn-Sham equations.

### **2.6.1 Basis Sets: The Plane Wave Basis**

To actually run any DFT calculations one must first choose a basis set for the wave functions. Some popular choices for a basis set include Slater-type orbitals, Gaussian-type orbitals, contracted Gaussian-type orbitals, and plane waves. While the first three basis sets are quite

popular in the quantum chemistry community, a plane wave basis set is often used in computational solid state and condensed matter physics. The reason for this is simple. Solid state and condensed matter physicists often deal in periodic systems to which a plane wave basis set lends itself well to. To see this, let's first look at Bloch's theorem, which states that if electrons move in a periodic potential then one can write their wave function as [59].

$$\Psi(\mathbf{k}, \mathbf{r}) = e^{i(\mathbf{k}\cdot\mathbf{r})}u(\mathbf{r}) \quad [53]$$

Where

$$u(\mathbf{r} + \mathbf{R}_i) = u(\mathbf{r}) \quad [54]$$

Bloch's theorem allows us to write the wave function of an electron in a periodic potential as the product of a periodic part,  $u(\mathbf{k}, \mathbf{r})$ , and a plane wave part,  $e^{i(\mathbf{k}\cdot\mathbf{r})}$ . It also tells us that the wave function is not periodic in space but can vary by some exponential phase factor even though all the observables, such as electron density, are periodic in space. However, more importantly, as part of our wave function already looks similar to a plane wave it makes sense to write the periodic part of our wave function using a plane wave expansion.

$$u(\mathbf{r}) = \sum_{\mathbf{G}} C(\mathbf{G})e^{i(\mathbf{G}\cdot\mathbf{r})} \quad [55]$$

Here we have specifically chosen to expand the periodic part of wave functions in terms of the reciprocal lattice vector  $\mathbf{G}$ . Plugging this equation into equation 53 we get:

$$\Psi(\mathbf{k}, \mathbf{r}) = \sum_{\mathbf{G}} C(\mathbf{G} + \mathbf{K}) e^{i((\mathbf{k}+\mathbf{G})\cdot\mathbf{r})} \quad [56]$$

Further plugging this new equation into the single particle Schrödinger's equation, eq. 27, and multiplying on the left by  $e^{i(\mathbf{k}+\mathbf{G}')\cdot\mathbf{r}}$  we get:

$$\sum_{\mathbf{G}'} [ |\mathbf{k} + \mathbf{G}'|^2 C(\mathbf{G} + \mathbf{K}) \delta_{\mathbf{G}\mathbf{G}'} + \int V(\mathbf{r}) e^{i(\mathbf{G}-\mathbf{G}')\cdot\mathbf{r}} d^3r C(\mathbf{G} + \mathbf{K}) ] = E(\mathbf{k}) C(\mathbf{G} + \mathbf{K}) \quad [57]$$

By diagonalizing this system of equations we can solve for the eigenfunctions and eigenvalues of the Kohn-Sham equations and thus solve for the electron density. Using this plane expansion has a few advantages. The basis is orthogonal, plane waves are easy to integrate, and the wave function is periodic in reciprocal space that is  $\Psi(\mathbf{k},\mathbf{r}) = \Psi(\mathbf{k}+\mathbf{G},\mathbf{r})$ . The disadvantage is that this method assumes a periodic system, meaning when running calculations your system interacts with images of itself in the x, y, and z directions. For non-periodic systems, like a surface or molecules, this can be problematic. The solution lies in placing vacuum strategically in the unit cell. For molecules one needs to place enough vacuum around their molecule to assure that it does not interact with its images. For surfaces one can use the slab method and allow the surface to extend infinitely in the x and y direction. For the z direction, however, one must place enough vacuum to assure that the surface, represented by a slab, does not interact with itself.

Finally we must mention, using this expansion, we cannot allow our sum over  $\mathbf{G}'$  to go to infinity as we could not compute that. Therefore, we must choose an appropriate cutoff for  $\mathbf{G}'$ . Usually this cutoff is given as an energy cutoff:

$$E_{\max} = \frac{\hbar^2}{2m} G_{\max}^2 \quad [58]$$

Choosing a larger cutoff will lead to more accurate results but increase the computational cost of the calculations. One should try several different plane wave energy cutoffs when running new calculations to ensure a well converged calculation.

### 2.6.2 k-point Sampling

As seen from equation 57, when using a plane wave expansion one is generally working in the reciprocal space. Therefore, we usually need to sample a few k-vectors in reciprocal space to calculate a well converged total energy. It turns out that solutions to equation 57 can be completely characterized by their behavior in the first Brillouin zone [59] (BZ). The BZ is the fundamental volume defined by the reciprocal lattice.

$$A_{\text{BZ}} = \mathbf{G}_1 \cdot (\mathbf{G}_2 \times \mathbf{G}_3) \quad (59)$$

DFT software packages usually save time by analyzing the symmetry of the system in question and using the symmetries of the point group of your system to reduce the BZ down to the so-called “irreducible BZ”. The software then only picks a few points in the irreducible BZ to save even more computational time. In this dissertation we use the Monkhorst and Pack grid method for sampling the BZ. This method samples k-points uniformly in the BZ [60]. The user only need specify the number of k-points they wish to sample in x, y, and z directions. The more k-points one samples the greater the accuracy, but the larger the computational cost. A large k-point grid is needed to accurately calculate the electronic properties of your systems, but not to reach structural convergence.

### 2.6.3 Pseudopotentials

One problem that exists when using a plane wave basis is that strong or deep potentials, resulting from localized states, require a huge number of plane waves to achieve reasonable accuracy. Researchers deal with this problem by introducing pseudopotentials [61,62]. The first step in the pseudopotential approximation is to break the potential into core and valence electronic states. As the core electrons are bound tightly to the atom they produce the most localized states and strongly oscillating wave functions. Moreover, they usually do not contribute to chemical bonding. Therefore, we can calculate their contribution to the potential once for an isolated atom. We can then keep this part of the potential frozen in further calculations. This approximation both reduces the number of electrons we have to deal with, and rids our calculation of the most localized and rapidly oscillating electronic states. However, valence states can still oscillate rapidly in the core region. To solve this problem, we divide the volume around the atom into a core and a valence region and create a pseudopotential. Outside the core region the pseudopotential and the real potential are identical. Inside the core region, the pseudopotential is constructed such that the new wave function, a pseudo wavefunction, is nodeless and converges smoothly to a finite value. This greatly reduces the number of plane wave required in each calculation and thus saves a great deal of computational time. In this dissertation, to take advantage of pseudopotentials and improve accuracy, all calculations are actually run using the projector augmented wave (PAW) [61,63]. In this method the Kohn-Sham equations are solved using pseudopotentials. After the pseudo wave functions have been calculated, projector wave functions are built using a projection procedure. These new projector wave functions have nodes inside the core regions of the atoms, and it is from these new

functions, which are more accurate than the pseudo wave functions, that the ground state properties of our system are calculated.

#### 2.6.4 General Algorithms for Solving the Kohn Sham equations

Now that we have covered some of the basic technical considerations of a DFT calculation, we will now go over the general algorithm all DFT software packages use to solve for the ground state of a quantum system. The general algorithm is illustrated in figure 1. First we must build our unit cell including the coordinates of each individual atom. Using the positions of each atom we can construct the external potential, step 1. After constructing the external potential we must choose the appropriate pseudopotentials and select a trial electron density, step 2. From the trial electron density we can then calculate the classical electrostatic potential,  $V_{ee}$ , and the exchange-correlation term,  $V_{xc}$ , step 3. With all the terms in our effective Hamiltonian set we can then solve the Kohn-Sham equations, step 4, which will allow us to calculate a new charge density and the corresponding total energy, step 5. If the change in the total energy of the system, advancing from one charge density to the next, is less than some predetermined value then the electronic calculation has converged. If the electronic calculation failed to converge then we build a new charge density using the density calculated in step 5. We then proceed back to step 3 continuing this process until our charge density has converged. Once the charge density has converged, we calculate the forces on each atom using the Hellmann-Feynman theorem [64] from quantum mechanics:

$$\mathbf{F}_i = \langle \Psi(\mathbf{R}) | H_i(\mathbf{R}) | \Psi(\mathbf{R}) \rangle \quad (60)$$



If the forces calculated this way are less than some predetermined condition, then the system has fully relaxed. If the forces are greater than the predetermined input condition then the atoms are moved using an optimization algorithm. In this dissertation we exclusively use the conjugate gradient [65,66] (CG) method or the quasi-Newton method [67]. After the atoms are moved we then calculate a new charge density and external potential and proceed back to step 3.

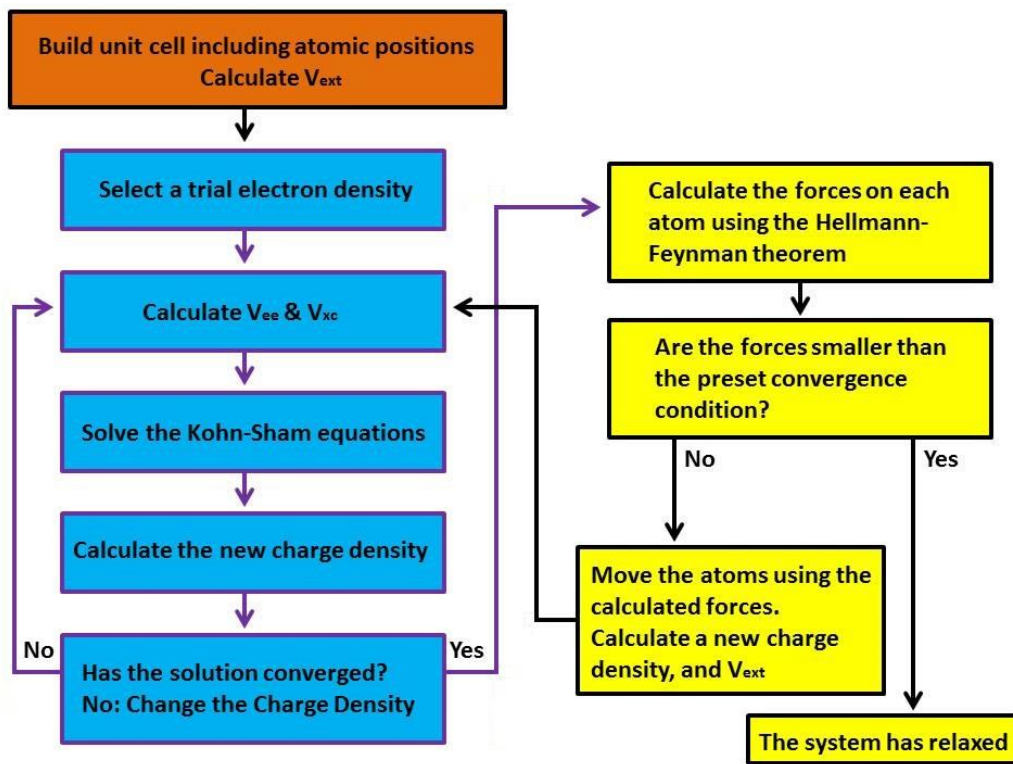


Figure 1: General algorithm for solving the Kohn-Sham equations.

## CHAPTER THREE: SCREENING THE VDW INCLUSIVE METHODS

In this chapter we explore the adsorption of pyridine and thiophene over several different transition metal surfaces with the purpose of screening the optB86b-vdW, optB88-vdW, optPBE-vdW, revPBE-vdW, rPW86-vdW2, and the SCAN+rVV10 functionals. To isolate the effect of the vdW interaction we also run calculations using the PBE functional which fails to properly describe long range correlation. It does not predict the correct  $1/r^6$  asymptotic behavior for molecules in the gas phase. We chose pyridine and thiophene for the purpose of screening as they are small organic molecules. Pyridine is composed of 11 atoms while thiophene is composed of only 9 atoms. Their small size allows us to efficiently run many calculations over a wide variety of surfaces. Moreover, as stated in the introduction, the vdW interaction is thought to play an important role in the binding of organic molecules to transition metal surfaces. Thus it makes sense to use systems of organic molecules, such as pyridine and thiophene, on transition metal surfaces to determine which vdW inclusive functional performs the best.

While the primary purpose of this chapter is to screen the optB86b-vdW, optB88-vdW, optPBE-vdW, revPBE-vdW, rPW86-vdW2, and SCAN+rVV10 functionals we also run these calculations in hopes of better understanding how pyridine and thiophene interact with transition metal surfaces, and how the vdW interaction mediates the adsorption process. As mentioned in chapter 1, the interaction of organic molecules with a substrate often determines the performance of various organic electronic devices. Therefore, we yearn to gain insight on how these small organic molecules, which are often used as the building blocks of larger organic molecules used in organic electronic devices, interact with our chosen transition metal substrates.

In the first five sections of this chapter we look exclusively at the optB86b-vdW, optB88-vdW, optPBE-vdW, revPBE-vdW, and rPW86-vdW functionals. In section one we explore the adsorption of pyridine on coinage metal surfaces: Cu, Ag, and Au(111). The vdW interaction should play an especially important role in the bonding of pyridine to these relatively unreactive surfaces. On these surfaces we also explore the effect of coverage, running calculations in both a 3x4 and 2x2 unit cell.

In the next section we look at the adsorption of pyridine on more reactive transition metal surfaces: Rh, Pt, Pd, and Ni(111) surfaces. By comparing the results in this section to the results in the previous section, where we explored the adsorption of pyridine on the coinage metal surfaces, we can more fully understand the role of the element of the surface in the adsorption of pyridine on (111) transition metal surfaces. We can also examine how the role of the vdW interactions changes in the adsorption of pyridine as we go from the right to the left side of the periodic table.

In the third section we examine adsorption of pyridine on Cu, Ag, Au, and Pt(110) surfaces. By changing the crystal face but keeping the metal the same, that is by going from Cu, Ag, Au, and Pt(111) to Cu, Ag, Au, and Pt(110), we can gain insight into how the coordination number of the surface atoms influences the bonding of pyridine to these transition metal surfaces. Note that atoms on an fcc(111) have coordination 9, while those on an fcc(110) have coordination 7.

In the fourth section of this chapter we change the molecule we study from pyridine to thiophene and explore its interaction with Cu(100) and Ni(100). Moving from pyridine to

thiophene allows us to examine the role of the heteroatom in the adsorption of organic molecules on transition metal surfaces.

Section five builds off of section four, investigating thiophene on Ag, Au, Cu, Rh, Pt, and Pd(100) surfaces. By probing the adsorption of thiophene over these group 9-11 transition metal surfaces, we aspire to gain a more complete understanding of the effect of the element of the surface on the adsorption process of thiophene.

In the last section we finally run calculations using the SCAN+rVV10 functional. We use it to study the adsorption of thiophene on Rh, Ir, and Ag(100) surfaces. With the results from section 5 and further calculations of thiophene on Ir(100) using optB88-vdW, we can compare the performance of SCAN+rVV10 with the vdW-DF method.

### **3.1 Pyridine on (111) Coinage Metals**

Pyridine on the (111) coinage metals has been extensively studied in the literature [67-85]. From the literature, one will notice that these systems can exhibit a wide range of behavior. Pyridine can bond to a coinage metal surface in one of three ways. It may bond through the lone pair of electrons situated around its N atom, resulting in a vertical adsorption configuration where the plane of the molecule sits perpendicular to the surface. It may bond through the  $\pi$ -orbitals of its aromatic ring, resulting in a flat configuration where the plane of the molecule sits parallel to the surface. Finally neither bonding through the N's lone pair of electrons nor the  $\pi$ -orbitals may dominate resulting in a tilted configuration. Additionally, changing the coverage of pyridine on these surfaces can induce a phase transition, forcing pyridine to move from a flat to a vertical configuration as one increases the coverage of pyridine [67-72]. The plethora of possible

final adsorption configurations and the possibility of a coverage driven phase transition provides a robust way to test any computational method. Therefore we study the adsorption of pyridine on the Cu, Ag, and Au(111) surfaces at two different coverages of pyridine with the goal of testing the optB86b-vdW, optB88-vdW, optPBE-vdW, revPBE-vdW, and rPW86-vdW2 functionals.

In the first subsection we address the computational details. In the next subsection we discuss the stability of the initial adsorption configurations. In the third subsection we go over the adsorption energetics and geometry of the equilibrium adsorption configurations. In the fourth subsection we tackle the electronic structure of the equilibrium adsorption configurations including charge transfer to the molecule, change in the surface's work function, and change in the d-band of the atoms that compose the first layer of substrate upon the adsorption of pyridine. In the fifth subsection we examine the role of coverage in this adsorption problem by discussing the results obtained in a smaller unit cell, i.e. at a higher coverage of pyridine. In the final subsection we present our conclusions.

### **3.1.1 Computational Details**

We perform all calculations in VASP version 5.3.5[86-89], which uses the PAW method. To model the exchange-correlation interaction we utilize the vdW inclusive optB86-vdW, optB88-vdW, optPBE-vdW, revPBE-vdW, and rPW86-vdW2 functionals. For comparison we also run calculations using a standard GGA type functional, the PBE functional.

As VASP uses periodic boundary conditions we model the (111) coinage metal surfaces using six-layer slabs. We place at least 25 Å of vacuum in between neighboring slabs to avoid

interaction between slabs. We construct all slabs using the calculated lattice constants, taken from reference 90, which we list in table 1. For comparison, we also list the experimental lattice constants, taken from reference 91, in table 1. In order to investigate the effects of coverage we explore two different superstructures. The first superstructure consists of a six-layer slab with 12 atoms composing each layer, a (3x4) atom unit cell. For this (3x4) unit cell we sample the BZ with a 6x6x1 Monkhorst-Pack grid. The second superstructure consists of a six-layer slab with 4 atoms composing each layer, a (2x2) atom unit cell. For this (2x2) unit cell we sample the BZ with a 12x12x1 Monkhorst-Pack grid. Other than this difference in k-point sampling we keep all the input parameters for the (2x2) and (3x4) unit cell calculations the same, including a 400 eV plane wave energy cutoff.

Table 1: Calculated lattice constants for Cu, Ag, and Au taken from reference 90. Experimental lattice constants taken from reference 91 are given for comparison.

Method	Cu(Å)	Ag(Å)	Au(Å)
optB86-vdW	3.598 <sup>90</sup>	4.110 <sup>90</sup>	4.140 <sup>90</sup>
optB88-vdW	3.626 <sup>90</sup>	4.147 <sup>90</sup>	4.178 <sup>90</sup>
optPBE-vdW	3.648 <sup>90</sup>	4.179 <sup>90</sup>	4.197 <sup>90</sup>
revPBE-vdW	3.702 <sup>90</sup>	4.258 <sup>90</sup>	4.261 <sup>90</sup>
rPW86-vdW2	3.747 <sup>90</sup>	4.329 <sup>90</sup>	4.352 <sup>90</sup>
PBE	3.635 <sup>90</sup>	4.154 <sup>90</sup>	4.170 <sup>90</sup>
Experimental	3.595 <sup>91</sup>	4.063 <sup>91</sup>	4.061 <sup>91</sup>

Before we place pyridine on the Cu, Ag, or Au(111) surfaces we allow both the molecule and substrate to relax separately until the forces on each atom were less than 0.02 eV/Å. To achieve this structural relaxation we use the CG method. Once we relax both the pyridine molecule and the substrate we place the pyridine molecule with its N atom approximately 3 Å

above the surface in one of the 20 adsorption configurations illustrated in figure 2. As figure 2 illustrates, 8 of the adsorption sites, a)-h), position the molecule with its plane perpendicular to the surface. We label these sites with a “v” for vertical. The remaining 12 sites, i)-t), position the molecule parallel to the surface. In the (3x4) unit cell we try all 20 adsorption sites. In the (2x2) unit cell we omit the flat bA1, bB2, fB2, and hB1 adsorption sites as those sites position neighboring pyridine molecules too close to one another. Finally, for the molecule/substrate system we allow all the atoms to undergo structural relaxation, again until the forces on each atom are less than  $0.02 \text{ eV/\AA}$ , except the atoms in the bottom three layers of the substrate which we hold at their positions in the relaxed substrate.

To measure the relative stability of each adsorption site we define adsorption energy as:

$$E_{\text{ads}} = -(E_{(\text{mol}|\text{metal})} - E_{\text{py}} - E_{\text{metal}}) \quad (61)$$

From left to right in this equation we have the adsorption energy,  $E_{\text{ads}}$ , the energy of the molecule/substrate system,  $E_{\text{mol}|\text{metal}}$ , the energy of the molecule in the gas phase,  $E_{\text{mol}}$ , and the energy of the clean surface,  $E_{\text{metal}}$ . With this definition a higher adsorption energy corresponds to a more stable adsorption configuration.

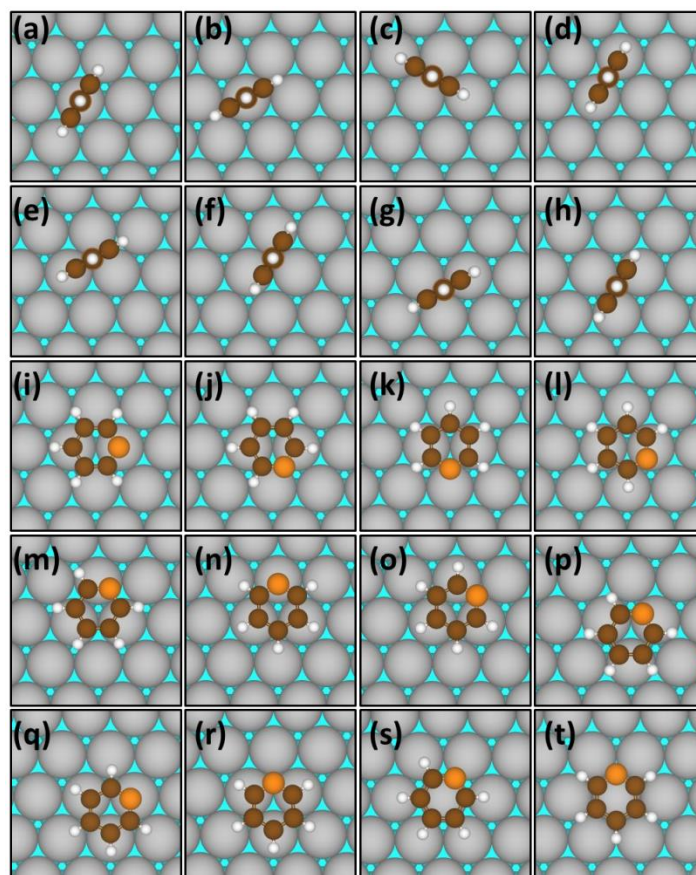


Figure 2: Initial adsorption sites a) v-a, b) v-a30, c)v-b, d)v-b90, e) v-fcc, f)v-fcc30, g)v-hcp, h)v-hvp30, i)bA1, j)bA2, k)bB1, l)bB2, m)fA, n)fB1, o)fB2, p)hA, q)hB1, r)hB2, s)t1, and t)t2 for pyridine adsorbed on the fcc (111) metal surfaces. Orange atoms represent N atoms, brown atoms represent C atoms, white atoms represent H atoms, silver atoms represent the first layer substrate atoms, and teal atoms represent the second layer and lower substrate atoms.

### 3.1.2 Stability of the Initial Adsorption Configurations

In the larger, (3x4), unit cell all the flat configurations are metastable meaning they possess a positive adsorption energy, pyridine does not move significantly off of the initial adsorption configuration, and these configurations do not yield the highest adsorption energy. The vertical v-a or v-a90 configurations, see figure 2 a) and b), always possess the largest adsorption energy. These two configurations, which place the molecule perpendicular to the surface with the molecule's N atom directly above a metal atom, are always very close in terms of adsorption



energy, demonstrating that rotating the molecule about the surface normal, once the molecule sits perpendicular on the surface, has little effect on the final adsorption energy.

Moving on, sites that end up being unstable, meaning they move to a different adsorption configuration during relaxation, are the vertical adsorption sites other than v-a or v-a30. Explicitly on Cu(111), optB86b-vdW, optB88-vdW, and optPBE-vdW predict v-fcc30 and v-hcp30 to be unstable. The optB86b-vdW and optB88-vdW functionals additionally predict v-fcc and v-hcp to be unstable. Finally, optB86b-vdW also predicts v-b90 to be unstable. These unstable adsorption sites result in a final adsorption site similar to the initial adsorption sites v-a and v-a30. Like v-a and v-a30, the pyridine's N atom in these unstable configurations is situated over a Cu atom. However unlike v-a or v-a30 the pyridine molecule in these unstable adsorption configurations is no longer strictly perpendicular to the surface acquiring a tilt angle between  $18.9^\circ$  and  $23.6^\circ$  away from the surface normal. For a visual representation of pyridine in this unstable adsorption site see figure 3. Figure 3 illustrates pyridine in this tilted final adsorption site that results from pyridine initially adsorbed in the v-fcc30 configuration on Au(111) using optB88-vdW. The unstable adsorption sites are also placed in boxes in figure 4. Figure 4 plots the adsorption energy, a), and N-Cu distances, what we define as adsorption height, b), for pyridine on Cu(111). From figure 4 a) one will note that the unstable adsorption sites possess adsorption energies close to the strictly vertical v-a and v-a30 configurations. This illustrates that one may rotate the molecule slightly towards the surface without changing the adsorption energetics. In other words, as long as pyridine's ring is far enough away from the surface and pyridine's N atom bonds to a Cu atom then pyridine will bond strongly to the surface relative to the other adsorption configurations.

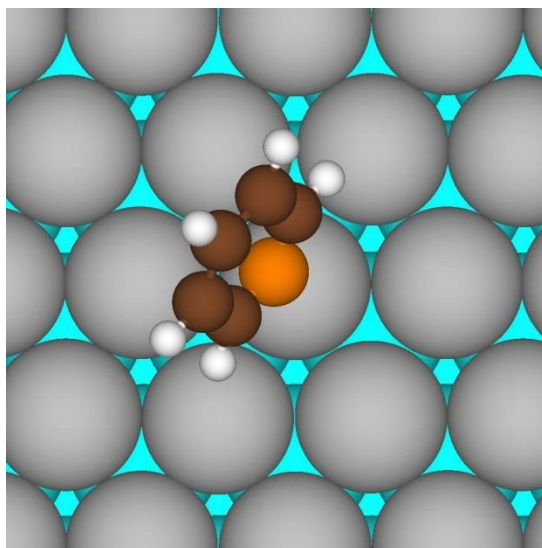


Figure 3: Final adsorption site for pyridine adsorbed initially in v-fcc30 on Au(111) calculated using optB88-vdW.

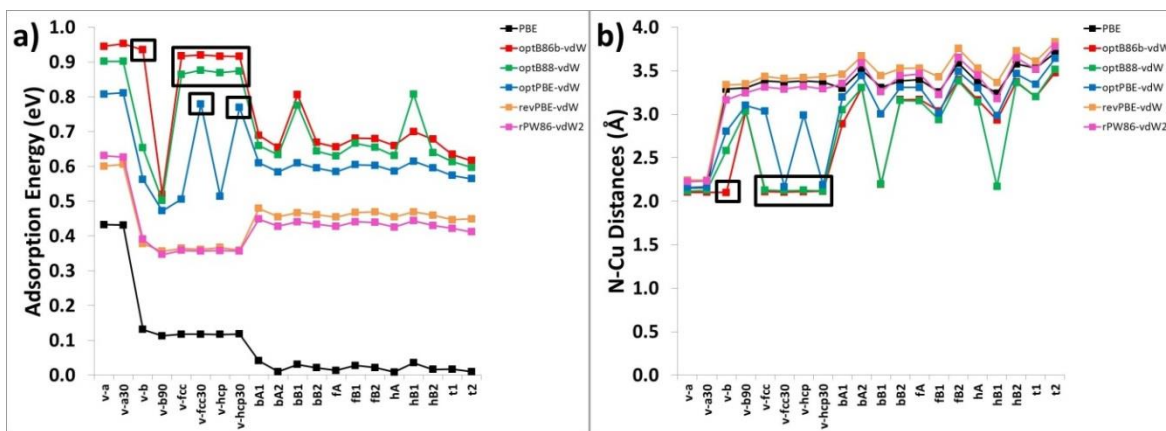


Figure 4: a) Adsorption energies and b) N-Cu distances (adsorption heights) for pyridine adsorbed on Cu(111).

Figure 4 a), in addition to illuminating how pyridine interacts with Cu(111), also illustrates the importance of the vdW interaction when describing this system. The vdW interaction enhances the adsorption energy of pyridine on Cu(111) by up to 0.52 eV going from the PBE to the optB86b-vdW functional. This enhancement appears to be asymmetrical though. Flat configurations benefit the most from the inclusion of the vdW interaction. Specifically, PBE,

our one functional that lacks vdW corrections, predicts the largest difference in adsorption energy between the flat configurations and the v-a30 configuration. For PBE we observe a 0.41 eV energy difference between the v-a30 configuration and the average adsorption energy of the flat configurations. For the vdW inclusive functionals, optB86b-vdW, optB88-vdW, optPBE-vdW, revPBE-vdW, and rPW86-vdW2, we observe a 0.28 eV, 0.24 eV, 0.22 eV, 0.14 eV, and a 0.19 eV energy difference between the v-a30 configuration and the average adsorption energy of the flat configurations. We also note that with the inclusion of the vdW interaction flat adsorption configurations yield higher adsorption energies than some vertical adsorption configurations. This is never the case for PBE where all the vertical configurations outclass all the flat configurations in terms of adsorption energy. Clearly the vdW interaction stabilizes the flat configurations more than the vertical configurations suggesting that long range dispersion is pivotal for the stability of a flat phase on Cu(111). The choice of exchange functional can also prove important to the description of this system. The optB86b-vdW functional predicts bB1 and the optB88-vdW functional predicts bB1 and hB1, both initially flat configurations, to pick up a  $27^\circ$  to a  $37^\circ$  tilt angle away from the surface, which results in these configurations having larger adsorption energies than the other flat configurations, see figure 4 a). The optPBE-vdW and revPBE-vdW methods both only differ with respect to optB86b-vdW and optB88-vdW in their choice of exchange functional, yet optPBE-vdW and revPBE-vdW fail to predict a flat configuration to pick up a large tilt angle away from the surface. Figure 4 b), which plots adsorption heights for all the initial adsorption configurations for pyridine on Cu(111), further demonstrates the difference in performance between optB86b-vdW and optB88-vdW, and optPBE-vdW and revPBE-vdW. The optB86b-vdW and optB88-vdW functionals predict the

few flat sites that pick up a sizable tilt angle away from the surface, and that have a relatively large adsorption energy, to also have small adsorption heights, less than 2.20 Å. These adsorption heights are similar to the adsorption heights of pyridine in v-a, v-a30, and the unstable vertical configurations.

On Ag(100) and Au(111) pyridine displays much of the same behavior as pyridine on Cu(111). Figure 5 a) plots the adsorption energies and figure 5 b) plots the N-Ag distances or adsorption heights for pyridine adsorbed on Ag(111). Figure 6 a) plots the adsorption energies and figure 6 b) plots the N-Au distances or adsorption heights for pyridine adsorbed on Au(111). Unstable configurations are again placed inside boxes. Starting with Ag(111), we observe that the v-a and v-a30 configurations regardless of functional give the largest adsorption energies. Moreover, the optB86b-vdW, optB88-vdW, optPBE-vdW, and rPW86-vdW2 functionals predict the v-hcp30 and v-fcc30 configurations to be unstable. These unstable sites on Ag(111) like the unstable sites on Cu(111) position the molecule such that the pyridine's N atom is above a metal atom. These final configurations, although initially completely vertical, pick up a tilt angle of up to 35° away from the surface normal. We also note that including the vdW interaction enhances the adsorption energy up to 0.48 eV. As on Cu(111), the vdW interaction enhances the flat configurations more than the vertical configurations. PBE predicts all the flat configurations to have lower adsorption energies than all of the vertical configurations. The vdW inclusive functionals, in contrast, predict the flat configurations to possess larger adsorption energies than the vertical configurations where pyridine's N atom is not on top of a metal atom, or rather the vertical configurations other than v-a, v-a30, or the unstable vertical configurations. Finally, we note that the v-a, v-a30, and the unstable vertical configurations possess the smallest adsorption

heights which is in line with their relatively large adsorption energies. Indeed, the results for pyridine on Ag(111) and pyridine on Cu(111) are strikingly similar with the only differences being that pyridine bonds more weakly to Ag(111) than Cu(111), and that on Cu(111) optB86b-vdW and optB88-vdW predict some flat configurations to pick up over a  $27^\circ$  tilt angle away from the surface.

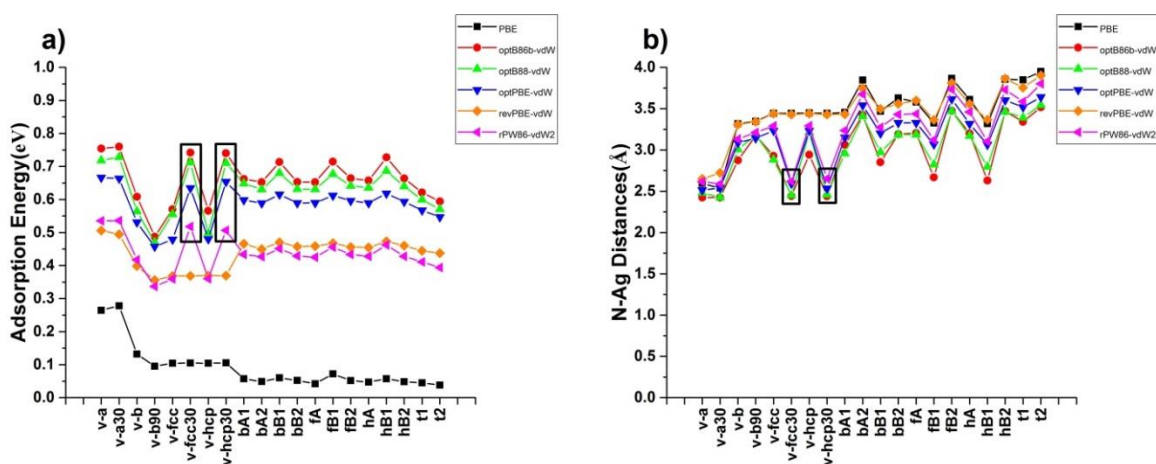


Figure 5: a) Adsorption energies and b) N-Ag distances (adsorption heights) for pyridine adsorbed on Ag(111).

On Au(111) we observe more of the same results. The adsorption configurations v-a and v-a30 always give the largest adsorption energies. Moreover we observe, similar to what was seen on Cu(111) and Ag(111), that optB86b-vdW and optB88-vdW predict v-fcc, v-fcc30, v-hcp, and v-hcp30 to be unstable adsorption configurations. When placed on these sites pyridine moves during relaxation such that the pyridine's N atom would be located above a Au atom after relaxation, and would acquire a tilt angle up to  $23^\circ$  away from the surface normal. We also observe that including the vdW interaction enhances the adsorption energy, by up to 0.52 eV, with flat configurations benefiting the most. As on the other metals, PBE predicts all the vertical

configurations to possess larger adsorption energies than all the flat configurations. In contrast, the vdW inclusive functionals predict the flat configurations to possess larger adsorption energies than the vertical configurations where pyridine's N atom is not on top of a Au atom, or rather the vertical configurations other than v-a, v-a30, and the unstable vertical configurations.

Furthermore, as on Cu(111), optB86b-vdW, optB88-vdW, and now rPW86-vdW2 predict some flat configurations to pick up a tilt angle of at least 20° away from the surface normal. These configurations have a larger adsorption energy than the other flat configurations that remained less inclined relative to the surface. Finally, we observe that the v-a, v-a30, and the unstable vertical configurations all had the smallest adsorption heights which is in line with their relatively large adsorption energies.

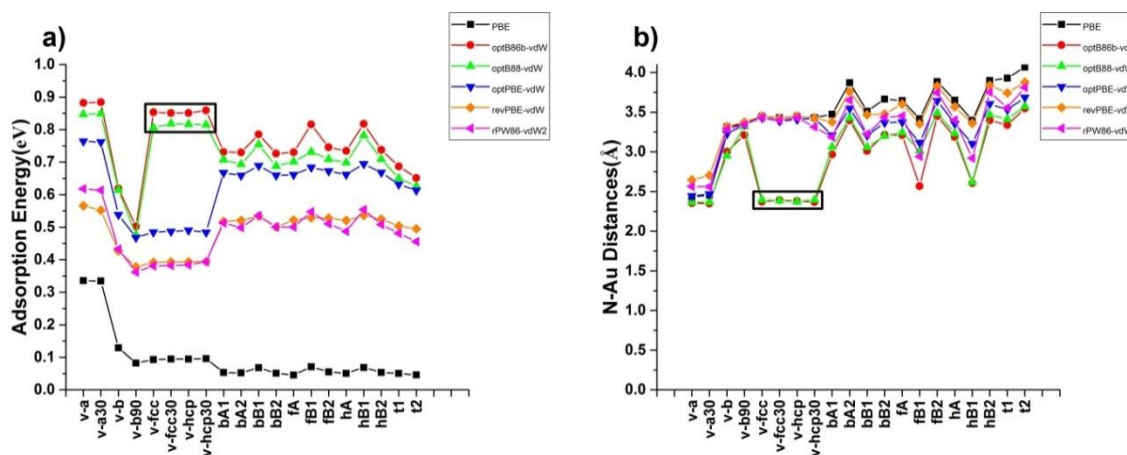


Figure 6: a) Adsorption energies and b) N-Au distances (adsorption heights) for pyridine adsorbed on Au(111).

Taking all these results together, we have demonstrated the importance of having the molecule's ring structure tilted away from the surface in order for the molecule to bond strongly with the surface. Only configurations in which pyridine's ring tilts away from the surface result

in relatively large adsorption energies and relatively short adsorption heights. Also of paramount importance to pyridine's stability on these (111) coinage metal surfaces is the proximity of the molecule's N atom to a metal atom. We note that if and only if pyridine's N atom ends up close to a metal atom does an adsorption configuration yield a relatively large adsorption energy. Strictly vertical configurations like v-b90 always gave small adsorption energies due to the large N-Metal distances. Finally, we note the importance of the vdW interaction when describing these systems. On each surface, including long range dispersion enhances the strength of the metal/molecule interaction with the flat configurations benefiting more than the vertical configurations.

Comparing with the literature, Davies and Shukla found pyridine to adsorb flat on Cu(111) at low coverage,  $2.8 \times 10^{14}$  molecules/cm<sup>2</sup> [80]. Zhong et al. found that pyridine undergoes a coverage driven phase transition on Cu(111) at approximately 0.7 ML, from a predominately flat phase to an inclined phase [70]. If you define a 1 ML the coverage at which one pyridine molecule resides on the surface per surface atom then 0.7 ML is approximately  $1.22 \times 10^{15}$  molecules/cm<sup>2</sup>. As our coverage is much lower than either  $1.22 \times 10^{15}$  molecules/cm<sup>2</sup> or  $2.8 \times 10^{14}$  molecules/cm<sup>2</sup>, our coverage is in fact  $1.37-1.49 \times 10^{14}$  molecules/cm<sup>2</sup> depending on the lattice constant we use, and pyridine is thought to move from a flat to vertical configuration as its coverage increases on these transition metal surfaces we should expect to observe pyridine to adsorb flat on Cu(111). We, however, unambiguously calculate pyridine to bond perpendicular to Cu(111), meaning our chosen functionals are perhaps poor choices to study the adsorption of pyridine on Cu(111).

On Ag(111) we also observe a disagreement with the available experimental studies. Bader et al. found pyridine to adsorb with a tilt angle of  $45^\circ$  to  $70^\circ$  on Ag(111) at low, sub-monolayer coverages[67]. Demuth et al. observed pyridine to undergo a coverage driven phase transition on Ag(111) at approximately  $3 \times 10^{14}$  molecules/cm<sup>2</sup> from a flat phase to an inclined and rotated N lone pair electron bonded phase[68]. Moreover, two other studies confirm the existence of this phase transition [69,72]. As our coverage,  $1.03\text{-}1.14 \times 10^{14}$  molecules/cm<sup>2</sup>, is lower than Demuth's coverage,  $3 \times 10^{14}$  molecules/cm<sup>2</sup>, we should expect pyridine to adsorb flat on Ag(111). However, again we unambiguously compute pyridine to adsorb in a vertical configuration on Ag(111). While one experimental study, in fact, observes pyridine to adsorb perpendicular to Ag(111) they also observe that pyridine forms a  $\sqrt{3} \times \sqrt{3} / 30^\circ$  overlayer [75], suggesting a much higher coverage than what we are simulating. In light of all this experimental evidence we must assume that our chosen functionals are poor choices to examine pyridine on Ag(111).

Finally, on Au(111) our functionals fair no better. Cai et al. observed pyridine, although in solution, to adsorb flat at low coverage [71]. Nevertheless one positive aspect of our results is that they agree with many of the available theoretical studies, which also predict pyridine to assume a vertical phase on Au(111) [81-83]. However, a few theoretical studies found flat and vertical pyridine configurations to have almost the same adsorption energies on Au(111), but they ran the calculations at either a lower coverage [84], using a  $5 \times 5$  unit cell, or using a higher performance meta-GGA functional [85], M06-L. These results demonstrate that on Au(111) our functionals can be outperformed by a more complex meta-GGA functional, and that our chosen functionals may also be poor choices to study the adsorption of pyridine on Au(111).



While all our functionals fail to predict pyridine to bond flat to any of our (111) coinage metal surfaces, the vdW inclusive functionals still are a marked improvement over the standard GGA type functional, PBE. PBE by far predicts the largest energy difference between flat and vertical adsorption configurations. The vdW interaction, captured using the vdW-DF and vdW-DF2 methods, stabilizes the flat adsorption configurations more than the vertical adsorption configurations, decreasing the overall energy difference between these two classes of adsorption sites. While the vdW inclusive functionals do not outright prefer flat adsorption configurations over vertical adsorption configurations, this decrease in the difference in adsorption energy between flat adsorption sites and vertical adsorption sites is a step in the right direction, and highlights the importance of the vdW interaction to the proper description of these pyridine/coinage metal systems.

### **3.1.3 Adsorption Heights, Energies, and Other Structural Information**

From now on we will only focus on the properties of the highest adsorption energy configurations, the configurations we would expect to be observed experimentally. By focusing on just one adsorption site we can better compare the performance of our functionals. Table 2 lists the adsorption energy ( $E_{\text{ads}}$ ) N-Metal distance or adsorption height, N-C distance, buckling of the first layer of the substrate, and tilt angle for pyridine adsorbed in the highest adsorption energy configuration on Cu, Ag, and Au(111). We define buckling of the first layer of the substrate throughout this dissertation as the maximum minus the minimum z-coordinate of the atoms that compose the first layer of the substrate. The tilt angle throughout this dissertation is defined as the angle the plane of the molecule makes with the surface normal.

Table 2: Adsorption Energy ( $E_{\text{ads}}$ ), N-Metal distance or adsorption height, N-C distance, buckling of the first layer of the substrate, and tilt angle ( $\Theta$ ) of the molecule for pyridine adsorbed on Cu, Ag, and Au(111).

Functional/Adsorption Site	Surface	$E_{\text{ads}}$ (eV)	N-Metal( $\text{\AA}$ )	N-C( $\text{\AA}$ )	Buckling ( $\text{\AA}$ )	$\Theta(^{\circ})$
PBE/v-a	Cu(111)	0.43	2.15	1.35	0.32	90
optB86b-vdW/v-a30		0.95	2.10	1.35	0.25	90
optB88-vdW/v-a30		0.90	2.13	1.35	0.28	90
optPBE-vdW/v-a30		0.81	2.17	1.35	0.29	90
revPBE-vdW/v-a30		0.61	2.24	1.36	0.30	90
rPW86-vdW2/v-a		0.63	2.23	1.35	0.34	90
PBE/v-a30	Ag(111)	0.28	2.54	1.35	0.20	90
optB86b-vdW/v-a30		0.76	2.43	1.35	0.13	90
optB88-vdW/v-a30		0.73	2.43	1.34	0.14	90
optPBE-vdW/v-a		0.67	2.51	1.35	0.16	90
revPBE-vdW/v-a		0.51	2.65	1.35	0.17	90
rPW86-vdW2/v-a30		0.54	2.59	1.35	0.16	90
PBE/v-a	Au(111)	0.34	2.43	1.35	0.18	90
optB86b-vdW/v-a30		0.88	2.35	1.35	0.11	90
optB88-vdW/v-a30		0.85	2.37	1.34	0.11	90
optPBE-vdW/v-a		0.76	2.45	1.35	0.13	90
revPBE-vdW/v-a		0.57	2.65	1.35	0.13	90
rPW86-vdW2/v-a		0.62	2.56	1.35	0.13	90

From the adsorption energies listed in table 2 we note that pyridine interacts the most strongly with Cu(111) followed by Au(111) followed by Ag(111). The adsorption heights mirror the adsorption energies if one assumes that the more strongly pyridine interacts with the surface then the closer the molecule should approach the surface. The one exception to this rule occurs using the revPBE-vdW functional which predicts pyridine on Ag(111) and Au(111) to have the same adsorption heights but different adsorption energies. While adsorption energy and adsorption height follow parallel trends according to element, the buckling of the first layer of the substrate is a more complex quantity. The Cu(111) surface buckles the most, which we would expect given it interacts the most strongly with pyridine. However the Ag(111) surface

buckles slightly more than the Au(111) surface, which is surprising given pyridine stronger interaction on Au(111). We currently have no theories to explain this anomalous behavior. Nevertheless, the buckling of the first layer of the substrate demonstrates that pyridine interacts strongly enough with these coinage metal surfaces to perturb their geometry. The last two quantities in table 2, the N-C distances and the tilt angle of the molecule, add little to what has already been said. The tilt angle of  $90^\circ$  for every functional/metal combination confirms what was stated previously, namely that pyridine prefers to adsorb completely perpendicular to these surface. The narrow range of N-C bond lengths, 1.34-1.36 Å, which are close to the gas phase N-C bond lengths, 1.34-1.35 Å, indicates once again that pyridine interacts relatively weakly with these coinage metal surfaces. Taking all the information from table 2 together we suggest that pyridine physisorbs strongly on the Cu, Ag, and Au(111) surfaces.

While each functional predicts pyridine to strongly physisorb on these coinage metal surfaces, there are some subtle differences between the performance of each functional. The adsorption energy follows a specific trend on each coinage metal surface:  $\text{PBE} < \text{revPBE-vdW} < \text{rPW86-vdW2} < \text{optPBE-vdW} < \text{optB88-vdW} < \text{optB86b-vdW}$ . The adsorption heights also follow certain trends. Among the vdW inclusive functionals the “opt-type” functionals, optB86b-vdW, optB88-vdW, and optPBE-vdW, all predict smaller adsorption heights than either the revPBE-vdW or the rPW86-vdW2 functionals. Furthermore, PBE predicts a smaller adsorption height than optPBE-vdW on Cu(111) and Au(111), and a larger adsorption height than optPBE-vdW on Ag(111). These results may suggest that revPBE-vdW and rPW86-vdW2 bind pyridine too far from these surfaces as these functionals predict larger adsorption heights than PBE. This idea is corroborated by a study finding these two functionals to be quite repulsive [2]. Due to the lack

of experimental studies that report adsorption heights or adsorption energies it is hard to judge which specific functional performs the best. However, in light of the large adsorption heights calculated by the revPBE-vdW and rPW86-vdW2 functionals, owing to their repulsive nature, and the fact that the PBE functional, as mentioned, predicts the largest energy difference between flat and vertical adsorption configurations, we must conclude that the opt-type functionals are the best choice, among our entire group of functionals, to study pyridine on the (111) coinage metal surfaces. Finally, the other three quantities listed in table 2 either vary little by functional, the tilt angle and N-C distances, or lack a striking trend, the buckling of the first layer of the substrate, and therefore cannot add anything meaningful to the discussion.

### 3.1.4 Electronic Structure Analysis

In order to further probe the interaction of pyridine with these (111) coinage metal surfaces we conduct an electronic structure analysis. We calculate the charge transfer to the molecule, the change in the width,  $\Delta W$ , and center,  $\Delta C$ , of the d-band of the atoms that compose the first layer of the substrate, and the change in the surface's work function upon the adsorption of pyridine. We list these quantities for the highest adsorption energy configurations in table 3. From table 3, we note pyridine exchanges little charge with any of the coinage metal substrates. On Cu(111) all the functionals except optB86b-vdW and optPBE-vdW predict no charge transfer from the substrate to the molecule. The optB86b-vdW and optPBE-vdW functionals predict the molecule to lose 0.1 (-e) to the substrate. Similarly, on Ag(111) all the functionals except PBE and optB86b-vdW predict no charge transfer from the substrate to the molecule. The PBE and optB86b-vdW functionals predict the molecule to lose 0.1 (-e) to the substrate. Finally, on Au(111) each functional predicts pyridine to lose 0.1 (-e) to the substrate. While the consistently

low charge transfer we observe fails to distinguish the performance of any particular functional, it reinforces our characterization of the interaction of pyridine with these coinage metal surfaces as strong physisorption.

Table 3: Charge transfer to the molecule, change in the width ( $\Delta W$ ) and the center ( $\Delta C$ ) of the atoms that compose the first layer of the substrate, and change in the surface's work function ( $\Delta\Phi$ ) for pyridine adsorbed on Cu, Ag, and Au(111) in the highest adsorption energy configuration.

Functional/Adsorption Site	Surface	Charge Transfer (-e)	$\Delta W$ (eV)	$\Delta C$ (eV)	$\Delta\Phi$ (eV)
PBE/v-a	Cu(111)	0	0.02	-0.03	-1.37
optB86b-vdW/v-a30		-0.1	-0.03	0.04	-1.44
optB88-vdW/v-a30		0	0.02	0.11	-1.27
optPBE-vdW/v-a30		-0.1	0.02	-0.03	-1.36
revPBE-vdW/v-a30		0	0.02	-0.03	-1.28
rPW86-vdW2/v-a		0	0.02	-0.03	-1.28
PBE/v-a30	Ag(111)	-0.1	0.02	-0.04	-1.02
optB86b-vdW/v-a30		-0.1	0.05	-0.07	-1.11
optB88-vdW/v-a30		0	0.06	-0.07	-1.11
optPBE-vdW/v-a		0	0.04	-0.05	-1.02
revPBE-vdW/v-a		0	0.01	-0.03	-0.91
rPW86-vdW2/v-a30		0	0.03	-0.03	-0.94
PBE/v-a	Au(111)	-0.1	0.04	-0.04	-1.20
optB86b-vdW/v-a30		-0.1	0.06	-0.05	-1.27
optB88-vdW/v-a30		-0.1	0.07	-0.06	-1.26
optPBE-vdW/v-a		-0.1	0.05	-0.04	-1.17
revPBE-vdW/v-a		-0.1	0.02	-0.02	-1.03
rPW86-vdW2/v-a		-0.1	0.04	-0.03	-1.07

The change in the width,  $\Delta W$ , and center,  $\Delta C$ , of the d-band of the atoms that compose the first layer of the substrate supports the idea that the interaction of pyridine with these coinage metal surfaces is strong physisorption. The d-band of the first layer of these substrates widens and shifts away from the Fermi energy by a small amount with the exception of Cu(111) as

calculated by optB86b-vdW, which predicts a small narrowing of the d-band and a shift of the d-band towards the Fermi energy, and Cu(111) as calculated by optB88-vdW, which predicts a shift of the d-band towards the Fermi energy. The reason for the disagreement of these two functionals with the rest of functionals is unknown. Nonetheless, looking at just the magnitude of  $\Delta W$  and  $\Delta C$  we clearly observe that pyridine interacts weakly with these transition metal surfaces. The magnitude of the shift of the d-band is never more than 0.11 eV and the magnitude of the widening of the d-band is never more than 0.07 eV. These values, which are small but not negligible, indicate strong physisorption.

The last quantity we list in table 3 is the change in the surface's work function upon the adsorption of pyridine. Overall, pyridine reduces these surfaces' work function. Now, while we observe similar results for the charge transfer and the modification of the surface's d-band across Cu, Ag, and Au(111), the change in the surface's work function varies noticeably between different metal surfaces. The decrease in the work function trends as: Cu(111) > Au(111) > Ag(111). Interestingly this is the exact same trend as the adsorption energy. This may indicate that among these coinage metal/pyridine systems the adsorption energy may be a good indicator of the expected change in the surface's work function and vice versa. Other than demonstrating this interesting correlation between adsorption energy and change in the surface's work function, these results provide us a convenient means to compare with experimental literature and provide a nice benchmark for future experiments as measuring the change in a surface's work function experimentally is both straightforward and often inexpensive. Unfortunately, Zhong et al. is the only experimental group to measure the change in these surfaces' work function upon the adsorption of pyridine. They recorded a continuous decrease in Cu(111)'s work function from

4.87 eV to 2.55 eV going from a clean Cu(111) surface to a 1 ML coverage of pyridine on Cu(111) [70]. This amounts to a maximum of a 2.32 eV decrease in Cu(111)'s work function. We are working at well below 1 ML so we should expect to observe less than a 2.32 eV decrease in Cu(111)'s work function, which is precisely what we observe, a 1.28 eV to 1.44 eV decrease in Cu(111)'s work function upon the adsorption of pyridine.

### 3.1.5 Effect of Coverage

In order to gauge the effect of coverage we ran calculations of pyridine on Au(111) and Ag(111) in a smaller 2x2 unit cell. For technical reasons we were unable to run calculations of pyridine on Cu(111) in the 2x2 unit cell. For Au(111) and Ag(111), however, in the 2x2 unit cell, like in the 3x4 unit cell, certain vertical configurations were unstable. Specifically in the 2x2 unit cell we calculate that when we place pyridine initially in the v-hcp30 or the v-fcc30 configuration, regardless of the metal composing the surface, the molecule moves during relaxation such that the final configuration results in pyridine's N atom positioned over a metal atom with the entire molecule tilted slightly off of the surface normal. For a comparison of these unstable configurations with the v-a and v-a30 configurations see table 4. Table 4 list the adsorption energy and tilt angle away from the surface, in circle brackets, of the initial v-a, v-a30, v-fcc30, and v-hcp30 configurations for pyridine adsorbed on Ag(111) and Au(111) in the 2x2 unit cell. From table 4 we note the vdW inclusive functionals predict v-a and v-a30 to possess roughly the same adsorption energy as the unstable v-fcc30 and v-hcp30 configurations except on Au(111) using optPBE-vdW and revPBE-vdW. Excluding these two cases, we note at most a 0.03 eV difference in adsorption energy between the stable v-a and v-a30 configurations and the configurations that result from the v-fcc30 and v-hcp30 configurations. Using optPBE-

vdW and revPBE-vdW on Au(111), however, we note a 0.14 eV and 0.09 eV difference in adsorption energy between the stable v-a and v-a30 configurations and the unstable configurations v-fcc30 and v-hcp30, respectively. This is almost certainly because optPBE-vdW and revPBE-vdW predict pyridine in v-fcc30 and v-hcp30 to possess a tilt angle of  $85^\circ$  and  $84^\circ$ , respectively after relaxation. The rest of the vdW inclusive functional/metal combinations predict pyridine in these unstable adsorption configurations to have a tilt angle somewhere between  $61^\circ$  and  $69^\circ$ , which appears to be the optimal tilt angle when pyridine moves into these adsorption configurations. Moving on, while PBE interestingly predicts no unstable adsorption sites in the  $3 \times 4$  unit cell, in the  $2 \times 2$  unit cell it predicts pyridine in v-fcc30 and v-hcp30 to be unstable. However, in contrast to the vdW inclusive functionals, PBE predicts these unstable adsorption sites to yield adsorption energies much smaller than their stable vertical counterparts, v-a and v-a30, and to have a tilt angle around  $80^\circ$  instead of around  $65^\circ$  away from the surface. This result reinforces the notion that the vdW interactions are critical in driving pyridine towards the surface and establishing a flat adsorption phase. Finally, we should mention that flat configurations would often tilt significantly, sometimes up to  $40^\circ$  away from the surface, even though the center of the molecule would not move off of its initial position.



Table 4: Adsorption energies and tilt angle away from the surface, in circle brackets, for pyridine adsorbed on Ag(111) and Au(111) in the initial v-a, v-a30, v-fcc30, and v-hcp30 configurations in the 2x2 unit cell.

Functional/Adsorption Site	Surface	v-a	v-a30	v-fcc30	v-hcp30
PBE	Ag(111)	0.17(90)	0.17(90)	0.09(83)	0.09(79)
optB86b-vdW		0.63(90)	0.62(90)	0.64(63)	0.63(64)
optB88-vdW		0.60(90)	0.62(90)	0.63(63)	0.63(63)
optPBE-vdW		0.55(90)	0.55(90)	0.56(62)	0.53(67)
revPBE-vdW		0.42(90)	0.42(90)	0.41(64)	0.41(65)
rPW86-vdW2		0.45(90)	0.45(90)	0.44(66)	0.46(63)
PBE	Au(111)	0.17(90)	0.15(90)	0.06(86)	0.08(80)
optB86b-vdW		0.69(90)	0.69(90)	0.69(63)	0.67(66)
optB88-vdW		0.67(90)	0.68(90)	0.68(63)	0.66(66)
optPBE-vdW		0.59(90)	0.59(90)	0.45(85)	0.60(61)
revPBE-vdW		0.45(90)	0.45(90)	0.43(67)	0.36(84)
rPW86-vdW2		0.48(90)	0.48(90)	0.47(69)	0.49(64)

From table 4, one may guess that the most stable adsorption sites on Ag(111) and Au(111) in the 2x2 unit cell were either the v-a or v-a30 configurations, or the configurations that result from pyridine moving off of the v-fcc30 or v-hcp30 configurations. This is true for every metal/functional combination except on Au(111) using rPW86-vdW2. On Au(111) rPW86-vdW2 calculates fB1 to produce the highest adsorption energy with a tilt angle of only 35°. For a list of all the adsorption energies, N-Metal distances, N-C distances, buckling of the first layer of the substrate, and tilt angles of the molecule for the highest adsorption energy configurations on each metal using each functional see table 5. In addition to illustrating the abnormal equilibrium adsorption configuration that rPW86-vdW2 predicts on Au(111), table 5 demonstrates the important effect coverage can have on the pyridine/coinage metal system. In the 2x2 unit cell we observe lower adsorption energies and larger N-Metal distances than in the 3x4 unit cell. Figure 7 which plots the adsorption energies and N-Metal distances for pyridine on Ag(111) and

Au(111) in both the 2x2 and the 3x4 unit cell for the highest adsorption energy configurations clearly illustrates this trend. Finally, we also observe a smaller or equal buckling of the first layer of the substrate in the 2x2 unit cell than in the 3x4 unit cell. All this data suggests that increasing the coverage of pyridine on Ag(111) and Au(111) decreases the strength of the pyridine/substrate interaction by a modest amount; not quite enough to reclassify the strength of the pyridine/substrate interaction. This agrees well with previous studies. Demuth et al. found pyridine to adsorb less strongly on Ag(111) as they increased the coverage of pyridine on the surface [68]. Bilić et al. also found, computationally, that increasing the pyridine coverage on Au(111) decreases the pyridine/substrate interaction [82].

Table 5: Adsorption Energy ( $E_{\text{ads}}$ ), N-Metal distances, N-C bond lengths, buckling of the first layer of the substrate, and tilt angle,  $\Theta$ , for pyridine adsorbed in the highest adsorption energy configurations in the 2x2 unit cell.

Funtional/Adsorption Site	Surafce	$E_{\text{ads}}$ (eV)	N-Metal( $\text{\AA}$ )	N-C( $\text{\AA}$ )	Buckling ( $\text{\AA}$ )	$\Theta(^{\circ})$
PBE/v-a	Ag(111)	0.17	2.69	1.34	0.17	90
optB86b-vdW/v-fcc30		0.64	2.55	1.34	0.14	63
optB88-vdW/v-fcc30		0.63	2.57	1.34	0.15	63
optPBE-vdW/v-fcc30		0.56	2.70	1.35	0.14	62
revPBE-vdW/v-a30		0.42	2.76	1.35	0.07	90
rPW86-vdW2/v-hcp30		0.46	2.76	1.35	0.16	63
PBE/v-a	Au(111)	0.17	2.70	1.34	0.12	90
optB86b-vdW/v-a30		0.69	2.48	1.34	0.09	90
optB88-vdW/v-fcc30		0.68	2.55	1.34	0.09	63
optPBE-vdW/v-hcp30		0.60	2.72	1.35	0.09	61
revPBE-vdW/v-a30		0.45	2.79	1.35	0.03	90
rPW86-vdW2/fB1		0.50	2.97	1.35	0.09	35

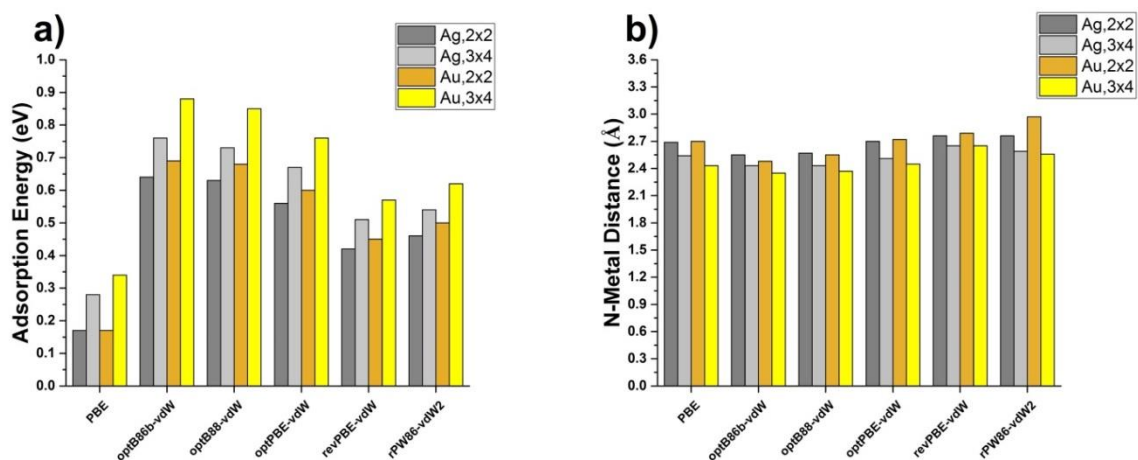


Figure 7: The adsorption energies and N-Metal distances for pyridine adsorbed on Ag(111) and Au(111) in both the 2x2 and 3x4 unit cell for the highest adsorption energy configurations.

In contrast to the pyridine/substrate interaction strength, decreasing the coverage of pyridine on Ag(111) and Au(111) appears to have little to no effect on the overall functional adsorption energy trend and the N-C bond lengths. Just as in the 3x4 unit cell the adsorption energy follows the trend  $\text{optB86b-vdW} > \text{optB88-vdW} > \text{optPBE-vdW} > \text{rPW86-vdW2} > \text{revPBE-vdW2} > \text{PBE}$  in the 2x2 unit cell, which one can see in figure 7. Moreover, the C-N bond lengths remain close to  $1.35\text{\AA}$ . This makes sense as going from the 3x4 unit cell to the 2x2 unit cell, which as stated decreases the pyridine/substrate interaction, cannot perturb the C-N bond lengths much from their values in the 3x4 unit cell as those values were already close to the gas phase pyridine N-C bond lengths. While N-C bond lengths may be unsurprising, the tilt angles in the 2x2 unit cell appear, at first glance, counterintuitive. As mention earlier in the section, the literature suggests that increasing the pyridine coverage should result in a more vertical adsorption configuration being favored. However as we increase coverage, going from the 3x4 to the 2x2 unit cell, the more tilted configurations that result from unstable adsorption sites overtake the strictly vertical v-a and v-a30 configurations in adsorption energy. However

when researchers found pyridine to go from a flat configuration to a vertical configuration on these surfaces as the coverage of pyridine increases they almost always report a tilt angle at high coverage of less than  $90^\circ$ . For example, on Ag(111) two groups found pyridine to adsorb with a tilt angle of  $70^\circ$  or  $55^\circ$  at high coverage [67,68]. Therefore it is not entirely unexpected that pyridine prefers to tilt somewhat off of the surface normal in the  $2 \times 2$  unit cell. The tilt angle of pyridine on Au(111) predicted by rPW86-vdW2 of only  $35^\circ$  may, however, be too low, indicating this functional could be especially inadequate to study the pyridine/Au(111) system.

Last, we perform an electronic structure analysis of pyridine on Ag(111) and Au(111) in the  $2 \times 2$  unit cell. We list the results in table 6, and figure 8 plots the change in the surface's work function and the change in the width of the d-band of the atoms that compose the first layer of the substrate for pyridine adsorbed on Ag(111) and Au(111) in the highest adsorption energy configurations in the  $2 \times 2$  and  $3 \times 4$  unit cell. First, the charge transfer to the molecule in the  $2 \times 2$  unit cell is about the same as in  $3 \times 4$  unit cell or slightly lower. More interesting though, the work function decreases even more as one moves from a low coverage to a higher coverage. Figure 8 a) displays this interesting and often drastic decrease in the surface's work function associated with increased pyridine coverage. The first thing one may notice from figure 8 a) is that rPW86-vdW2 predicts a relatively small decrease in the change in the Au(111) work function compared to the other functionals. This probably occurs because rPW86-vdW2 predicts a relatively flat adsorption configuration to be the most stable. Regardless, this increase in the magnitude of the change in surface's work function as one increases the coverage of pyridine is expected. Often an increased coverage of organic molecules on a transition metal surface further decreases the surface's work function. Zhong et al., as already mentioned, found Cu(111)'s

work function to decrease continually with increased pyridine coverage [70]. It is very likely the same case for Ag(111) and Au(111). Moving on, we note that increasing the coverage leads to a larger magnitude for the change of the width,  $\Delta W$ , and center,  $\Delta C$ , of the d-band of the atoms that compose the first layer of the substrate. Now increasing the coverage obviously decreases the number of the surface atoms per pyridine molecule. So while the increased coverage decreases the overall pyridine/substrate interaction, it also eliminates atoms in the substrate located far from the pyridine molecule that interact negligibly with the molecule, which is why, overall, we observe the d-band of the surface to change more in the 2x2 unit cell. Figure 8 b) plots the change in the width of the d-band,  $\Delta W$ , for pyridine adsorbed on Ag(111) and Au(111) in the highest adsorption energy configurations in the 2x2 and 3x4 unit cells and clearly shows the more perturbed d-band in the 2x2 unit cell. Finally, we note, as opposed to in the 3x4 unit cell, all the functionals agree that pyridine causes the surface's d-band to widen and shift away from the Fermi energy.

Table 6: Charge transfer to the molecule, change in the width ( $\Delta W$ ) and the center ( $\Delta C$ ) of the atoms that compose the first layer of the substrate, and change in the surface's work function for pyridine adsorbed on Ag(111) and Au(111) in the highest adsorption energy configuration in the 2x2 unit cell.

Funtional/Adsorption Site	Surafce	Charge Transfer (-e)	$\Delta W$ (eV)	$\Delta C$ (eV)	$\Delta\Phi$ (eV)
PBE/v-a	Ag(111)	0	0.07	-0.07	-2.06
optB86b-vdW/v-fcc30		0	0.13	-0.12	-2.06
optB88-vdW/v-fcc30		0	0.13	-0.12	-2.07
optPBE-vdW/v-fcc30		0	0.08	-0.09	-1.89
revPBE-vdW/v-a30		0	0.07	-0.08	-1.94
rPW86-vdW2/v-hcp30		0	0.07	-0.06	-1.80
PBE/v-a	Au(111)	0	0.10	-0.08	-2.24
optB86b-vdW/v-a30		-0.1	0.17	-0.15	-2.51
optB88-vdW/v-fcc30		-0.1	0.17	-0.14	-2.26
optPBE-vdW/v-hcp30		0	0.09	-0.09	-2.01
revPBE-vdW/v-a30		0	0.10	-0.09	-2.07
rPW86-vdW2/fB1		0	0.07	-0.07	-1.35

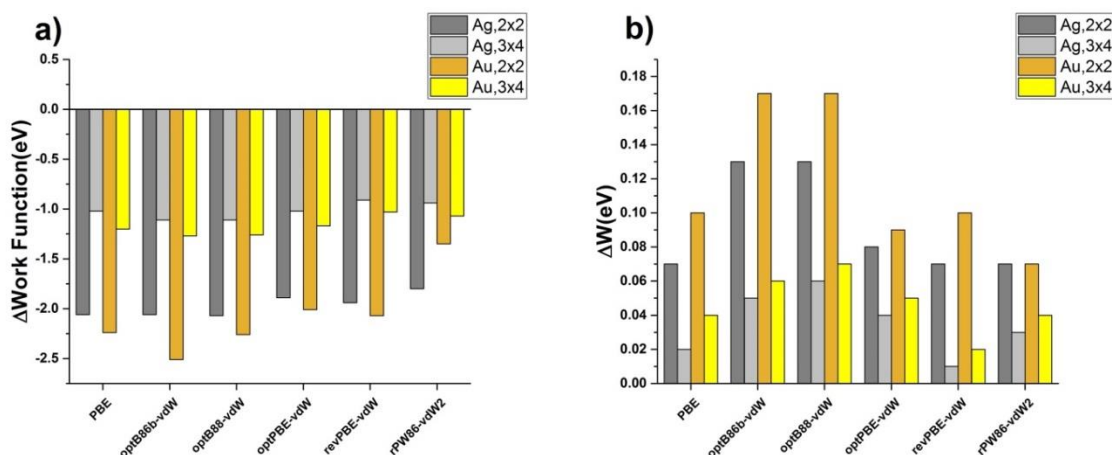


Figure 8: The change in the surface's work function and the change in the width of the d-band of the atoms that compose the first layer of the substrate for pyridine adsorbed on Ag(111) and Au(111) in the highest adsorption energy configurations in the 2x2 and 3x4 unit cell.

### 3.1.6 Conclusions

From the 2x2 unit cell results, in line with experimental insight and other theoretical investigations, we found that increasing the pyridine coverage decreases the molecule/surface interaction as indicated by lower adsorption energies and larger adsorption heights. In addition, our chosen functionals also predict a larger decrease in the surface's work function in the 2x2 unit cell in accordance with experimental observations. These functionals, with the exception of rPW86-vdW2, even predict an appropriate tilt angle for pyridine adsorbed on Ag(111) and Au(111) in the 2x2 unit cell. The rPW86-vdW2 functional, unlike the other functionals, predicts pyridine to assume a relatively flat configuration, with a tilt angle of 35° away from the surface, on Au(111) in the 2x2 unit cell. For this reason we must conclude that rPW86-vdW2 is a poor choice to study pyridine on Au(111). In spite of the relative success of the opt-type functionals, revPBE-vdW, and PBE in the smaller 2x2 unit cell, in the 3x4 unit cell all functionals perform poorly. The literature suggests that pyridine should orient itself parallel to these surfaces yet all of the functionals predict pyridine to stand upright. For this reason we must conclude all of the functionals are inadequate to study the adsorption of pyridine on the (111) coinage metal surfaces. PBE especially performs poorly as it gives the largest energy difference between flat adsorption configurations and vertical adsorption configurations. Clearly we need a better type of exchange-correlation functional to study this class of adsorption problem.

Even in light of our chosen functionals failure we still, however, learned much about the adsorption of pyridine on the coinage metals surface. We discovered that the vdW interactions play a key role in cutting the adsorption energy difference between flat and vertical configurations. As stated PBE, our one vdW exclusive functional, most strongly favored vertical

adsorption configurations, indicating that a proper description of long range dispersion is necessary for accurately describing the pyridine/coinage metal system. Finally, we unearthed that pyridine bonds relatively weakly to these surfaces as indicated by large adsorption heights and low adsorption energies in both unit cells, allowing us to categorize the interaction of pyridine with Cu, Ag, and Au(111) as strong physisorption.

### **3.2 Pyridine on (111) Reactive Metals**

Motivated by the failure of the opt-type functionals, revPBE-vdW, rPW86-vdW2, and PBE in describing the pyridine/coinage metal system, we choose to study the adsorption of pyridine on Pt, Pd, Rh, and Ni(111). Pyridine on these surfaces, as on the coinage metal surfaces, has been extensively studied [92-108]. First we wish to see whether our chosen functionals perform any better on these more reactive surfaces. In addition to examining whether our functionals perform better for the pyridine/reactive metal systems than for the pyridine/coinage metal systems, we hope these systems allow us an opportunity to meaningfully differentiate the performance of our functionals. We also wish to further explore the role the element plays in the adsorption of pyridine on single crystal surfaces.

In the first subsection of this chapter we address the details of our calculations. In the second subsection we discuss the stability of each adsorption site. In the third subsection we focus solely on the adsorption sites with the highest adsorption energies, the equilibrium adsorption configurations, and analyze their adsorption energies, adsorption heights, and other structural information. In the fourth subsection we perform an electronic structure analysis of the equilibrium adsorption configurations including charge transfer to the molecule, change in the surface's work function, and change in the d-band of the atoms that compose the first layer of the



substrate upon the adsorption of pyridine. Ni(111), being our only ferromagnetic surface, necessitated spin polarized calculations, and we devote subsection five to analyzing the change in the average magnetic moment of the atoms that compose the first layer of the Ni(111) substrate upon the adsorption of pyridine. Finally in the last subsection we present our conclusions.

### 3.2.1 Computational Details

As for the pyridine/coinage metal systems, we run all calculations using VASP. This time, however, we use version 5.4.1, which also utilizes the PAW method. We again made use of the vdW inclusive optB86-vdW, optB88-vdW, optPBE-vdW, revPBE-vdW, and rPW86-vdW2 exchange-correlation functionals, and, for comparison, the PBE exchange-correlation functional, which, as mentioned, lacks a proper description of long range dispersion forces.

To build our Pt, Pd, Rh, and Ni(111) surfaces we use the calculated lattice constants listed in table 7. For comparison we list the experimental lattice constants in table7. Again we take the calculated lattice constants from reference 90 and experimental lattice constants from reference 91. To build our surfaces we construct 6 layer slabs with each layer measuring 3 atoms in width and 4 atoms in length, a 3x4 atom surface. As VASP uses periodic boundary conditions we place at least 27 Å of vacuum in between neighboring slabs. Furthermore, we relax the molecule and the substrate separately before we place the molecule on the substrate. Once both the molecule and substrate relax, we place the molecule on the surface in one of the 20 adsorption sites explored in the previous section covering pyridine on the coinage metals, see figure 2. We then anchor the bottom three layers of the substrate at their positions in the relaxed substrate and allow the rest of the molecule/substrate system to undergo further structural relaxation.

Table 7: Calculated lattice constants for Rh, Pt, Pd and Ni taken from reference 90. Experimental lattice constants taken from reference 91 are given for comparison.

Method	Rh	Pt	Pd	Ni
optB86-vdW	3.820 <sup>90</sup>	3.960 <sup>90</sup>	3.919 <sup>90</sup>	3.489 <sup>90</sup>
optB88-vdW	3.846 <sup>90</sup>	3.988 <sup>90</sup>	3.951 <sup>90</sup>	3.511 <sup>90</sup>
optPBE-vdW	3.858 <sup>90</sup>	3.999 <sup>90</sup>	3.970 <sup>90</sup>	3.529 <sup>90</sup>
revPBE-vdW	3.896 <sup>90</sup>	4.040 <sup>90</sup>	4.023 <sup>90</sup>	3.571 <sup>90</sup>
rPW86-vdW2	3.957 <sup>90</sup>	4.117 <sup>90</sup>	4.091 <sup>90</sup>	3.610 <sup>90</sup>
PBE	3.842 <sup>90</sup>	3.980 <sup>90</sup>	3.960 <sup>90</sup>	3.525 <sup>90</sup>
Experimental	3.793 <sup>91</sup>	3.913 <sup>91</sup>	3.876 <sup>91</sup>	3.509 <sup>91</sup>

Finally, we achieve structural relaxation using the CG method. We set the force criterion for each structural relaxation at 0.02 eV/Å, the plane wave energy cutoff at 400 eV, and sample the BZ with a 6x6x1 Monkhorst-Pack grid. In order to access the stability of each adsorption configuration we again define adsorption energy according to equation 61. As one will remember, using equation 61, a higher adsorption energy corresponds to a more stable adsorption site.

### 3.2.2 Equilibrium Adsorption Configurations

Many initial pyridine adsorption sites are unstable on Rh, Pd, Pt, and Ni(111). Pyridine in some initially flat and vertical adsorption sites move into a tilted configuration. Just like pyridine on the coinage metal surfaces these unstable sites result in pyridine possessing a modest tilt angle away from the surface normal and result in the N atom of the molecule positioned over a metal atom. See figure 3 for an illustration of these types of tilted configurations. Furthermore, pyridine in some flat adsorption sites move to other flat adsorption sites; almost always bB1 but occasionally hA. Finally only revPBE-vdW's description of pyridine of Pt(111) leads to pyridine in every adsorption site being stable or metastable.

Just as we observed that both flat and vertical adsorption sites could be unstable on these surfaces, we also observe that both flat and vertical adsorption sites could be the most stable adsorption sites depending on the surface and the functional used. Concerning specific adsorption geometries, the sites v-a or v-a30 are always the most stable vertical adsorption sites. The site bB1 or sites that moved to bB1 are the most stable flat adsorption sites. To see which functional favored a flat or vertical adsorption site on each metal see figure 9. Figure 9 plots the energy difference,  $\Delta E$ , between the vertical configuration with the highest adsorption energy and the flat configuration with the highest adsorption energy for each functional/metal combination. Figure 9 gives a general impression for how strongly a functional preferred a vertical adsorption configuration on a particular metal with larger values of  $\Delta E$  in figure 9 corresponding to a stronger preference for a vertical adsorption site. From figure 9 we note that optB86b-vdW and optB88-vdW both favor a flat adsorption site on each metal surface with pyridine on Rh(111) most strongly favoring a flat adsorption site followed by pyridine on Pd(111), then pyridine on Ni(111), and finally pyridine on Pt(111). Comparing with the literature, a theoretical study by Kolsbjerg et al. agrees that pyridine adsorbs flat on Pt(111). They found, using optB88-vdW, that pyridine preferentially bonds in the flat bB1 configuration [108]. Moving on to the optPBE-vdW functional we note slightly different behavior. The optPBE-vdW functional predicts pyridine to assume a flat configuration on all the metals except Ni(111). PBE agrees with optPBE-vdW that pyridine should adsorb in a vertical configuration on Ni(111). However it also predicts pyridine to adsorb in a vertical configuration on Pt(111). Furthermore, the revPBE-vdW predicts pyridine to adsorb in a vertical configuration on even more metals: Pt, Rh, and Ni(111). On Pd(111) revPBE-vdW predicts flat and vertical adsorption sites to be nearly

equal in adsorption energy. Finally, using rPW86-vdW we note that pyridine strongly prefers a vertical adsorption site on each metal surface.

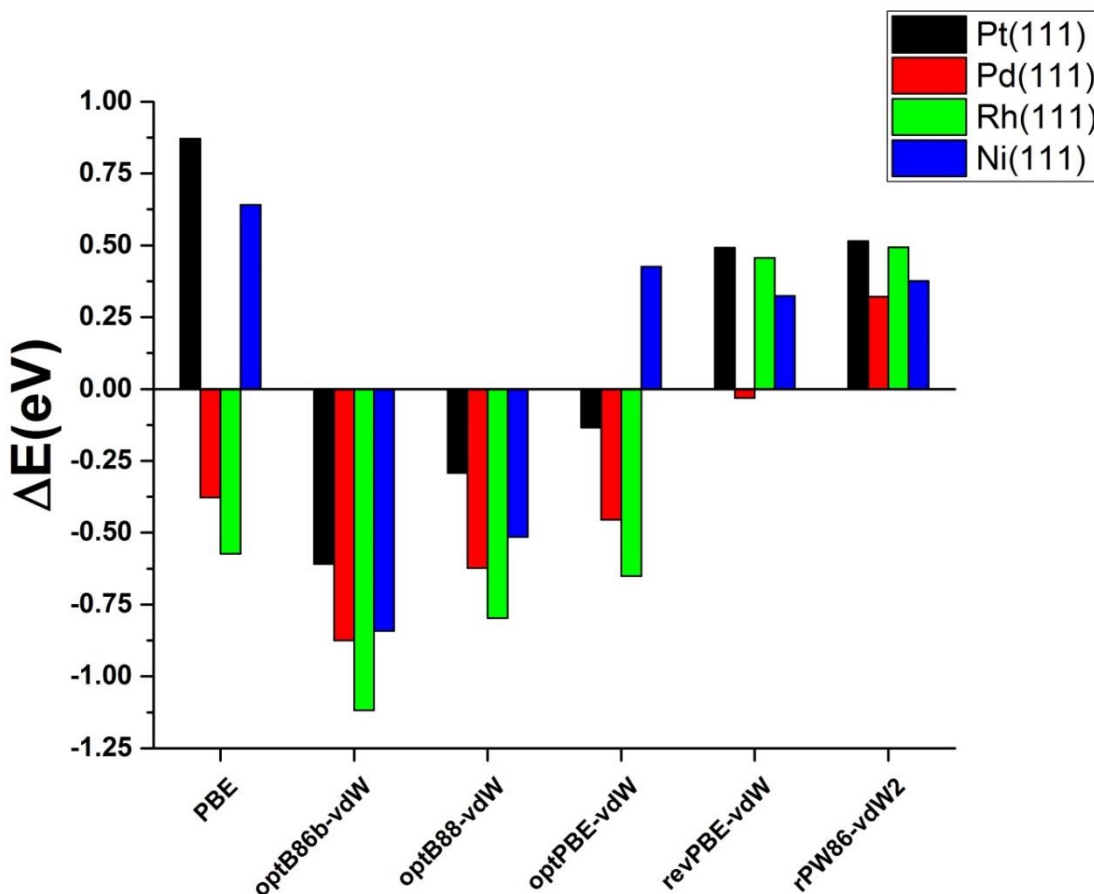


Figure 9: Energy difference,  $\Delta E$ , between the vertical adsorption configuration (tilt angle =  $90^\circ$ ) with the highest adsorption energy and the flat adsorption configuration (tilt angle  $< 10^\circ$ ) with the highest adsorption energy. A larger  $\Delta E$  corresponds to a particular functional more strongly favoring a vertical adsorption configuration on a given surface.

With such a contrast in the performance of our chosen functions it is now possible to assess, in depth, the performance of each one. On Rh(111) at room temperature Netzer and Rangelov found pyridine to adsorb flat at low coverage and inclined at high coverage [92]. While they fail to provide an exact coverage we may reasonably expect pyridine to adsorb flat on Rh(111) as we

are working at a reasonably low coverage and at 0 K. As one lowers the temperature of other pyridine/transition metal systems one notes a general increased preference for flat configurations [96], meaning it is likely pyridine on Rh(111) behaves in the same way. If pyridine bonds parallel to the Rh(111) surface then we can say, confidently, that the opt-type functionals perform the best for this system. Moving on, Netzer and Mack found at room temperature and at 1ML coverage that pyridine adsorbs inclined on Pd(111) [94,95]. Grassian and Mutterties agree with the previous study that pyridine adsorbs inclined on Pd(111) around room temperature, 310K. At lower temperature, 170K, they found pyridine to adsorb flat on Pd(111) at 1 ML coverage [96]. Similarly Waddill and Kesmodel observed pyridine to adsorb flat on Pd(111) at 150 K and at 1 ML coverage [97]. Given that others observed pyridine to bond flat at low temperature and 1 ML coverage we should expect to calculate pyridine to adsorb flat on Pd(111). With the expectation that pyridine bonds parallel to Pd(111), the opt-type functionals provide the best description of pyridine on Pd(111). Moving on, on Ni(111) Aminpirooz et al. found pyridine to adsorb tilted  $20^\circ$  off of the surface normal at room temperature and 1 ML coverage [98]. At 125 K and low exposure Fritzsche et al. found pyridine to adsorb with a tilt angle of  $18^\circ(+2^\circ/-4^\circ)$  off of the surface [99]. At an even lower temperature, 120 K, and low coverage Cohen and Merrill observed pyridine to adsorb flat on Ni(111). At a higher coverage they found pyridine to tilt away from the surface [100]. Given these experimental results we may reasonably expect pyridine to adsorb flat or nearly flat on Ni(111) at low coverage and temperature suggesting optB86b-vdW and optB88-vdW perform the best for the pyridine/Ni(111) system. Finally on Pt(111) Haq and King found pyridine to adsorb flat on Pt(111) at low temperature and coverage [101]. At room temperature and 1 ML coverage

Horsley et al. found pyridine to adsorb vertical on Pt(111) [102]. At 240 K and 1 ML coverage Johnson et al. observed pyridine to adsorb with a tilt angle of  $52^\circ$  ( $\pm 6^\circ$ ) away from the surface [104]. Finally Wöckel et al. observed pyridine to adsorb flat on Pt(111) at low exposure and at temperatures ranging from 120K-250K [106]. Given this data we should expect pyridine to adsorb flat on Pt(111) at our simulated low coverage and temperature, which again suggests the opt-type functionals perform the best.

Using the large array of final adsorption configurations we determine that the optB86b-vdW and the optB88-vdW perform the best for the reactive metal/pyridine system. They predict pyridine to strongly favor a flat adsorption configuration on Rh, Pt, Pd, and Ni(111). In the next section by exploring the geometric details of the equilibrium adsorption site for each functional/metal surface combination we expect to further differentiate the performance of each functional and increase our understanding of how pyridine interacts with these surfaces.

### **3.2.3 Adsorption Heights, Energies, and Other Structural Information**

In table 8 we list the adsorption energy, N-Metal distance or adsorption height, N-C bond length, buckling of the first layer of the substrate, and tilt angle for the adsorption site on each metal with the highest adsorption energy for pyridine adsorbed on Rh, Pt, Pd, and Ni(111) as predicted by each functional. We list the adsorption sites in table 8 by the initial adsorption site that leads to the highest adsorption energy configuration. Note all the initial flat configurations listed in table 8 move approximately to bB1. We also, for convenience, plot the adsorption energy for the highest adsorption energy configuration as predicted by each functional on each metal surface in figure 10 a). From table 8 we notice a surprising adsorption energy trend focused around PBE. If PBE predicts a vertical adsorption site to give the highest adsorption

energy, which it does on Pt(111) and Ni(111), then the adsorption energy by functional proceeds as  $\text{PBE} < \text{revPBE-vdW} < \text{rPW86-vdW2} < \text{optPBE-vdW} < \text{optB88-vdW} < \text{optB86b-vdW}$ . This adsorption energy trend is the exact trend we noticed in the previous section where we studied the adsorption of pyridine on the coinage metal surface. If, however, PBE predicts a flat adsorption site to give the highest adsorption energy, which it does on Pd(111) and Rh(111), then the adsorption energy by functional proceeds as  $\text{revPBE-vdW} < \text{rPW86-vdW2} < \text{PBE} < \text{optPBE-vdW} < \text{optB88-vdW} < \text{optB86b-vdW}$ . PBE's two distinct performances on these surfaces are not fully yet understood. We would also like to mention that, like the pyridine/coinage metal systems, the opt-type functionals all consistently give the highest adsorption energy. Looking at the adsorption energy by metal we note another set of two distinct trends. PBE and the opt-type functionals predict the pyridine/substrate interaction strength to go as  $\text{Ni(111)} < \text{Pt(111)} < \text{Pd(111)} < \text{Rh(111)}$ . The revPBE-vdW and rPW86-vdW2 functionals predict the pyridine/substrate interaction strength to go as  $\text{Ni(111)} < \text{Pd(111)} < \text{Rh(111)} < \text{Pt(111)}$ . These two adsorption trends illustrate the importance of carefully choosing your exchange functional when describing the pyridine/reactive metal system. The opt-type functionals and revPBE-vdW all share the same correlation functionals but pair it with a different exchange partner. Using the revPBE-vdW functional, with its unique exchange functional, instead of the other vdW functionals can lead to a completely different pyridine adsorption energy hierarchy. The importance of one's choice of exchange functional for describing these systems is also highlighted by the reality that, as stated in the previous section, methods that only vary in their choice of exchange functionals can predict very different equilibrium adsorption configurations. The optB86b-vdW and optB88-vdW functionals predict pyridine to adsorb flat on Ni(111) while

the optPBE-vdW and revPBE-vdW functionals predict pyridine to adsorb vertical on Ni(111).

Clearly, the exchange functional, in addition to the correlation functional, is a key to the proper description of these systems.

Table 8: Adsorption energies, N-Metal distances (adsorption heights), N-C distances, buckling of the first layer of the substrate, and tilt angles ( $\Theta$ ) of the molecule for pyridine adsorbed on Rh, Pt, Pd and Ni(111) in the adsorption configuration with the highest adsorption energy.

Funtional/Adsorption Site	Surafce	$E_{\text{ads}}$ (eV)	N-Metal( $\text{\AA}$ )	N-C( $\text{\AA}$ )	Buckling ( $\text{\AA}$ )	$\Theta(^{\circ})$
PBE/hB1	Rh(111)	1.43	2.13	1.40	0.18	1
optB86b-vdW/hB1		2.60	2.12	1.40	0.16	1
optB88-vdW/fB2		2.22	2.15	1.39	0.20	1
optPBE-vdWhB1		1.95	2.15	1.40	0.18	1
revPBE-vdW/v-a30		1.02	2.17	1.36	0.22	90
rPW86-vdW2/v-a		1.06	2.19	1.36	0.24	90
PBE/v-a30	Pt(111)	0.96	2.10	1.36	0.24	90
optB86b-vdW/fB2		2.22	2.15	1.40	0.17	1
optB88-vdW/fB1		1.84	2.16	1.39	0.24	1
optPBE-vdW/bB1		1.55	2.18	1.40	0.30	2
revPBE-vdW/v-a30		1.12	2.15	1.36	0.24	90
rPW86-vdW2/v-a30		1.16	2.16	1.36	0.25	90
PBE/fB2	Pd(111)	1.12	2.17	1.38	0.20	1
optB86b-vdW/bB1		2.23	2.16	1.39	0.20	1
optB88-vdW/hB1		1.92	2.17	1.38	0.17	2
optPBE-vdW/bA2		1.63	2.20	1.39	0.20	1
revPBE-vdW/bB1		0.93	2.24	1.39	0.26	3
rPW86-vdW2/v-a		0.97	2.21	1.36	0.21	90
PBE/v-a30	Ni(111)	0.72	1.99	1.36	0.30	90
optB86b-vdW/hA		2.13	1.95	1.39	0.20	2
optB88-vdW/hB1		1.72	1.97	1.39	0.21	2
optPBE-vdW/v-a30		1.10	2.01	1.36	0.30	90
revPBE-vdW/v-a30		0.85	2.06	1.36	0.33	90
rPW86-vdW2/v-a		0.88	2.06	1.36	0.36	90



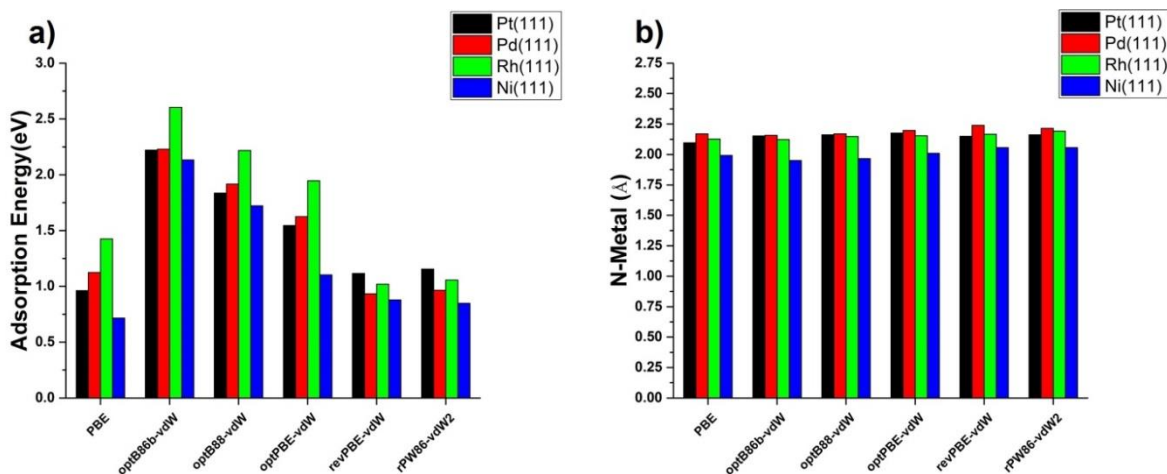


Figure 10: a) The adsorption energies and b) N-Metal distances (adsorption heights) for pyridine adsorbed on Pt, Pd, Rh, and Ni(111) in the highest adsorption energy configurations.

Moving on, this large spread of adsorption energies contrasts sharply with the narrow range of N-Metal distances. Figure 10 b plots the N-Metal distances or adsorption heights for the highest adsorption energy configuration on each metal surface as predicted by each functional. We also, as stated, list the values in table 8. From table 8 and figure 10 b we note that the N-Metal distances vary relatively little by functional. The largest variation with respect to functional choice occurs over Ni(111) where there exists a  $0.11 \text{ \AA}$  or 5.6% difference between the functionals that predict the largest N-Ni distance, rPW86-vdW2 and revPBE-vdW, and the functional that predicts the smallest N-Ni distance, optB86b-vdW. N-Metal distances vary little with respect to metal surface too, except perhaps on Ni(111). We compute the N-Metal distances of pyridine over Rh(111), Pd(100), and Pt(111) to be almost the same. On Ni(111) we observe the shortest N-Metal distances. For the buckling of the first layer of the substrate too, listed in table 10, we observe a relatively narrow range of values across all functional and metal surface combinations. The buckling of the first layer of the surface ranges from  $0.16 \text{ \AA}$  to  $0.24 \text{ \AA}$  on Rh(111),  $0.17 \text{ \AA}$  to

0.30Å on Pt(111), 0.17Å to 0.26Å on Pd(111), and 0.20Å to 0.36Å on Ni(111) with no clear trend across any of the functionals. Finally the tilt angle of the molecule,  $\Theta$ , and the N-C bond lengths vary simply with respect to whether a functional predicts a flat or a vertical configuration to be the most stable. They do not vary by metal surface. Starting with the tilt angle, the vertical configurations stay at  $90^\circ$ , and the tilt angle of the flat configurations stay below  $4^\circ$ . None of the equilibrium configurations exhibit an intermediate incline. As with tilt angle, the flat configurations possess N-C bond lengths different than the vertical configurations. If a functional predicts a flat adsorption configuration then the N-C bond lengths fall in between 1.38Å to 1.40Å. . If a functional predicts a vertical adsorption configuration then the N-C bond lengths fall at 1.36Å. The longer bond lengths of the flat configurations are not surprising given that in a flat configuration the C atoms of pyridine's aromatic ring are now able to interact with the surface.

Comparing with the literature, only one experimental study details the interaction energy, the N-C bond lengths, or the N-Metal distances of pyridine on Rh, Pt, Pd, or Ni(111). This study focused on the adsorption of pyridine on Ni(111) and reported a N-Ni bond length of 1.97 +/- 0.03 Å [99]. This N-Ni bond length is exactly the value optB88-vdW calculates and is within range of the values calculated by the PBE and optB86b-vdW functionals. This suggest those three functionals, PBE, optB86b-vdW and optB88-vdW, provide the best description of pyridine on Ni(111). However we already opined that the optB86b-vdW and optB88-vdW perform optimally for pyridine on Ni(111) based on the results of the equilibrium adsorption configurations. Nonetheless it is nice that the N-Ni bond lengths further support the conclusion that the optB86b-vdW and optB88-vdW functionals provide the best description of pyridine on

Ni(111). We should also mention we find good agreement with the Kolsbjerg et al. who also computationally found an increase in intermolecular bond lengths when pyridine moves from a vertical to flat configuration on Pt(111) [108].

Given the above structural analysis and adsorption energetics we can categorize the interaction of pyridine on these surfaces as ranging from strong physisorption to strong chemisorption depending on what functional we use on each substrate. The functionals that predict pyridine to stand vertical on the surface calculate a situation analogous to that of pyridine on the coinage metals where we determined pyridine to strongly physisorb. Therefore these functionals must also predict pyridine to strongly physisorb on these reactive metal surfaces. The functionals that predict pyridine to assume a flat configuration result in much larger adsorption energies and longer N-C bond lengths. Therefore these functionals predict pyridine to chemisorb. Finally we must mention in passing that of all the structural analysis above, the most surprising values must be the N-Metal distances. Particularly surprising is that pyridine on Ni(111) resulted in both the shortest N-Metal distances and the smallest adsorption energies. Intuitively one may think that shorter N-Metal distances should lead to larger adsorption energies as pyridine being closer to the surface should result in a stronger interaction with it. Clearly we need a deeper analysis to come up with a satisfactory explanation for this phenomenon.

### **3.2.4 Electronic Structure Analysis**

In order to better understand the nature of the adsorption of pyridine on Rh, Pt, Pd, and Ni(111) we perform an electronic structure analysis of the highest adsorption configuration on each metal surface using each functional. For the highest adsorption energy configuration on each metal as predicted by each functional we calculate the charge transfer to the molecule, the

change in the work function of the surface, and the change in the width,  $\Delta W$ , and the center,  $\Delta C$ , of the d-band of the atoms that compose the first layer of the substrate. We list the values for these quantities in table 9. From table 9 we note that the charge transfer from the substrate to the molecule depends heavily on whether the functional in question predicts pyridine to adsorb in a flat or a vertical configuration with flat configurations taking much more charge from the substrate. For this reason in figure 11 a) we plot the charge transfer to the pyridine molecule for the functional/metal combinations that lead to a flat adsorption site and in figure 11 b) we plot the charge transfer to the pyridine molecule for the functional/metal combinations that lead to a vertical adsorption site. From figure 11 a) we perceive, for the charge transfer to the molecule in flat configurations, a modest dependence on the type of metal in the substrate. The overall trend for the charge transfer for flat configurations proceeds as  $\text{Pt}(111) < \text{Pd}(111) < \text{Rh}(111) < \text{Ni}(111)$  with pyridine on  $\text{Pt}(111)$  leading the molecule to lose up to 0.1 (-e) to the substrate and pyridine on  $\text{Ni}(111)$  leading the molecule to gain 0.4 (-e) from the substrate. For the functional/metal combinations that lead to a vertical adsorption site we note little to no dependence on the type of metal. Vertical configurations result in the molecule losing 0.0 (-e) to 0.2 (-e) to the substrate. This difference in charge transfer results between flat and vertical adsorption configurations is not at all surprising as when pyridine moves from a flat to a vertical adsorption configuration it completely changes how the molecule binds to the surface. As we mentioned when pyridine bonds perpendicular to the surface it bonds through the lone pair of electrons around its N atom. This type of bonding, as our results demonstrate, leads to the pyridine molecule giving up charge to or taking less charge from the substrate. Furthermore, when pyridine bonds parallel to the surface it bonds through the  $\pi$ -orbitals of its ring. This type of bonding, as our results

demonstrate, leads to the pyridine molecule taking more charge from the substrate. As to why the vertical configurations all yield roughly the same charge transfer while the charge transfer of the flat configurations depend on the substrate is an open question and deserves further study. Nonetheless the charge transfer results demonstrate the importance of choosing a functional that predicts the proper equilibrium adsorption site. Not only will one receive the wrong geometric data from a functional that forecasts the wrong adsorption site but also a vastly different picture of the charge transfer to the molecule, which can be very important for many practical applications.

Table 9: Charge transfer to the molecule, change in the work function ( $\Delta\Phi$ ), and change in the width ( $\Delta W$ ) and the center ( $\Delta C$ ) of the d-band of the atoms that compose the first layer of the substrate for pyridine adsorbed on Rh, Pt, Pd and Ni(111) in the highest adsorption energy configuration.

Funtional/Adsorption Site	Surface	Charge Transfer (-e)	$\Delta\Phi$ (eV)	$\Delta W$ (eV) (up/down)	$\Delta C$ (eV) (up/down)
PBE/hB1	Rh(111)	0.3	-0.77	0.33	-0.07
optB86b-vdW/hB1		0.2	-0.82	0.33	-0.09
optB88-vdW/fB2		0.2	-0.81	0.32	-0.09
optPBE-vdW/hB1		0.3	-0.77	0.28	-0.08
revPBE-vdW/v-a30		-0.1	-1.33	0.06	-0.01
rPW86-vdW2/v-a		-0.1	-1.34	0.04	-0.01
PBE/v-a30	Pt(111)	-0.2	-1.51	0.12	-0.08
optB86b-vdW/fB2		-0.1	-1.14	0.57	-0.29
optB88-vdW/fB1		-0.1	-1.14	0.49	-0.28
optPBE-vdW/bB1		0.0	-1.10	0.47	-0.28
revPBE-vdW/v-a30		-0.2	-1.46	0.09	-0.08
rPW86-vdW2/v-a30		-0.2	-1.43	0.07	-0.08
PBE/fB2	Pd(111)	0.1	-0.82	0.28	-0.22
optB86b-vdW/bB1		0.1	-0.90	0.30	-0.23
optB88-vdW/hB1		0.1	-0.87	0.30	-0.21
optPBE-vdW/bA2		0.1	-0.85	0.26	-0.21
revPBE-vdW/bB1		0.1	-0.81	0.21	-0.19
rPW86-vdW2/v-a		-0.1	-1.30	0.05	-0.06
PBE/v-a30	Ni(111)	-0.1	-2.25	0.14/-0.01	-0.19/-0.03
optB86b-vdW/hA		0.4	-0.99	0.32/0.13	-0.13/-0.04
optB88-vdW/hB1		0.4	-0.37	0.20/0.15	0.02/-0.13
optPBE-vdW/v-a30		0.0	-1.59	0.18/-0.02	-0.20/0.06
revPBE-vdW/v-a30		-0.1	-1.29	0.06/-0.10	-0.27/-0.28
rPW86-vdW2/v-a		-0.1	-2.04	0.02/0.00	-0.06/0.00

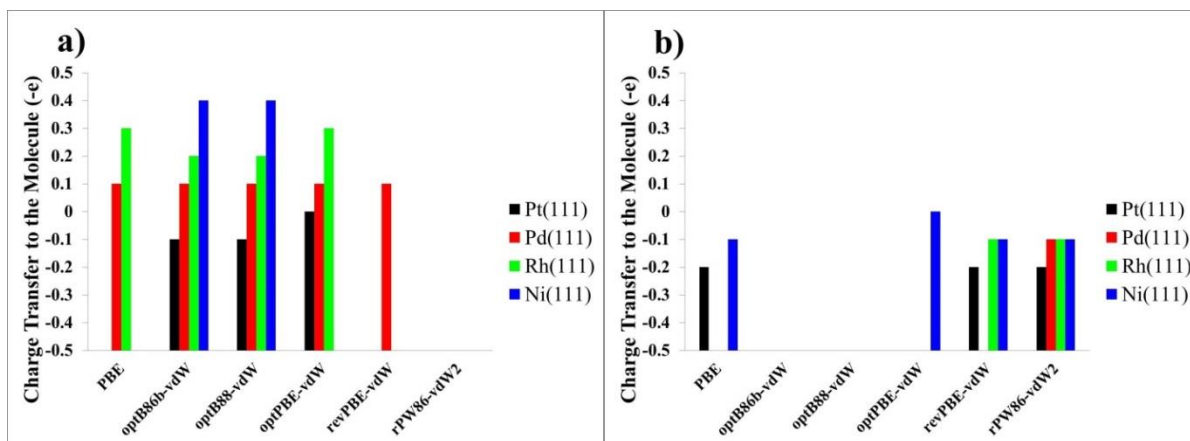


Figure 11: a) Charge transfer to the pyridine molecule for functional/metal combinations that lead to a flat equilibrium adsorption site and b) charge transfer to the pyridine molecule for functional/metal combinations that lead to a vertical equilibrium adsorption site for pyridine adsorbed on Pt, Pd, Rh, and Ni(111).

Moving on, the change in the surface's work function mirrors the charge transfer results.

Adsorption sites, on the same metal, that lead to more charge transfer to the pyridine molecule also lead to the surface having a larger work function. To understand why this happens we must consider the origins of a metal's work function. Two factors contribute to a metal's work function: the chemical potential of the bulk metal and the surface dipole consisting of negative charge on the vacuum side of the interface and positive charge on the bulk side of the interface [109]. When a molecule adsorbs on a metal surface it changes the surface's work function by modifying the surface dipole moment. Moreover, an adsorbate can modify the surface dipole in three distinct ways. First the electron clouds of the molecule, when they approach the surface, “pushback” the negative charge at the surface, reducing the surface dipole and thus reducing the surface's work function. Second charge transfer from the substrate to the molecule can modify the surface dipole, and thus the surface's work function either increasing or decreasing it depending on the sign of the charge transfer. Finally if the molecule possesses a dipole moment

that dipole moment can either add or subtract to the surface dipole depending on its orientation [109]. Now when pyridine sits flat on one of our surfaces we end up with more charge around the pyridine atom than when pyridine sits upright. This extra charge around pyridine in the interface region of our system when pyridine sits flat on these surfaces serves to increase the surface dipole counteracting the initial “pushback” effect of the molecule, meaning that flat adsorption configurations should lead to less of a decrease in the surface’s work function than vertical adsorption configurations, which is exactly what we calculate. Pyridine also possesses a dipole moment that aligns antiparallel to the surface dipole when pyridine sits upright on the surface. This should further weaken the surface dipole, and gives us another reason why pyridine in a vertical configuration lowers the surface’s work function more than pyridine in a flat configuration. Moving forward, among the different metal surfaces we also notice prominent trends. The change in Rh(111)’s work function is very roughly the same as the change in Pd(111)’s work function with vertical adsorption sites leading to about the same decrease in the surface’s work function on both surfaces, about 1.3 eV, and with flat adsorption sites leading to about the same decrease in the surface’s work function on both surfaces, roughly around 0.80 eV to 0.90 eV. On Pt(111) we note larger changes in the surface’s work function than those observed on Rh(111) or Pd(111). On Pt(111) flat adsorption sites lead to a decrease in Pt(111)’s work function ranging from 1.10 eV to 1.14 eV, and vertical adsorption sites lead to a decrease in Pt(111)’s work function ranging from 1.43 eV to 1.51 eV. Finally on Ni(111) we note a large spread values for the change in the work function even among comparable adsorption sites with optB86b-vdW predicting the smallest decrease in the surface’s work function at 0.37 eV and PBE predicting the largest decrease in the surface’s work function at



2.25 eV. Comparing with the available experimental literature, we note that Gland and Somorjai measured a 1.7 eV to 2.7 eV decrease in Pt(111)'s work function at 250° C [105]. This agrees well with our values. As the work function of a surface should change continually from the clean surface work function value to the saturated surface work function value, our values, less than -1.7 eV, at an intermediate coverage make sense. Moving on, Netzer and Mack found pyridine to decrease Pd(111)'s work function by 1.15 eV at 1 ML coverage and at room temperature [94,95]. The magnitude of this value for the change in Pd(111)'s work function is larger than all our calculated value except using rPW86-vdW2. Given again that the work function of a surface should change continually and that no one has ever observe pyridine to become more inclined as one decreases coverage, which would according to our results lead to a larger decrease in the surface's work function, this data suggests again that the rPW86-vdW2 may be ill-suited to describe the adsorption of pyridine on reactive metal surfaces. Finally Netzer and Rangelov observed a 1.65 eV decrease in Rh(111)'s work function at room temperature and at saturation coverage [92], which is again consistent with our results. Unfortunately, to the author's knowledge, no studies exist that document the change in Ni(111)'s work function upon the adsorption of pyridine. Given the large range of values we calculate for the change in Ni(111)'s work function, the experimental change in Ni(111)'s work function could be quite useful for discerning which functional provides the best description of pyridine on Ni(111).

The last two values we list in table 9 are the change in the width,  $\Delta W$ , and the change in the center,  $\Delta C$ , of the d-band of the atoms that compose the first layer of the substrate. For Pt, Pd, and Rh(111) we note  $\Delta W$  and  $\Delta C$  follow several distinct trends. First all the functionals

unanimously predict the d-band of the Pt, Pd, and Rh(111) surfaces to widen and shift away from the Fermi energy. Moreover, as with the charge transfer to the pyridine molecule and the change in the surface's work function, the modification of the d-band depends on whether a specific functional predicts a flat or a vertical adsorption site to be the most stable adsorption site.

Vertical adsorption configurations result in a smaller change in the surface's d-band than flat configurations. We anticipate this though as in a vertical configuration not only does pyridine, generally, bond less strongly to the surface than in a flat configuration but also in a vertical configuration pyridine only interacts with the surface through its N atom, which itself only bonds with one metal atom, meaning one metal atom in the surface has its d-band significantly perturbed. In a flat configuration, however, pyridine interacts with the surface through its aromatic ring, establishing not only a N-Metal bond but also up to five C-Metal bonds, resulting in many more atoms in the surface having their d-bands significantly perturbed. Naturally one would expect to calculate a larger modification of the d-band of the surface for pyridine in a flat configuration. For an illustration of the smaller change in the surface's d-band for vertical adsorption configurations we plot in figure 12 the d-band of Pd(111) before and after the adsorption of pyridine. Note in figure 12 f) the rPW86-vdW2 functional, which calculates a vertical adsorption site to be the most stable adsorption site, predicts a much smaller change to the surface's d-band than the other functionals which all calculate a flat adsorption site to be the most stable adsorption site. Moving along, if one looks at the change in the d-band by metal one will notice pyridine on Pt(111) results in the largest shift and widening of the d-band of the surface. This matches the results for the charge transfer and change in the surface's work function where pyridine on Pt(111) also leads to the smallest charge transfer from the surface to

the molecule, in most cases it actually gives charge to the substrate, and the largest change in the surface's work function, suggesting all three quantities, the change in the surface's work function, the charge transfer, and the modification of the surface's d-band, are likely tied together. Lastly on Rh(111) and Pd(111) we calculate pyridine to widen the d-band of both surfaces by approximately the same amount but to shift the d-band of Pd(111) farther away from the Fermi energy than the d-band of Rh(111), which is likely a result of the different amounts of predicted charge transfer to the molecule from each surface. Finally on Ni(111) we perform spin-polarized calculations as Ni is a ferromagnetic material. We observe, as we did for the change in Ni(111)'s work function, an exceedingly large array of results for the change in the surface's d-band. The only quantity all the functionals agree on is  $\Delta W$  of the up states, which all the functionals agree widens by some amount. This begs the question why do all of our chosen functionals disagree so strongly with one another concerning the modification of the Ni(111)'s d-band. Currently we cannot give a satisfactory answer. Pyridine on Ni(111) appears to be at the limit of PBE, the vdW, and vdW2 methods accuracy. This system presents a clear challenge to these functionals and as such may in the future be a quality system to test new computational methods.

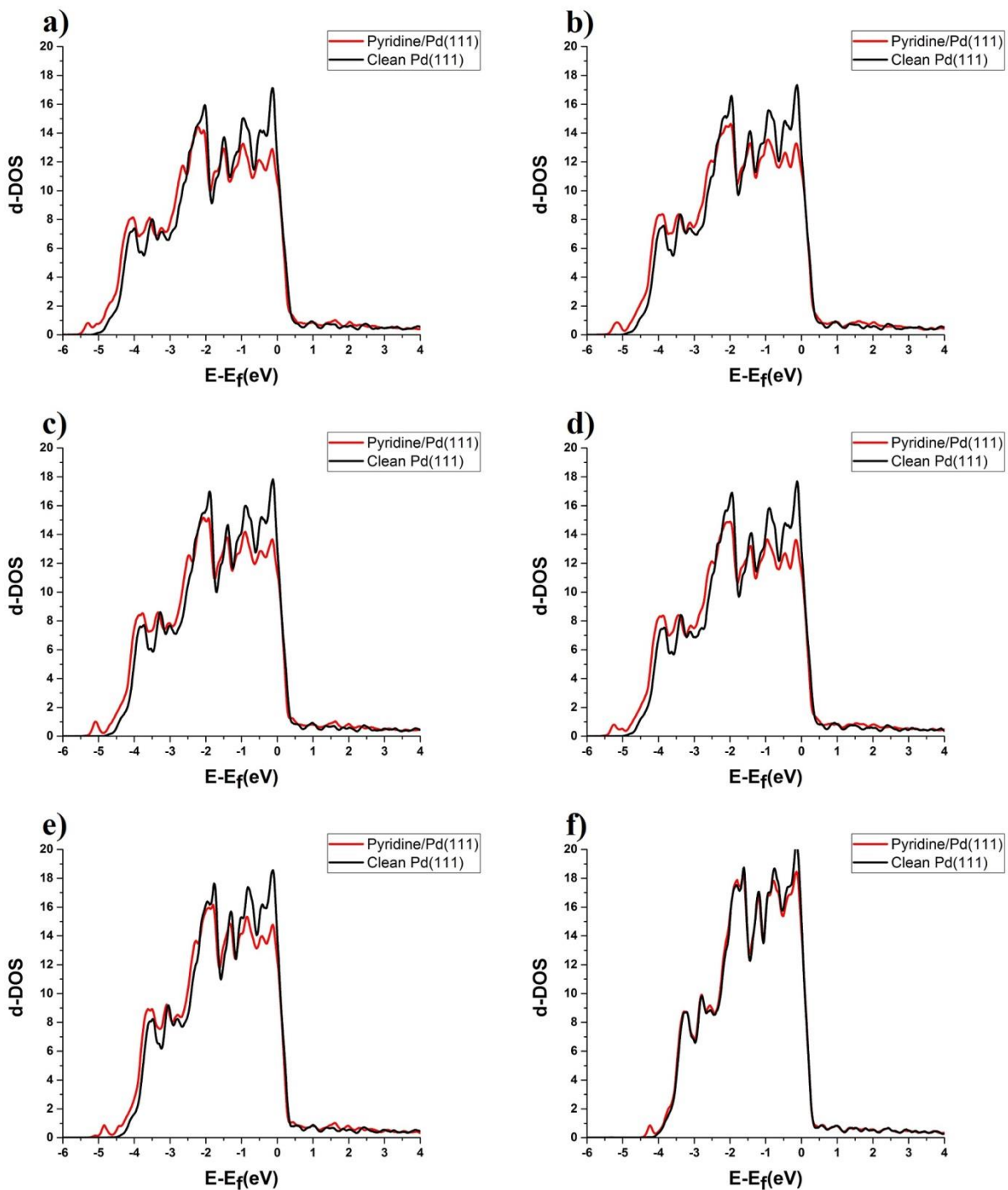


Figure 12: The d-band of the atoms that compose the first layer of the Pd(111) substrate before, black line, and after, red line, the adsorption of pyridine as calculated using the optB86b-vdW, b) optB88-vdW, c) optPBE-vdW, d) PBE, e) revPBE-vdW, and f) rPW86-vdW2 functionals

Not only have we demonstrated in this subsection that pyridine on Ni(111) is a challenging test system for our computational methods and thus a good candidate for screening future computational methods, we have also revealed important information about the other surfaces. Of Rh, Pt, and Pd(111), pyridine on Pt(111) results in the largest modification of the surface's electronic structure. We hypothesize this likely occurs because on Pt(111) all of our chosen functionals predict the pyridine molecule to take the smallest amount of charge from the surface. In almost all cases pyridine actually gives charge to Pt(111). This excess charge in the substrate probably causes the larger change in the work function of the surface and a larger modification of the surface's d-band. In any case, the larger modification of the electronic structure of Pt(111) upon the adsorption of pyridine is definitely an important distinction for this system

### **3.2.5 Change in Magnetization of Ni(111)**

As we observe the up and down d-states of Ni(111) to shift unequally upon the adsorption of pyridine we should also observe a change in the average magnet moment of the atoms that compose the first layer of the Ni(111) substrate. To that end in table 10 we list the average change in the magnet moment of the atoms that compose the first layer of the Ni(111) substrate,  $\Delta\mu$ , upon the adsorption of pyridine. From table 10 we note in agreement with the calculated values for the change in the d-band of the surface, a large range for the values of  $\Delta\mu$ . The optPBE-vdW and rPW86-vdW2 functionals predict an increase of  $\mu$  while the other functionals predict a decrease of  $\mu$  with the revPBE-vdW functional predicting the largest decrease,  $0.38 \mu_B$ .

These results again highlight that pyridine on Ni(111) sits at the edge of our functionals' accuracy. All of our chosen functionals appear to have trouble describing the electronic structure of pyridine on Ni(111). That is not to say that none of our functionals come close to describing

the reality of pyridine on Ni(111), but rather that some better, more consistent methods are needed to tackle this system. These results also indicate that pyridine on Ni(111) could be exceptionally useful for screening future computational methods given the demanding nature of the problem.

Table 10: Change in the average magnetic moment of the atoms that compose the first layer of the Ni(100) substrate,  $\Delta\mu$ , upon the adsorption of pyridine.

Functional/ Adsorption Site	$\Delta\mu(\mu_b)$
PBE/v-a30	-0.07
optB86b-vdW/hA	-0.10
optB88-vdW/hB1	-0.12
optPBE-vdW/v-a30	0.07
revPBE-vdW/v-a30	-0.38
rPW86-vdW2/v-a	0.12

### 3.2.6 Conclusions

Pyridine on Rh, Pt, Pd, and Ni(111) behaves much differently than pyridine on the coinage metal surfaces. For the pyridine/coinage metal systems, PBE, optB86b-vdW, optB88-vdW, optPBE-vdW, revPBE-vdW, and rPW86-vdW2 all perform nearly the same. They predict pyridine to adsorb perpendicular to the surface with relatively large adsorption heights making screening our different functionals exceedingly difficult. In contrast on the reactive metal surfaces our chosen functionals often disagree. Some functionals predict pyridine to adsorb parallel to the surface while others predict pyridine to adsorb perpendicular to the surface. Along with a distinct adsorption geometry, these vertical adsorption configurations are characterized by less charge transfer to the molecule and a smaller modification of the surface's electronic structure. Using these discrepancies in the performance of our functionals we conclude that the

optB86b-vdW and the optB88-vdW functionals are the best suited to study the adsorption of pyridine on reactive metal surfaces.

As our functionals calculate a diverse collection of results we also suggest that pyridine on the reactive metal surfaces could provide a useful test for any future computational methods.

Pyridine on Ni(111) may be especially useful to screen future computational methods as our functionals give the widest array of results on Ni(111). Primarily our functionals disagree the most about the electronic structure of the Ni(111) substrate after the adsorption of pyridine with practically no agreement being found regarding the change in the d-band of the atoms that compose the first layer of the substrate and the change in the average magnetic moment of the atoms that compose the first layer of the substrate.

Despite finding many dissimilarities between the performance of our chosen functionals we were able to concretely categorize the adsorption of pyridine on these surfaces as ranging from strong physisorption to strong chemisorption with functionals that predict a vertical adsorption site predicting strong physisorption and functionals that predict a flat adsorption site predicting strong chemisorption. In the case of vertical adsorption sites we observe much the same behavior as pyridine on Cu(111), which we categorized as strong physisorption, meaning that vertical adsorption configurations on these reactive metals must also display strong physisorption. For flat adsorption sites we observe a significantly more pronounced stretching of the N-C bonds and a much larger modification of the electronic structure of the molecule/substrate system. Therefore, we classify pyridine in the flat adsorption sites as strong chemisorption.

### **3.3 Pyridine on (110) Metal Surfaces**

Reproduced from W. Malone, J. von der Heyde, A. Kara, Competing adsorption mechanisms of pyridine on Cu, Ag, Au, and Pt(110) surfaces, *J. Chem. Phys.*, 149 (2018) 214703, with the permission of AIP Publishing

Thus far in our examination of the adsorption of pyridine on transition metal surfaces we have chiefly focused on the role of the element by studying the adsorption of pyridine on Cu, Ag, Au, Rh, Pt, Pd, and Ni(111). In the this next section we expand our focus and consider the role the structure of the surface plays in adsorption of pyridine on transition metal surfaces by exploring the interaction of pyridine with Cu, Ag, Au, and Pt(110). We choose these specific (110) metal surfaces to have a mix of both coinage and reactive metals to compare to our results from the previous sections where we explored the adsorption of pyridine on (111) transition metal surfaces.

Moreover, by examining how pyridine interacts with Cu, Ag, Au, and Pt(110) not only can we explore the role of surface structure on the adsorption of pyridine on transition metal surfaces we can also further screen the vdW, vdW2, and PBE methods. Like pyridine on the other transition metal surfaces we studied, many have studied pyridine on Cu, Ag, Au, and Pt(110) [110-132]. These experimental and sometimes theoretical investigations provide us a wealth of results to compare with our own, and can allow us to further critique the performance of the PBE, optB86b-vdW, optB88-vdW, optPBE-vdW, revPBE-vdW, and rPW86-vdW2 functionals.

We should mention that Au(110) and Pt(110) in reality reconstruct [133-138]. This surface reconstruction undoubtedly will affect our results. However the main goal of this section is to



again compare the performance of our six chosen functionals to which a perfect Au(110) and Pt(110) surface should suffice.

In the first subsection we present our computational details. In the second subsection we discuss the equilibrium adsorption configurations and any instability among the initial adsorption configurations. In the third subsection we explore the adsorption heights, energies, and other structural information of the equilibrium adsorption configurations. In the fourth subsection we detail the results of our electronic structure analysis of our pyridine/(110) transition metal systems, and finally in the fifth subsection we present our conclusions.

### 3.3.1 Computational Details

We perform all calculations using VASP version 5.4.1, which, as stated in previous sections, utilizes the PAW method. To the model the exchange-correlation interaction we again employ the PBE, optB86b-vdW, optB88-vdW, optPBE-vdW, revPBE-vdW, and rPW86-vdW2 functionals. To build our (110) surfaces we use the theoretical lattice constants listed in table 1 and table 7. We create each (110) surface using 5 layer thick slabs measuring 3 by 3 atoms, meaning each layer of our slab possesses 9 atoms with the entire slab containing 45 atoms. As VASP uses periodic boundary conditions we place at least 21 Å of vacuum in between neighboring slabs. After we build the surfaces and the pyridine molecule, we relax the molecule and the surface separately before placing the molecule on the surface in one of 20 adsorption sites illustrated in figure 13. 8 of these adsorption sites place the molecule with its plane perpendicular to the surface, see figure 13 a)-h). We label these sites with a “v”. The remaining 10 adsorption sites place the molecule with its plane parallel to the surface, see figure i)-t). For each adsorption site we place the molecule such that its N atom is approximately 2.7 Å above the

surface. Once we situate the molecule on the surface we allow all the atoms in our system to undergo full structural relaxation except the bottom two layers of the substrate which we hold at their relaxed positions in the clean substrate.

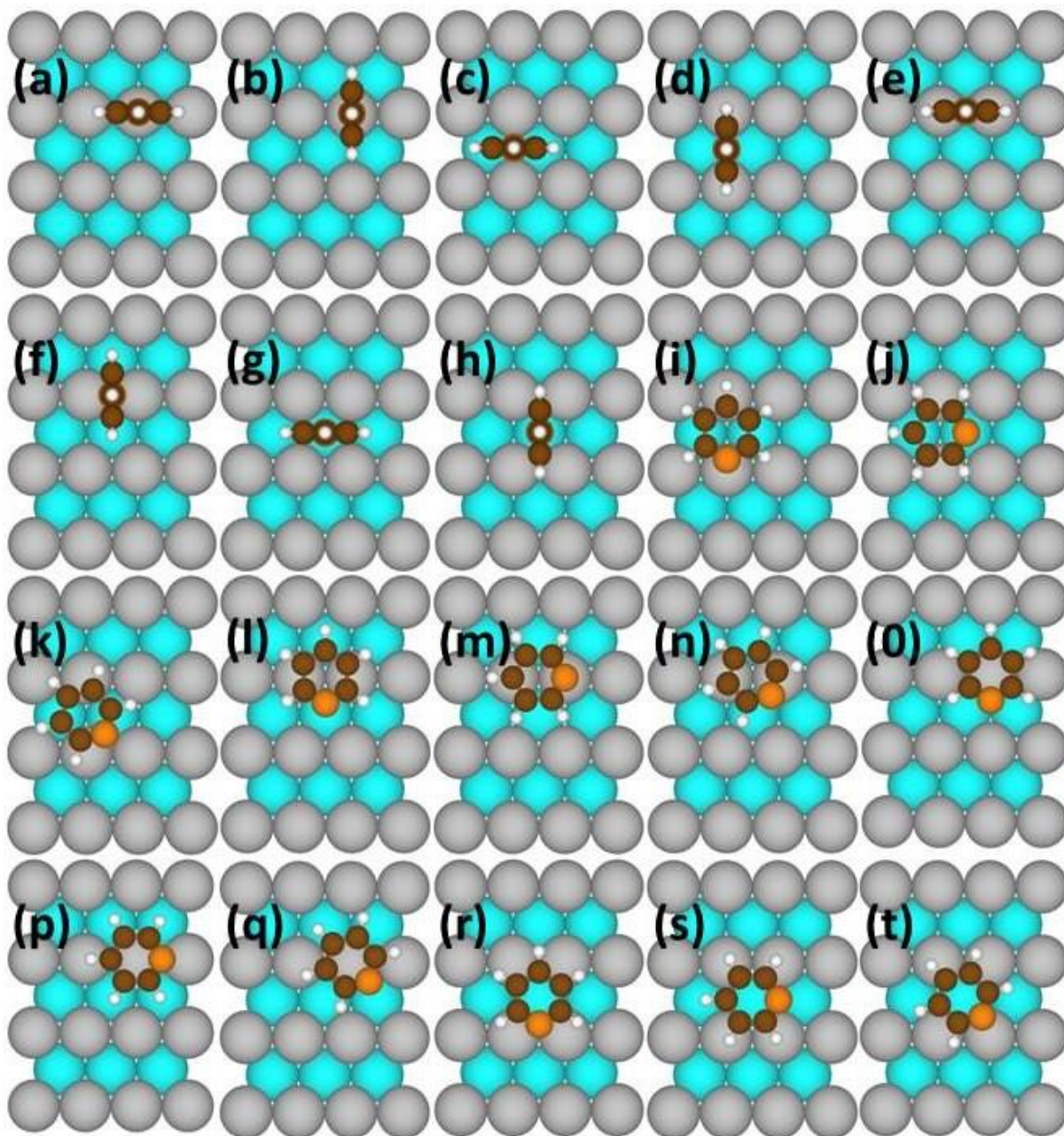


Figure 13: Initial adsorption sites a) v-top, b) v-top90, c)v-blong, d)v-blong90, e) v-bshort, f)v-bshort90, g)v-tr, h)v-tr90, i)bridgeL1, j)bridgeL2, k)bridgeL3, l)bridgeS1, m)bridgeS2, n)bridgeS3, o)top1, p)top2, q)top3, r)trough1, s)trough2, and t)trough3 for pyridine adsorbed on the fcc (110) metal surfaces. Orange atoms represent N atoms, brown atoms represent C atoms, white atoms represent H atoms, silver atoms represent the first layer metal atoms, and teal atoms represent the second layer and lower substrate atoms.

Finally, we relax all structures using the CG method. We set the plane energy cutoff at 400 eV, the force criterion at 0.02 eV/Å, and sample the BZ using a 6x6x1 Monkhorst-Pack. We again define the adsorption energy of each adsorption site using equation 61. One will remember that when using equation 61 a higher adsorption energy corresponds to a more stable adsorption site.

### 3.3.2 Equilibrium Adsorption Configurations

On the coinage metals v-top90, see figure 13, results in the largest adsorption energy. As opposed to pyridine on the (111) surfaces, rotating the molecule, once vertical, about its  $C_{2v}$  axis, from v-top90 to v-top for example, appreciably lowers the adsorption energy almost certainly due to the lower symmetry of the (110) surface. Moreover, pyridine in some of the initially flat configurations over the coinage metal surfaces prove unstable and can pick up a tilt angle away from the surface if the molecule's N atom is located close enough to a metal atom. Atodiresei et al. also calculated initially flat adsorption configurations to tilt away from both Cu(110) and Ag(110) in their own computation study [115]. Not only do our results agree well with the available theoretical literature but also the available experimental literature. Several experimental studies report pyridine to bond to Cu(110) with its molecular plane perpendicular to the surface [110-114] in agreement with our results. Lee et al. found pyridine to bond upright on Cu(111) at a coverage of  $9.0 \times 10^{13}$  molecule/cm<sup>2</sup> [110], and even observed pyridine to adsorb in v-top90, the same equilibrium adsorption site we calculate to be the most stable. Moreover, Douherty et al. found pyridine to bond upright on Cu(110) at a coverage of  $1.98 \times 10^{13}$  molecules/cm<sup>2</sup> [112]. Our coverage of pyridine on Cu(110) ranges from  $1.12$ - $1.21 \times 10^{14}$  molecules/cm<sup>2</sup>, close to the coverage studied by Lee et al, so naturally we would expect to

observe pyridine bonded in a vertical configuration on Cu(110). Finally one experimental study finds pyridine to adsorb on Cu(110) with its molecular plane tilted, approximately  $20^\circ \pm 15^\circ$ , away from the surface normal, and rotated by  $60^\circ (+15^\circ/-28^\circ)$  relative to the  $\langle 110 \rangle$  direction [111]. However, they work at a relatively high coverage, 0.4 ML, compared to our own. At higher coverage it is understandable that they observe pyridine to begin to tilt in order to minimize intermolecular interactions and to allow more room for pyridine to adsorb on the surface. Moreover, Lee et al. confirms that pyridine begins to rotate away from  $v\text{-top}90$  as one increases the coverage of pyridine [110]. Moving on, one study found pyridine to bond perpendicular on Ag(110) after reaching a coverage of  $3.925 \times 10^{13}$  molecules/cm<sup>2</sup> [117] while another study found pyridine to bond flat on Ag(110) at a coverage of  $6.9 \times 10^{16}$  molecules/cm<sup>2</sup> [118]. As we ran our calculations around  $9 \times 10^{13}$  molecules/cm<sup>2</sup> we should expect to calculate pyridine to bond perpendicular to Ag(110), which is precisely what we, in fact, calculate. Other studies find pyridine to undergo a phase transition from a flat to a vertical configuration on Ag(110) as one increases the coverage of pyridine. While none of the studies give the exact coverage this occurs they all agree it happens below a monolayer [119-121,123]. We must also mention some theoretical studies, using LDA, that predict pyridine to adsorb in the flat trough3 configuration [118,119]. However, given the experimental study that predicts pyridine to adsorb perpendicular to the surface around our coverage we attribute the favoring of trough3 to error caused by using the less accurate LDA approach. Finally to the author's knowledge pyridine has only been studied on Au(110) in solution. However these studies found pyridine to bond perpendicular to Au(110)[127,128].

Overall we find excellent agreement between our results and the available literature with both the literature and our results suggesting that pyridine bonds with its plane perpendicular to the Cu, Ag, and Au(110) surfaces. While our functionals unanimously predict pyridine to bond upright on Cu, Ag, and Au(110), we should mention this preference for a vertical adsorption site is often small. To illustrate this particular detail we plot in figure 14 the energy difference,  $\Delta E$ , between v-top90, and the initially flat adsorption site trough3 for any functional/metal combination that predicts v-top90 to be the most stable adsorption site. We pick trough3 as it is often the most stable adsorption site on Pt(110). Furthermore, in figure 14 the number besides each data point corresponds to the tilt angle away from the surface pyridine picked up when initially placed in trough3. In v-top90 pyridine always remained vertical. From figure 14 we first note the often small energy difference, 0.02 eV to 0.20 eV, between the vertical v-top90 configuration and the tilted trough3 configuration. Second from figure 14 we notice pyridine's propensity to pick up a tilt angle, 15° to 52°, when placed initially flat. Figure 14 also suggests the vdW interaction is the key to keeping pyridine flat on these surfaces. PBE, our one functional that lacks a proper description of the vdW interaction, yields the largest tilt angles out of all the functionals. Lastly figure 14 illustrates an important difference between the performance of rPW86-vdW2 and the rest of the functionals. The rPW86-vdW2 functional predicts v-top90 to be the most stable adsorption site on Pt(110). The rest of the functionals predict a flat adsorption site to be the most stable adsorption site on Pt(110). Different functionals predicting different adsorption geometries is exactly what we observed when we studied pyridine on the (111) reactive metal surfaces.

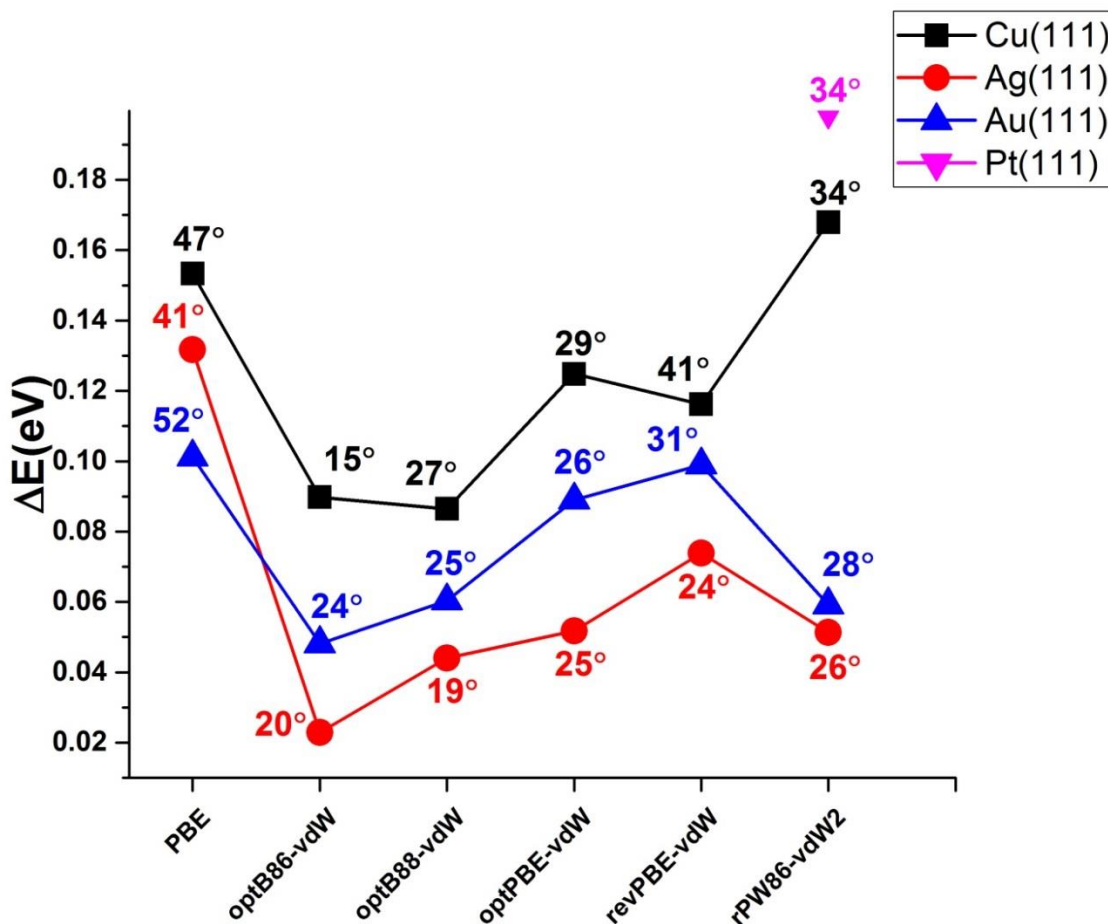


Figure 14: The difference in adsorption energy ( $\Delta E$ ) between the vertical adsorption site v-top90 and trough3. The number by each data point corresponds to the tilt angle pyridine picks up when initially placed in trough3. Pyridine in v-top90 always remains perpendicular to the surface,  $\Theta = 90^\circ$ . Only metal/functional combinations that predict v-top90 to be the most stable adsorption site are shown.

In contrast to the (111) reactive metals though, on Pt(110) most of our functionals agree concerning the equilibrium adsorption site. PBE, optB86b-vdW, optB88-vdW, optPBE-vdW, and revPBE-vdW all predict pyridine to adsorb flat or close to flat in the trough3 configuration or a configuration close to trough3. The trough3 configuration is not always the most stable adsorption configuration on Pt(110). Certain functionals, all the functionals except revPBE-vdW which predicts the actual trough3 adsorption site to be the most stable adsorption site and

rPW86-vdW2 which predicts v-top90 to be the most stable adsorption site, would sometimes predict pyridine, when placed initially in a flat adsorption site other than trough3, to move off of its initial adsorption site to approximately trough3. Specifically the optPBE-vdW and optB88-vdW functionals predict top1, when relaxed, to give the final adsorption site with the largest adsorption energy. The PBE and optB86b-vdW functionals predict bridgeS3, when relaxed, to give the final adsorption site with the largest adsorption energy. During this relaxation to this new adsorption site pyridine would rotate about the axis perpendicular to the surface such that the resulting adsorption site would boast a more favorable alignment of pyridine's C atoms with the surface's metal atoms. This new adsorption site would be close to trough3, but not exactly trough3. Figure 15 illustrates this new adsorption site, as calculated by PBE, next to the trough3 adsorption site for comparison. For a detailed comparison of this new adsorption site with trough 3 we list in table 11 the adsorption energy and the tilt angle away from the surface for the highest adsorption energy configuration and trough3 on Pt(110) as calculated by PBE, optB86b-vdW, optB88-vdW, and optPBE-vdW. Table 11 also lists the initial configuration that led to the highest adsorption energy configuration. One must remember all the listed configurations, except trough3 which was stable, relax to the highest adsorption energy configuration illustrated in figure 14. From table 11 we note a surprisingly large energy difference between trough3 and this new configuration. The slight rotation of the pyridine molecule leads to quite a hefty gain in adsorption energy. We also note that pyridine in the configuration close to trough3, surprisingly, possesses a larger tilt angle than the initial trough3 configuration. While we can attribute the much larger adsorption energy of the new configuration to the favorable matching of the C atoms and the metal atoms in the first layer of the substrate, the reason for the larger tilt angle is



unknown. Finally we must mention that that, in contrast to pyridine on the (110) coinage metals, there exists a rather large difference between the adsorption energies of flat and vertical adsorption configurations on Pt(110) as calculated by all the functionals except rPW86-vdW2. Specifically, we observe a 1.39 eV, 1.02 eV, 0.83 eV, 0.26 eV, and a 0.83 eV energy difference between the most stable flat adsorption site and v-top90 as calculated by optB86b-vdW, optB88-vdW, optPBE-vdW, revPBE-vdW, and PBE respectively.

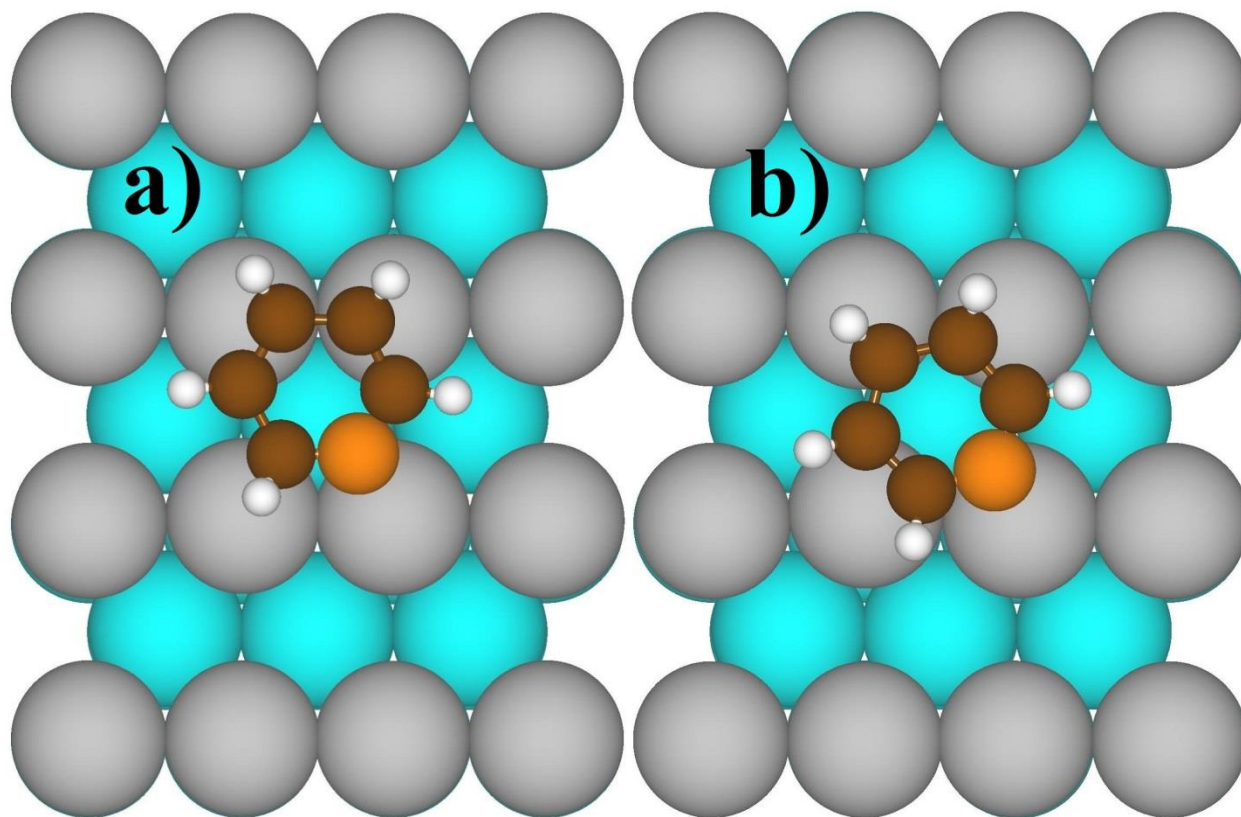


Figure 15: a) The new adsorption site that gave the highest adsorption energy for pyridine on Pt(110) as calculated by PBE, optB86b-vdW, optB88-vdW, and optPBE-vdW, and b) the trough3 adsorption site. PBE calculated these two specific adsorption geometries, but the opt-type functionals calculate nearly identical configurations.

Table 11: Adsorption energy and tilt angle away from the surface ( $\Theta$ ) for pyridine adsorbed in the adsorption site that leads to the largest adsorption energy and trough3.

Functional/ Initial Adsorption Site	Adsorption Energy	$\Theta(^{\circ})$
PBE/bridgeS3	2.61	9
PBE/trough3	1.88	3
optB86b-vdW/bridgeS3	3.35	10
optB86b-vdW/trough3	3.03	3
optB88-vdW/top1	2.88	9
optB88-vdW/trough3	2.61	4
optPBE-vdW/top1	2.57	9
optPBE-vdW/trough3	2.31	4

This drastic difference in performance between rPW86-vdW2 and the rest of the functionals in their description of pyridine on Pt(110) gives us another opportunity to comment about their competence. Unfortunately few studies detail the adsorption of pyridine on Pt(110). However given rPW86-vdW2's poor performance describing the adsorption of pyridine on the (111) reactive metals and given that the rPW86-vdW2 and revPBE-vdW functionals are highly repulsive at short-range, which can lead to inaccurate energies and an overestimation of bonds [2], we suggest rPW86-vdW2 predicts the wrong equilibrium adsorption site rather than the other functionals. It may predict too large of a repulsion between pyridine and the surface or between neighboring pyridine molecules leading pyridine to, incorrectly, bond with its plane perpendicular to Pt(110).

### **3.3.3 Adsorption Heights, Energies, and Other Structural Information**

After our brief discussion about which adsorption site leads to the highest adsorption energy configuration, we may now go into further detail describing the equilibrium adsorption site in order to learn more about the adsorption of pyridine on (110) transition metal surfaces and the role of the vdW interaction in the adsorption process. Table 12 lists the adsorption energy ( $E_{\text{ads}}$ ), the N-Metal distances (adsorption heights), the buckling of the first ( $B_1$ ) and second ( $B_2$ ) layer of the substrate, and the tilt angle of the molecule from the surface ( $\Theta$ ) for the highest adsorption energy configuration on each metal surface as predicted by each functional. Starting with the adsorption energies we note that the vdW interaction enhances the adsorption energy of pyridine on the (110) coinage metal surfaces just as it did on the (111) coinage metal surfaces. We note up to a 480 meV, 430 meV, and a 500 meV enhancement in the adsorption energy going from PBE to any of the vdW inclusive functionals. This increase in adsorption energy is best seen in

figure 17 a) which plots the adsorption energy for the highest adsorption energy configuration on each metal surface as predicted by each functional. Figure 17 a) also demonstrates that the vdW interaction may increase or decrease the strength of the pyridine/Pt(110) interaction with the opt-type functionals enhancing the adsorption energy over PBE, and revPBE-vdW and rPW86-vdW2 functionals providing a diminution in the adsorption energy over PBE. We observed this same trend when studying pyridine over the (111) reactive metals. If we look at the specific functional trend we note on the coinage metals the adsorption energy proceeds as  $PBE < revPBE-vdW < rPW86-vdW2 < optPBE-vdW < optB88-vdW < optB86b-vdW$  and on the reactive metals the adsorption energy proceeds as  $rPW86-vdW2 < revPBE-vdW < PBE < optPBE-vdW < optB88-vdW < optB86b-vdW$ . Again we see the opt-type functionals predict the largest adsorption energies just as they predicted the largest adsorption energies for pyridine on the (111) transition metal surfaces. Moving forward, if we look by metal all the functionals agree pyridine interacts the strongest with Pt(110) followed by Cu(110) followed by Au(110) followed by Ag(110). Comparing with the experimental literature, Lee et al. found an adsorption energy of pyridine on Cu(110) to be 0.97 eV in good agreement with our results [110]. On the theoretical side, Atodiresei et al. found an adsorption energy of 0.758 eV and 0.381 eV for pyridine on Cu(110) and Ag(110) respectively. When including the vdW interaction, using DFT-D2, they noted a jump in adsorption energy to 0.972 eV and 0.537 eV for pyridine on Cu(110) and Ag(110) respectively [115]. We agree with Atodiresei et al. in both that pyridine bonds more strongly to Cu(110) than Ag(110), and that the vdW interaction enhances the strength of the pyridine substrate interaction.

Table 12: Adsorption energy ( $E_{\text{ads}}$ ), N- Metal distance (adsorption heights), buckling of the first layer of the substrate ( $B_1$ ), buckling of the second layer of the substrate ( $B_2$ ), and the tilt angle of the molecule away from the surface ( $\Theta$ ) for pyridine adsorbed on Au, Ag, Cu, and Pt(110) in the highest adsorption energy configuration.

Functional/Adsorption Site	Surface	$E_{\text{ads}}$ (eV)	N- Metal( $\text{\AA}$ )	$B_1$ ( $\text{\AA}$ )	$B_2$ ( $\text{\AA}$ )	$\Theta(^{\circ})$
PBE/v-top90	Au(110)	0.58	2.30	0.14	0.03	90
optB86b-vdW/v-top90		1.08	2.24	0.06	0.02	90
optB88-vdW/v-top90		1.05	2.24	0.06	0.04	90
optPBE-vdW/v-top90		0.96	2.29	0.06	0.03	90
revPBE-vdW/v-top90		0.76	2.38	0.10	0.04	90
rPW86-vdW2/v-top90		0.78	2.38	0.13	0.09	90
PBE/v-top90	Ag(110)	0.44	2.39	0.14	0.02	90
optB86b-vdW/v-top90		0.87	2.33	0.08	0.01	90
optB88-vdW/v-top90		0.84	2.32	0.04	0.01	90
optPBE-vdW/v-top90		0.78	2.39	0.08	0.01	90
revPBE-vdW/v-top90		0.61	2.53	0.14	0.02	90
rPW86-vdW2/v-top90		0.64	2.49	0.14	0.03	90
PBE/v-top90	Cu(110)	0.71	2.06	0.22	0.03	90
optB86b-vdW/v-top90		1.19	2.02	0.15	0.01	90
optB88-vdW/v-top90		1.14	2.04	0.19	0.04	90
optPBE-vdW/v-top90		1.05	2.07	0.19	0.02	90
revPBE-vdW/v-top90		0.84	2.13	0.21	0.03	90
rPW86-vdW2/v-top90		0.88	2.11	0.20	0.02	90
PBE/bridgeS3	Pt(110)	2.16	2.08	0.20	0.27	11
optB86b-vdW/bridgeS3		3.35	2.08	0.18	0.25	10
optB88-vdW/top1		2.88	2.08	0.18	0.29	9
optPBE-vdW/top2		2.57	2.10	0.21	0.29	9
revPBE-vdW/trough3		1.71	2.13	0.22	0.28	11
rPW86-vdW2/v-top90		1.42	2.16	0.09	0.06	90

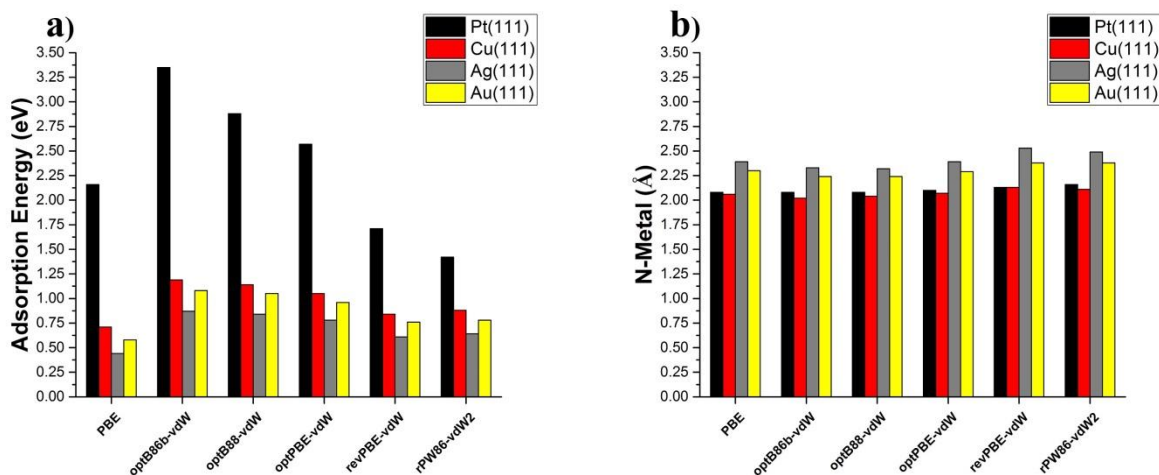


Figure 16: a) The adsorption energies and b) N-Metal distances or adsorption heights for pyridine adsorbed on Pt, Cu, Ag, and Au(110) in the highest adsorption energy configuration.

Continuing forward, figure 17 b) plots the adsorption heights for the highest adsorption energy configuration on each metal surface as predicted by each functional, which we also list in table 12. From figure 17 b) and table 12 we note that the adsorption heights display a modest dependence on functional. The adsorption heights range 0.08 Å on Pt(110), 0.11 Å on Cu(110), 0.21 Å on Ag(110), and 0.14 Å on Au(110) with the opt-type functionals always calculating the smallest adsorption heights, proving consistent with the adsorption energy trends. Among the vdW inclusive functionals the opt-type functionals predict the largest adsorption energies. Given the opt-type functionals predict the strongest pyridine/substrate interaction we would expect them also to bond pyridine the closest to the surface. Moving on, looking by metal we again note the adsorption heights, for the most part, follow trends already established by the adsorption energies. On the coinage metals the adsorption heights go as Ag(110) > Au(110) > Cu(110), which is what we would expect given the adsorption energies of pyridine on these surfaces. On Pt(110), however, we note adsorption heights close to Cu(110), which is surprising given

pyridine bonds much more strongly to Pt(110) than to Cu(110). It may be that 2 Å is an approximate limit on how close pyridine's N atom can approach any transition metal surface. Finally on Pt(110) we note that PBE calculates an adsorption height more in line with the opt-type functionals' results than either revPBE-vdW's results or rPW86-vdW2's results. This may be further evidence that those two functionals are too repulsive. Comparing with the available experimental literature we find good agreement with Gießel et al. who found N-Cu distances of 2.00 +/- 0.02 Å. This agrees well optB86b-vdW which predicts a N-Cu distance of 2.02 Å. We should also note we find fair agreement between our results and the available theoretical literature. Atodiresei et al. calculated for pyridine on Cu(110) a N-Cu distance of 2.02 Å [115], exactly the value we calculate using the optB86b-vdW functional. They also calculated in agreement with other studies [118,119] the N-Ag distance of pyridine on Ag(110) to be 2.35 Å [115], close to the values, 2.32 Å to 2.53Å, we calculate for the N-Ag distance. Finally on Au(110) Li et al. calculated a N-Au distance of 2.33 Å [130], which is close to our values which range from 2.24 Å to 2.38 Å.

Looking at the remainder of the data in table 12 we note a large buckling of the first layer of the substrate when pyridine adsorbs on the coinage metal surfaces with pyridine on Cu(110) giving the largest buckling of the first layer of the substrate. This proves consistent with the adsorption energetics as among the coinage metals pyridine interacts the most strongly with Cu(110), and thus we should expect to calculate the largest buckling of the first layer of the substrate on this metal. On Pt(110) we not only observe a large buckling of the first layer of the substrate but also a large buckling of the second layer of the substrate for every functional except rPW86-vdW2. This is undoubtedly a product of every functional except rPW86-vdW2

predicting pyridine to bond flat on Pt(110). When pyridine bonds flat on Pt(110) every atom in the pyridine molecule can interact with the surface. This contrasts to when pyridine bonds vertical on Pt(110) allowing only the molecule's N atom an opportunity to interact with the surface. This stronger interaction of pyridine when flat on the surface probably causes the large buckling of the second layer of the substrate, and is why rPW86-vdW2 fails to predict a large buckling of the second layer of the substrate. Finally, the last column in table 11, the tilt angle of the molecule, recaps what we described in the previous section. If a functional favors a vertical configuration, v-top90, then the molecule remains strictly vertical. If a functional favors a flat configuration then the molecule's plane remains close to being parallel to the surface,  $\Theta \leq 11^\circ$ .

### 3.3.4 Electronic Analysis

In order to gain a deeper understanding of the adsorption of pyridine on Cu, Ag, Au, and Pt(110) we perform an electronic structure analysis. We compute and list in table 13 the charge transfer to the molecule, the change in the width ( $\Delta W$ ) and the change in the center ( $\Delta C$ ) of the d-band of the atoms composing the first layer of the substrate, and the change in the surface's work function ( $\Delta\Phi$ ). From table 13 we note that pyridine donates charge to the substrate whenever it stands upright on the surface and takes charge from the substrate when it sits flat on the surface. This change in the sign of the charge transfer when pyridine goes from flat to vertical on the surface was precisely what we observed when we studied pyridine on the (111) reactive metals. We again attribute this phenomenon to the difference in the nature of pyridine's interaction with the surface whenever it changes its orientation. In an upright configuration pyridine bonds mainly to the surface through the lone pair of electrons situated around its N atom. This results in a situation where pyridine donates charge to the substrate. In a flat



configuration, pyridine bonds to the surface through the  $\pi$ -orbitals of its aromatic ring. This results in a situation where pyridine takes charge from the substrate. Two studies also independently calculated both little charge transfer between Ag(110) and pyridine and that the little charge transfer between pyridine and Ag(110) flips sign when the molecule goes from a flat to a vertical adsorption configuration [118,119], strengthening our conjecture. Finally we should touch on that among the coinage metal surfaces pyridine donates the most charge to Au(110), likely due to Au being the most electronegative coinage metal studied here.

Table 13: Charge transfer to the molecule, change in the surface's work function ( $\Delta\Phi$ ) and change in the width ( $\Delta W$ ) and center ( $\Delta C$ ) of the atoms that compose the first layer of the substrate upon the adsorption of pyridine.

Functional/Adsorption Site	Surface	Charge Transfer (-e)	$\Delta\Phi$ (eV)	$\Delta W$ (eV)	$\Delta C$ (eV)
PBE/v-top90	Au(110)	-0.2	-0.92	0.05	-0.06
optB86b-vdW/v-top90		-0.2	-0.95	0.07	-0.07
optB88-vdW/v-top90		-0.2	-0.96	0.06	-0.07
optPBE-vdW/v-top90		-0.1	-0.95	0.07	-0.07
revPBE-vdW/v-top90		-0.1	-0.90	0.05	-0.05
rPW86-vdW2/v-top90		-0.2	-0.89	0.06	-0.05
PBE/v-top90	Ag(110)	-0.1	-0.75	0.06	-0.03
optB86b-vdW/v-top90		-0.1	-0.79	0.07	-0.03
optB88-vdW/v-top90		-0.1	-0.79	0.07	-0.04
optPBE-vdW/v-top90		-0.1	-0.74	0.06	-0.03
revPBE-vdW/v-top90		-0.1	-0.70	0.05	-0.03
rPW86-vdW2/v-top90		-0.1	-0.71	0.05	-0.03
PBE/v-top90	Cu(110)	0.0	-1.03	0.05	-0.04
optB86b-vdW/v-top90		-0.1	-1.03	0.06	-0.05
optB88-vdW/v-top90		-0.1	-1.04	0.05	-0.04
optPBE-vdW/v-top90		0.0	-1.03	0.05	-0.04
revPBE-vdW/v-top90		-0.1	-0.99	0.04	-0.04
rPW86-vdW2/v-top90		0.0	-1.01	0.05	-0.04
PBE/bridgeS3	Pt(110)	0.08	-0.62	0.58	-0.34
optB86b-vdW/bridgeS3		0.05	-0.66	0.69	-0.37
optB88-vdW/top1		0.05	-0.68	0.52	-0.33
optPBE-vdW/top2		0.06	-0.62	0.28	-0.27
revPBE-vdW/trough3		0.07	-0.60	-0.08	-0.17
rPW86-vdW2/v-top90		-0.16	-0.88	-0.40	0.05

Moving on, all of the functionals predict the d-band of each surface to widen and shift away from the Fermi energy except rPW86-vdW2 which predicts the d-band of the Pt(110) surface to shift towards the Fermi energy and narrow, and revPBE-vdW which predicts the d-band of Pt(110) to narrow, indicating that revPBE-vdW and again rPW86-vdW2 may be weak choices to study the adsorption of pyridine on reactive metal surfaces. We do not know why revPBE-vdW

and rPW86-vdW disagree with the other functionals but it may be related to rPW86-vdW2 predicting the wrong adsorption site and to both functionals predicting a relatively weak pyridine/Pt(110) interaction. Moving forward, for the coinage metals we observe that pyridine only shifts and widens the d-band of the surface slightly, mirroring the situation on the (111) coinage metals where we observed a minimal perturbation of the surface's d-band. We note at most a 0.07 eV widening of the d-band and a 0.07 eV shift of the d-band for the coinage metals. We attribute pyridine's minimal disturbance of the surface's d-band to pyridine's overall weak interaction with the coinage metal surfaces. In contrast pyridine interacts quite strongly with Pt(110), resulting a large change to the surface's d-band. On Pt(110) we note pyridine can widen the d-band of the surface by up to 0.69 eV and shift the d-band of the surface by up to 0.37 eV.

Finishing off with the work function calculations, we note that for the coinage metal surfaces the magnitude of the work function change goes as  $\text{Ag}(110) < \text{Au}(110) < \text{Cu}(110)$ . This interestingly follows the exact trend as the adsorption energy. On the other hand, on Pt(110) we note on average the smallest change in the surface's work function. We accredit this to most functionals predicting pyridine to take charge from and not donate charge to the Pt(110) surface. When pyridine takes charge from the surface it increases the surface dipole, increasing the surface's work function and counteracting the so-called "pushback effect", leading to a smaller overall change in the surface's work function. (see our discussion in section 3.2.4). The rPW86-vdW2 results back up this claim as the rPW86-vdW2 functional, which predicts pyridine to donate charge to the Pt(110) substrate, predicts a noticeably larger change in Pt(110)'s work function. In this case the extra charge serves to reduce the surface dipole and thus further decrease the surface's work function. Finally, comparing with the literature we note good

agreement. Heskett et al. observed the work function of the Ag(110) surface to decrease by 1.7 eV at saturation [123]. We should and in fact calculate a change in Ag(110)'s work function less than 1.7 eV.

### 3.3.5 Conclusions and Brief Comparison to the (111) Metal Surfaces

The PBE, optB86b-vdW, optB88-vdW, optPBE-vdW, revPBE-vdW, rPW86-vdW2 functionals all predict pyridine to strongly physisorb on the (110) coinage metal surfaces. This physisorption is strikingly similar to the physisorption we observe when we place pyridine on the (111) coinage metal surfaces. This strong physisorption is characterized by relatively low adsorption energies, relatively large adsorption heights, and both a small alteration to the surface's geometric and electronic structure. On Pt(110), in contrast, we observe pyridine to chemisorb, either weakly or moderately depending on the functional, or strongly physisorb if using the rPW86-vdW2 functional. The chemisorption of pyridine on Pt(110) is characterized by relatively large adsorption energies, small adsorption heights, and both a large change of the surface's geometric and electronic structure. Pyridine's strong physisorption on Pt(110) as calculated by rPW86-vdW2 is close in nature to that of pyridine's strong physisorption on the (110) coinage metal surfaces.

Excluding rPW86-vdW2, overall, we note that most of our functionals accurately describe the adsorption of pyridine on the (110) transition metal surfaces. All of our functionals predict, correctly, for pyridine to adsorb vertical on the coinage metal surfaces. Moreover, every functional except rPW86-vdW2 predicts, probably correctly, pyridine to adsorb flat on Pt(110). Not only does the rPW86-vdW2 functional fail to predict the correct adsorption site of pyridine on Pt(110) it also, in disagreement with the other functionals, predicts a small buckling of both

the first and second layer of the Pt(110) substrate. Moreover, rPW86-vdW significantly disagrees with the other functionals concerning the charge transfer to the pyridine molecule from Pt(110) and the change in Pt(110)'s work function. Finally the rPW86-vdW2 functional and now also the revPBE-vdW functional disagree with the other functionals regarding the modification of the Pt(110) surface's d-band. From these results we learn two lessons. First the rPW86-vdW2 functional and, to a lesser extent, the revPBE-vdW functional appear to be poor choices to study the adsorption of pyridine on (110) transition metal surfaces. Second we learn that out of the systems studied in this section the pyridine/Pt(110) system is the hardest for DFT to model. We find the most disagreement among our chosen functionals about the equilibrium geometric and electronic structure of this particular system.

However, the contention we find among our functionals concerning pyridine on Pt(111) is still relatively minor compared to the disagreement we find when we attempted to model pyridine on the (111) reactive metal surfaces. On the (111) reactive metal surfaces many of our chosen functionals, not just rPW86-vdW2, disagree about the equilibrium adsorption geometry, or the electronic structure of the equilibrium adsorption geometry. This highlights the main, albeit subtle, effect the surface coordination has on the pyridine adsorption problem. The higher coordination surfaces present a more difficult adsorption problem to study. Our chosen functionals largely provide a consensus of how pyridine interacts with the (110) transition metal surfaces. Not only do our functionals agree, for the most part, on how pyridine interacts with the (110) transition metal surfaces, but their description of these systems seems to be largely correct. In contrast PBE, optB86b-vdW, optB88-vdW, optPBE-vdW, revPBE-vdW, and rPW86-vdW2 struggle to provide an accurate description of pyridine on the (111) transition metal surfaces, and

often contradict one another. Specifically on the (111) coinage metal surfaces none of our chosen functionals can provide the correct equilibrium geometry. These results suggest we need a better class of functional for this type of adsorption problem. On the (111) reactive metal surfaces our chosen functionals perform a little better with optB86-vdW and optB88-vdW functionals consistently providing the experimentally determined adsorption geometry. Overall, we note that because of the difficulty PBE, optB86b-vdW, optB88-vdW, optPBE-vdW, revPBE-vdW, and rPW86-vdW2 have describing pyridine on (111) transition metal surfaces that pyridine on high coordination surfaces makes for a better test than pyridine on low coordination surfaces for computational methods.

Despite the underperformance of our chosen functionals in their description of pyridine on the (111) transition metal surfaces, there exist broad similarities in our results for pyridine on the (111) and (110) transition metal surfaces. First all of our functionals agree that pyridine always bonds more strongly to our reactive metal surfaces whether we are studying pyridine on (111) surfaces or (110) surfaces. They also agree that no matter the surface coordination the vdW interaction enhances the interaction of pyridine on the coinage metal surfaces. The vdW interaction, predictably, plays an important role in the bonding of pyridine to these less reactive surfaces. On the more reactive surfaces, Pt, Pd, Ni, and Rh, the vdW interaction may either enhance or diminish the interaction of pyridine with the surface with revPBE-vdW and rPW86-vdW2 always diminishing the pyridine/surface interaction. These functionals have been demonstrated in the past to be too repulsive at short range [2], and here too they prove too repulsive to accurately describe pyridine on these reactive metal surfaces, where pyridine frequently bonds close to the surface. Finally all the functionals seem to agree that over all our

transition metal surfaces, regardless of surface coordination, changing the orientation of the molecule on the surface significantly changes the charge distribution of the system. This knowledge may prove useful for future molecular electronic applications that involve pyridine or pyridine derivatives.

### **3.4 Thiophene on Ni(100) and Cu(100)**

Reproduced with permission from W Malone, H. Yildirim, J. Matos and A. Kara, A van der Waals Inclusive Density Functional Theory Study of the Nature of Bonding for Thiophene Adsorption on Ni(100) and Cu(100) Surfaces, J. Phys. Chem. C, 121 (2017) 6090. Copyright 2017 American Chemical Society

Until now we limited our study to the adsorption of pyridine on single crystal transition metal surfaces. Now we move on to study the adsorption of thiophene ( $C_4H_4S$ ) on single crystal transition metal surfaces. Thiophene shares an aromatic structure with pyridine. However, thiophene possesses one less C and H atom than pyridine and also instead of a N atom has a S atom. By swapping N for S we can, to a certain extent, probe the effect the heteroatom has on the adsorption of small molecules on single crystal transition metal surfaces. Moreover, as stated in the introduction to this chapter the vdW interaction is thought to play a central role in the bonding of organic molecules to transition metal substrates. Thiophene, like pyridine, is a small organic molecule, allowing us another small system where the vdW interaction is thought to be important to rapidly and efficiently seen many computational methods. Finally, thiophene is often the building block of larger oligothiophenes, which are often used in molecular electronic devices such as thin film transistors [139-143], and organic light-emitting diodes [144,145]. Therefore, by studying the adsorption of thiophene on transition metal surfaces we

hope to better our understanding of how the related oligothiophenes interact with substrates. By increasing our knowledge of how oligothiophenes interacts with substrates we hope to contribute to the rational design of organic electronic devices in a small way.

We will start our examination of thiophene on transition metal surfaces by exploring thiophene on Ni(100) and Cu(100). Many studies have explored the adsorption of thiophene on these two surfaces [146-153], giving us a nice benchmark to compare with our own work. Moreover, several of these studies found thiophene to decompose over Ni(100) often breaking a single C-S bond [147-150,153]. The rupturing of thiophene over Ni(100) should provide us with an additional way to screen our computational methods.

In the first subsection we describe our computational details. In the second subsection we present the equilibrium adsorption configurations. In the third subsection we cover the adsorption geometry, adsorption energetics, and other structural information of thiophene in the most stable adsorption site on each surface. In forth subsection we perform an electronic structure analysis including the charge transfer to the molecule and modification of the surface's d-band for thiophene in the most stable adsorption site on each surface. In the fifth subsection we discuss the change thiophene induces in the average magnetic moment of the atoms composing the first layer of the Ni(100) substrate. In final subsection we present our conclusions.

### **3.4.1 Computational Details**

We perform all calculations in VASP version 5.3.3., which, as stated, uses the PAW method. We again model the exchange-correlation interaction using the PBE, optB86b-vdW, optB88-



vdW, optPBE-vdW, revPBE-vdW, and rPW86-vdW2 functionals. To model the Ni(100) and Cu(100) surfaces we use 5 layers slabs with at least 21 Å of vacuum in between neighboring slabs. Each layer in the slab, which we construct using the theoretical lattice constants in table 1 and table 7, measures 3 atoms long and 3 atoms wide (3x3 unit cell). We relax the substrate and the molecule separately before placing the molecule in 1 of 12 adsorption sites, pictured in figure 17, on either Cu(100) or Ni(100). 6 of these adsorption sites position the molecule with its plane perpendicular to the surface and we label them with a “v”, see figure 17 (a)-(k). The remaining 6 adsorption sites position the molecule with its plane parallel to the surface, see figure 17 (i)-(l). Whether we position the molecule in a flat or a vertical adsorption site we always situate thiophene such that its S atom sits approximately 2.5 Å above the surface. Once we place the molecule over the relaxed substrate we allow all the coordinates of the molecule/substrate system to undergo complete structural relaxation except the bottom two layers of the substrate which we anchor at their positions in the relaxed substrate. To achievement structural relaxation we use the CG method. For Ni(100) we run spin-polarized calculations. Finally we set the force criterion for structural relaxation at 0.01 eV/Å, sampled the BZ with a 6x6x1 Monkhorst-Pack grid, and set the plane wave energy cutoff at 400 eV.

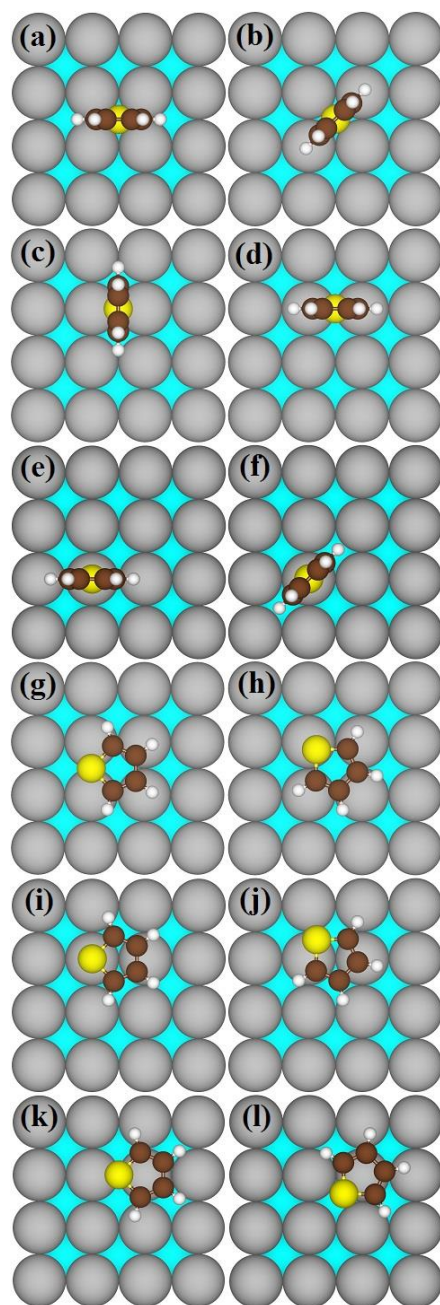


Figure 17: Initial adsorption sites a) v-hollow0, b) v-hollow45, c) v-bridge0, d) v-bridge90, e) v-atop0, f) v-atop45, g) hollow0, h) hollow45, i) bridge0, j) bridge45, k) atop0, and l) atop45 for thiophene adsorbed on the fcc (100) metal surfaces. Yellow atoms represent S atoms, brown atoms represent C atoms, white atoms represent H atoms, silver atoms represent substrate atoms in the first layer, and teal atoms represent substrate atoms in the second layer and lower.

To evaluate the stability of each adsorption site in figure 17 we again defined adsorption energy using equation 61. Using equation 61, as one will remember, a more positive adsorption energy corresponds to a more stable adsorption site. Furthermore, to save computational time, we calculate the adsorption energy of all 12 adsorption sites for only the optB88-vdW and PBE functional. We pick optB88-vdW as our previous studies indicated it as one of the best vdW inclusive functionals. We pick PBE to have one functional that does not properly account for long range dispersion for comparison. Once we isolate the adsorption site with the highest adsorption energy we run calculations of just that one adsorption site with the rest of the functionals.

### **3.4.2 Equilibrium Adsorption Configurations**

As stated we only run calculations for all 12 adsorption sites using the PBE and optB88-vdW functionals. Figure 18 plots the adsorption energies for thiophene on Ni(100) and Cu(100) using the PBE and optB88-vdW functionals. In figure 18 we indicate unstable adsorption sites using arrows pointing from the initial adsorption site to the final adsorption site. From figure 18 one may notice that on Cu(100) both PBE and optB88-vdW predict thiophene when placed initially in bridge45 to move to hollow45. On Ni(100) we compute quite a few more unstable adsorption sites than just bridge45. The optB88-vdW functional predicts the bridge0 and atop45 site to be unstable moving to hollow45 site. The PBE functional predicts atop45 to move to hollow45, bridge0 to move to hollow0, v-hollow0 to move to v-bridge0, and v-bridge90 to move to v-atop0.

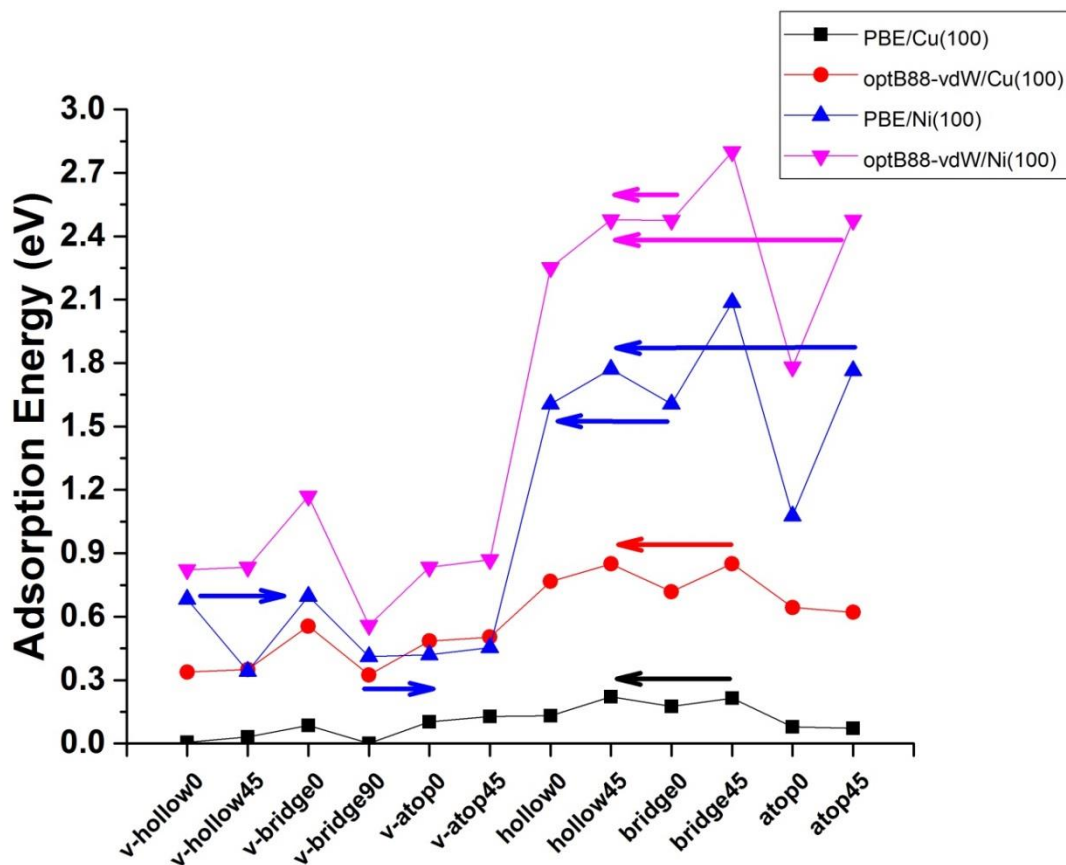


Figure 18: Adsorption energies for thiophene adsorbed on Cu(100) and Ni(100) as calculated using the PBE and optB88-vdW functionals. Unstable adsorption sites are indicated with an arrow pointing from the initial adsorption site towards the final adsorption site. Note that thiophene in bridge45 on Ni(100) spontaneously broke apart.

From figure 18 we also note that thiophene prefers to bonds flat on the surface. The adsorption energy of flat configurations is notably larger, especially on Ni(100), than the adsorption energy of vertical configurations. This is probably due to thiophene possessing two lone pairs of electrons around its S atom. The two lone pairs of electrons around its S atom, as opposed to just a single pair around pyridine's N atom, presumably makes it more difficult for thiophene to bond with its plane perpendicular to the surface as a result of both lone pairs competing to bond with the surface.

Finally from figure 18 we also note that both PBE and optB88-vdW predict the most stable adsorption site on Cu(100) to be hollow<sup>45</sup>. On Ni(100), in contrast, both functionals predict bridge<sup>45</sup> to be the most stable adsorption site, or rather they predict bridge<sup>45</sup> to be the initial adsorption site, that when relaxed, gives the most stable adsorption geometry. In truth both functionals predict thiophene to spontaneously rupture, in agreement with the literature [147-150,153], over bridge<sup>45</sup>. We illustrate this fracturing of thiophene, characterized by the breaking of a single C-S bond, in figure 19. The most stable intact configuration on Ni(100), as on Cu(100), is indeed hollow<sup>45</sup>.

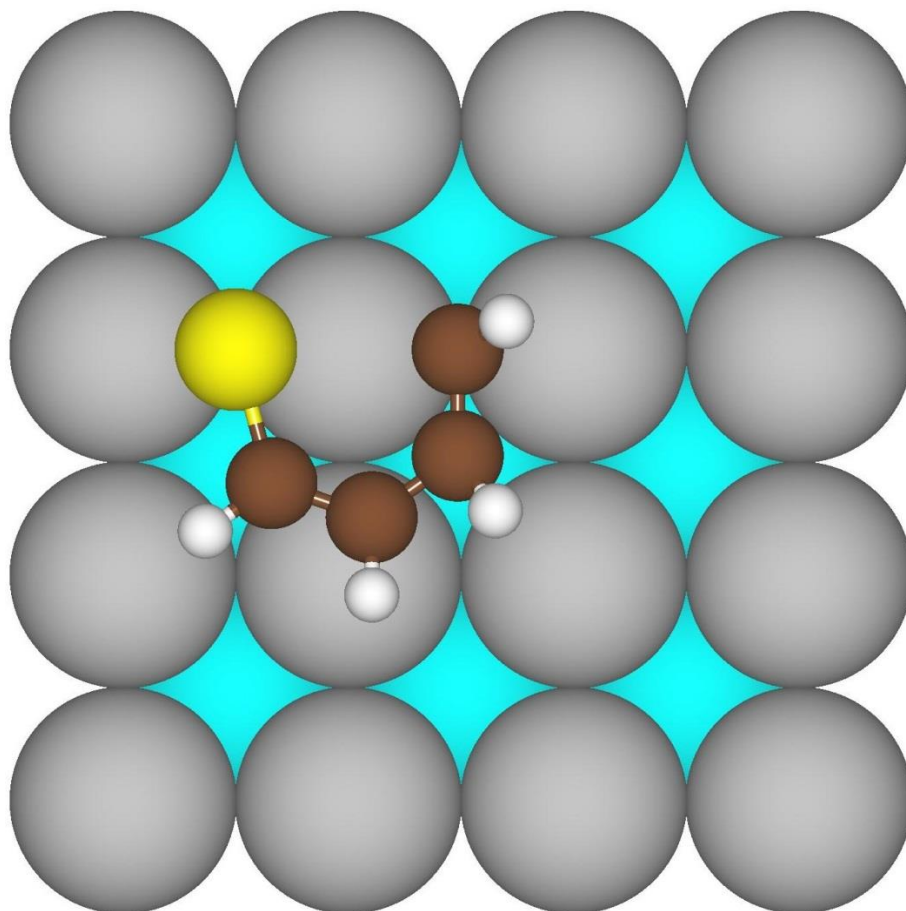


Figure 19: Thiophene broken over the bridge<sup>45</sup> site.

### 3.4.3 Adsorption Heights, Energies, and Other Structural Information

Since thiophene breaks apart over Ni(100) we run calculations of thiophene in a broken configuration, see figure 19, and in hollow45, the most stable intact adsorption configuration, for comparison on Ni(100) using the remainder of the functionals. On Cu(100) we ran calculations for just the hollow45 configuration using the rest of the functionals. We list in table 14 the adsorption energies ( $E_{\text{ads}}$ ), the adsorption heights ( $H_s$ ), the buckling of the first layer of the substrate, and the tilt angle ( $\Theta$ ) of the molecule in the hollow45 adsorption site on Cu(100) and in the hollow45 and the broken configuration on Ni(100). We define the adsorption height as the S z-coordinate minus the average of the z-coordinates of the atoms that compose the first layer of the substrate, and we define the tilt angle and buckling of the first layer of the substrate as we have done in previous sections. Starting with the adsorption energy, which we also plot in figure 20 a), we note that all of the functionals unanimously predict thiophene to bond less strongly to Cu(100) than Ni(100). Focusing on Cu(100) we note the adsorption energy goes as  $\text{PBE} < \text{revPBE-vdW} < \text{rPW86-vdW2} < \text{optPBE-vdW} < \text{optB88-vdW} < \text{optB86-vdW}$ . We note that this was the exact same trend we calculated when we studied pyridine on the coinage metal surfaces. Two other trends also reemerge from when we explored pyridine on the coinage metal surfaces. First the vdW interaction always seems to enhance the molecule/surface interaction. On Cu(100) the vdW interaction enhances the adsorption energy up to 0.78 eV. Second we note that the opt-type functionals always calculate the largest adsorption energies of our vdW inclusive functionals. On Ni(100) also many of the trends we observed when studying pyridine on reactive metals reemerge. The adsorption energy of thiophene on Ni(100) goes as  $\text{rPW86-vdW2} < \text{revPBE-vdW} < \text{PBE} < \text{optPBE-vdW} < \text{optB88-vdW} < \text{optB86b-vdW}$ . Again as with pyridine

on the reactive metals, we calculate the opt-type functionals to yield the largest adsorption energies, enhancing the overall molecule/substrate interaction over PBE. The revPBE-vdW and rPW86-vdW2 functionals again predict lower adsorption energies than PBE, which we again attribute to their highly repulsive nature at short distances [2]. The fact that the approximate functional trends remain when crossing over from pyridine adsorption on transition metal surfaces to thiophene adsorption on transition metal surfaces indicates that the accuracy of each functional relative to each other functional changes little when transitioning from one organic molecule to another. This suggests that the best functional to study the adsorption of pyridine and thiophene on transition metal surfaces is most likely the best functional to study any number of organic molecules on transition metal surfaces. It indicates that our functionals have transferability. Finally we must mention that we calculate large differences in adsorption energy between intact and broken configurations on Ni(100), indicating that once thiophene breaks over Ni(100) it binds quite strongly to the surface.

Table 14: The adsorption energy ( $E_{\text{ads}}$ ), adsorption height ( $H_s$ ), buckling of the first layer of the substrate, and tilt angle ( $\Theta$ ) for thiophene adsorbed on the Cu(100) and Ni(100).

Funtional	System/Site	$E_{\text{ads}}$ (eV)	$H_s$ (Å)	Buckling (Å)	$\Theta$ ( $^\circ$ )
PBE	Cu(100)/Hollow45	0.22	2.56	0.13	14
optB86b-vdW		1.00	2.30	0.13	1
optB88-vdW		0.85	2.43	0.08	3
optPBE-vdW		0.73	2.61	0.10	8
revPBE-vdW		0.50	3.03	0.05	6
rPW86-vdW2		0.51	3.05	0.05	4
PBE	Ni(100)/Hollow45	1.77	2.11	0.24	-1
optB86b-vdW		2.79	2.10	0.21	-1
optB88-vdW		2.48	2.12	0.22	-1
optPBE-vdW		2.18	2.13	0.23	-1
revPBE-vdW		1.49	2.16	0.26	0
rPW86-vdW2		1.22	2.18	0.27	0
PBE	Ni(100)/broken	2.09	1.75	0.37	
optB86b-vdW		3.18	1.76	0.35	
optB88-vdW		2.80	1.78	0.40	
optPBE-vdW		2.46	1.80	0.41	
revPBE-vdW		1.71	1.83	0.45	
rPW86-vdW2		1.42	1.86	0.53	

Moving onto the adsorption height, which we also plot in figure 20 b), we note the adsorption height of thiophene on Ni(100) does not depend heavily one's choice of functional. This mirrors our results for pyridine on the reactive metal surfaces in which we also noted a lack of a strong dependence of the adsorption height or N-Metal distances on functional. On Ni(100) we also notice much smaller adsorption heights for the broken configuration than for the intact hollow45 configuration. This matches the adsorption energy trend. Broken thiophene adsorbs more strongly to the surface than intact thiophene and therefore, all things being equal, broken thiophene should bond closer to the surface. Thiophene's adsorption height on Cu(100) is also in line with the established adsorption energy trends. We compute thiophene to interact more weakly with Cu(100) than Ni(100) and accordingly compute thiophene to bond further away



from Cu(100) than Ni(100). Moving along, on Cu(100), in contrast to Ni(100), we perceive that the adsorption height does vary modestly with respect to functional. The revPBE-vdW and rPW86-vdW2 functionals compute noticeably higher adsorption heights than the rest of the functionals. This, to some extent makes sense, given these two functionals also predict the lowest adsorption energies for thiophene on Cu(100). It is curious though that for our one coinage metal surface, Cu(100), the adsorption heights vary somewhat with functional while for one reactive metal surface, Ni(100), the adsorption heights vary little with functional. Even more curious, we observed this same theme when studying the adsorption of pyridine on transition metal surfaces. The propensity of different functionals to predict organic molecules to bond to coinage metal surfaces at different heights and to reactive metal surfaces at the same height appears to be a universal characteristic of our specific group of functionals.

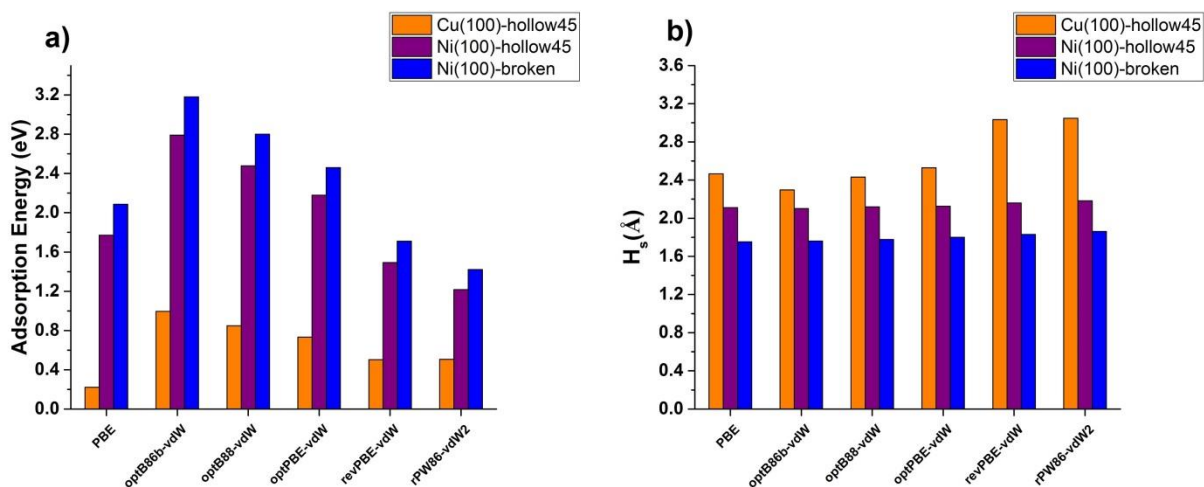


Figure 20: a) Adsorption energy and b) adsorption height ( $H_s$ ) for thiophene adsorbed on Cu(100) and Ni(100).

Taking a brief respite to compare with the literature, we find good agreement between our results and the available literature. Hu et al. thoroughly studied the adsorption of thiophene on

Cu(100) using various DFT methods [151]. In table 15 we list the values we calculate and Hu and coworkers calculate for the adsorption energy and the S-Cu distance for thiophene on Cu(100) in hollow45. Overall we note excellent agreement between Hu et al.'s results and our own. Any disagreement may be a product of He et al. decision to anchor the S atom with respect to the underlying substrate [151]. Also using DFT, Mittendorfer et al. found thiophene to spontaneously rupture over bridge45. They found the adsorption energy of this broken site to be 2.57 eV and of hollow45 to be 2.23 eV [153] to which we find good qualitative agreement with our results. As this group ran these calculations using the PW91 functional we should not expect exact agreement with our results. In another theoretical study using PBE, Orita et al. also found thiophene to break over bridge45. They calculated the adsorption energy for the broken configuration to be 2.88 eV and adsorption energy of hollow45 to be 2.46 eV [150]. These values deviate moderately from the values we calculate using the PBE functional. We attribute this though to the different coverage Orita and colleagues used. Finally in an experimental study, Imanishi et al. observed a S-Cu bond length of 2.43 Å for thiophene on Cu(100) [146], agreeing well with our PBE and optB88-vdW results ( see table 15). On Ni(100) they found the S atom of thiophene to sit close to a bridge site [146], precisely what we calculate when thiophene breaks over bridge45 (see figure 19).

Table 15: Adsorption energy ( $E_{\text{ads}}$ ) and S-Cu distances for thiophene adsorbed on Cu(100) in the hollow45 configuration. Values in circle brackets are taken from reference 151.

Funtional	System/Site	$E_{\text{ads}}$ (eV)	S-Cu (Å)
PBE	Cu(100)/Hollow45	0.22 (0.21)	2.47 (2.47)
optB86b-vdW		1.00 (1.02)	2.33 (2.33)
optB88-vdW		0.85 (0.88)	2.43 (2.47)
optPBE-vdW		0.73 (0.77)	2.57 (2.54)
rPW86-vdW2		0.51 (0.51)	3.04 (2.99)

Continuing on with the last two properties listed in table 14, we note that thiophene stays flat on the Ni(100) surface. On Cu(100) too, thiophene stays close to flat on the surface with a maximum tilt angle of  $14^\circ$  as calculated using PBE. This differs strikingly from pyridine which tended to pick up large tilt angles on Cu(111) and sometimes on Ni(111). Finally we note that the buckling of the surface goes as  $\text{Cu}(100)/\text{hollow45} < \text{Ni}(100)/\text{hollow45} < \text{Ni}(100)/\text{broken}$  with thiophene on Ni(100) in a broken configuration resulting in the surface to buckle up to 0.53 Å. The specific buckling trend is altogether unsurprising as the thiophene interacts the most strongly with the surface when broken over Ni(100) and the most weakly with the surface when adsorbed in hollow45 over Cu(100). The buckling of the surface along with the rest of the geometric properties we discussed here allows us to categorize the bonding of thiophene to Ni(100) as strong chemisorption. When thiophene adsorbs on Ni(100) we note a large change to both the structure of the thiophene molecule, evident by thiophene breaking a single C-S bond over Ni(100), and to the surface, evident by the large buckling of the surface. Thiophene on Ni(100) also results in large adsorption energies and small adsorption heights. For Cu(100) we categorize thiophene's interaction with the surface as ranging from weak physisorption, using the PBE functional, to strong physisorption, using the optB86b-vdW functional. When thiophene interacts with Cu(100) neither the surface's nor the molecule's structure changes much. We also calculate relatively small adsorption energies and relatively large adsorption heights for thiophene on Cu(100).

### 3.4.4 Electronic Analysis

To further explore the nature of the interaction of thiophene with Ni(100) and Cu(100) we perform an electronic structure analysis of thiophene on Ni(100) on Cu(100). Specifically we

calculate, and list in table 16, the charge transfer to the thiophene molecule and the change in the center ( $\Delta C$ ) and width ( $\Delta W$ ) of the d-band of the atoms that compose the first layer of the substrate for thiophene in hollow45 on Cu(100) and Ni(100) and thiophene in the broken configuration on Ni(100). From table 16 we find little dependence of the charge transfer on the specific functional. Figure 21, which plots the charge transfer to thiophene from Ni(100) or Cu(100), nicely illustrates that the charge transfer is fairly independent of one's choice of functional. Moving deeper, on Cu(100) we note almost no charge transfer between the thiophene molecule and the Cu(100) surface. In contrast we note thiophene takes a large amount of charge from Ni(100) when placed in either the hollow45 or the broken configuration. Figure 21 nicely illustrates the fact that thiophene takes much more charge from Ni(100) than Cu(100) and that in a broken configuration thiophene draws an especially large amount of charge from Ni(100), up to 0.8  $-e$ . This leads us to conclude that a charge transfer process may mediate the breaking of thiophene over Ni(100). We will further explore this idea in section 4.1 of this dissertation. For now we will make a quick comparison to the literature. Imanishi et al. reported a 1.0  $-e$  and a 1.4  $-e$  charge transfer to thiophene when adsorbed on Cu(100) and Ni(100) respectively[146]. While we agree that more charge is transferred to thiophene when on Ni(100), we do not agree about the exact magnitudes of the charge transfer. This disagreement deserves further study, but will not be covered in this dissertation.

Table 16: Charge transfer to the molecule and change in the center ( $\Delta C$ ) and width ( $\Delta W$ ) of the atoms that compose the first layer of the substrate upon the adsorption of thiophene.

Funtional	System/Site	Charge Transfer (-e)	$\Delta C$ (eV)	$\Delta W$ (eV)
PBE	Cu(100)/Hollow45	0.0	-0.07	0.14
optB86b-vdW		0.1	-0.24	0.30
optB88-vdW		0.0	-0.14	0.25
optPBE-vdW		0.0	-0.07	0.18
revPBE-vdW		0.0	-0.03	0.04
rPW86-vdW2		0.0	-0.03	0.00
PBE	Ni(100)/Hollow45 Down/up	0.3	-0.21/0.02	0.68/0.07
optB86b-vdW		0.3	-0.23/0.00	0.67/0.09
optB88-vdW		0.3	-0.21/0.00	0.61/0.11
optPBE-vdW		0.3	-0.19/0.00	0.63/0.09
revPBE-vdW		0.3	-0.17/0.02	0.60/0.07
rPW86-vdW2		0.3	-0.17/0.02	0.47/0.07
PBE	Ni(100)/broken Down/up	0.8	-0.26/0.03	0.77/0.42
optB86b-vdW		0.8	-0.28/0.02	0.77/0.45
optB88-vdW		0.7	-0.26/0.02	0.79/0.51
optPBE-vdW		0.7	-0.26/0.00	0.77/0.45
revPBE-vdW		0.7	-0.24/0.02	0.70/0.37
rPW86-vdW2		0.7	-0.24/0.00	0.61/0.40

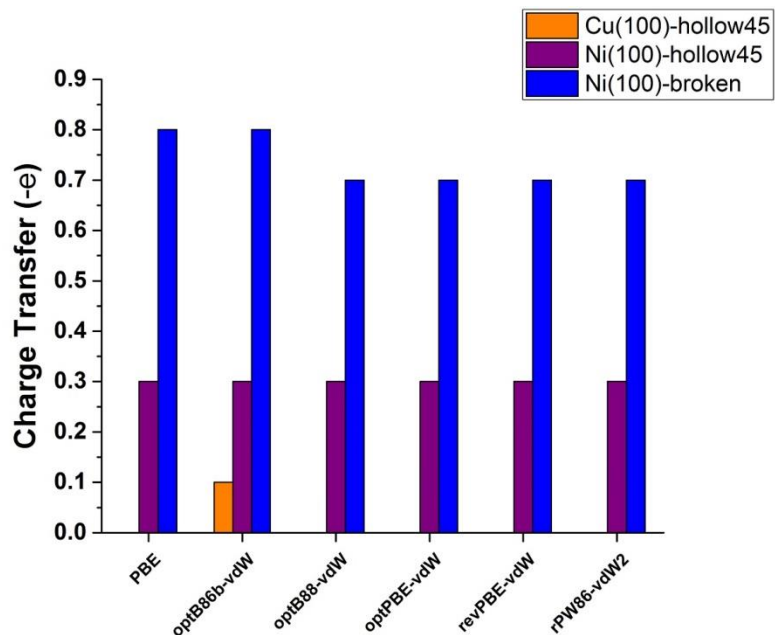


Figure 21: Charge transfer to the thiophene molecule from the Ni(100) or the Cu(100) surface.

Finishing up, we will now discuss the modification of the surface's d-band upon the adsorption of thiophene. First we will reiterate that for Ni(100) we perform spin-polarized calculations. With that in mind, thiophene widens and shifts the d-band of the first layer of the substrate of both Cu(100) and Ni(100), both spin up and spin down states, away from the Fermi energy. This widening and shift of Cu(100)'s d-band roughly correlates with the strength of the thiophene/Cu(100) interaction. The revPBE-vdW, rPW86-vdW2, PBE, and optPBE-vdW functionals predict the weakest thiophene/Cu(100) interaction and also the smallest modification of the Cu(100) surface's d-band. In contrast, the optB86b-vdW and optB88-vdW functionals predict thiophene to interact a little more strongly with Cu(100) and also predict a larger modification of the Cu(100) surface's d-band. On Ni(100), as thiophene interacts much stronger with Ni(100) than Cu(100), we unsurprisingly observe a much larger modification of the surface's d-band with a maximum widening of 0.79 eV and a maximum shift of 0.28 eV.

Astonishingly though, the modification of the spin down states appears to be much larger than the modification of the spin up states. From table 16 we note that the up states of the atoms that compose the first layer of the Ni substrate experience a small shift or no shift at all, and a small widening compared to the down states. We observed a similar asymmetrical shifting of the spin up and down states when we studied the adsorption of pyridine on Ni(100). Like pyridine, thiophene's asymmetrical modification of the spin up and spin down states should lead to a change of the average magnetic moment of the atoms that compose the first layer of the substrate.

### **3.4.5 Change in the Magnetization of Ni(100)**

As the first layer of the Ni(100) substrate experiences an asymmetrical modification of its spin up and spin down states we naturally calculate the change in the average magnetic moment of the atoms that compose the first layer of the Ni(100) substrate,  $\Delta\mu$ . We list these results in table 17. From table 17 we notice a  $0.18 \mu_b$  to a  $0.22 \mu_b$  decrease in the average magnetic moment of the atoms that compose the first layer of the Ni(100) substrate when we place thiophene in hollow45. When we place thiophene in the broken configuration we note a somewhat larger decrease, ranging from  $0.25 \mu_b$  to a  $0.28 \mu_b$ , in the average magnetic moment of the atoms that compose the first layer of the Ni(100) substrate. This larger magnitude of the change in the average magnetic moment of the atoms that compose the first layer of the Ni(100) substrate for the broken configuration should be partly expected as thiophene interacts more strongly with Ni(100) and receives more charge from the substrate in a broken configuration than in an intact configuration. Compared to pyridine, we note the functionals come to a relative agreement about the value for the change in the average magnetic moment of the atoms that

compose the first layer of the Ni(100) substrate, illustrating that our chosen functionals have an easier time describing the adsorption thiophene on Ni(100) than the adsorption of pyridine on Ni(111). Pyridine, and its lone pair of electrons, again appears to present a challenge to PBE and our vdW inclusive functionals. Finally we should mention that several studies also found organic molecules to reduce the magnetic moment of ferromagnetic surfaces [154-157], lending support to our own results.

Table 17: Change in the average magnetic moment ( $\Delta\mu$ ) of the atoms that compose the first layer of the Ni(100) substrate upon the adsorption of thiophene.

Funtional	System/Site	$\Delta\mu(\mu_b)$
PBE	Ni(100)/Hollow45 Down/up	-0.20
optB86b-vdW		-0.22
optB88-vdW		-0.21
optPBE-vdW		-0.20
revPBE-vdW		-0.18
rPW86-vdW2		-0.19
PBE	Ni(100)/broken Down/up	-0.27
optB86b-vdW		-0.28
optB88-vdW		-0.28
optPBE-vdW		-0.27
revPBE-vdW		-0.26
rPW86-vdW2		-0.25

### 3.4.6 Conclusions

Overall we find thiophene to adsorb much more strongly on Ni(100) than on Cu(100). The adsorption of thiophene on Cu(100) is characterized by relatively weak adsorption energies, large adsorption heights, minimal perturbation of the geometry of thiophene and surface, a small modification of the surface's electronic structure, and almost no charge transfer to the thiophene molecule. For these reasons we characterize the adsorption thiophene on Cu(100) as ranging from weak physisorption, using the PBE functional, to strong physisorption, using the optB86b-



vdW functional. In contrast on Ni(100) we observe pyridine to strongly chemisorb. This chemisorption is characterized by large adsorption energies, small adsorption heights, a large perturbation of the geometry of thiophene and the surface culminating in thiophene breaking over the surface, a large modification of the surface's electronic structure, and a large charge transfer to the thiophene molecule.

As for which functional gives the best description of the thiophene/transition metal surface system we tentatively put forth the optB88-vdW functional. Although we observe fairly homogenous results across all our functionals the optB88-vdW functional correctly predicts the experimental S-Cu metal bond length. We also note that the revPBE-vdW and rPW86-vdW2 functionals, yet again, seem to perform the worse. These two functional again demonstrate their overly repulsive nature by predicting a diminution of the thiophene/Ni(100) adsorption strength compared to PBE. Despite that we may make a few strong statements about the performance of our chosen functionals it is much harder to screen their performance using thiophene on transition metal surfaces. All of our functionals predict the exact same equilibrium adsorption geometry, a nearly identical amount of charge transfer, a similar modification of the surface's d-band, and a similar change in the average magnetic moment of the first layer of the Ni(100) surface. Compared with pyridine on the reactive metal surfaces, we observe very homogeneous results. This again indicates that the pyridine/reactive metal surface system is especially difficult to describe, or, rather, the thiophene/transition metal surface system is easy to describe.

### **3.5 Thiophene on Ag, Au, Pt, Pd, and Rh(100)**

Reproduced from W. Malone, J. Matos and A. Kara, Adsorption of thiophene on transition metal surfaces with the inclusion of van der Waals effects, Surf. Sci., 669 (2018) 121, with the permission of Elsevier Publishing

As all our functionals predict nearly the same adsorption properties for thiophene on Ni(100) and Cu(100) we decide to see if this is also the case for thiophene on Ag, Au, Pt, Pd, and Rh(100). However, even if our chosen functionals predict considerably different adsorption trends for thiophene on these metals, screening these molecules may prove difficult due to the lack of literature. Researchers have only studied thiophene on Pd(100) [158,159]. Still by studying these systems we can learn more about how thiophene interacts with transition metal surfaces and the role the choice of the element in the surface plays for thiophene adsorption, which both are important due to the use of thiophene derivatives in molecular electronics.

In first subsection we give the details of our calculations. In the second subsection we present the equilibrium adsorption configurations. In the third subsection we detail the adsorption geometry, adsorption energetics, and other structural information of thiophene in the most stable adsorption site on each surface. In fourth subsection we perform an electronic structure analysis including the charge transfer to the molecule and modification of the surface's d-band for thiophene in the most stable adsorption site on each surface. In the last subsection we present our conclusions.

#### **3.5.1 Computational Details**

We perform all calculations using VASP version 5.4.1., which as stated many times before uses the PAW method. Again we utilize the PBE, optB86b-vdW, optB88-vdW, optPBE-vdW,

revPBE-vdW, and rPW86-vdW2 functionals to model the exchange-correlation interaction. We model our surfaces, as in the previous section, using 5 layer slabs with each layer measuring 3 by 3 atoms. As VASP uses periodic boundary conditions we place 25 Å of vacuum in between neighboring slabs. Moreover, we built each slab using the theoretical lattice constants listed in table 1 and table 7. We relax the substrate and the molecule separately before placing the molecule on the substrate in one of the 12 adsorption sites illustrated in figure 17. Once we position the molecule on the surface we allow all the coordinates of the molecule/substrate system to undergo complete structural relaxation except the atoms composing the bottom two layers of the substrate, which we hold at their positions in the relaxed substrate.

To achieve structural relaxation we use the CG method with a force criterion of 0.02 eV/Å. We also set the plane wave energy cutoff at 400 eV and sample the BZ with a 6x6x1 Monkhorst-Pack grid. To access the stability of each adsorption sites we define the adsorption energy using equation 61. We will remind the reader when using equation 61 a higher adsorption energy corresponds to a more stable adsorption site.

### 3.5.2 Equilibrium Adsorption Configurations

All adsorption sites on the coinage metals surfaces, Ag(100) and Au(100), are either stable or metastable, meaning thiophene when placed on either Ag(100) or Au(100) always results in a positive adsorption energy and the thiophene molecule stays in its initial adsorption site. On the reactive metals all vertical adsorption sites are stable or metastable, while some flat adsorption sites are unstable. In contrast to when we placed pyridine on the reactive metal surfaces where the pyridine molecule would, when unstable, move primary to one adsorption site, bB1 (see section 3.2), when we place thiophene on the reactive metal surfaces the thiophene molecule

could, when unstable, move to bridge0, top0, a hollow site between hollow0 and hollow45, or hollow45. This difference between pyridine and thiophene suggests that the potential energy landscape of the two molecules on reactive metals surfaces can be quite dissimilar.

Moving forward, the hollow45 adsorption site, a flat adsorption site, renders the highest adsorption energy for thiophene on both the reactive and the coinage metal surfaces. This again differs with respect to pyridine on the transition metal surfaces where, depending on the metal and the functional we used, a flat configuration could give the largest adsorption energy or a vertical configuration could give the largest adsorption energy. Not only was hollow45 always the most energetically favorable adsorption site, but in truth all of the flat adsorption sites yield larger adsorption energies than all of the vertical adsorption sites. Figure 22 plots the energy difference,  $\Delta E$ , between the flat adsorption configuration with the highest adsorption energy, hollow45, and the vertical adsorption configuration with the highest adsorption energy. In essence  $\Delta E$  measures how strongly thiophene favors a flat adsorption site on a particular metal surface using a particular functional. From figure 22 we note the thiophene strongly favors a flat adsorption site on the reactive metal surfaces, Rh, Pt, and Pd(100), with optB86b-vdW most strongly favoring a flat adsorption site followed by optB88-vdW, optPBE-vdW, PBE, revPBE-vdW, and rPW86-vdW2. Looking by metal we note  $\Delta E$  goes as Pd(100) < Rh(100) < Pt(100), but the difference in  $\Delta E$  values between the different reactive metal surfaces is small compared to the difference in  $\Delta E$  between the reactive and coinage metal surfaces. On the coinage metal surfaces we still notice thiophene's preference for a flat adsorption configuration, but this preference is much less pronounced than for the reactive metal surfaces. On the reactive metal

surfaces the largest  $\Delta E$  we calculate is 2.14 eV on Pt(100) using the optB86b-vdW functional. On the coinage metal surfaces, in contrast, the largest  $\Delta E$  we calculate is 0.43 eV on Au(100) using the optB86b-vdW functional. Clearly thiophene much more strongly prefers to bond flat on the reactive metal surfaces than on the coinage metal surfaces. Finally on the coinage metal surfaces we note that  $\Delta E$  increases as  $\text{PBE} < \text{revPBE-vdW} < \text{rPW86-vdW2} < \text{optPBE-vdW} < \text{optB88-vdW} < \text{optB86b-vdW}$ . As PBE gives the lowest  $\Delta E$  for thiophene on the coinage metal surfaces it may be that the vdW interaction plays an important role in keeping the molecule with its plane parallel to these surfaces.

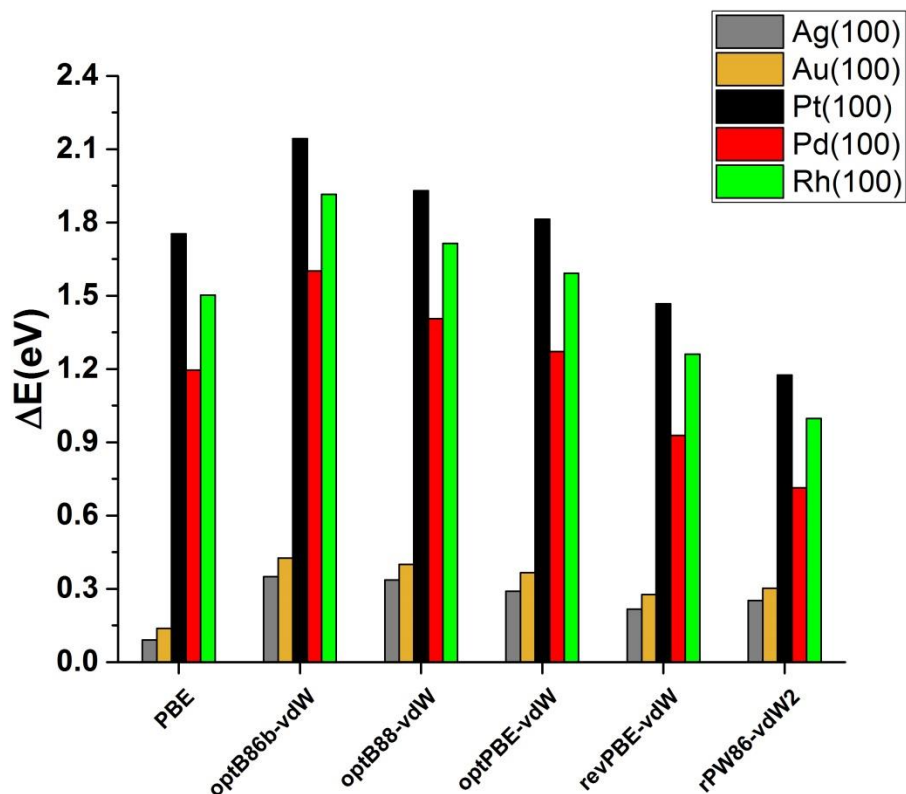


Figure 22: Energy difference,  $\Delta E$ , between the flat configuration (hollow45) with highest adsorption energy and the vertical adsorption configuration (tilt angle =  $90^\circ$ ) with the highest adsorption energy. A larger  $\Delta E$  corresponds to a particular functional more strongly favoring a flat adsorption configuration on a given surface.

### 3.5.3 Adsorption Heights, Energies, and Other Structural Information

As stated the configuration with the highest adsorption energy is always hollow45 for these systems. From now on we will focus our analysis on that configuration. Table 18 lists the adsorption energy ( $E_{\text{ads}}$ ), the adsorption height ( $H$ ), the C-S bond lengths, the buckling of the first layer of the substrate, and the tilt angle of the molecule relative to the surface ( $\Theta$ ) for thiophene on Ag, Au, Pt, Pd, and Rh(100) in the hollow45 configuration. We define adsorption height in this section as the distance from the S atom to the nearest metal atom. Starting with the

adsorption energy we note that the thiophene/substrate interaction strength proceeds as Ag (100) < Au(100) < Pd(100) < Rh(100) < Pt(100) with the adsorption energies on the coinage metals being, unsurprisingly, much smaller than the adsorption energies on the reactive metals. Figure 23 a) plots the adsorption energies of thiophene on the various metal surfaces in the hollow45 configuration for convenience. Starting with the coinage metal surfaces, if we look by functional we observe that the adsorption energies go as PBE < revPBE-vdW < rPW86-vdW2 < optPBE-vdW < optB88-vdW < optB86b-vdW. As one will notice the vdW interaction always enhances the thiophene/substrate interaction on the coinage metal surfaces with a maximum enhancement of 0.66 eV on Ag(100) and of 0.76 eV on Au(100) using the optB86b-vdW functional. The enhancement of the molecule/coinage metal surface interaction by the vdW interaction is exactly what we observed when studying pyridine on the coinage metal surfaces, and it again suggests the vdW interaction plays an important role in the bonding of organic molecules to coinage metal surfaces. On the reactive metal surfaces we note the adsorption energy proceeds as rPW86-vdW2 < revPBE-vdW < PBE < optPBE-vdW < optB88-vdW < optB86b-vdW. We calculated similar trends when we explored the adsorption of pyridine on the reactive metal surfaces with rPW86-vdW2 and revPBE-vdW both predicting a lower adsorption energy than PBE and the opt-type functionals predicting a higher adsorption energy than PBE. We again attribute revPBE-vdW and rPW86-vdW2's diminution of the adsorption energy compared to PBE to the overly repulsive nature of these method's exchange functionals. These trends demonstrate the importance of choosing an appropriate method to model the organic molecule/reactive metal system. Unfortunately due to the lack of experimental studies we cannot definitely state which method gives the correct experimental adsorption energy. However, we can state that we find

good agreement with a theoretical study by Orita and coworkers who found thiophene's adsorption energy on Pd(100) to be 2.20 eV [159], which is between our PBE and optPBE-vdW results. Moreover, we can also say, based on rPW86-vdW2 and revPBE-vdW's poor performance describing pyridine on the transition metal surfaces and the highly repulsive nature of these functionals at short range, that the opt-type functionals probably calculate adsorption energies close to what one should observe experimentally.



Table 18: Adsorption energies ( $E_{\text{ads}}$ ), adsorption heights (H), C-S bond lengths, buckling of the first layer of the substrate, and tilt angle of the molecule relative to the surface plane ( $\Theta$ ) for thiophene adsorbed on Ag, Au, Rh, Pt, and Pd(100) in the hollow45 configuration.

Funtional/Adsorption Site	Surafce	$E_{\text{ads}}$ (eV)	H (Å)	C-S(Å)	Buckling (Å)	$\Theta$ ( $^{\circ}$ )
PBE	Ag(111)	0.13	3.16	1.72	0.05	4
optB86b-vdW		0.79	2.88	1.72	0.04	2
optB88-vdW		0.74	2.95	1.72	0.03	2
optPBE-vdW		0.67	3.10	1.73	0.03	2
revPBE-vdW		0.49	3.36	1.73	0.06	0
rPW86-vdW2		0.50	3.27	1.74	0.04	1
PBE	Au(111)	0.19	2.95	1.72	0.08	7
optB86b-vdW		0.95	2.77	1.73	0.06	3
optB88-vdW		0.88	2.84	1.72	0.07	4
optPBE-vdW		0.78	2.98	1.73	0.05	3
revPBE-vdW		0.58	3.29	1.73	0.05	1
rPW86-vdW2		0.61	3.22	1.74	0.06	2
PBE	Rh(111)	2.40	2.28	1.81	0.17	-1
optB86b-vdW		3.47	2.28	1.82	0.15	-1
optB88-vdW		3.13	2.29	1.82	0.15	-1
optPBE-vdW		2.87	2.30	1.83	0.16	-1
revPBE-vdW		2.18	2.32	1.84	0.17	0
rPW86-vdW2		1.82	2.36	1.84	0.17	0
PBE	Pt(111)	2.72	2.27	1.83	0.27	0
optB86b-vdW		3.77	2.27	1.83	0.23	0
optB88-vdW		3.42	2.28	1.84	0.24	0
optPBE-vdW		3.15	2.29	1.84	0.25	0
revPBE-vdW		2.43	2.31	1.86	0.26	0
rPW86-vdW2		2.05	2.34	1.87	0.25	0
PBE	Pd(111)	2.02	2.28	1.80	0.18	0
optB86b-vdW		3.03	2.28	1.80	0.15	0
optB88-vdW		2.73	2.29	1.80	0.15	0
optPBE-vdW		2.45	2.31	1.81	0.15	0
revPBE-vdW		1.76	2.34	1.81	0.16	0
rPW86-vdW2		1.50	2.38	1.82	0.15	1

Moving on, we note that the trends in the adsorption height on the coinage metal surfaces closely mirrors the trends in the adsorption energies. Figure 23 b) plots the adsorption heights for thiophene adsorbed on our various transition metal surfaces in the hollow45 configuration for

convenience. The opt-type functionals calculate the lowest adsorption heights among the vdW inclusive functionals while the revPBE-vdW and rPW86-vdW2 functionals give the highest adsorption heights among the vdW inclusive functionals. This is exactly what we would expect given the adsorption energy trends put forth in the previous paragraph. The PBE functional is a little odd as it consistently predicts the lowest adsorption energy among all the functionals considered, but calculates an adsorption height close to optPBE-vdW. This may be a result of PBE's lack of a nonlocal correlation term. Moving further, on the reactive metal surfaces we note that the adsorption height does not depend heavily on the functional or the metal. It is not clear why this occurs. Despite that the adsorption height varies little with respect to functional on the reactive metal surfaces we can still make a comparison with the literature. Terada and colleagues experimentally found thiophene's S-Pd bond length to be  $2.30 \pm 0.03 \text{ \AA}$  [158], which sits in the range of values for the adsorption height calculated by the opt-type functionals and PBE, suggesting again that these functionals provide the best description of the thiophene/Pd(100) system. We should also mention we note good agreement with Orita and coworkers who calculated thiophene's S-Pd bond length to be  $2.32 \text{ \AA}$  [159].

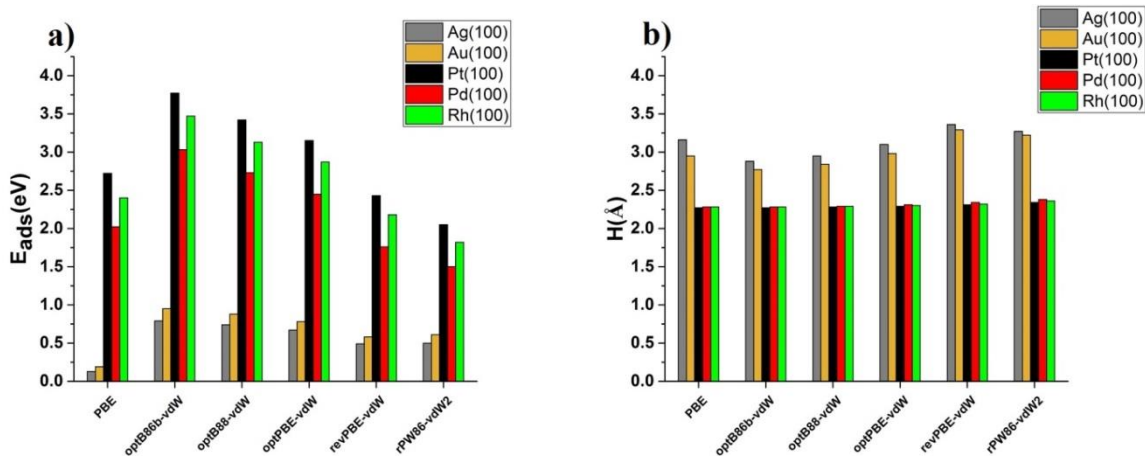


Figure 23: Adsorption energies ( $E_{ads}$ ), and adsorption heights ( $H$ ) for thiophene adsorbed on Ag, Au, Rh, Pt, and Pd(100) in the hollow45 configuration.

Moving along with our analysis, we find that the C-S bond lengths of thiophene on the coinage metal surfaces to be roughly the same, ranging from 1.72 Å to 1.74 Å. On the reactive metal surfaces we note the C-S bonds stretch, undoubtedly, due to thiophene's stronger interaction with these surfaces. Specifically we observe, although the distinction is small, thiophene's C-S bonds to follow the adsorption energy trend and increase moving from Rh(100) to Pd(100) to Pt(100). The buckling of the first layer of the surface to a large part also mirrors trends in the adsorption energetics. Explicitly we note the buckling of the first layer of the substrate increases as  $Ag(100) \sim Au(100) < Pd(100) \sim Rh(100) < Pt(100)$ . Finally, the last quantity in table 18, the tilt angle of the molecule, sums up what we stated in the previous section. Thiophene prefers to bond with its molecular plane parallel to these surfaces. We note close to a  $0^\circ$  tilt angle for thiophene on the reactive metal surfaces and a very small tilt angle,  $> 7^\circ$ , for thiophene on the coinage metals surfaces. Comparing with the literature, we find fair agreement. In perfect agreement with our results, Terada et al. found thiophene's tilt angle on Pd(100) to be  $0^\circ \pm 10^\circ$  [158]. They also observed C-S bond lengths of  $1.73 \text{ \AA} \pm 0.05 \text{ \AA}$  [158],

which is a bit short compared to our C-S bond lengths. A proper description of thiophene's C-S bond lengths on Pd(100) may be an area of future improvement for DFT. Comparing with theory, we find excellent agreement. Orita et al. found thiophene's C-S bond lengths on Pd(100) to be 1.82 Å and also found, as mentioned, thiophene to bond flat on Pd(100) [159].

Overall, despite the limited amount of available literature, our geometric analysis suggests that the opt-type functionals provide the best description of thiophene on Ag, Au, Pt, Pd, and Rh(100). This matches the results of our calculations of pyridine on various transition metal surfaces where we also concluded that the opt-type functionals perform the best. Other analogues exist between our calculations of thiophene and pyridine on transition metal surfaces. For example, we observe much of the same energetic trends for both molecules. The opt-type functionals always calculate the largest adsorption energies. On the coinage metal surfaces, PBE always yields the lowest adsorption energies, and on the reactive metal surfaces the revPBE-vdW and rPW86-vdW2 functionals yield the smallest adsorption energies. Besides allowing us to draw similarities between thiophene and pyridine on transition metal surfaces and allowing us to distinguish the opt-type functionals as the best performing functionals, these results permit us to categorize the interaction of thiophene with Au(100) and Ag(100) as weak to strong physisorption depending on the functional used. This physisorption is characterized by low adsorption energies, high adsorption heights, and very little perturbation of the molecule's or the surface's geometric structure upon adsorption. Moreover, the inclusion of the vdW interaction appears paramount to the description of thiophene's strong physisorption on these coinage metal surfaces, providing the necessary enhancement in adsorption energy to characterize the interaction as strong physisorption. On the reactive metal surfaces the vdW interaction appears

to play a less prominent role and we categorize the interaction of thiophene with the reactive metal surfaces as chemisorption; a chemisorption characterized by high adsorption energies, low adsorption heights, and a large perturbation of the molecule's and the surface's geometric structure upon adsorption.

#### **3.5.4 Electronic Analysis**

In order to gain a better understanding of how thiophene interacts with these Ag, Au, Rh, Pt, and Pd(100) we perform an electronic structure analysis of the thiophene/substrate systems including charge transfer to the thiophene molecule and the change in the center ( $\Delta C$ ) and the width ( $\Delta W$ ) of the atoms that compose the first layer of the substrate. We list these results in table 19. We also plot the charge transfer to the thiophene molecule in figure 24. From figure 24 and table 19 we note little charge transfer from the Ag(100) surface to the molecule with optB86b-vdW and optB88-vdW being the only functionals to predict any charge transfer at all. This small to nonexistent charge transfer probably results from the weak interaction of thiophene with Ag(100), which is even weaker than the interaction of thiophene with Au(100). In contrast to this small to nonexistent charge transfer between thiophene on Ag(100), on Au(100) and Pt(100) we calculate the molecule to donate a modest amount of charge to the surface. Thiophene on Pd(100) also donates a small amount of charge to the surface although the amount is almost always smaller than the charge donated to either Pt(100) or Au(100). Finally on Rh(100) we compute thiophene to take a small amount of charge from the surface instead of donating charge to the surface. Rh(100)'s propensity to donate charge to thiophene may mean thiophene is closer to breaking a C-S bond on Rh(100) than any of the other surfaces as on Ni(100) we noted a large charge transfer from the surface to thiophene that accompanied

thiophene breaking one C-S bond on Ni(100). This relationship between charge transfer and the ability of a surface to break C-S bonds will be explored in detail later in this dissertation. For now we will move onto the change in the width and center of the d-band of the atoms that compose the first layer of the surface.

Table 19: Charge transfer from the surface to the thiophene molecule, and change in the center ( $\Delta C$ ) and width ( $\Delta W$ ) of the atoms that compose the first layer of the substrate for thiophene adsorbed on Ag, Au, Rh, Pt, and Pd(100) in the hollow45 configuration.

Funtional	Surface	Charge Transfer (-e)	$\Delta C$ (eV)	$\Delta W$ (eV)
PBE	Ag(100)	0.0	-0.03	0.00
optB86b-vdW		-0.1	-0.09	0.02
optB88-vdW		-0.1	-0.07	0.02
optPBE-vdW		0.0	-0.05	0.02
revPBE-vdW		0.0	-0.03	0.00
rPW86-vdW2		0.0	-0.03	0.00
PBE	Au(100)	-0.1	-0.05	0.03
optB86b-vdW		-0.2	-0.10	0.03
optB88-vdW		-0.2	-0.10	0.03
optPBE-vdW		-0.1	-0.07	0.03
revPBE-vdW		-0.1	-0.03	0.00
rPW86-vdW2		-0.1	-0.05	0.02
PBE	Rh(100)	0.1	-0.16	0.19
optB86b-vdW		0.1	-0.16	0.17
optB88-vdW		0.1	-0.17	0.16
optPBE-vdW		0.1	-0.16	0.17
revPBE-vdW		0.1	-0.14	0.16
rPW86-vdW2		0.1	-0.12	0.14
PBE	Pt(100)	-0.2	-0.31	0.17
optB86b-vdW		-0.2	-0.31	0.17
optB88-vdW		-0.2	-0.33	0.17
optPBE-vdW		-0.2	-0.31	0.17
revPBE-vdW		-0.1	-0.30	0.17
rPW86-vdW2		-0.1	-0.30	0.16
PBE	Pd(100)	-0.1	-0.28	0.17
optB86b-vdW		-0.1	-0.30	0.17
optB88-vdW		-0.1	-0.28	0.16
optPBE-vdW		-0.1	-0.26	0.14
revPBE-vdW		0.0	-0.26	0.17
rPW86-vdW2		-0.1	-0.23	0.14

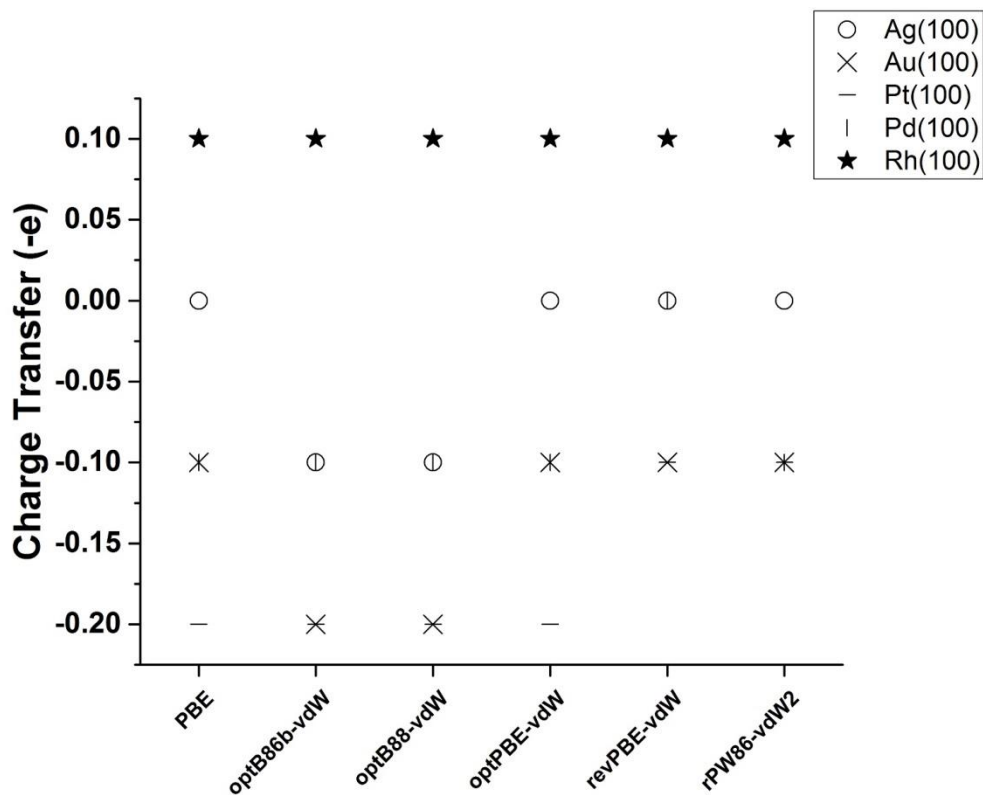


Figure 24: Charge transfer from the surface to the molecule for thiophene adsorbed on Ag, Au, Rh, Pt, and Pd(100) in the hollow45 configuration.

The change in the width and center of the d-band of the atoms that compose the first layer of the surface are often good indicators of strength of the interaction of an adsorbate with a surface. The larger the change in the width and center of the d-band of the surface layer, the stronger the adsorbate interacts with the surface. From table 19 we note that each functional universally predicts the d-band of each surface to shift away from the Fermi energy, and either remain at the same width or widen. On the reactive metals we calculate large values for the widening and shift of the d-band of the surface layer. On Pt(100) we note the largest magnitudes for the shift of the d-band of the surface layer ranging from 0.30 eV to 0.33 eV. Pd(100) yields the second largest magnitudes for the shift of the d-band of the surface layer ranging from 0.23 eV to 0.30 eV.



Finally on Rh(100) we note the smallest magnitudes for the shift of the d-band of the surface layer for the reactive metals ranging from 0.12 eV to 0.17 eV. For the widening of the d-band, we note that the d-band of all the reactive metal surfaces widen by similar amounts. We note a 0.14 eV to 0.19 eV widening of Rh(100)'s d-band, a 0.16 eV to 0.17 eV widening of Pt(100)'s d-band, and a 0.14 eV to 0.17 eV widening of Pd(100)'s d-band. As the values for the widening of the d-band of the surface layer are so close together they may be a less than ideal way to distinguish the strength of the molecule/substrate interaction for our three reactive metal surfaces. However, both the widening and the shift of the d-band of the surface layer for the reactive metals are much larger than for the coinage metals. On the coinage metals we note a maximum widening of the surface's d-band of 0.03 eV, which is much lower than the maximum widening of the surface's d-band for the reactive metals, 0.19 eV, and a maximum shift of the surface's d-band of 0.10 eV, which is much lower than the maximum shift of the surface's d-band for the reactive metals, 0.33 eV. This data supports our claim that thiophene physisorbs on the coinage metal surfaces and chemisorbs on the reactive metal surfaces. We would also like to point out the opt-type functionals on each surface often predict the largest magnitudes of both the widening and the shift of the d-band of the atoms that compose the first layer of the surface, which lines up well with their prediction of the largest adsorption energies on each surface.

### **3.5.5 Conclusions**

In the previous subsections we demonstrated thiophene physisorbs on the coinage metal surfaces and chemisorbs on the reactive metal surfaces. Thiophene's physisorption on the coinage metal surfaces is characterized by small adsorption energies, high adsorption heights, and minor perturbations to the electronic and geometric structure of the adsorbate/substrate

system. In contrast thiophene's chemisorption on the reactive metals is characterized by large adsorption energies, low adsorption heights, and significant perturbations to the electronic and geometric structure of the adsorbate/substrate system. These trends of thiophene physisorbing on the coinage metal surfaces and chemisorbing on the reactive metal surfaces were also present when we studied the adsorption of thiophene on Cu(100) and Ni(100). While our results allow us to classify the strength of the thiophene/substrate interaction for these surfaces, they do not permit us to say much about the performance of each individual functional mainly due to a lack of experimental results. With the limited experimental results we possess and looking at the description our chosen functionals gave of pyridine on transition metal surfaces, we were able to scrutinize the performance of the revPBE-vdW functional and the rPW86-vdW2 functionals. We were also able to tentatively put forth optB88-vdW as the best functional to model thiophene on these surfaces.

More importantly though, we again noted several similarities between our calculations of thiophene on transition metal surfaces and our calculations of pyridine on transition metal surfaces. For example, for both thiophene and pyridine on transition metal surfaces we observed that the opt-type functionals always calculated the largest adsorption energies. On the coinage metal surfaces we noted that the PBE functional always computed the smallest adsorption energies, and on the reactive metal surfaces the revPBE-vdW and the rPW86-vdW2 functionals always computed the largest adsorption energies. This suggests a certain degree of transferability of our results. The trends we observe for thiophene and pyridine on transition metal surfaces should hold for other organic molecules on transition metal surfaces. As a result,

the screening of our methods in this dissertation may be widely applied to any system of organic molecules on transition metal surfaces.

### **3.6 Using SCAN+rVV10 to Explore Thiophene on Ag, Rh, and Ir(100)**

Until now we have only looked at the same six functionals: PBE, optB86b-vdW, optB88-vdW, optPBE-vdW, revPBE-vdW, and rPW86-vdW2. We now move on and study the SCAN+rVV10 functional. Specifically we utilize the SCAN+rVV10 functional to study the adsorption of thiophene on the Ag, Rh, and Ir(100) surfaces. In the previous sections we demonstrated the superior performance of the optB88-vdW and optB86b-vdW functionals. Therefore we compare our SCAN+rVV10 results to results obtained using the optB88-vdW functional. By using SCAN+rVV10, a meta-GGA functional, and comparing its results to the results computed using optB88-vdW, a standard GGA functional, we hope to determine whether meta-GGA functionals can provide a better description of organic molecules on transition metal surfaces and justify their increased computational time. Moreover, as we explored thiophene on Ag(100) and Rh(100) using the optB88-vdW functional we do not need to run any more optB88-vdW calculations for those surfaces. For Ir(100) we have not run any optB88-vdW calculations and, therefore, need to run calculations of thiophene on Ir(100) using optB88-vdW. Finally, we chose the Ag, Rh, and Ir(100) surfaces to have a mix of both reactive and coinage metal surfaces as our previous results demonstrated two distinct adsorption trends on these two classes of surfaces.

In the first subsection of this section we present our computational details. In the second subsection we discuss the equilibrium adsorption sites and the stability of all the initial adsorption sites. In the third subsection we present an energetic and geometric analysis of the

equilibrium adsorption configurations including adsorption heights and energies. In the fourth subsection we study the electronic properties of the equilibrium adsorption configurations including the change in the surface’s work function, the charge transfer to the molecule, and the change in the surface’s d-band. In the final subsection we present our conclusions.

### 3.6.1 Computational Details

We perform all calculations using VASP version 5.4.4., which utilizes the PAW method. To model our surfaces we again use 5 layer slabs with each layer measuring 3 by 3 atoms, a (3x3) unit cell. We place at least 20 Å of vacuum in between neighboring slabs to avoid interactions between neighboring slabs in the z-direction. We construct each slab with the theoretical lattice constants listed in table 20. Furthermore, we allow the molecule and the surface to relax separately before we place the molecule on the surface. Once on the surface we allow all coordinates of the molecule/substrate system to undergo structural relaxation except the bottom two layers of the substrate which we hold at their positions in the relaxed substrate. To achieve structural relaxation we use the CG method. All together we try 12 different adsorption sites which we illustrate in figure 17. When we place the molecule in one of these adsorption sites we make sure that the S atom of the molecule sits approximately 2.7 Å above the surface.

Table 20: Calculated lattice constants for Rh, Ag, and Ir using optB88-vdW and SCAN+rVV10. Experimental lattice constants are also given for comparison.

Method	Rh(Å)	Ag(Å)	Ir(Å)
optB88-vdW	3.846	4.147	3.887
SCAN+rVV10	3.774 <sup>29</sup>	4.058 <sup>29</sup>	3.784 <sup>29</sup>
Experiment	3.793 <sup>91</sup>	4.063 <sup>91</sup>	3.832 <sup>91</sup>

Finally to model the exchange-correlation interaction we utilize the optB88-vdW functional and the SCAN+rVV10 functional. We also set the plane wave energy cutoff at 400 eV, set the force criterion at 0.02 eV/Å, and sample the BZ using a 6x6x1 Monkhorst-Pack grid. To access the stability of each adsorption site we again use equation 61. Using equation 61 one will remember that a higher adsorption energy corresponds to a more stable adsorption site.

### 3.6.2 Equilibrium Adsorption Configurations

After running all of our calculations we find that all of our chosen configurations are stable or metastable on Ag(100), meaning that thiophene sticks to its initial adsorption site on Ag(100). Figure 25 a) plots the adsorption energies of thiophene on each adsorption configuration on Ag(100). From figure 25 a) we note that both SCAN+rVV10 and optB88-vdW predict nearly identical adsorption energies for thiophene on Ag(100). Additionally they both predict hollow45 to be the most energetically favorable adsorption site. They also both predict v-bridge0 to be the most energetically favorable vertical adsorption site, and they both predict flat adsorption sites to be much more stable than vertical adsorption sites.

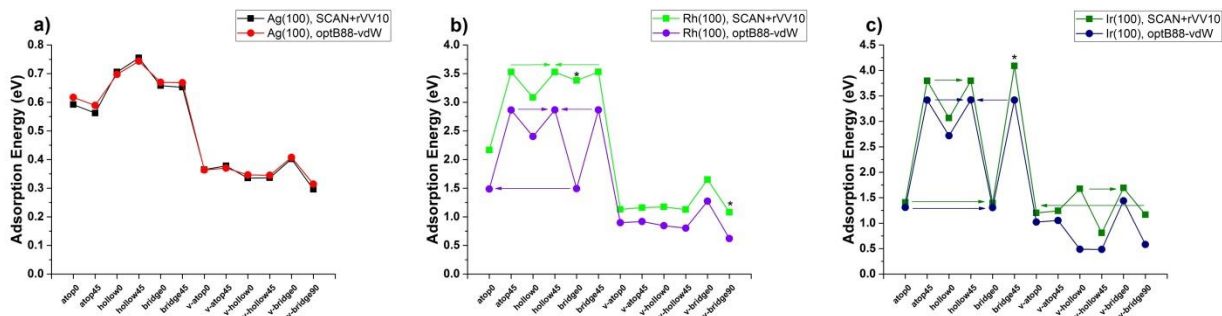


Figure 25: Adsorption energies for thiophene on a) Ag(100), b) Rh(100), and c) Ir(100) as calculated using the SCAN+rVV10 functional and the optB88-vdW functional. Unstable adsorption sites are denoted with an arrow pointing from the initial adsorption site to the final adsorption site. Unstable adsorption sites that lead to new adsorption sites are labeled with a \*.

On Rh(100), see figure 25 b) which plots the adsorption energies of thiophene on each adsorption configuration on Rh(100), we note SCAN+rVV10 and optB88-vdW also agree on these three features. They agree that hollow45 is the most energetically favorable adsorption site, that v-bridge0 is the most energetically favorable vertical adsorption site, and that the flat adsorption sites are much more stable than the vertical adsorption sites. However on Rh(100) SCAN+rVV10 and optB88-vdW now disagree about the overall strength of the thiophene/Rh(100) interaction with the SCAN+rVV10 functional predicting a systematic increase in the adsorption energy over the optB88-vdW functional. In addition to disagreeing about the strength of the thiophene/Rh(100) interaction both functionals now also disagree about the stability of several adsorption sites. We denote unstable adsorption sites in figure 25 b) in one of two ways. If thiophene in the unstable adsorption site moves to an adsorption site illustrated in figure 17 we denote the unstable adsorption site with an arrow pointing from the initial adsorption site towards the final adsorption site. We use a 0.03 eV energy cutoff to determine if the unstable adsorption site moves to an adsorption site illustrated in figure 17; that is the final adsorption site must be within 0.03 eV of one of the adsorption sites illustrated in

figure 17 to warrant the use of an arrow. If the adsorption energy is greater than 0.03 eV we use a \* to indicate the final adsorption is entirely new. From figure 17 b) we note that optB88-vdW predicts atop45 and bidge45 to move to hollow45, and bridge0 to move to atop0. The SCAN+rVV10 functionals agrees with optB88-vdW that bridge45 and atop45 should move to hollow45, but it also predicts bridge0 to move almost to hollow45 and v-bridge0 to move almost to v-atop0. We say almost as these final configurations were relatively close to hollow45 and v-atop0. However they fail the 0.03 eV energy cutoff, and thus we classify them as “new” adsorption sites. The adsorption energy of the v-bridge0 configuration is not within 0.03 eV of the adsorption energy of v-atop0 most likely to thiophene acquiring a 23° tilt angle away from the surface normal during relaxation in the v-bridge0 configuration. The bridge0 adsorption energy is not within 0.03 eV of the adsorption energy of hollow45 most likely due to the molecule acquiring a small amount of rotation about the z-axis compared to hollow45 when initially placed in bridge0.

On Ir(100) too we notice that optB88-vdW and SCAN+rVV10 disagree about the stability of some of the initial adsorption sites. The optB88-vdW functional predicts atop0 to move to bridge0, and atop45 and bridge45 to move to hollow45. The SCAN+rVV10 functional, while agreeing that atop0 moves to bridge0 and atop45 moves to hollow45 predicts v-hollow0 to move to v-bridge0, v-bridge90 to move to v-atop0, and thiophene in bridge45 to spontaneously break a single C-S bond, resulting in the adsorption site pictured in figure 19. SCAN+rVV10 predicts thiophene in this broken adsorption configuration to possess the largest adsorption energy in contrast to optB88-vdW which predicts thiophene in hollow45 to possess the largest adsorption energy. Overall, similar to what we observed on Rh(100), the SCAN+rVV10 functional

calculates much larger adsorption energies for thiophene on Ir(100) than optB88-vdW. Still both functionals agree that v-bridge0 is the most stable vertical adsorption site and that the flat adsorption sites are much more stable than the vertical adsorption sites.

Clearly some rather large discrepancies exist between the results of SCAN+rVV10 and optB88-vdW for thiophene on our two reactive metal surfaces, Ir(100) and Rh(100). The SCAN+rVV10 functional predicts larger adsorption energies and different adsorption sites to be unstable on Rh(100) and Ir(100) than optB88-vdW. More impressively though, SCAN+rVV10 predicts thiophene to spontaneously break a single C-S bond over bridge45 on Ir(100) like thiophene ruptured on Ni(100). Moreover, the SCAN+rVV10 functional predicts this new adsorption site to be more stable than hollow45. In order to explore these discrepancies further we discuss, in detail, the adsorption geometry and energetics of the equilibrium adsorption sites.

### **3.6.3 Adsorption Heights, Energies, and Other Structural Information**

In order to further understand the discrepancies between optB88-vdW and SCAN+rVV10 we list in table 21 the adsorption energies ( $E_{\text{ads}}$ ), the adsorption heights ( $H$ ), the C-S bond lengths, the buckling of the first layer of the surface, and the tilt angle ( $\Theta$ ) of the molecule relative to the surface for thiophene adsorbed on Ag, Rh, and Ir(100) in the highest adsorption energy configurations. We define the adsorption height in this section as the distance from the S atom to the nearest metal atom. Figure 26 a) also plots the adsorption energies for the highest adsorption energy configurations on each surface plus the adsorption energy of bridge45 on Ir(100) using optB88-vdW and the adsorption energy of hollow45 on Ir(100) using SCAN+rVV10 for comparison. We already discussed adsorption energies qualitatively in the previous section, but now we can discuss exact values. From figure 26 a) and table 21 we note, as was stated in the



previous section, that SCAN+rVV10 and optB88-vdW predict thiophene to have nearly the same adsorption energy on Ag(100), within 0.01 eV. In contrast on Rh(100) and Ir(100), as we again mention in the previous section, SCAN+rVV10 predicts much higher adsorption energies than optB88-vdW. Explicitly we note that SCAN+rVV10 predicts nearly a 20% enhancement of thiophene's adsorption energy on Ir(100) and nearly a 23% enhancement of thiophene's adsorption energy on Rh(100). Clearly SCAN+rVV10 handles the adsorption of thiophene on these two reactive surfaces much differently than optB88-vdW.

Table 21: Adsorption energies ( $E_{\text{ads}}$ ), adsorption heights (H), C-S bond lengths, buckling of the first layer of the substrate, and tilt angle of the molecule relative to the surface plane ( $\Theta$ ) for thiophene adsorbed in the hollow45 configuration on Ag, Rh, and Ir(100), and in the bridge45 configuration on Ir(100). \* Note optB88-vdW predicts thiophene to move from bridge45 to hollow45 on Ir(100). \*\* Note SCAN+rVV10 predicts thiophene to break over bridge45 on Ir(100).

Funtional/Adsorption Site	Surafce	$E_{\text{ads}}$ (eV)	H (Å)	C-S(Å)	Buckling (Å)	$\Theta$ (°)
SCAN+rVV10/hollow45	Ag(111)	0.75	2.84	1.71/1.71	0.03	1
optB88-vdW/hollow45		0.74	2.95	1.72/1.72	0.03	2
SCAN+rVV10/hollow45	Rh(111)	3.53	2.25	1.80/1.80	0.18	-1
optB88-vdW/hollow45		2.87	2.29	1.82/1.82	0.15	-1
SCAN+rVV10/bridge45**	Ir(111)	4.09	2.28	1.80/3.00	0.30	-1
SCAN+rVV10/hollow45		3.80	2.29	1.82/1.82	0.17	-1
optB88-vdW/bridge45*		3.42	2.33	1.84/1.84	0.16	-1
optB88-vdW/hollow45		3.42	2.33	1.84/1.84	0.16	-1

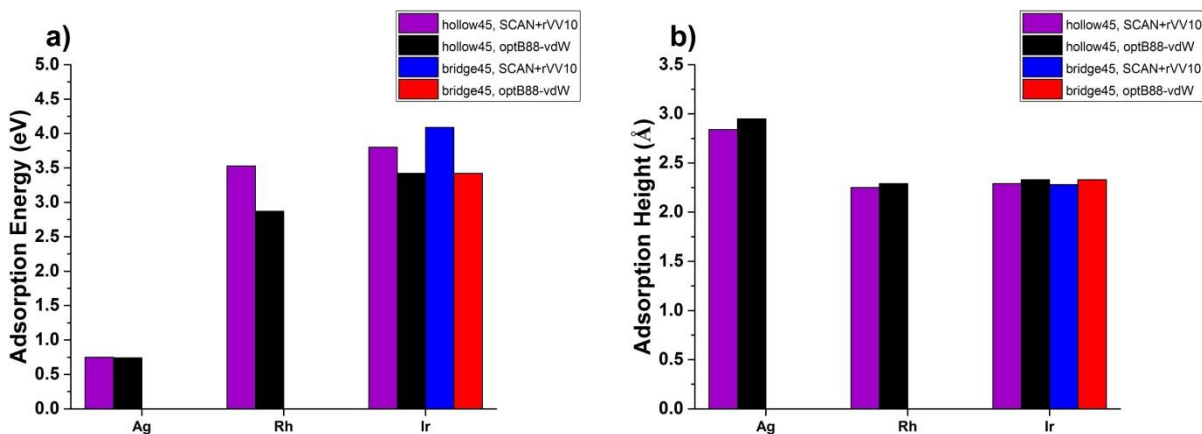


Figure 26: Adsorption energies ( $E_{\text{ads}}$ ), and adsorption heights ( $H$ ) for thiophene adsorbed in the hollow45 configuration on Ag, Rh, and Ir(100), and in the bridge45 configuration on Ir(100). Note optB88-vdW predicts thiophene to move from bridge45 to hollow45 on Ir(100), and SCAN+rVV10 predicts thiophene to break over bridge45 on Ir(100).

Despite SCAN+rVV10's prediction of thiophene's much higher adsorption energies on the reactive metal surfaces, SCAN+rVV10 predicts thiophene to sit only slightly lower on the Ir(100) and Rh(100) surfaces than optB88-vdW. Figure 26 b) plots the adsorption heights of thiophene on Ag, Rh, Ir (100) in the hollow45 configuration and in the bridge45 configuration on Ir(100). From figure 26 b) and table 21 we see that SCAN+rVV10 calculates adsorption heights of 2.25 Å on Rh(100), and of 2.28 Å and 2.29 Å on Ir(100) while optB88-vdW calculates adsorption heights of 2.29 Å on Rh(100), and of 2.33 Å on Ir(100). On Ag(100) too, SCAN+rVV10 predicts slightly lower adsorption heights than optB88-vdW with SCAN+rVV10 predicting an adsorption height of 2.84 Å and optB88-vdW predicting an adsorption height of 2.95 Å. These slightly smaller adsorption heights further indicate the SCAN+rVV10 functional estimates a larger thiophene/substrate interaction than the optB88-vdW functional. Bear in mind though the differences in adsorption height between these two functionals are approaching the

limit of the accuracy of our calculations. The buckling of the first layer of the substrate more potently suggests that SCAN+rVV10 binds thiophene more strongly to the Ir(100) and Rh(100) surface than optB88-vdW. The SCAN+rVV10 functional predicts the Rh(100) and Ir(100) substrates to buckle up to 0.03 Å and 0.14 Å more than the optB88-vdW functional, respectively. As we already discussed though, perhaps the most telling sign of SCAN+rVV10 predicting a larger thiophene/Ir(100) interaction than optB88-vdW is that SCAN+rVV10 predicts thiophene to rupture over Ir(100) in the bridge<sub>45</sub> site. This breaking of thiophene is characterized by the breaking of a C-S bond. The distance between the S atom and the cleaved C atom is 3.00 Å compared to the 1.80 Å distance between the S atom and the intact C atom. The rest of the results for C-S bond lengths in table 21 reveal that optB88-vdW, neglecting the case where thiophene breaks over Ir(100), generally predicts longer C-S bond lengths than SCAN+rVV10. This is quite interesting considering all the geometric results we have described thus far indicate SCAN+rVV10 predicts a stronger interaction of thiophene with Rh(100) and Ir(100), and a stronger thiophene/substrate interaction is usually accompanied by longer C-S bonds. The reason for this oddity is unknown and perhaps deserves further study. Finally, we note that both functionals predict thiophene to sit flat on these surfaces with a tilt angle relative to the surface of less than 2°.

So far we have established that SCAN+rVV10 and optB88-vdW provide similar descriptions of thiophene on Ag(100). The similar description these two functionals provide of the thiophene/Ag(100) system may be due to the large distance thiophene sits over Ag(100). At these distances the nonlocal correlation term describing the vdW interaction tends to dominate more. It may be that the vdW and the rVV10 correlation functionals handle the long range

thiophene/Ag(100) interaction in a similar manner. On Ir(100) and Rh(100) thiophene bonds much closer to the surface allowing the SCAN functional to contribute more to the description of the adsorption process. While SCAN+rVV10 definitely supplies a different description of thiophene on Rh(100) and Ir(100) than optB88-vdW, it is difficult to say which functional performs better due to a lack of experimental results. However a recent theoretical study by Patra and colleagues found SCAN to overbind CO on a variety of transition metal surfaces compared to PBE. They suggest this error is a density-driven error [160]. There are two main types of errors one makes when approximating the exact exchange-correlation functional, a functional error and a density-driven error. The functional error is the energy difference between the application of your functional to the exact density and application of the exact functional to the exact density [160]. The density-driven error is the energy difference between applying your functional to its self-consistent density and applying your functional to the true density [160]. For most functionals, functional errors dominate. For SCAN, Patra and coworkers argue SCAN's error on CO results from a density-driven error. Specifically they claim the error arises from a density-driven self-interaction error. They further assert that this error leads to spurious charge transfer between the CO molecule and the surface [160]. They also claim that this error is most likely present for most to all molecule/transition metal surface systems [160]. We already observe that SCAN+rVV10 binds thiophene more strongly to Rh(100) and Ir(100) than optB88-vdW. If we also observe that SCAN+rVV10 predicts more charge transfer from the surface to the thiophene molecule than optB88-vdW it may be that SCAN+rVV10 provides a poor description of thiophene on Rh(100) and Ir(100). The SCAN+rVV10 functional may overbind thiophene to Rh(100) and Ir(100).

### 3.6.4 Electronic Analysis

In order to study if SCAN+rVV10 overbinds thiophene to Rh(100) and Ir(100) we perform an electronic structure analysis of the adsorbate/substrate system. We calculate and list in table 22 the charge transfer to the thiophene molecule ( $\Delta q$ ), the change in the center ( $\Delta C$ ) and the width ( $\Delta W$ ) of the atoms that compose the first layer of the substrate, and the change in the work function of the surface ( $\Delta \Phi$ ) for thiophene adsorbed in the hollow45 configuration on Ag, Rh, and Ir(100), and in the bridge45 configuration on Ir(100). For convenience figure 27 plots the charge transfer for thiophene adsorbed in the hollow45 configuration on Ag, Rh, and Ir(100), and in the bridge45 configuration on Ir(100). From figure 27 and table 22 we notice that SCAN+rVV10, across all metals, indeed predicts the thiophene molecule to take much more charge from the surface than optB88-vdW. Specifically we observe that SCAN+rVV10 calculates thiophene to take 0.3 (-e) more charge from Ag(100), 0.6 (-e) more charge from Rh(100), and up to 0.7 (-e) more charge from Ir(100) than optB88-vdW. This large amount of charge that SCAN+rVV10 predicts thiophene to take from the surfaces along with SCAN+rVV10's large adsorption energies for these systems supports the claim made by Patra and coworkers. Just as SCAN predicts an overbinding of CO to transition metal surfaces [160], the SCAN+rVV10 functional probably predicts an overbinding of thiophene to Rh(100) and Ir(100) due to a density-driven self-interaction error. This suggests that the optB88-vdW functional, a GGA functional, outperforms the SCAN+rVV10 functional, a meta-GGA functional, for these types of organic molecule/transition metal substrate systems, which is disappointing considering SCAN+rVV10 is much more computationally expensive than optB88-

vdW. This result also highlights the fact that just because a functional is, in theory, more accurate does not mean it will outperform less accurate functionals for every system.

Table 22: The charge transfer from the surface to the thiophene molecule ( $\Delta q$ ), the change in the width ( $\Delta W$ ) and the center ( $\Delta C$ ) of the d-band of the atoms that compose the first layer of the substrate, and the change in the surface's work function ( $\Delta\Phi$ ) for thiophene adsorbed in the hollow45 configuration on Ag, Rh, and Ir(100), and in the bridge45 configuration on Ir(100). \* Note optB88-vdW predicts thiophene to move from bridge45 to hollow45 on Ir(100). \*\* Note SCAN+rVV10 predicts thiophene to break over bridge45 on Ir(100).

Funtional/Adsorption Site	Surafce	$\Delta q(-e)$	$\Delta W(eV)$	$\Delta C(eV)$	$\Delta\Phi(eV)$
SCAN+rVV10/hollow45	Ag(111)	0.2	0.02	-0.07	-0.59
optB88-vdW/hollow45		-0.1	0.02	-0.07	-0.53
SCAN+rVV10/hollow45	Rh(111)	0.7	0.21	-0.18	-1.02
optB88-vdW/hollow45		0.1	0.16	-0.17	-1.02
SCAN+rVV10/bridge45**	Ir(111)	0.8	0.38	-0.28	0.07
SCAN+rVV10/hollow45		0.7	0.28	-0.24	-0.13
optB88-vdW/bridge45*		0.1	0.23	-0.21	-1.23
optB88-vdW/hollow45		0.1	0.23	-0.21	-1.23

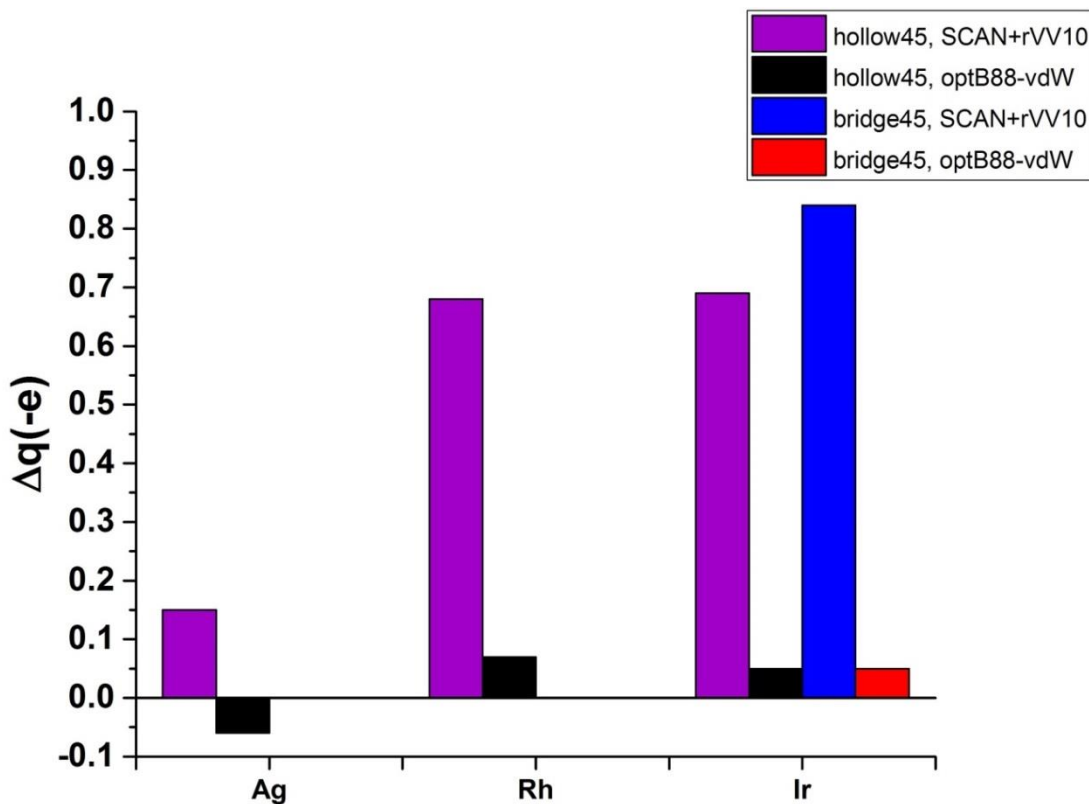


Figure 27: The charge transfer from the surface to the thiophene molecule ( $\Delta q$ ) for thiophene adsorbed in the hollow45 configuration on Ag, Rh, and Ir(100), and in the bridge45 configuration on Ir(100). Note optB88-vdW predicts thiophene to move from bridge45 to hollow45 on Ir(100), and SCAN+rVV10 predicts thiophene to break over bridge45 on Ir(100).

Moving on, the results for the change in the center and width of the d-band of the atoms that compose the first layer of the surface appear to be good indicators of the strength of thiophene's interaction with each surface. The change in the width and center of the atoms that compose the first layer of the substrate increase as  $\text{Ag}(100) < \text{Rh}(100) < \text{Ir}(100)$ , which is the exact same trend for the adsorption energies. Moreover, the results for the change in the width and center of the d-band of each surface also fits into the narrative that SCAN+rVV10 overbinds thiophene to Rh(100) and Ir(100), or least demonstrates again that SCAN+rVV10 bonds thiophene more

strongly to Rh(100) and Ir(100) than optB88-vdW. Both SCAN+rVV10 and optB88-vdW predict the d-band of the Ir(100) and Rh(100) surface to widen and shift away from the Fermi energy. The SCAN+rVV10 functional, however, consistently predicts more widening and a larger shift of the surface's d-band than optB88-vdW. SCAN+rVV10 predicts the d-band of the Rh(100) surface to widen by 0.21 eV and shift 0.18 eV away from the Fermi energy while optB88-vdW predicts the d-band of the Rh(100) surface to widen by 0.16 eV and shift 0.17 eV away from the Fermi energy. Furthermore on Ir(100), SCAN+rVV10 predicts the d-band of the surface to widen up to 0.38 eV and shift up to 0.28 eV away from the Fermi energy while optB88-vdW only predicts the d-band of the surface to widen by 0.23 eV and shift by 0.21 eV away from the Fermi energy. These results again indicate that SCAN+rVV10 binds thiophene more strongly to Rh(100) and Ir(100) than optB88-vdW. Finally on Ag(100) we note both SCAN+rVV10 and optB88-vdW predict thiophene causes about the same modification to the d-band of the surface. This is consistent with our previous analysis which also demonstrated SCAN+rVV10 and optBB8-vdW provide a similar description of thiophene on Ag(100).

The last quantity we list in table 22 is the change in the surface's work function upon the adsorption of thiophene. On Ir(100) we note optB88-vdW predicts a much larger change in the surface's work function than SCAN+rVV10. This agrees well with results of the charge transfer. If we will remember our discussion in section 3.2 an adsorbate can change the surface dipole, and thus the work function of the surface, in several ways. It can lower the surface dipole through the "pushback" effect where the electron clouds of the adsorbate "pushback" the charge at the surface. The adsorbate can exchange charge with the surface, modifying the surface dipole. Finally if the molecule has a dipole moment oriented perpendicular to the surface or if



the adsorption process induces a geometric distortion in the molecule that creates a dipole moment oriented perpendicular to the surface then the molecule's dipole can interact with and change the surface dipole. In the case of thiophene the molecular dipole must be induced by the surface as thiophene in the gas phase does not possess a dipole moment perpendicular to its molecular plane. Now SCAN+rVV10 predicts thiophene to take much more charge from Ir(100) than optB88-vdW. This extra charge in the interface region, in theory, would counteract the “pushback” effect and increase the surface dipole leading SCAN+rV10 to predict thiophene covered Ir(100) to have a higher work function than optB88-vdW, which is precisely what we calculate. This simple correlation between charge transfer to the molecule and change in the surface's work function breaks down, however, when we look at Rh(100) and Ag(100). On these surfaces SCAN+rVV10 again predicts thiophene to take more charge from the surface than optB88-vdW yet both functionals predict nearly the same change in each surface's work function. Clearly on these surfaces there is a complex competition between the charge transfer, the “pushback” effect, and possibly even a molecular dipole effect. To that end we group the change in the work function of the surface due to the charge transfer and the “pushback” effect into a quantity we label  $\Delta\Phi_{\text{chg}}$ . Thus the total change in the surface's work function would be the sum of  $\Delta\Phi_{\text{chg}}$  and the change in the work function due to any induced molecular dipole moment,  $\Delta\Phi_{\text{mol}}$ , which we can directly calculate with VASP. VASP gives us a dipole moment,  $\mu_{\text{mol}}$ . Using this dipole moment we can calculate its contribution to the change in the work function using equation 62. Equation 62 is the change in a surface's work function due to a dipole layer. It comes from the solution to the Helmholtz equation,

$$\Delta\Phi = \frac{e}{\epsilon_0 A} \mu \quad (62)$$

where  $e$  is the charge of an electron,  $\epsilon_0$  is the vacuum permeability,  $A$  is the area of our surface, and  $\mu$  is the dipole moment. Table 23 lists thiophene's induced dipole moment perpendicular to the surface ( $\mu_{\text{mol}}$ ), the change in the surface's work function due to the molecular dipole moment ( $\Delta\Phi_{\text{mol}}$ ), the change in the surface's work function due to charge transfer and the "pushback effect" ( $\Delta\Phi_{\text{chg}}$ ), as calculated by equation 63, and the total change in the surface's work function ( $\Delta\Phi$ ).

$$\Delta\Phi_{\text{chg}} = \Delta\Phi - \Delta\Phi_{\text{mol}} \quad (63)$$

As one can see from table 23, on Ag(100) both functionals predict the "pushback" to contribute the most to the change in Ag(100)'s work function. The adsorption process on Ag(100) fails to induce a dipole moment in thiophene, and there is a small amount of charge transferred from the surface to thiophene. On Rh(100) the surface now induces a notable dipole moment in thiophene which helps to contribute to the decrease in the surface's work function. Concerning charge transfer, the optB88-vdW functional predicts little charge transfer from Rh(100) to thiophene, and therefore the remaining decrease in the surface's work function must result from the "pushback" effect. The SCAN+rVV10 functional, in contrast, predicts a large charge transfer from Rh(100) to thiophene. This charge transfer must be competing fiercely with the "pushback" effect, or most of the charge transfer to thiophene as predicted by SCAN+rV10 must be above the molecule as both SCAN+rVV10 and optB88-vdW predict thiophene to decrease Rh(100)'s work function by the same amount. On Ir(100) we note the surface induces an even larger dipole moment in thiophene than Rh(100), which is not surprising given that thiophene interacts more strongly with Ir(100) than Rh(100). The optB88-vdW functional calculates that

the “pushback” effect contributes alongside this induced molecular dipole moment to give the total decrease in Ir(100)’s work function. In contrast, SCAN+rVV10 predicts the large charge from the surface to Rh(100) to completely overwhelm the “pushback” effect, leading to a positive value for  $\Delta\Phi_{\text{chg}}$ , and a small overall decrease in Ir(100)’s work function.

Table 23: The induced dipole moment of thiophene perpendicular to the surface ( $\mu_{\text{mol}}$ ), the contribution to the change in the work function of the surface from the induced dipole moment of thiophene perpendicular to the surface ( $\Delta\Phi_{\text{mol}}$ ), the contribution to the change in the work function of the surface from the charge transfer to the thiophene molecule and the “pushback” effect ( $\Delta\Phi_{\text{chg}}$ ), and the total change in the surface’s work function ( $\Delta\Phi$ ) for thiophene adsorbed in the hollow45 configuration on Ag, Rh, and Ir(100)

Functional/Adsorption Site	Surface	$\mu_{\text{mol}}(-e)$	$\Delta\Phi_{\text{mol}}(\text{eV})$	$\Delta\Phi_{\text{chg}}(\text{eV})$	$\Delta\Phi(\text{eV})$
SCAN+rVV10/hollow45	Ag(111)	-0.01	-0.02	-0.57	-0.59
optB88-vdW/hollow45		-0.01	-0.02	-0.51	-0.53
SCAN+rVV10/hollow45	Rh(111)	-0.33	-0.93	-0.09	-1.02
optB88-vdW/hollow45		-0.32	-0.87	-0.15	-1.02
SCAN+rVV10/hollow45	Ir(111)	-0.35	-0.98	0.85	-0.13
optB88-vdW/hollow45		-0.35	-0.93	-0.30	-1.23

### 3.6.5 Comparison to optB88-vdW and Conclusions

Overall we have seen that SCAN+rVV10 and optB88-vdW give a similar description of thiophene on Ag(100). This may be due to the weak nature of the interaction of thiophene with Ag(100) and the large adsorption heights associated with that weak interaction. At these large distances the rVV10 and vdW nonlocal correlation functionals, which both describe the long range interactions, may perform similarly. On our two reactive metal surfaces, Rh(100) and Ir(100), thiophene bonds much closer to the surface and we begin to notice significant differences in the performance of these two functionals. The SCAN+rVV10 functional predicts a consistent increase in the adsorption energy of thiophene on these surfaces compared to optB88-vdW. Along with these higher adsorption energies, SCAN+rVV10 predicts slightly

lower adsorption heights and a larger buckling of the surface than optB88-vdW. Perhaps the most telling sign of the difference in the performance of SCAN+rVV10 and optB88-vdW is that SCAN+rVV10 predicts the most energetically favorable adsorption site on Ir(100) to be when thiophene breaks apart over the bridge45 configuration. In contrast optB88-vdW predicts the most energetically favorable adsorption site on Ir(100) to be hollow45. In tandem with predicting a stronger thiophene/reactive metal surface interaction, SCAN+rVV10 also predicts much more charge transfer from the surface to thiophene than optB88-vdW. Moreover, a previous study of CO on various transition metal surfaces pointed out that SCAN is plagued by a density-driven self-interaction error. This error causes SCAN to both overbind CO on transition metal surfaces compared to PBE, and to predict a spurious amount of charge transfer to from the surface to CO. They also suggest that this error is probably present for other molecule/transition metal surface systems [160]. Given this study and our observation that SCAN+rVV10 predicts large adsorption energies and a large amount of charge transfer compared to our GGA type functional, optB88-vdW, we assert that SCAN+rVV10 suffers from the same error found in SCAN, namely SCAN+rVV10 predicts thiophene to overbind to Ir(100) and Rh(100).

This demonstrates again the importance of picking an optimal functional for your system. In the case of thiophene on reactive metal surfaces, opting for the SCAN+rVV10 functional may result in an overbinding of thiophene, spurious charge transfer, and an incorrect prediction of the surface's work function. Compound these errors with the large computational cost of SCAN+rVV10 and we must strongly suggest using the optB88-vdW functional for any organic molecule/transition metal substrate system.

## **CHAPTER FOUR: OTHER APPLICATIONS OF DENSITY FUNCTIONAL THEORY**

Until now the focus of this dissertation has been screening the performance of various functionals using systems of small organic molecules on various transition metal surfaces. In this chapter we take the optB88-vdW functional, one of the functionals we found in the previous chapter to perform well, and apply it to systems of technological interest. In the first section of this chapter we study the adsorption of thiophene on various new transition metal surfaces including Cr(100), V(100), Ta(100), W(100), Mo(100), Nb(100), Al(100), and Co(10-10). This time we use these systems to model the hydrodesulfurization (HDS) process, the process used to remove S from petrochemicals and natural gas. This process is extremely important from an economic and environmental point of view. In the next section we look at polythiophenes on Au(111). Polythiophenes are often used in molecular electronic devices. However there is concern these molecules may break apart on substrates like Au, resulting in a less than optimal situation for the creation of a practical device. In the last section we study 5,14-dihydro-5,7,12,14-tetraazapentacene (DHTAP) on Cu(110). We investigate DHTAP, a derivative of pentacene, as an alternative to pentacene in organic electronic devices as pentacene has long-term stability issues under ambient conditions.

### **4.1 Studying the Initial Steps of Thiophene Hydrodesulfurization**

Reproduced from W. Malone, W. Kaden, A. Kara, Exploring thiophene desulfurization: The adsorption of thiophene on transition metal surfaces, Surf. Sci., 686 (2019) 30, with the permission of Elsevier Publishing

The removal of sulfur from crude-oil feedstocks via HDS leads to cleaner fuels. As mentioned in the introduction of this chapter, the burning of S containing compounds in fuels contributes to smog and acid rain. In order to meet stricter environmental standards improving HDS catalysis has drawn a large amount of attention in recent decades [161]. To improve HDS catalysis many have focused on simple, sulfur containing probe molecules to extract key properties likely to be important to larger, more complicated sulfur containing molecules present in crude oil feedstocks [37, 162-178].

Thiophene, as noted, is one of the simplest sulfur containing compounds, but also one of the hardest to desulfurize [37], making it an ideal candidate to study HDS. Many studies detail the desulfurization of thiophene yet the process is still poorly understood [162-168]. The standard schools of thought predict thiophene can break apart in one of two parallel reaction pathways, the direct desulfurization pathway and the hydrogenative desulfurization pathway. In either case the reactants are thiophene and  $H_2$  and the products are  $H_2S$  and other hydrocarbons, mainly butane. We chose to avoid putting H in our system to save computational time and too see if thiophene can spontaneously rupture over any other surfaces besides Ni(100). While industrially available catalysts are usually oxide supported multi-metallic sulfides many have chosen to study HDS reactions using single-crystalline systems such as Mo [173-181]. The rationale behind such a choice is to allow a more rapid screening of different materials while minimizing the impact to the results; the active sites in industrially available catalysis are often metal sites or S vacancies [173], which are exactly the sites available for study on single-crystalline surfaces.

For the above reasons in this section we study the adsorption of thiophene on Cr(100), V(100), Ta(100), W(100), Mo(100), Nb(100), Al(100), and Co(10-10) in hopes of better understanding the HDS process. In the first subsection we provide the details of our calculation. In the second subsection we cover the adsorption energetics and geometry of any adsorption site/metal surface combinations that broke thiophene apart, and the most stable adsorption site on each metal surface that keeps thiophene intact. In the third subsection we discuss the charge transfer to the thiophene molecule for the same adsorption sites discussed in the last subsection. In the fourth subsection we delve into the change in the surface's work function and the modification of the d-band of the atoms that compose the first layer of the substrate for the same adsorption sites discussed in the last two subsections. In the fifth subsection we try to map our data to known periodic HDS trends, and in the last subsection we present our conclusions.

#### **4.1.1 Computational Details**

We perform all calculations employing VASP version 5.4.4., which uses the PAW method. To model the exchange-correlation interaction we use the optB88-vdW functional, the functional we found in the previous chapter of this dissertation to give the best description of organic molecules on transition metal surfaces. Furthermore, we model our surfaces using 5 layer slabs with each layer measuring 3 by 3 atoms. To avoid slab/slab interaction in the z-direction we place at least 20 Å of vacuum in between slabs. We construct each slab using the theoretical lattice constants listed in table 24. We also list the experimental lattice constants in table 24 for comparison. After constructing the substrate and the molecule, we allow both systems to undergo complete structural relaxation before placing the molecule on the substrate. As the body-centered cubic (BCC)(100) and face-centered cubic(FCC)(100) surfaces share the same

symmetry we use the same adsorption sites on these surfaces. Specifically after the molecule and substrate relax separately, we place the molecule approximately with its S atom 2.7 Å above the surface in one of the 12 adsorption sites illustrated in figure 17. The hexagonal close packed (HCP) (10-10) surface, possessing a completely different geometry than both the FCC(100) surface and the BCC(100) surface, necessitates the inclusion of new, different adsorption sites. As the first two layers of the HCP(10-10) surface boast the same symmetry as the FCC(110) surface, on Co(10-10) we place thiophene with its S atom 2.7 Å above the surface in one of the 20 adsorption sites pictured in figure 13. As in the rest of this dissertation, we neglect accounting for the substrate’s geometry beyond the second layer in our choice of adsorption sites as the geometry of the third layer and beyond should only have minimal effects on the adsorption properties of the organic molecule.

Table 24: Calculated lattice constants for Al, Ir, W, Mo, Cr, Ta, Nb, V, and Co using the optB88-vdW functional. Experimental lattice constants, taken from reference 91, 182, or 183, are given for comparison.

Metal	optB88-vdW	Experimental
Al	4.053	4.019 <sup>182</sup>
Ir	3.887	3.832 <sup>91</sup>
W	3.178	3.161 <sup>182</sup>
Mo	3.154	3.141 <sup>182</sup>
Cr	2.834	2.880 <sup>182</sup>
Ta	3.306	3.299 <sup>182</sup>
Nb	3.317	3.293 <sup>182</sup>
V	2.969	3.024 <sup>182</sup>
Co	2.489,4.095	2.492,4.069 <sup>183</sup>

Finally, to achieve structural relaxation we use the CG method. We set the force criterion at 0.02 eV/Å, set the plane wave energy cutoff at 400 eV, and sample the BZ using a 6x6x1



Monkhorst-Pack grid. To access the stability of each adsorption site we use equation 61. With equation 61 a higher adsorption energy corresponds to a more stable adsorption site.

#### 4.1.2 Adsorption Energetics and Geometry

In this subsection we explore the adsorption energetics and geometry of any adsorption site/transition metal surface combination that broke thiophene apart, and the most energetically favorable adsorption site on each transition metal surface that keeps thiophene intact. In fact thiophene breaks at least 1 C-S bond on Mo(100), W(100), Cr(100), Ta(100), Nb(100), and V(100). These broken configurations result in the highest adsorption energies on these surfaces. For the remainder of the surfaces, thiophene remains intact and the hollow<sub>45</sub> configuration or the bridge<sub>S1</sub> configuration on Co(10-10) results in the largest adsorption energy. Figure 28 illustrates the adsorption geometry of any adsorption site/transition metal surface combination that broke at least one C-S bond. From figure 28 we note that thiophene breaks 1 C-S bond over Mo(100), 1 or 2 C-S bonds over W(100) and Cr(100), and 2 C-S bonds over V, Nb, and Ta (100). We also note the presence of 4 active sites. Thiophene could break a single C-S bond over bridge<sub>0</sub>, 1 or 2 C-S bonds over bridge<sub>45</sub> or hollow<sub>0</sub>, and 2 C-S bond over atop<sub>45</sub>. In addition to specific active sites, thiophene assumes only a few final configurations after losing 1 or 2 C-S bonds. When thiophene breaks one C-S bond it may end up with its S atom and cleaved C atom straddling a single metal atom with the center of the molecule over a bridge site. We have already seen this site when thiophene breaks over Ni(100), and among the surfaces we study here it is the most popular configuration in which thiophene breaks only 1 C-S bond. The second configuration that results when thiophene breaks one C-S bond is that it may end up with its S atom and cleaved C atom straddling a single metal atom with the center of the molecule over a

hollow site. This configuration only occurs when thiophene breaks over Mo(100) in the hollow0 configuration. The last configuration that results when thiophene breaks one C-S bond is that it may end up with its S atom and cleaved C atom straddling a hollow site with the center of the molecule approximately over a metal atom. This configuration only occurs when thiophene breaks over W(100) in the bridge0 configuration. Moving further, when thiophene breaks two C-S bonds it usually results in atomic S and C<sub>4</sub>H<sub>4</sub> on the surface. These products can assume several configurations on our (100) surfaces. First thiophene may break apart such that the S atom bonds to a hollow site and remaining hydrocarbon fragment bonds across a bridge site. Thiophene can assume this configuration on Cr(100), Ta(100), and W(100). Second thiophene may break apart such that the S atom still bonds to a hollow site but now the remaining hydrocarbon fragment bonds across a hollow site instead of a bridge site. This configuration only occurs when thiophene breaks apart over Ta(100) in the bridge45 configuration. Third thiophene may break apart such that the S atom bonds to a locally deformed 3-fold hollow site with the remaining hydrocarbon fragment bonded across a bridge site. Thiophene can assume this configuration on Nb(100) and Ta(100) after initially being placed in the atop45 configuration. Finally, thiophene may break apart to S and 2C<sub>2</sub>H<sub>2</sub> on V(100). When the hydrocarbon fragment, C<sub>4</sub>H<sub>4</sub>, further degrades on V(100) the S atom and the two C<sub>2</sub>H<sub>2</sub> molecules prefer to bond to hollow sites.

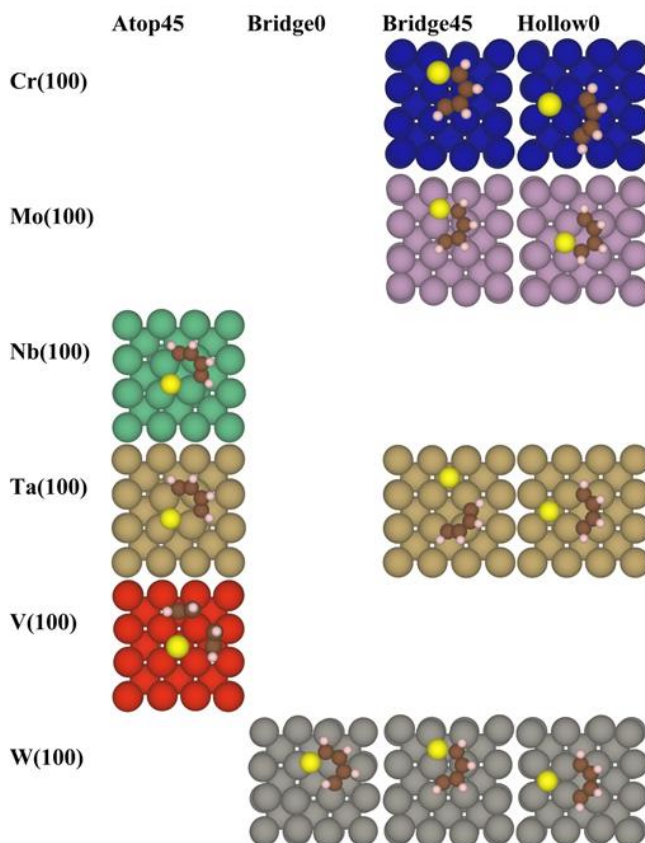


Figure 28: An illustration of any adsorption configurations that result in thiophene breaking at least one C-S bond.

As thiophene breaks a number of ways over these surfaces we list in table 25 the adsorption energies ( $E_{\text{ads}}$ ), the S-Metal distances, the z-coordinate of the S atom minus the average of the z-coordinates of the atoms that compose the first layer of the substrate ( $S_z\text{-Surface}_z$ ), and the buckling of the first layer of the substrate for each configuration that broke at least one C-S bond and the hollow45 configuration. As mentioned, for the surfaces that keep thiophene intact hollow45 or bridgeS1 for Co(10-10) yields the highest adsorption energy or in the case of thiophene Al(100) hollow45 ties for the highest adsorption energy with bridge0 and bridge45. From table 25, we note that among the transition metal surfaces that result in thiophene breaking

1 or 2 C-S bonds, adsorption sites that break more C-S bonds lead to a higher adsorption energy. This makes sense given that a larger thiophene/substrate interaction should be necessary to break more C-S bonds. For transition metal surfaces that result in multiple adsorption sites breaking one C-S bond we note the preferred final adsorption site is when thiophene ends up with its S atom and cleaved C atom straddling a single metal atom with the center of the molecule over a bridge site. For transition metal surfaces that result in multiple adsorption sites breaking two C-S bonds we note the preferred final adsorption site is when the S atom bonds to a hollow site and the remaining hydrocarbon fragment bonds across a bridge site. If we look at the adsorption energies by metal, figure 29 a) plots the adsorption energy for the highest adsorption energy configuration on each surface, we note the adsorption increases as  $\text{Al}(100) < \text{Co}(10-10) < \text{Ir}(100) < \text{Nb}(100) < \text{Mo}(100) < \text{Ta}(100) < \text{Cr}(100) < \text{V}(100) < \text{W}(100)$ . From this trend we see that surfaces that left thiophene intact result in the lowest adsorption energies. This again makes sense given that a larger thiophene/substrate interaction should be necessary to break more C-S bonds. The Nb(100) results, however, challenge this notion. On Nb(100) thiophene breaks two C-S bonds and the resulting adsorption energy is lower than when thiophene only breaks a single C-S bond on Mo(100).

Table 25: Adsorption energy ( $E_{\text{ads}}$ ), S-Metal distances, the z-coordinate of the S atom minus the average of the z-coordinates of the atoms that compose the first layer of the substrate ( $S_z$ -Surface $_z$ ), and the buckling of the first layer of the substrate for each configuration that broke at least one C-S bond and the hollow45 configuration on each transition metal surface.

Metal/Adsorption Site	$E_{\text{ads}}$ (eV)	S-Metal ( $\text{\AA}$ )	( $S_z$ -Surface $_z$ ) ( $\text{\AA}$ )	C-S( $\text{\AA}$ )	Buckling ( $^\circ$ )
Al(100)/hollow45	0.53	3.58	3.53	1.72/1.72	0.05
Co(10-10)/bridgeS1	1.90	2.27	1.73	1.81/1.81	0.12
Ir(100)/hollow45	3.42	2.33	2.22	1.84/1.84	0.16
Nb(100)/atop45	4.27	2.37	1.97	3.13/3.13	0.49
V(100)/atop45	7.17	2.38	1.18	3.15/3.16	0.57
Cr(100)/bridge45	5.48	2.31	1.85	1.82/3.11	0.19
Cr(100)/hollow0	6.87	2.34	1.44	3.27/3.90	0.17
Mo(100)/bridge45	5.16	2.46	1.88	1.82/3.29	0.19
Mo(100)/hollow0	4.59	2.39	1.89	1.81/2.93	0.18
Ta(100)/atop45	4.37	2.35	1.96	3.11/3.11	0.41
Ta(100)/bridge45	6.03	2.56	1.06	3.89/5.29	0.43
Ta(100)/hollow0	6.14	2.56	1.07	3.75/3.75	0.37
W(100)/bridge0	4.66	2.42	2.06	1.82/3.11	0.22
W(100)/bridge45	5.76	2.48	1.89	1.84/3.30	0.16
W(100)/hollow0	7.34	2.50	1.53	3.56/3.57	0.26

To further explore this inconsistency we plot the S-Metal distances in figure 29 b) for the adsorption sites with the highest adsorption energy on each surface. Configurations that broke one C-S bonds are denoted by a dot. Configurations that broke two C-S bonds are denoted by two dots. We will again remind the reader we list these values in table 25 for a larger assortment of adsorption sites. From figure 29 b) and table 25 we note a relatively narrow range of S-Metal distances. With the exception of Al(100), where we observe very large S-Metal distances, we observe S-Metal distances ranging from 2.27  $\text{\AA}$  to 2.56  $\text{\AA}$ . This is reminiscent of when we explored thiophene on Rh, Pt, and Pd(100) where we observed similar S-Metal distances across all three substrates. For those systems, and these systems too, there appears to be some optimal S-Metal distance that does not change readily with the element in the surface. For that reason,

we also plot ( $S_z$ -Surface $_z$ ) in figure 29 b) for the adsorption sites with the highest adsorption energy on each surface. We will again remind the reader we list these values in table 25 for a larger assortment of adsorption sites. ( $S_z$ -Surface $_z$ ) as one will remember is the z-coordinate of the S atom minus the average of the z-coordinates of the atoms that compose the first layer of the substrate, meaning it measures how close the S atom approaches the surface plane. Unlike the values of S-Metal the values of ( $S_z$ -Surface $_z$ ) vary heavily with surface composition, and much more closely follow the adsorption energy trends. Thiophene on Al(100) and Ir(100) both give the highest values for ( $S_z$ -Surface $_z$ ) and also the lowest adsorption energies. Our four surfaces that thiophene interacts the most strongly with, W(100), Ta(100), Cr(100), and V(100), are also the surfaces where the S atom sinks the closest to the surface plane. The values for ( $S_z$ -Surface $_z$ ) also nicely explains why we calculate a relatively small adsorption energy on Nb(100). The S atom on Nb(100), with a ( $S_z$ -Surface $_z$ ) value of 1.97 Å, remains relatively far from the surface. Why does the S atom on Nb(100) remain relatively far from the surface? We believe it is because thiophene, when it breaks apart on Nb(100), deforms the surface such that the S atom rests on a 3-fold hollow site instead of a 4-fold hollow site with the more compact geometry of the 3-fold hollow site preventing the S atom from further approaching the surface. The results of thiophene on Ta(100) in atop45 support this claim. On Ta(100) in atop45 thiophene breaks 2 C-S bonds, and deforms the surface such that the S atom sits on a deformed 3-fold hollow site. In this configuration the adsorption energy is much lower and the ( $S_z$ -Surface $_z$ ) distance much higher than when thiophene breaks 2 C-S bonds over Ta(100) such that the S atom sits over a 4-fold hollow site. This effectively solves our mystery of the low adsorption energy of thiophene on Nb(100). Finally we should mention that the only surface in which the values of ( $S_z$ -Surface $_z$ )

and adsorption energy do not correlate well is Co(10-10). This almost certainly occurs because of the open nature of the (10-10) surface which allows the S atom to approach the surface without a strong interaction with the substrate.

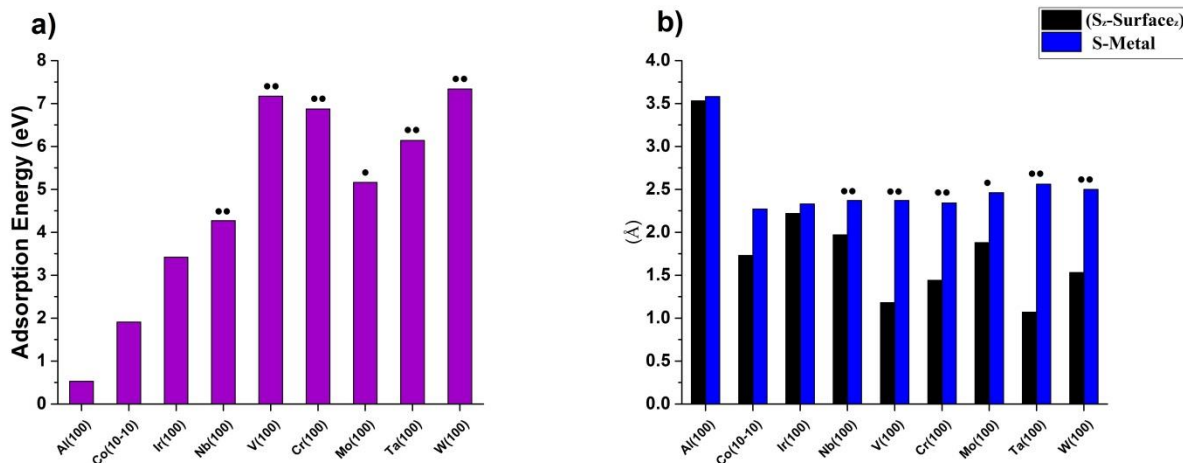


Figure 29: a) The adsorption energies, and b) ( $S_z$ -Surface $_z$ ) distances and S-Metal distances of thiophene adsorbed on Al(100), Co(10-10), Ir(100), Nb(100), V(100), Cr(100), Mo(100), Ta(100), and W(100) in the adsorption site that led to the highest adsorption energy. A single dot over a bar means that thiophene broke one C-S bond in the highest adsorption energy configuration on that specific transition metal surface. A double dot over the bar means that thiophene broke two C-S bonds in the highest adsorption energy configuration on that specific transition metal surface.

Moving on to the rest of the data in table 25, we observe short C-S bond lengths for thiophene on Al(100). This fits the narrative already established by the small adsorption heights and large adsorption energies we observe on this surface, namely that thiophene interacts weakly with Al(100). On Co(10-10) and Ir(100) we calculate much larger C-S bond lengths, 1.81Å to 1.84Å, which is indicative of thiophene's stronger interaction with these surfaces. Moving on, when thiophene breaks 1 C-S bond the remaining C-S bond takes on this range of values too, 1.81Å to 1.84Å. In contrast the severed C-S bond distance sits in a much larger range of values, 2.93 Å to 3.30 Å. We calculate an even larger range of C-S distances when thiophene breaks 2 C-S bonds,

3.11 Å to 5.29 Å. This large flexibility in the C-S distances when thiophene breaks 2 C-S is to be expected though as when thiophene completely breaks apart we are measuring the distances between atomic sulfur and parts of a hydrocarbon fragment instead of measuring distances between atoms in the same molecule. Moreover, the final resting place of S atom and the hydrocarbon fragment may vary greatly from adsorption site to adsorption site given our low coverage. Moving on to the buckling of the first layer of the substrate, we observe a buckling of the first layer of the substrate in the range of 0.05 Å to 0.16 Å when thiophene remains intact, 0.16 Å to 0.22 Å when thiophene breaks 1 C-S bond, and 0.17 Å to 0.57 Å when thiophene breaks 2 C-S bonds. If it was not for thiophene on Cr(100) in the hollow0 configuration where thiophene breaks 2 C-S bonds and the first layer of the substrate only buckles 0.17 Å, all the adsorption sites that broke 2 C-S bonds would buckle the surface more than the adsorption sites that broke only 1 C-S bond. This indicates that the buckling of the first layer of the substrate is a good indicator of the molecule/surface interaction strength.

From the small buckling of the surface, unperturbed C-S bonds, large ( $S_z$ -Surface $_z$ ) distances, and small adsorption energies, we note that thiophene interacts quite weakly with Al(100). We attribute this weak interaction of thiophene with Al(100) to Al's lack of d-orbitals, which interact strongly with thiophene's molecular orbitals. We also demonstrate that thiophene can indeed break apart over these transition metal surfaces. When thiophene breaks apart over these surfaces we note very large adsorption energies, up to 7.34 eV. This would indicate that once thiophene breaks apart over these transition metal surfaces it is quite hard to remove the S atom and remaining hydrocarbon fragment from the surface. This suggests, in agreement at the very least with the available literature documenting the interaction of thiophene on Mo [177,178], that



after the initial layer of thiophene decomposes over these surfaces further thiophene desulfurization occurs over an adsorbed overlayer of S and C.

#### **4.1.3 The Desulfurization of Thiophene as a Process Mediated by Charge Transfer Process**

To gain even more insight about the desulfurization process we calculate the charge the thiophene molecule gains upon adsorption. Table 26 lists the charge thiophene gains in the highest adsorption energy configuration and the hollow<sup>45</sup> configuration on each transition metal surface,  $\Delta q_{\text{mol}}$ . From table 26 there appears to be a weak correlation between the charge transfer to the thiophene molecule and the number of C-S bonds broken, meaning the desulfurization process may be triggered by charge transfer. The configurations that keep thiophene intact result in thiophene gaining at most 1.6 (-e) from the surface. the configuration in which thiophene breaks one C-S bond results in thiophene gaining 1.7 (-e) from the surface, and the remaining configurations in which thiophene breaks completely apart result in the remnants of thiophene acquiring at least 2.1 (-e) from the surface. To explore this apparent trend in detail, in figure 30 a) we plot the average of the two C-S distances vs. the charge transfer to the thiophene molecule for each flat configuration. In figure 30 we also include the data for thiophene on Ni(100) as thiophene breaks one C-S bond on Ni(100). The green circle in figure 30 a) groups all the configurations in which thiophene breaks two C-S bonds, the red circle in figure 30 a) groups all the configurations in which thiophene breaks one C-S bond, and the purple circle in figure 30 a) groups all the configurations in which thiophene remains intact. From figure 30 a) we note that there is indeed a weak correlation between the charge transfer to the thiophene molecule and the number of C-S bonds broken. The adsorption sites that break two C-S bonds transfer more charge to the thiophene molecule, or rather the remnants of the thiophene molecule, than

adsorption sites that only break a single C-S bond. However, also evident from figure 30 a) is that there is significant overlap in the charge transfer to the thiophene molecule when thiophene breaks one C-S bond or remains intact. When thiophene gains  $\sim 0.7(-e)$  to  $\sim 1.7(-e)$  it may or may not break one C-S bond. As this demonstrates that the charge transfer to the thiophene molecule cannot perfectly predict whether or not thiophene will remain intact or break one C-S bond, we list in table 26 the charge the S atom gains in the highest adsorption energy configuration and the hollow<sup>45</sup> configuration on each transition metal surface,  $\Delta q_s$ . From table 26 we see that the values for the charge transfer to the S atom hint at a strong correlation between the charge the S atom gains and how many C-S bonds thiophene breaks. For the intact configurations thiophene's S atom only gains at most 0.3 (-e), for our one configuration where thiophene breaks a single C-S bond the S atom gains 0.6 (-e), and for the rest of the configurations, where thiophene breaks two C-S bonds, the S atom takes over 1 (-e) from the surface. To further explore this possible trend in figure 30 b) we plot the average of the two C-S distances vs. the charge the S atom gains. In figure 30 b) three zones exist denoting intact thiophene, thiophene with one broken C-S bond, and thiophene with two broken C-S bonds. These three zones are now almost completely separated. If the S atom gains at least 1 (-e) then thiophene breaks two C-S bonds. Neglecting Ni(100), if the S atom gains at least 0.6 (-e) but less than 1 (-e) then thiophene breaks one C-S bond, and finally if the S atom gains less than 0.6 (-e) thiophene remains intact. As alluded to, thiophene on Ni(100) is the one outlier to this trend. If we place thiophene on Ni(100) the S atom only needs 0.4 (-e) before thiophene breaks one C-S bond. The reason thiophene on Ni(100) bucks the trend set by the other metal surfaces is unknown. Still even with the result of thiophene on Ni(100) we can make some strong

statements concerning the relationship between desulfurization and the charge transfer to the S atom. A charge transfer of approximately 1.0 (-e) to the S atom is both a sufficient and necessary condition for thiophene to break two C-S bonds. A charge transfer of 0.4 (-e) to the S atom is a necessary condition for thiophene to break one C-S bond. The desulfurization of thiophene, characterized by the breaking of C-S bonds, appears to be a process triggered by charge transfer. This framing of the desulfurization of thiophene as a process mediated by charge transfer agrees well with the literature. Previous studies claim that a C-S bond session is triggered by charge transfer from the substrate to thiophene's lowest unoccupied molecular orbital (LUMO), situated around its S atom [179,184].

Table 26: The charge transfer to the thiophene molecule ( $\Delta q_{\text{mol}}$ ), and the charge transfer to the S atom ( $\Delta q_{\text{s}}$ ) for thiophene on Cr(100), V(100), Ta(100), W(100), Mo(100), Nb(100), Al(100), and Co(10-10) in the highest adsorption energy configuration and in the hollow45 configuration.

Metal/Adsorption Site	$\Delta q_{\text{mol}}$ (eV)	$\Delta q_{\text{s}}$ ( $\text{\AA}$ )
Al(100)/hollow45	0.0	-0.1
Co(10-10)/bridgeS1	0.3	0.2
Ir(100)/hollow45	0.1	0.1
Nb(100)/atop45	2.3	1.1
Nb(100)/hollow45	1.6	0.3
V(100)/atop45	3.7	1.2
V(100)/hollow45	1.4	0.3
Cr(100)/hollow0	2.6	1.1
Cr(100)/hollow45	1.1	0.3
Mo(100)/bridge45	1.7	0.6
Mo(100)/hollow45	1.1	0.3
Ta(100)/hollow0	2.7	1.3
Ta(100)/hollow45	1.6	0.3
W(100)/hollow0	2.1	1.1
W(100)/hollow45	1.2	0.3

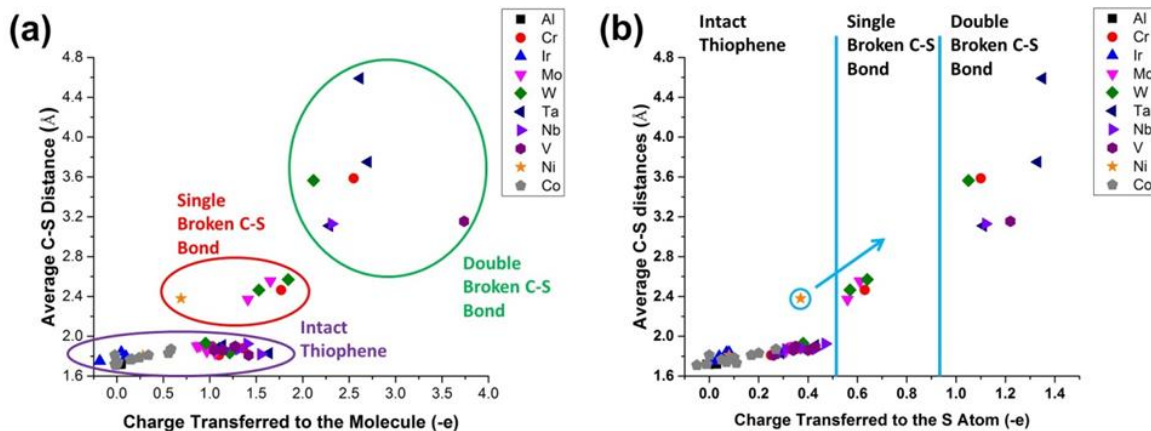


Figure 30: a) The average of the two C-S distances vs. the charge transfer to the thiophene molecule, and b) the average of the two C-S distances vs. the charge transfer to the S atom for thiophene adsorbed on Ni(100), Cr(100), V(100), Ta(100), W(100), Mo(100), Nb(100), Al(100), and Co(10-10) in all the flat configuration. In b) thiophene takes only 0.4 (-e) from Ni(100), putting it in the “intact” section, yet thiophene breaks one C-S bond over Ni(100). Therefore, an arrow exists pointing from our one Ni(100) point to the single broken C-S bond section.

#### 4.1.4 Work Function and Density of State Calculations

To further understand the nature of the desulfurization of thiophene on these surfaces we perform additional electronic structure analysis. Specifically we calculate and list in table 27 the change in the width ( $\Delta W$ ) and center ( $\Delta C$ ) of the d-band (p-band for Al(100)) of the atoms that compose the first layer of the substrate, and the change in the surface’s work function upon the adsorption of thiophene in the configuration with the highest adsorption energy and in the hollow45 configuration. From table 27 we note that for Co(10-10) and Al(100) the change in the width and center of the d-band (p-band for Al(100)) are minimal. As thiophene interacts the most weakly with Al(100) and Co(10-10) it makes sense that we accordingly observe the p-band of Al(100) and the d-band of Co(10-10) to change only slightly. Turning our attention to Co(10-10), our one ferromagnetic surface, we note the spin up states and the spin down states widen by

approximately the same amount. However, the spins up states shift towards the Fermi energy while the spin down states shift away from the Fermi energy. The different values of the shift of the spin up states and the spin down states leads to an average decrease of the magnetic moment of the Co(10-10) surface of  $0.16 \mu_B/\text{atom}$ . We observed this same decrease of the average magnetic moment of the atoms that compose the first layer of Ni(100) surface upon the adsorption of thiophene. Thiophene appears to lower the average magnetic moment of ferromagnetic surfaces, which could prove useful for applications in organic electronic devices in the future. Moving on to the rest of the transition metal surfaces, we note that the d-band of the rest of the surfaces widens. This agrees well with our studies of thiophene on Ni(100) and Cu(100), and on Rh(100), Pt(100), Pd(100), Ag(100), and Au(100) where we observed thiophene to widen the d-band of those surfaces too. For the shift of the d-band of the atoms that compose the first layer of the substrate, we note the d-band of some of the surfaces shift away from the Fermi energy, Ir(100), Nb(100), W(100), Cr(100), and Mo(100), while the d-band of the rest of surfaces, V(100) and Ta(100), shift towards the Fermi energy. The reason for these differences among the different transition metal surfaces is unknown and perhaps deserves further study. Finally we note, among adsorption sites on the same transition metal surface, that adsorption sites that keep thiophene intact result in about the same amount of widening and shift of the surface's d-band as adsorption sites that broke C-S bonds with perhaps the exception of W(100) and Mo(100). On these surfaces sites that broke C-S bonds result in a much larger shift of the surface's d-band. Even with the results from Mo(100) and W(100), the change of the d-band of the atoms composing the first layer of the surface, interestingly, appears to be relatively insensitive to the state thiophene is in on the surface.

Table 27: Change in the width ( $\Delta W$ ), and center ( $\Delta C$ ) of the d-band (p-band for Al(100)) of the atoms that compose the first layer of the substrate, and the change in the work function ( $\Delta\Phi$ ) for thiophene on Cr(100), V(100), Ta(100), W(100), Mo(100), Nb(100), Al(100), and Co(10-10) in the highest adsorption energy configuration and in the hollow45 configuration.

Metal/Adsorption Site	$\Delta W$ (eV)	$\Delta C$ (Å)	$\Delta\Phi$ (eV)
Al(100)/hollow45	0.05	0.07	-0.23
Co(10-10)/bridgeS1 (Up/down)	0.10/0.09	0.09/-0.12	-0.66
Ir(100)/hollow45	0.23	-0.21	-1.23
Nb(100)/atop45	0.26	-0.17	0.23
Nb(100)/hollow45	0.23	-0.12	-0.16
V(100)/atop45	0.42	0.07	0.05
V(100)/hollow45	0.37	0.14	-0.26
Cr(100)/hollow0	0.21	-0.17	-0.10
Cr(100)/hollow45	0.23	-0.19	-0.46
Mo(100)/bridge45	0.28	-0.30	-0.15
Mo(100)/hollow45	0.26	-0.21	-0.32
Ta(100)/hollow0	0.49	0.14	0.04
Ta(100)/hollow45	0.52	0.16	-0.33
W(100)/hollow0	0.31	-0.31	-0.04
W(100)/hollow45	0.28	-0.24	-0.41

Moving on, we also list the change in the surface's work function ( $\Delta\Phi$ ) upon the adsorption of thiophene in the configuration with the highest adsorption energy and in the hollow45 configuration. Among the transition metal surfaces that keep thiophene intact we note the change in the surface's work function follows the trend in adsorption energy. Thiophene interacts the most weakly with Al(100) and we also observe the smallest change in Al(100)'s work function. Thiophene interacts the most strongly with Ir(100) and we also observe the largest change in Ir(100)'s work function. There exists no such trend on transition metal surfaces where thiophene breaks apart. For all the adsorption sites listed in table 27 where thiophene breaks apart we note either a small increase in the surface's work function, in the case of Ta(100), V(100), and Nb(100), or a small decrease in the surface's work function, in the case of

W(100), Mo(100), and Cr(100). The fact that the work function of these surfaces remains close to unchanged when thiophene breaks apart probably results from the large charge transfer from the surface to thiophene. This large charge transfer reduces the surface dipole and counteracts any initial change in the surface's work function due to the "pushback" effect. Further evidence for this idea comes from the change in these surfaces' work function when thiophene remains intact in the hollow<sup>45</sup> configuration. In these cases we calculate a moderate decrease in the surface's work function accompanied by a smaller charge transfer to the thiophene molecule. In any case, this difference in the calculated work function for thiophene broken on the substrate and intact on the substrate could be used as a powerful experimental tool to check if thiophene does indeed break apart over these surfaces.

#### **4.1.5 Charge Transfer & Adsorption Energy vs Periodic HDS Trends**

Thus far we have observed that the d-band of the atoms that compose the first layer of the substrate is relatively insensitive to whether thiophene remains intact or breaks apart over the surface. We have also framed the desulfurization of thiophene, as characterized by the breaking of C-S bonds, as a process mediated by charge transfer. Now we try to draw correlations between our data presented in the previous subsections to experimental HDS turnover rates. To that end in figure 31 we plot the experimental thiophene HDS turnover rates on transition metal sulfides, taken from reference 171, vs. our calculated charge transfer to thiophene's S atom and the adsorption energy of thiophene, creating a so-called 3-D volcano plot. We divide our plot into four regions bounded by the lines  $q \approx 0.05$  (-e) and  $q \approx 0.5 * E - 0.625$  (-e). In region IV we note that thiophene suffers from a weak interaction with the surface, resulting in very low HDS turnover rates. In region III we note that thiophene induces too much charge transfer relative to

the strength of the thiophene/substrate interaction, resulting in low HDS turnover rates. Region I and II appear to be the optimal regions where we observe high HDS turnover rates. In these regions we also see both a strong correlation between the activity and, the adsorption energy and charge transfer. The HDS turnover rates appear to increase with decreasing adsorption energy, and decrease with respect to the amount the charge transfer to the S atom strays from the horizontal boundary line separating the two regions. These trends suggest the S atom hydrogenation or desorption may limit the overall HDS reaction rate. Finally the difference between region I and region II is that region I is an area steeply limited by charge transfer, which is why Pd(100), located in region I, exhibits both a lower adsorption energy and HDS turnover rate than either Rh(100) or Ir(100). Region II, in contrast, is characterized by a gradually charge-transfer inhibited area.

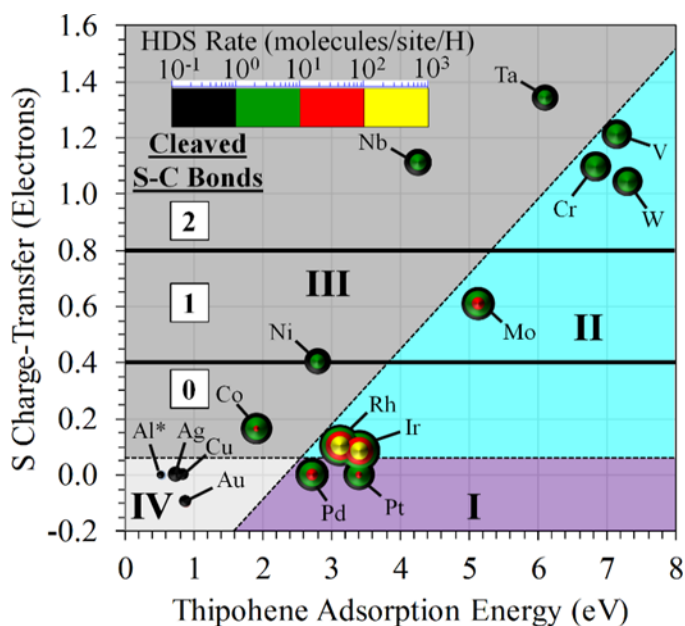


Figure 31: Previously reported thiophene HDS activities, taken from reference 171, plotted as a function of both adsorption energy and charge transfer to the S atom. Activities are represented using log-scaled, color-contrasted, contoured features.



In the past several groups have created similar “super-volcano-surfaces” by comparing the adsorption energies of several key steps in a given reaction pathway [185,186]. Our three-dimensional relation has the advantage of being much more computationally efficient. Instead of running multiple calculations on each different surface for each different reaction step we need, in theory, run only one structural relaxation per surface. We can extract both the adsorption energy and charge transfer to the molecule in one calculation. We also save computational time by exploring bare metal surfaces instead of the transition metal sulfides in their reaction environments. In this advantage also resides our method’s greatest weakness. Our method is only valid to the extent our vastly simplified systems relate to the “real” experimental systems. None the less, our method presents a refreshing approach to looking at the HDS process and possibly other reactions utilizing heterogeneous catalysis. Further testing is needed though to firmly establish whether our approach of using charge transfer and adsorption energy to model turnover rates can be used to predict new, more active catalysis.

#### **4.1.6 Conclusions**

Overall we have demonstrated thiophene can break apart over Cr(100), Nb(100), Ta(100), W(100), Mo(100), and V(100). This was the very first time it was shown, computationally, that thiophene can break C-S bonds on most of these transition metal surfaces. Furthermore, on V(100) this is the first time anyone has calculated thiophene to spontaneously break apart into atomic S and  $2C_2H_2$ . Moreover our 3-D volcano plot of the experimental thiophene HDS turnover rates on transition metal sulfides, taken from reference 171, vs. our calculated charge transfer to thiophene’s S atom and adsorption energy of thiophene offers a possible new, efficient way to screen for active HDS catalysis. Further testing is needed though to confirm that

the charge transfer to the S atom and the adsorption energies of the thiophene on bare metal surfaces are related to the experimental HDS turnover rates on supported transition metal sulfides. Never the less we have confidently established a relationship between the charge transfer to the S atom and thiophene's propensity to break C-S bonds on these surfaces. Thiophene's desulfurization on these metals is triggered by a charge transfer process. Thiophene's S atom needs at least 0.4 (-e) to break one C-S bond, and at least 1.0 (-e) to break two C-S bonds. In "real" HDS, thiophene on supported transition metal sulfides thiophene must, at some point, also break C-S bonds. Therefore, charge transfer is likely an integral part of the "real" HDS process. We have also demonstrated, in agreement with the available literature, that on bare metal surfaces further thiophene desulfurization, after the initial layer of thiophene is desulfurized, probably occurs on a layer of adsorbed S and C. Evidence for this statement comes from the large adsorption energies that occur when thiophene breaks apart on these surfaces. These large adsorption energies would make it difficult to remove thiophene from the surface once its C-S bonds break.

#### **4.2 Polythiophenes on Au(111)**

Reproduced with permission from T. Jiang, W. Malone, Y. Tong, D. Drago, A. Bendounan, A. Kara, V.A. Esaulov, Thiophene Derivatives on Gold and Molecular Dissociation Processes, J. Phys. Chem. C, 121 (2017) 27923. Copyright 2017 American Chemical Society.

As stated previously, thiophene, in addition to being a HDS target, is a building block of larger, more complex molecules. These larger thiophene derivative  $\pi$ -conjugated systems show promise for use in molecular electronic applications [187-198]. Critical to the performance of these devices are the electron transport properties of the system, which are, in turn, determined

by the characteristics of the thiophene/electrode interface. If thiophene was to rupture on the electrode surface it could hinder the charge transport, which would be undesirable in a molecular electronic device. Now we have already demonstrated that thiophene can rupture over transition metal surfaces like Ni(100) or Mo(100). However recent studies have indicated that thiophene may also break apart on the less reactive coinage metals [196,197, 199-206] including Au, a popular electrode material.

In order to explore the possibility of Thiophene breaking over Au we perform calculations of thiophene (1T), bithiophene (2T), and terthiophene (3T) adsorbed on Au(111) in collaboration with our experimental associates. Our experimental associates use X-ray photoelectron spectroscopy (XPS) to study the adsorption of a series of polythiophene molecules (nT, n = 1-4, 6),  $\alpha$ ,  $\omega$ -diquaterthiophene (DH4T), and dihexylsexithiophene (DH6T) on Au(111) and Au films grown on mica. As we only study polythiophenes up to 3T, as a consequence of limited computational time, we will only focus on the experimental results of 1T, 2T, and 3T on Au(111) and Au films grown on mica. In order to facilitate a more direct comparison of our DFT results to the experimental XPS results we calculate the core level binding energy (CLBE) of the S 2p state. We also calculate the adsorption energy of each polythiophene on Au(111) and the geometrical properties of each substrate/adsorbate system.

In subsection one of this section we discuss our computational details. In the second subsection we discuss our results, both experimental and computational, for 1T. In the third subsection we discuss our results for 2T. In the fourth subsection we discuss our results for 3T, and in the last subsection we present our conclusions.

### 4.2.1 Computational Methods

We perform all calculations using VASP version 5.3.5., which utilizes the PAW method. Furthermore for all our calculations we use a 400 eV plane wave energy cutoff, sample the BZ using a 6x6x1 Monkhorst-Pack grid, and use a 0.02 eV/Å force criterion for structural relaxation, which we achieve using the CG method. To model the exchange-correlation interaction we use the optB88-vdW functional.

For our 1T calculations we construct our thiophene molecule and place it in several adsorption sites with its plane perpendicular or parallel to the Au(100) surface. To explore the possibility that thiophene breaks over Au(111) we study several systems in which the thiophene molecule assumes a possible broken configuration. First we study a broken thiophene alkene chain,  $(\text{CH}_2(\text{CH}_3)_3\text{-SH})$ . Then we study, for comparison, a short chain alkanethiol,  $(\text{CH}_3(\text{CH}_2)_3\text{-SH})$ . Finally we also study a broken thiophene metallocycle, a thiophene molecule with a broken C-S bond with an Au adatom incorporated into the ring structure. We illustrate all of these molecules in figure 32. For all these systems we run calculations in both a 4x4 and  $\sqrt{7}\times\sqrt{7}$  unit cell. In the  $\sqrt{7}\times\sqrt{7}$  unit cell, due to its small size, we only run calculations in which the molecule is standing vertical on the surface. Moreover in the  $\sqrt{7}\times\sqrt{7}$  unit cell we also model Au(111) using 6 layer slabs while in the 4x4 unit cell we model Au(111) using 5 layer slabs. In both unit cells we relax the molecule and the substrate separately before we place the molecule on the substrate except the broken thiophene metallocycle, which we cannot relax in the gas phase as it could reform back to thiophene. Finally, we allow all the coordinates of the molecule/substrate system to relax except the bottom two layers of the substrate which we hold at their values in the relaxed substrate.

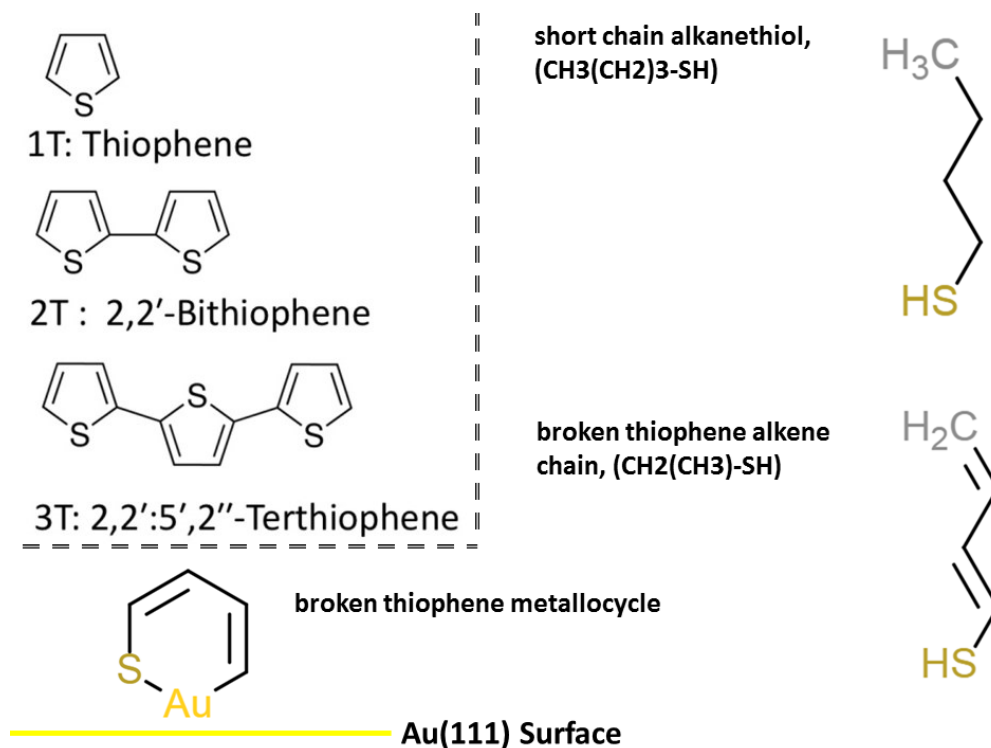


Figure 32: Thiophene derivatives studied in this section.

For our 2T calculations we try several adsorption sites with the plane of the molecule perpendicular to the surface. To explore the possibility of bithiophene breaking over Au(100) we simply break a single one of bithiophene's C-S bonds and allow it to relax. Given bithiophene's large size we only allow it to relax in the 4x4 unit cell. Again we relax the molecule, with the exception of broken bithiophene as the molecule may reform during gas phase relaxation, and surface separately before placing the molecule on the surface. Once we place the intact molecule on the surface we allow all the atomic coordinates of the system to undergo full structural relaxation except the bottom two layers of the substrate which we hold at their values in the relaxed substrate. For broken bithiophene, in addition to holding the atomic coordinates of the bottom two layers of the substrate at their relaxed values, we also only let the

molecule relax in the z-direction to prevent the molecule from reforming and to save computational time.

For our 3T calculations we run all calculations on a 5x5 4 layer slab or a 2x6 4 layer slab. In both unit cells we explore configurations where the plane of the molecule is perpendicular to the surface. We only study flat configurations, configurations in which the plane of the molecule is parallel to the surface, in the 5x5 unit cell. For configurations where the plane of the molecule is perpendicular to the surface we look at two different kinds of configurations. In the 2x6 unit cell we look at configurations where the long axis of the molecule is either parallel or perpendicular to the surface. In the 5x5 unit cell we only look at configurations where the long axis of the molecule is parallel to the surface, see figure 33 which illustrates some of the initial terthiophene configurations we explore. Moreover, when we place terthiophene with its long axis parallel to the surface we explore configurations where one S atom points towards the surface or two S atoms point towards the surface, see figure 33 again. Moving on, in both unit cells we relax the molecule and the substrate separately before placing the molecule on the substrate. Once we place the molecule on the substrate we allow the top two layers of the substrate to undergo structural relaxation, and the molecule to undergo structural relaxation in only the z-direction to save time. To explore the possibility of terthiophene breaking apart we simply break one C-S bond and allow broken terthiophene to relax, also only in the z-direction, on the surface with its molecular plane perpendicular to the surface and its long axis parallel to the surface. Finally throughout this section we calculate the adsorption energies again using equation 61. With equation 61 a higher binding energy corresponds to a more stable adsorption site.

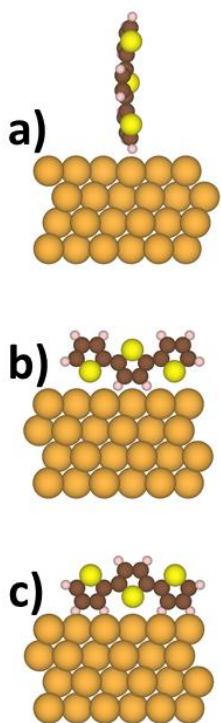


Figure 33: a) Terthiophene with its long axis perpendicular to the surface, b) terthiophene with its long axis parallel to the surface with two S atoms pointing towards the surface, and c) terthiophene with its long axis parallel to the surface with one S atom pointing towards the surface

#### 4.2.2 1T

In general our experimental collaborators find their XPS spectra could be fit with multiple doublet components. Specifically they find  $2P_{3/2}$  peaks lying approximately at (A) 161.10 eV, (B) 162.05 eV, (C) 163.75 eV, (C') 163.35 eV, and (D) 164.05 eV. Figure 34 displays the S2P XPS spectra for thiophene on Au evaporated on mica for two samples prepared under identical conditions. Figure 35 displays the S2P XPS spectra for thiophene on Au(111). From figure 34 and figure 35 we note that components A and B dominate the S2P XPS spectra for thiophene. For Au grown on mica the relative intensities of A and B can vary a great deal from sample to

sample, but in general component A seems to be of higher intensity. We also note the presence of a small C' component in the spectra. When we move to thiophene on Au(111) the spectra is again dominated by components A and B, but this time with component B being more dominant than component A. Furthermore, a small C' component is also present in the spectra. Finally, our experimental collaborators find that increasing the photon flux by 50 times leads to a steady increase in the C' peak, indicating that this peak may be the result of X-ray damage to the sample.

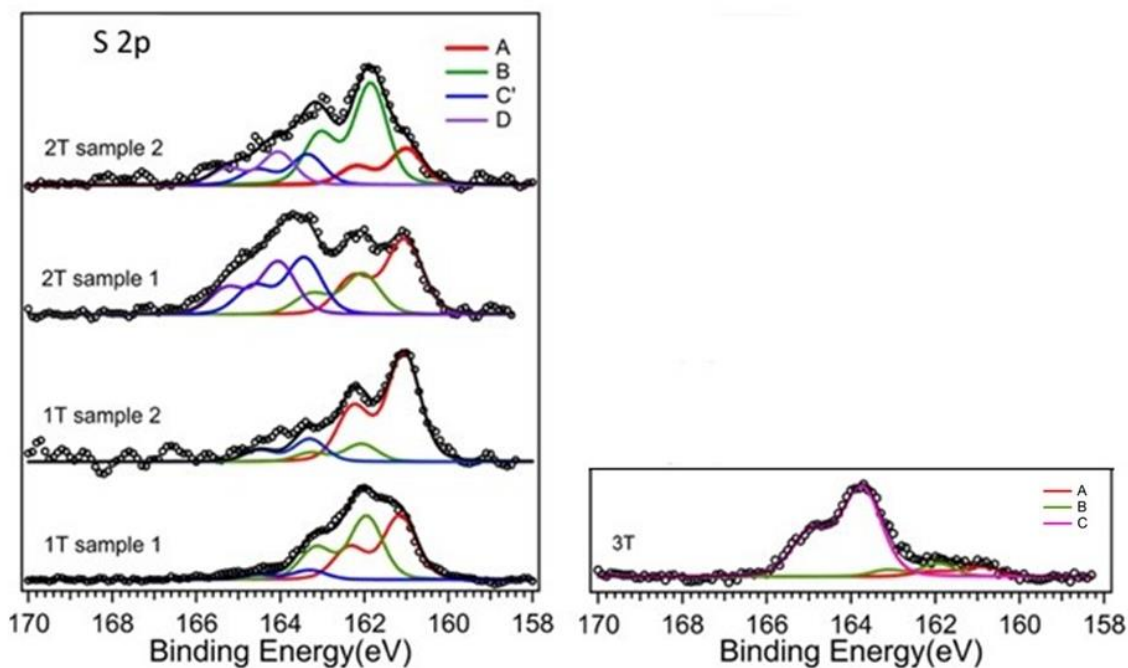


Figure 34: XPS spectra with fits for 1T, 2T, and 3T on Au grown on mica.



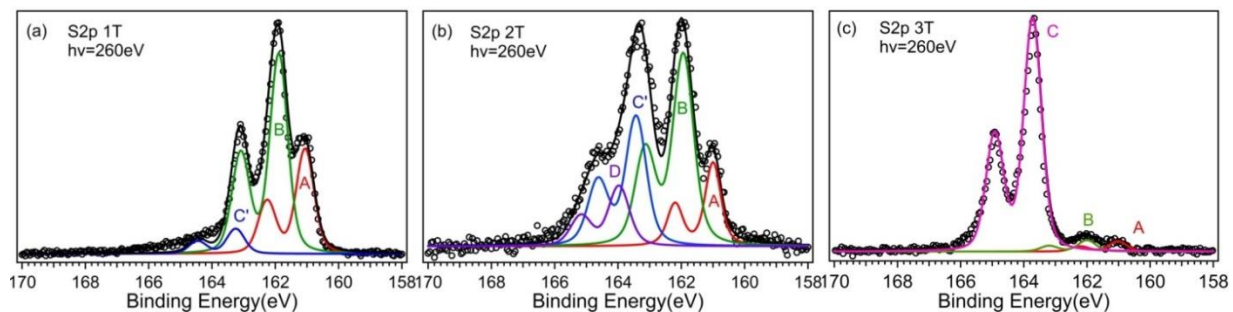


Figure 35: XPS spectra with fits for 1T, 2T, and 3T on Au(111).

In order to determine the origin of each component in the spectra we calculate and list in table 28 the S2P binding energies, adsorption energy, and the S-Au distances for thiophene and thiophene derivatives that could form from thiophene dissociation on Au(111). From table 28 we note that the adsorption energies for the metallocycle are quite low. In fact some configurations we put the metallocycle in leads to negative adsorption energies, indicating an unstable adsorption site. For this reason the presence of a broken thiophene metallocycle on the surface may be unlikely. As far as the adsorption energies of the other molecules, we note the adsorption energies increase going from the  $\sqrt{7}\times\sqrt{7}$  unit cell to the  $4\times 4$  unit cell, and increase going from vertical to flat adsorption sites. We also note that the alkene chain and the alkane chain yield, by far, the largest adsorption energies. Moving on to the S2P binding energies, we note a wide array of values for the S2P binding energies. Along with listing the values for the S2P binding energies in table 28, we also plot the S2P binding energies in figure 36. Each hash in figure 36 corresponds to a different adsorption site. From figure 36 and table 28 we note the magnitude of the S2P binding energies are higher when the molecule is in the presence of an adatom, and lower when the molecule is in the less compact  $4\times 4$  unit cell. We also note the S2P binding energies can vary modestly with adsorption site. More striking though, is that with the

exception of the case of thiophene standing up in the presence of an adatom the S2P binding energies for intact thiophene, broken thiophene, and alkanethiol overlap. To compare with experiment we rely on a 20 eV shift of the S2P binding energies. The absolute values of the calculated CLBEs have no meaning, and, therefore, we must rely on shifts and differences in the calculated CLBEs to compare with experiment. Using a 20 eV shift of the S2P binding energies so that a 182 eV energy corresponds to the experimental 162 eV energy, we see that peaks A and B from the XPS data may be caused by both intact and broken thiophene molecules.

Table 28: Adsorption energy ( $E_{\text{ads}}$ ), S2p Binding Energy, and S-Au distances for intact thiophene, broken thiophene, and an alkane chain adsorbed on Au(100) in the  $4 \times 4$  and  $\sqrt{7} \times \sqrt{7}$  unit cell.

Molecule	Unit Cell	$E_{\text{ads}}$ (eV)	S2p Binding Energies (eV)	S-Au(Å)
Alkane chain	$4 \times 4$	2.39-2.55	-180.96 to -181.27	2.43-2.46
	$\sqrt{7} \times \sqrt{7}$	1.93-2.18	-181.20 to -181.98	2.40-2.49
Alkene chain Broken 1T	$4 \times 4$	1.68-1.86	-180.84 to -181.40	2.46-2.47
	$\sqrt{7} \times \sqrt{7}$	1.43-1.51	-181.68 to -182.19	2.44-2.51
Metallocycle Broken 1T	$4 \times 4$	0.06	-180.98	2.54
	$\sqrt{7} \times \sqrt{7}$	0.32	-181.76	2.85
Thiophene	$4 \times 4$	0.50-0.59	-180.86 to -181.26	2.77-3.25
	$\sqrt{7} \times \sqrt{7}$	0.35-0.38	-181.97 to -182.26	2.82-3.43
	$4 \times 4$ (flat)	0.83-0.98	-181.08 to -181.54	2.95-3.77
Thiophene with an adatom	$4 \times 4$	0.48-0.89	-180.69 to -182.04	3.46-4.54
	$\sqrt{7} \times \sqrt{7}$	0.61-0.72	-182.87 to -183.17	3.42-4.54
	$4 \times 4$ (flat)	0.89-1.21	-181.61 to -182.10	4.10-5.40

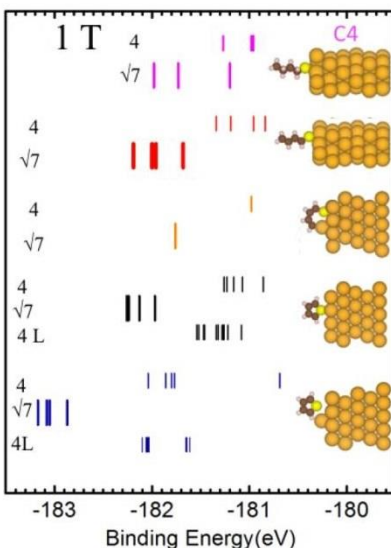


Figure 36: CLBEs for, from bottom to top, intact thiophene with an adatom, intact thiophene without an adatom, broken thiophene metallocycle, broken thiophene alkene chain, and an alkane chain. The  $4 \times 4$  unit cell calculations are denoted by a 4. The  $\sqrt{7} \times \sqrt{7}$  unit cell calculations are denoted by a  $\sqrt{7}$ , and L corresponds to configurations where thiophene is flat on the surface. Each hash corresponds to the CLBE of a S atom in a molecule in a particular adsorption site. Hashes are located horizontally from the S atom they belong to

#### 4.2.3 2T

Figure 34 plots the XPS spectra for bithiophene on Au grown on mica, while figure 35 plots the XPS spectrum for bithiophene on Au(100). From figure 34 we notice that for bithiophene on Au grown on mica, in addition to observing a strong A and B component, we also now observe a strong C' and C component in the XPS spectra. Just like for thiophene, the relative intensity of each peak we observe in the spectrum can change from sample to sample. Finally, the bithiophene on Au(111) spectrum is similar to the bithiophene on Au grown on mica spectrum except instead of peak C we observe peak D in the spectrum of bithiophene on Au(111).

Again in order to determine the origin of each component in the spectra we calculate and list in table 29 the S2P binding energies, adsorption energy ( $E_{\text{ads}}$ ), and the S-Au distances for intact

and broken bithiophene. For the S2P binding energies and the S-Au distances we list the data for both S atoms in the bithiophene molecule. From table 29 we note that broken bithiophene is unstable, meaning bithiophene with a single broken C-S bond on Au(100) gives a negative adsorption energy. In contrast intact bithiophene yields small positive adsorption energies on Au(100). As broken bithiophene on Au(111) gives negative adsorption energies it may be an intermediate step in the process of bithiophene breaking apart into other molecules on the surface such as thiophene and thiophene fragments. Moving on, we also calculate the S atom in broken bithiophene to bond somewhat closer to the Au in the surface than the S atom in intact bithiophene. Looking at CLBEs for intact bithiophene, which we plot in figure 37, we note magnitudes somewhat higher than those we found for thiophene. Specifically we note CLBEs from -183.39 eV to -182.99 eV. Breaking the bithiophene molecule shifts the CLBE of the S atom with the broken C-S bond to lower values. The CLBE of the unmodified S atom also shifts to lower values, but the magnitude of the shift is smaller than the shift the S atom with the broken C-S bond experiences. Given this data it may be reasonable to attribute peak C in the bithiophene on Au grown on mica spectra to intact bithiophene, and peaks A and B to broken thiophene derivatives.

Table 29 Adsorption energy ( $E_{\text{ads}}$ ), S2p binding energies for each S atom in the molecule, and S-Au distances for each S atom in the molecule for intact bithiophene and broken bithiophene on Au(111) in a 4x4 unit cell.

Molecule	First S (broken S in broken 2T)			Second S	
	$E_{\text{ads}}$ (eV)	S2p (eV)	S-Au(Å)	S2p (eV)	S-Au(Å)
2T gas phase		-185.64		-185.64	
2T	0.60 to 0.71	-182.99 to -183.39	2.89 to 3.29	-182.99 to -183.39	2.89 to 3.29
Broken 2T	-4.73 to -3.06	-181.76 to -182.88	2.65 to 3.01	-182.56 to -183.28	2.65 to 3.01

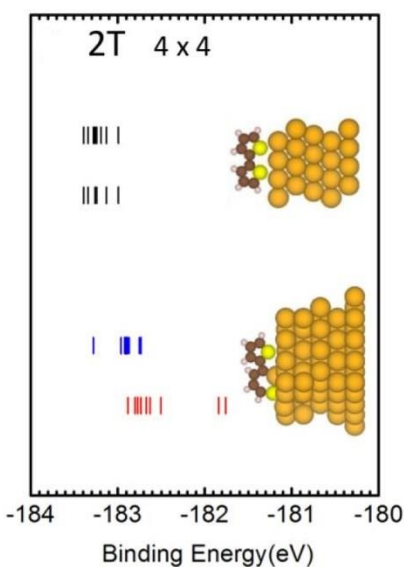


Figure 37: CLBEs of, from bottom to top, broken bithiophene and intact bithiophene in the 4x4 unit cell. Each hash corresponds to the CLBE of a S atom in a particular adsorption site. Hashes are located horizontally from the S atom they belong to.

Finally we must mention that when we place bithiophene on Au(111) occasionally the molecule would drag an Au atom partially out of the surface, resulting in a large buckling of the

first layer of the substrate, 1.0 Å to 1.6 Å. Figure 38 illustrates two adsorption configurations where bithiophene would drag an Au atom partially out of the surface. This large distortion of the surface may be part of the reason why broken bithiophene is unstable.

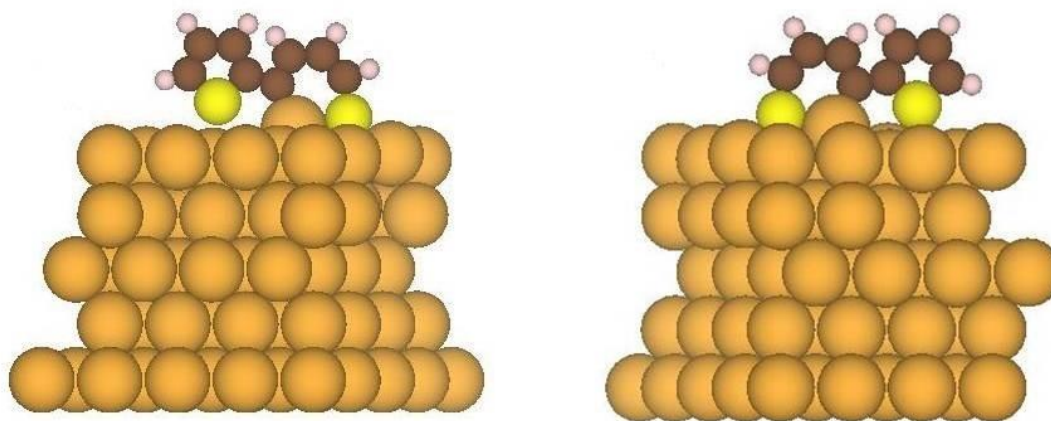


Figure 38: Two adsorption configurations where broken bithiophene dragged an Au atom out of the surface.

#### 4.2.4 3T

In the 3T spectrum, both for 3T on Au grown on mica and 3T on Au(111), we note the presence of peaks A through C, see figure 34 and figure 35. However, peaks A and B can be very small with peak C dominating the 3T spectrum. To compare with these experimental results, we calculate and list in table 30 the S2P binding energies, adsorption energy ( $E_{\text{ads}}$ ), and the S-Au distances for intact and broken terthiophene with its long axis parallel to the surface. We first note that the CLBEs of the central and side S atoms differ by 0.35 eV in the gas phase with the magnitude of the central S atom's CLBE being higher than the magnitude of the CLBE of the side S atoms. Moreover, putting the 3T molecule on the surface seems to increase the difference in the CLBEs between the central and side S. In the 5x5 unit cell we calculate CLBEs

ranging from -182.68 eV to -182.62 eV for central S atom and CLBE ranging from -182.30 eV to -182.14 eV for the side S atoms when terthiophene is sitting upright on the surface. The energy difference of the CLBEs of the side S atoms and central S atoms vary from approximately 0.3 eV to 0.5 eV. For all the S atoms we calculate S-Au distances ranging from 3.37 Å to 3.91 Å or 5.46 Å to 5.77 Å depending if the S atom belongs to a thio unit that points to or away from the surface. Overall for intact terthiophene standing up in the 5x5 unit cell we observe that the CLBEs are rather insensitive to whether the S atom points towards or away from the surface, and the position of the terthiophene molecule on the surface. Instead the CLBEs of the S atoms are much more sensitive to the position of the S atom in the terthiophene molecule. Moving along, when we place terthiophene flat on the surface we note slightly higher magnitudes of the CLBEs. However, we still note that the magnitudes of the CLBEs of the central S atom are higher than the magnitudes of the CLBEs of the side S atoms. Furthermore, when we break terthiophene the CLBEs of all three S atoms change slightly. The magnitude of the CLBE of the unmodified exterior S atom in broken terthiophene may be higher than the magnitude of the CLBE of the exterior S atoms in intact terthiophene. The magnitude of the CLBE of the interior S atom in the broken terthiophene molecule may be a little higher or about the same as the magnitude of the CLBE of the interior S atom in intact terthiophene. For the S atom with the broken C-S bond we note that the magnitude of the CLBE may be slightly lower than that of the exterior S atoms in intact terthiophene. Finally breaking the terthiophene molecule does not change the S-Au distances significantly. Moving on, when we place terthiophene in the smaller 2x6 unit cell we note larger adsorption heights than when we place terthiophene in the large 5x5 unit cell. Along with these higher adsorption heights we note CLBEs with much higher magnitudes. The larger

magnitudes of the CLBES, which are much closer to the gas phase CLBES of terthiophene, probably result from terthiophene's S atoms being, on average, further away from the surface. Even though the magnitudes of the CLBES are larger in the 2x6 unit cell, we still observe that the magnitude of the CLBE of the central S atom is somewhat higher than the magnitude of the CLBES of the side S atoms.



Table 30: Adsorption energy ( $E_{\text{ads}}$ ), S2p Binding Energies for each S atom in the molecule, and S-Au distances for each S atom in the molecule for intact terthiophene and broken terthiophene on Au(111) in the 5x5 and 2x6 unit cell. In these configurations terthiophene has its long axis parallel to the surface.

Molecule	$E_{\text{ads}}$ (eV)	First S		Second S		Third S (broken S in 3T)	
		S2p (eV)	S-Au(Å)	S2p (eV)	S-Au(Å)	S2p (eV)	S-Au(Å)
3T gas phase		-184.66		-185.01		-184.66	
3T 5x5 (up)	0.58-0.64	-182.20 to -182.30	3.38-3.61	-182.62 to -182.64	5.50-5.69	-182.20 to -182.30	3.37-3.57
3T 5x5 (down)	0.21-0.55	-182.14 to -182.27	5.56-5.77	-182.64 to -182.68	3.53-3.91	-182.18 to -182.27	5.46-5.77
Broken 3T 5x5 (up)	-1.91 to -1.86	-182.23 to -182.41	3.46-3.85	-182.56 to -182.60	5.55-5.70	-181.98 to -182.19	3.32-3.72
3T 5x5 L	1.68-1.84	-182.52 to -182.71	3.60-3.89	-182.99 to -183.19	3.32-3.89	-182.52 to -182.71	3.60-3.89
3T 2x6 (up)	1.06-1.07	-184.25 to -184.27	3.52-3.86	-184.82	5.63-5.81	-184.25 to -184.27	3.58-3.83
3T 2x6 (down)	1.10-1.13	-184.27 to -184.28	5.80-5.99	-184.86 to -184.87	3.82-4.18	-184.27	5.87-6.00

As for adsorption energies, we note the following general trends. Terthiophene interacts with Au(111) more strongly when two S atoms are pointing towards the surface. Terthiophene also interacts more strongly to the surface when sitting flat on the surface. These trends reflect what we have observed so far in this dissertation. Thiophene and thiophene derivatives prefer to bond flat on transition metal surfaces with as many atoms as possible in close contact with the surface. For broken terthiophene, we calculate, just as we calculated for broken bithiophene, a negative adsorption energy. This suggests that terthiophene with one broken bond may be an intermediate state to a completely dissociated terthiophene molecule. Finally, reducing the coverage of terthiophene, moving from a 5x5 unit cell to a 2x6 unit cell, increases the adsorption energy for vertical adsorption configurations. This may result from an increase in the intermolecular forces when one reduces coverage.

Thus far we have only discussed terthiophene with its long axis parallel to the surface, now we take a brief respite to discuss terthiophene with its long axis perpendicular to the surface, see figure 33 a). In table 31 we list the S2P binding energies, adsorption energy ( $E_{\text{ads}}$ ), and the S-Au distances for intact and broken terthiophene with its long axis perpendicular to the surface. We note from table 31, perhaps unsurprisingly, that positioning terthiophene with its long axis perpendicular to the surface reduces its adsorption energy. Moving the S atoms, on average, further away from the surface again appears to reduce the adsorption energy. We also note for terthiophene with its long axis perpendicular to the surface a large difference in the CLBE of the central S and the CLBEs of the side S atoms. This difference amounts to 1 eV for terthiophene in the compact 2x6 unit cell, and 1.8 eV for terthiophene in the larger 5x5 unit cell, which is much greater than the difference in the CLBEs of the central S atom and side S atoms for

terthiophene with its long axis parallel to the surface in either a flat or a vertical adsorption configuration.

Table 31: Adsorption energy ( $E_{\text{ads}}$ ), S2p Binding Energies for each S atom in the molecule, and S-Au distances for each S atom in the molecule for intact terthiophene with its long axis perpendicular to Au(111) in the 5x5 and 2x6 unit cell.

Molecule	$E_{\text{ads}}$ (eV)	First S		Second S		Third S	
		S2p (eV)	S-Au( $\text{\AA}$ )	S2p (eV)	S-Au( $\text{\AA}$ )	S2p (eV)	S-Au( $\text{\AA}$ )
3T gas phase		-184.66		-185.01		-184.66	
3T 2x6	0.30	-183.07	12.18	-184.82	8.34	-183.02	4.45
3T 5x5	0.49	-181.40	12.18	-182.34	8.35	-181.34	4.47

As we are primarily interested in comparing our theoretical results with experimental XPS spectra, we plot in figure 39 the CLBEs of terthiophene. Each hash on the graph corresponds to a CLBE of a S atom in intact or broken terthiophene in a particular adsorption site. Hashes are located horizontally from the S atom they belong to. The inserted scale at the bottom corresponds to the shifted scale we use to compare with experimental XPS values. Figure 39 demonstrates the two largest factors that can cause variability in the CLBE: the position of the S atom in the terthiophene molecule and whether the molecule is sitting flat or vertical on the surface. The two distinct CLBEs of the side S atoms and central S atom, which exist in every terthiophene calculation we perform, cannot be mapped to just one peak, peak C. Therefore, in figure 40, we try to fit the XPS spectrum of terthiophene using two components. We found the best fit using peaks at 163.67 eV and 164.03 eV. The fit actually reproduces the high-energy tail of the spectrum better than the fit dominated by one component. Thus we can attribute the two dominate components in the 3T spectrum to the different S atoms, either side or central S atoms,

in the terthiophene molecules. We can also attribute the A and B peaks to either a completely broken terthiophene molecule, with the same features as thiophene, or atomic S on the surface.

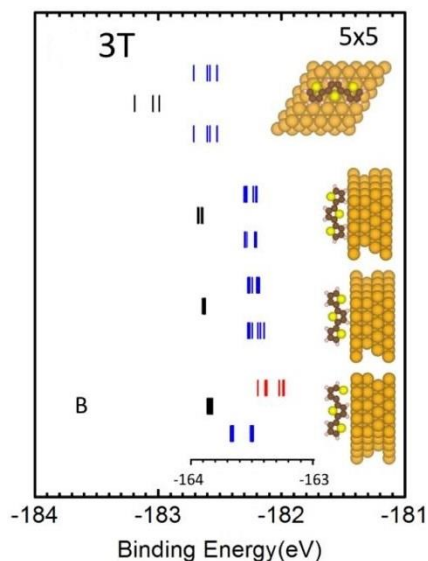


Figure 39: CLBEs for, from bottom to top, broken terthiophene, intact terthiophene with two S atoms pointing towards the surface, intact terthiophene with one S atom pointing towards the surface, and terthiophene sitting flat on the surface. Each hash corresponds to the CLBE of a S atom in a particular adsorption site. Hashes are located horizontally from the S atom they belong to.

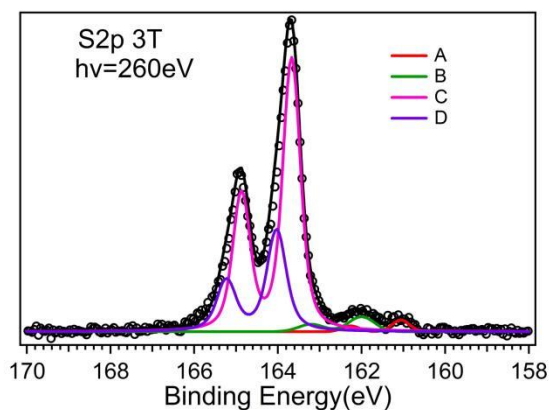


Figure 40: Fit of the 3T XPS spectra on Au(111) taking into account the difference in CLBEs between the central S atom the side S atoms.

#### 4.2.5 Conclusions

Overall our CLBE calculations are able to provide valuable insight into the origin of the various peaks present in the XPS spectra of thiophene, bithiophene, and terthiophene on Au(111) and on Au grown on mica. We calculate the CLBE of intact and various dissociated versions of thiophene to overlap, indicating the possible presence of dissociated thiophene on Au(111) and on Au grown on mica. In the bithiophene XPS spectra we observe many of the same peaks present in the thiophene spectra indicating that bithiophene too may dissociate over Au. For terthiophene we consistently calculate different CLBEs for the interior S atom and the exterior S atoms. This provides the inspiration to fit the 3T spectrum using two peaks instead of one. For terthiophene we also compute the highest adsorption energy when the molecule sits flat on the surface, and the lowest adsorption energy when the molecule stands with its long axis perpendicular to the surface, demonstrating S's propensity to remain close to the Au(111) surface. For all three molecules, 1T, 2T, and 3T, we observe that the CLBEs vary little with respect to adsorption site. In contrast, changing the packing density of the molecule on the surface can significantly alter the CLBEs.

The presence of dissociated thiophene on Au has important implications for molecular electronics. It may significantly affect the charge transfer along the chains of intact molecules, affecting the performance of the device. This ability of Au to dissociate thiophene and its derivatives may significantly be effected by the morphology of the surface. We observed a high degree of variability in our XPS spectra from sample to sample under seemingly identical sample preparation conditions. The presence of a large varying number of defects or adatoms may be responsible for the variability of our experimental results.

In the context of this dissertation these results present a delightful example of a practical use of DFT. Using DFT we have illuminated the possible origin of various peaks in the XPS spectra of thiophene and thiophene derivatives on Au, which is a system relevant in the field of molecular electronic devices. This also illustrates the importance of testing new computational methods. In a system where the interpretation of the experimental results remains shrouded, one must make sure they are using a high quality computational method in order to come to the correct interpretation. A method can only be confirmed to be of the highest quality after extensive testing on systems well-studied experimentally. We only decided to use the optB88-vdW functional after extensive testing much of which was completed in the previous chapter of this dissertation.

#### **4.3 DHTAP on Cu(110)**

Reproduced with permission from A. Thomas, W. Malone, T. Leoni, A. Ranguis, Z. Chen, O. Siri, A. Kara, P. Zeppenfeld, and C. Becker, Growth of Dihydrotetraazapentacene Layers on Cu(110), *J. Phys. Chem. C*, 122 (2018) 10828. Copyright 2018 American Chemical Society.

As mentioned in the previous section, much research has been devoted to study organic semiconductors with the ultimate goal of producing high-quality OLED, O-LEFTs, OFETs, and OTFT for the commercial market. Pentacene films, due to their charge carrier mobility which is similar to that of amorphous Si, have often been used as a benchmark [207]. Pentacene films exhibit poor long-term stability under ambient conditions though [208], which began the search for pentacene alternatives. Of all the alternatives explored to date, nitrogen-containing oligoacene derivatives, such as DHTAP, stand out because of their high stability under ambient conditions [209,210]. In this section we study the adsorption of DHTAP on Cu(110) using DFT.

Our calculations are guided by our experimental collaborators study of the DHTAP/Cu(110) system using scanning tunneling microscopy (STM) and low-energy electron diffraction (LEED). Our hope is that we can sufficiently illuminate the adsorption properties of DHTAP on Cu(110) to determine if this system would be ideal for use in molecular electronic devices. We expect, due the presence of DHTAP's imine groups, the molecule to strongly chemisorb through Cu-N bonds.

#### 4.3.1 Computational Details

We perform all calculations using VASP version 5.4.1, which the reader will be aware of uses the PAW method. To account for the exchange-correlation interaction we utilize the optB88-vdW functional. We model the Cu(110) surface using five layer slabs. Between slabs we place at least 19 Å of vacuum. As our experimental collaborators found several different super structures for the DHTAP/Cu(110) system, we construct three different unit cells described by the matrices  $\begin{pmatrix} 6 & 0 \\ 1 & 2 \end{pmatrix}$ ,  $\begin{pmatrix} 7 & 0 \\ 1 & 2 \end{pmatrix}$ , and  $\begin{pmatrix} 6 & -1 \\ 1 & 2 \end{pmatrix}$ . For the lattice constant of our Cu(110) surface we use the calculated value given in table 1. Moreover, we relax the substrate and the molecule separately before placing the molecule on the substrate. Once we place the molecule on the substrate we allow all the atomic coordinates to undergo complete structural relaxation except the bottom two layers of the substrate. We hold the atomic coordinates of the atoms in the bottom two layers of the substrate at their positions in the clean, relaxed substrate. Furthermore, we achieve structural relaxation using the CG method. We set the force criterion at 0.02 eV/Å, use a 400 eV plane wave energy cutoff, and sample the BZ using a 6x6x1 Monkhorst-Pack grid.

To find the equilibrium adsorption configuration we try four different adsorption sites illustrated in figure 41. These adsorption sites position the molecule with its center over the closely packed rows, a) and b), or over the troughs, c) and d), on the Cu(110) surface. To access the stability of DHTAP we again define adsorption energy using equation 61. With equation 61 a higher adsorption energy corresponds to a more stable adsorption site.

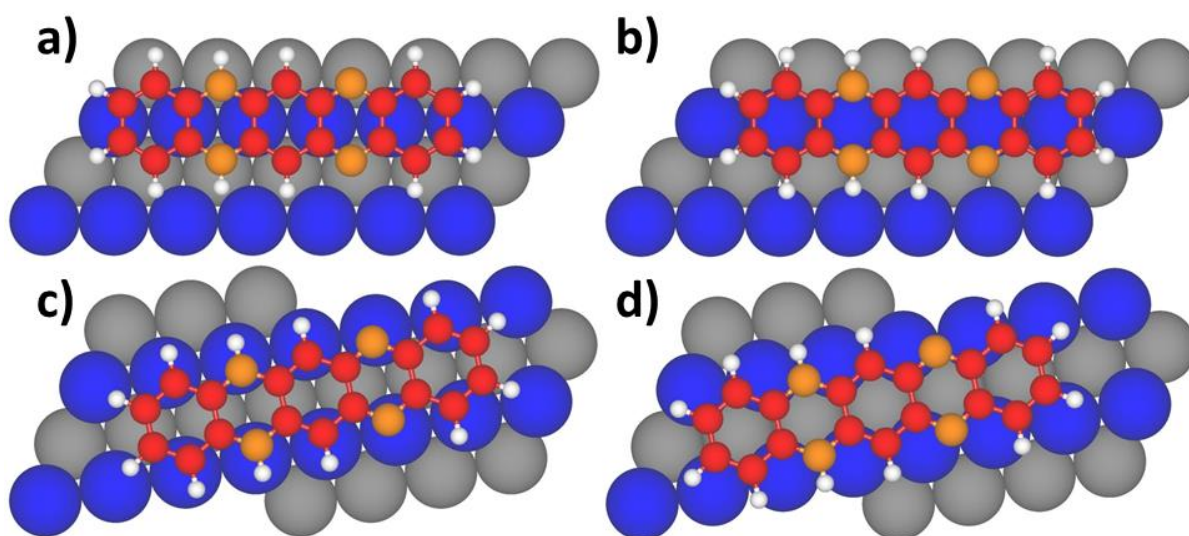


Figure 41: Initial adsorption configurations a) C1, b) C2, c) C3, and d) C4 for DHTAP adsorbed on Cu(110). White atoms correspond to H atoms, red atoms correspond to C atoms, orange atoms correspond to N atoms, blue atoms correspond to Cu atoms in the first layer, and silver atoms correspond to Cu atoms in the second layer and lower.



### 4.3.2 STEM and LEED measurements

The highest experimental packing density of DHTAP on Cu(110) our collaborators could achieve corresponds to a unit cell described by the matrix  $\begin{pmatrix} 6 & 0 \\ 0 & 1 \end{pmatrix}$ , or a packing density of 0.904 molecules/nm<sup>2</sup>. With that coverage corresponding to 1 ML, we show in figure 42 the STM images of DHTAP deposited at room temperature on Cu(110) at a coverage of 0.1 ML. From figure 42 we note individual DHTAP molecules or small clusters of DHTAP on Cu(110). We also observe DHTAP to adsorb flat on the surface as evident by the low apparent height in the images, 110 pm. At a 0.1 ML we also observe DHTAP molecules to adsorb on Cu(110) with its long molecular plane along the (-110) direction. Moreover it is evident from these images that the molecules are laterally displaced (along the (-110) direction) by 0.255 nm or exactly one Cu lattice spacing, which leads to a stacking direction that is tilted by an angle of +/- 19.5° relative to the (100) direction. Moreover, evident from figure 42 b), which shows an STM image with the atomically resolved substrate, is that the molecules sit over the trenches as opposed to the closely-packed rows on the Cu(110) surface.

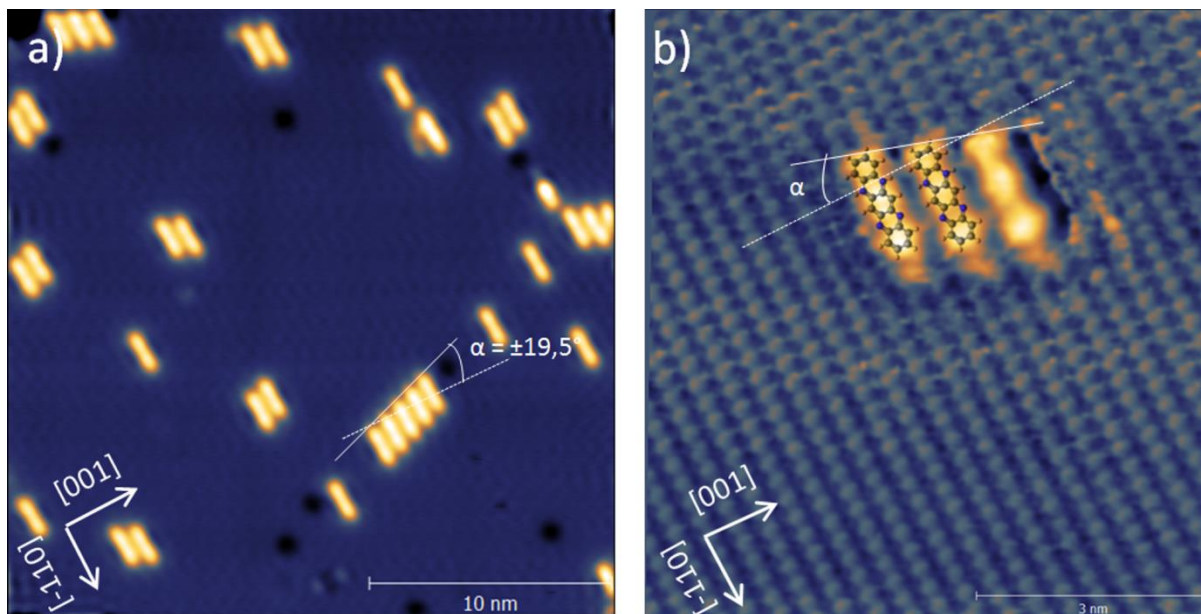


Figure 42: a) STM image of DHTAP deposited at room temperature on Cu(110). DHTAP molecules appear as bright yellow rods. Panel b) illustrates an STM image of the atomically resolved substrate with a DHTAP trimer. The coverage for both images was 0.1 ML. Overlaid on the STM image is a ball-and-stick model of DHTAP. Tunneling parameters: a)  $I_t = 50$  pA,  $V_{\text{sample}} = +0.5$  V and b)  $I_t = 6$  nA,  $V_{\text{sample}} = -0.10$  mV.

Increasing the coverage of DHTAP on Cu(110) leads to two superstructures defined by the matrices  $(7\ 0\ | 1\ 2)$  and  $(6\ -1\ | 1\ 2)$ . Figure 43 illustrates the STM images of DHTAP deposited on Cu(110) at room temperature at a coverage of a) 0.35 ML and b) 0.50 ML. At 0.35 ML we observe one-dimensional stacks of molecules wandering along the (001) direction. There does not appear to be aggregation along the (-110) direction, suggesting the intermolecular forces along this direction are weak to negligible. Moving to 0.5 ML we see that two-dimensional islands begin to form. Zooming into these two-dimensional islands, see figure 43 c) and d), we note the presence of the superstructures defined by the matrices  $(7\ 0\ | 1\ 2)$  and  $(6\ -1\ | 1\ 2)$ . Just as at 0.1 ML, the stacking of molecules along the (001) direction is offset by the distance of one Cu nearest neighbor distance in the (-110) direction. Finally we notice that increasing the

coverage increases the average length of the molecular rows. At 0.35 ML the average length of the molecular rows is 2.30 nm. At 0.50 ML the average length of the molecular rows is 4.60 nm.

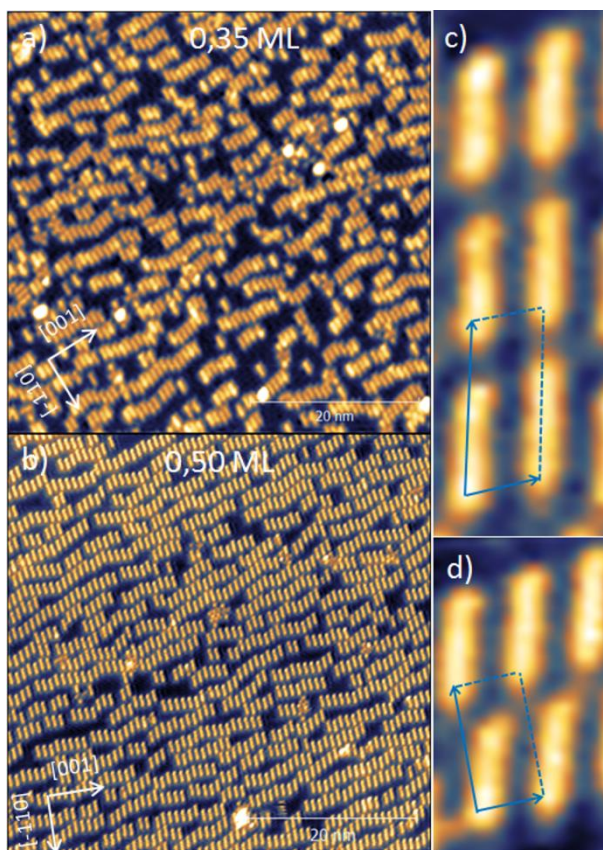


Figure 43: STM images of DHTAP deposited on Cu(110) at room temperature at a coverage of a) 0.35 ML and b) 0.50 ML. The images in c) and d) are high-resolution zooms of the image in b), and reveal two structures that can be described by the matrices  $\begin{pmatrix} 7 & 0 \\ 1 & 2 \end{pmatrix}$  and  $\begin{pmatrix} 6 & -1 \\ 1 & 2 \end{pmatrix}$ , respectively. Tunneling parameters:  $I_t = 100 \text{ pA}$ ,  $V_{\text{sample}} = +0.5 \text{ V}$ .

To explore the effect of the deposition temperature our colleagues deposit DHTAP at three different temperatures, 240K, 300K, and 430K, at a coverage of 0.8 ML. Figure 44 illustrates the STM images of these three different experiments. At low deposition temperature, 240 K, we observe no long-range order. At deposition temperature of 300 K, as for DHTAP deposited at room temperature at a coverage of 0.5 ML, we begin to see the formation of two-dimensional

islands. Inside these two-dimensional islands we again observe the superstructures defined by the matrices  $(7\ 0\ | 1\ 2)$  and  $(6\ -1\ | 1\ 2)$ . Finally at a deposition temperature of 430 K we observe long-range order. The DHTAP molecules form a highly order structure that can be describe with a  $(7\ 0\ | 1\ 2)$  matrix. The packing density for this highly ordered structure is  $0.775\ \text{molecules/nm}^2$ .

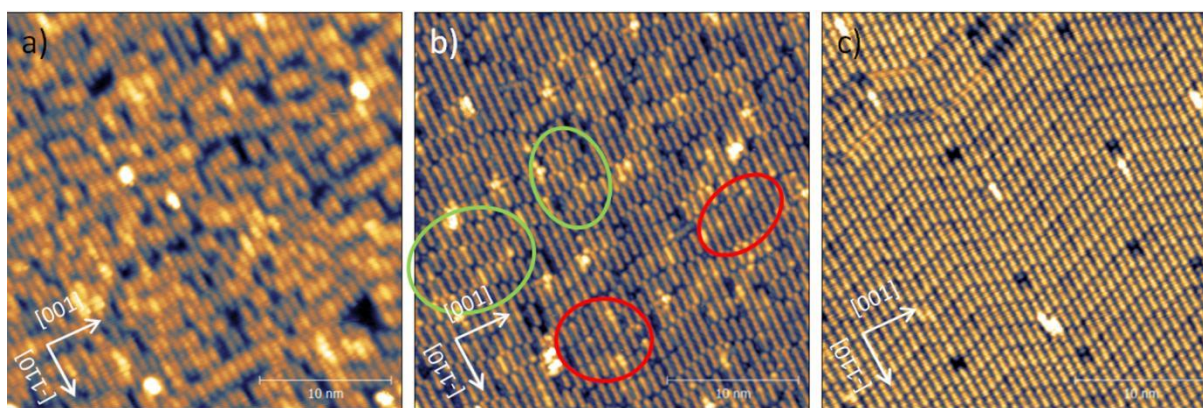


Figure 44: STM of 0.8ML of DHTAP deposited on Cu(110) at temperatures of a) 240 K, b) 330 K, and c) 430 K. Tunneling parameters:  $I_t = 100\ \text{pA}$ ,  $V_{\text{sample}} = +0.5\ \text{V}$ .

Even though the DHTAP deposited at 430 K at a coverage of 0.8 ML appears rather compact, we could achieve an even higher coverage. We illustrate the STM images and LEED patterns of DHTAP deposited on Cu(110) at 240K, 330K, and 430 K at the highest coverage in figure 45. For all three deposition temperatures we observe an inclination of  $\pm 19.5^\circ$  of the short superstructure axis relative to the (100) direction. At a deposition temperature of 240 K the DHTAP molecules condense mostly in to a phase that can be described by a  $(6\ -1\ | 1\ 2)$  matrix. In this phase the DHTAP molecules exhibit a lot of stacking defects and the long range order is limited to a few nanometers. At our high deposition temperature, 430 K, we observe much more order. At a deposition temperature of 430 K most of the DHTAP molecules condense into a

structure defined by the matrix  $(6\ 0\ | 1\ 2)$ , which is the most compact structure we could observe and the packing density we define as 1 ML. In this phase we can see a slightly undulation of the molecules along the  $(-110)$  direction. At an intermediate deposition temperature we could observe both  $(6\ 0\ | 1\ 2)$  and  $(6\ -1\ | 1\ 2)$  superstructures with about 80% of the surface being covered with the  $(6\ 0\ | 1\ 2)$  superstructure. All our structures were confirmed by LEED. Figure 45 d)-f) illustrate the LEED patterns for DHTAP deposited at 240 K, 330 K, and 430 K, respectively, at a coverage of 1M. The simulated LEED patterns, which we created using LEEDpat using the superstructure matrices determined by STEM, are overlaid in figure 44 d)-f). Green ellipsoids correspond to areas of the  $(6\ -1\ | 1\ 2)$  superstructure, and red ellipsoids correspond to areas of the  $(6\ 0\ | 1\ 2)$  superstructure.



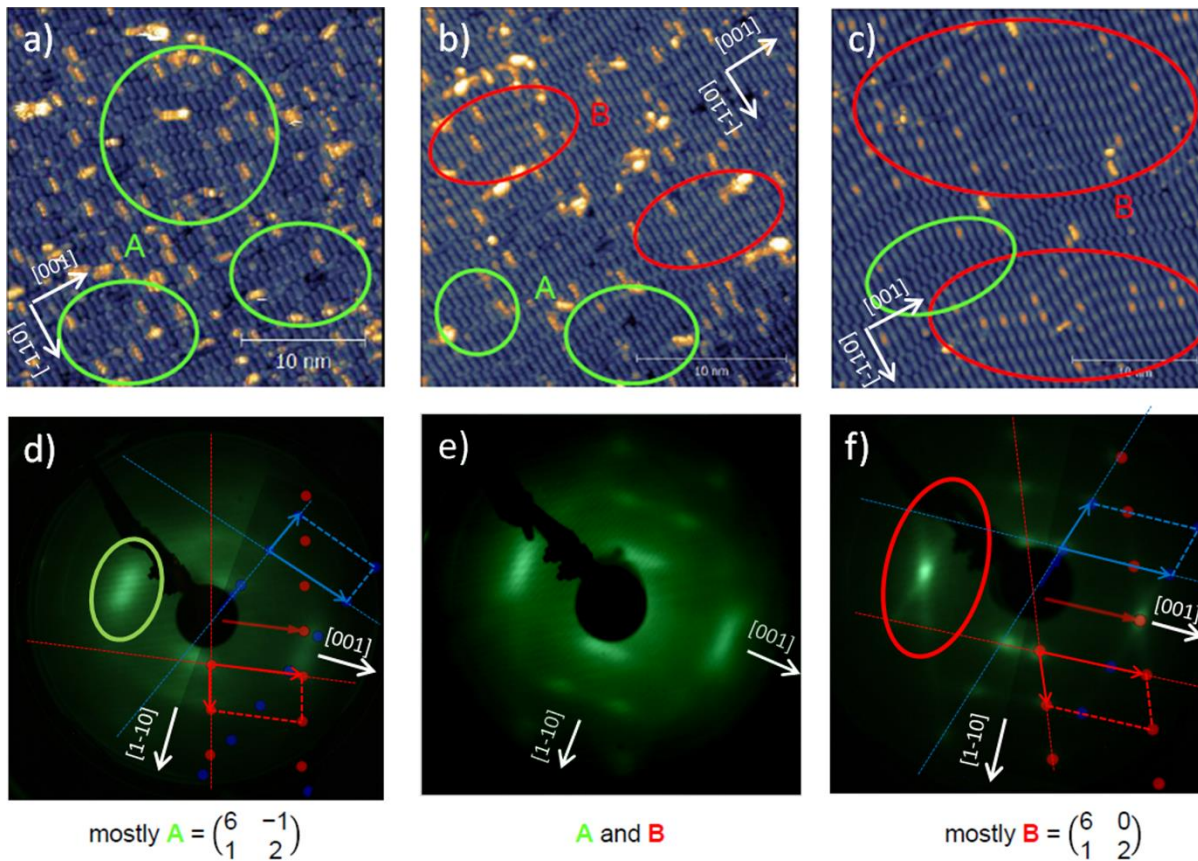


Figure 45: STM of 1 ML of DHTAP deposited on Cu(110) at temperatures of a) 240 K, b) 330 K, and c) 430 K. Tunneling parameters:  $I_t = 100$  pA,  $V_{\text{sample}} = +0.5$  V. The panels d)-f) illustrate the LEED patterns of the surfaces in panels a)- c) respectively. LEED patterns were acquired using an electron beam energy of 17.6 eV. Overlaid in panels d)-f) are the simulated LEED patterns for the  $(6\ 0\ | \ 1\ 2)$  and  $(6\ -1\ | \ 1\ 2)$  structures. Red and blue arrows correspond to the unit cell vectors of the two mirror domains.

### 4.3.3 DFT calculations

In agreement with all the STM images we find the most stable adsorption geometry, regardless of coverage, to be when DHTAP sits over the trough on the Cu(110) surface with its N atoms bonded to the Cu atoms of the surface, or rather adsorption site C3. Furthermore, we also observe that DHTAP, when we would place it in adsorption site C4, would relax to adsorption site C3, illustrating the N-Cu interaction seems to be the driving force for the final

adsorption configuration. Figure 46 illustrates the final adsorption configuration of DHTAP when initially placed on adsorption site C3 in the  $(6\ 0\ | 1\ 2)$ ,  $(7\ 0\ | 1\ 2)$ , and  $(6\ -1\ | 1\ 2)$  unit cells.

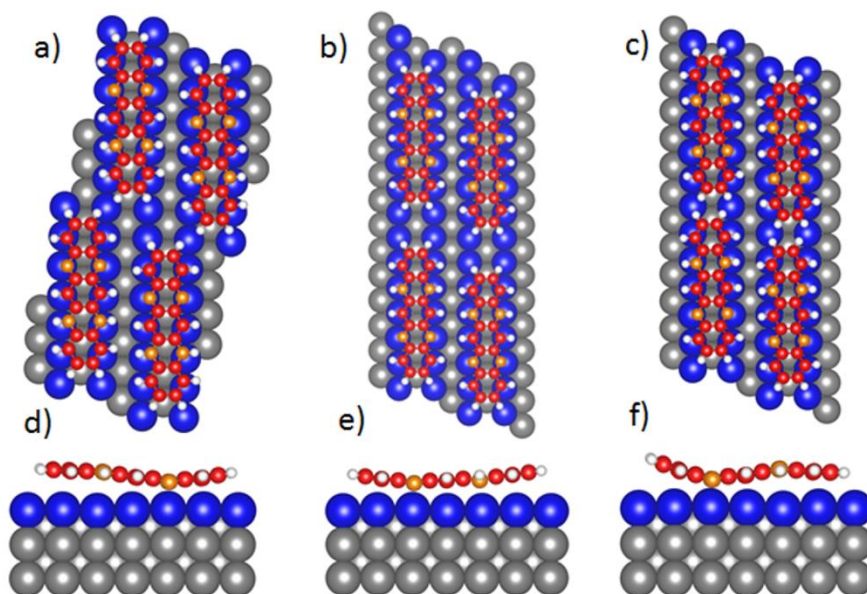


Figure 46: Calculated equilibrium adsorption geometries for DHTAP on Cu(110) in the, a) and d),  $(6\ -1\ | 1\ 2)$  unit cell, b) and e), the  $(7\ 0\ | 1\ 2)$  unit cell, c) and f), and the  $(6\ 0\ | 1\ 2)$  unit cell. Orange atoms correspond to N atoms, red atoms correspond to C atoms, white atoms correspond to H atoms, blue atoms correspond to first layer Cu atoms, and silver atoms correspond to second layer and lower Cu atoms. Pictures a) through c) are top views of the systems. Pictures d) through f) are side views of the systems which illustrate the buckling of the molecule.

Table 32 lists the adsorption energy ( $E_{\text{ads}}$ ), the surface adsorption energy (Surface  $E_{\text{ads}}$ ), the adsorption height ( $H_{\text{ads}}$ ), the N-Cu distances, the buckling of the first layer of the surface ( $B_s$ ), the buckling of the molecule ( $B_m$ ), and the charge transfer from the surface to the molecule ( $\Delta q$ ) for DHTAP adsorbed on Cu(110) in our three different unit cells. Starting with adsorption energy ( $E_{\text{ads}}$ ), we note large adsorption energies, 2.93 eV to 3.08 eV. Comparing to pentacene, which is known to chemisorb on Cu(110), we note our adsorption energies are much higher than the calculated adsorption energy for an isolated molecule of pentacene on Cu(110), 1.59 eV [211], or

the experimentally determined adsorption energy of a monolayer of pentacene on Cu(110), 2.1 eV [212]. This large adsorption energy we observe would suggest DHTAP chemisorbs on Cu(110). Along with this large adsorption energy we note short N-Cu distances, roughly 2 Å. Again these values are much lower than the C-Cu distances observed for pentacene on Cu(110) [213], 2.29 Å. These low N-Cu distances further support the notion that DHTAP chemisorbs on Cu(110). Comparing the N-Cu distances with adsorption heights, which we define as the average z-coordinate of the atoms composing the DHTAP molecule minus the average z-coordinate of the Cu atoms composing the first layer of the substrate, we note the adsorption heights in each unit cell are moderately higher than the N-Cu distances. Part of the reason the adsorption heights are large compared to the N-Cu distances is that the DHTAP molecule experiences significant buckling on Cu(110). Pentacene has also been reported to buckle on Cu(110) [213,214], Cu(111) [215], and Al(100) [216]. Specifically, we observe a 0.92 Å buckling of the molecule in the (7 0 | 1 2) unit cell with N atoms of the molecule closest to the surface, see figure 46 d). This buckling is consistent with the STM images. Figure 47 overlays the calculated final adsorption configuration of DHTAP on Cu(110) in each unit cell on the corresponding STM image. From figure 47 b) we note the STM image suggests the lowest apparent height corresponds to the N atoms in the (7 0 | 1 2) unit cell. For DHTAP on Cu(110) in the (6 -1 | 1 2) unit cell we note slightly more buckling of the molecule, 0.98 Å, with the extremities of the molecule further from the Cu(110) surface than the center portion of the molecule. The STM images again support the DFT calculations. From Figure 47 a) we note the extremities of the molecule appear the brighter than the center of the molecule. Finally for DHTAP in the (6 0 | 1 2) unit cell we calculate the molecule to assume a s-shape with one end of



the molecule pointing towards the surface and the other end of the molecule pointing away from the surface leading to a large buckling of the molecule, 1.50 Å. This final adsorption geometry is again supported by the STM images. In figure 47 c) we note bright protrusions between neighboring molecules. We attribute this interesting s-shape the molecule takes to steric hindrance between the molecules, which must be avoided to achieve the high packing density seen in the (6 0 | 1 2) unit cell. The large buckling of the molecule, no matter the unit cell, suggests DHTAP chemisorbs on Cu(110). Finally, the large charge transfer from the substrate to the DHTAP molecule during relaxation, 0.6 to 0.8 (-e), also suggests a strong DHTAP/Cu(110) interaction which in turn suggests DHTAP chemisorbs on Cu(110). Altogether, we categorize the interaction of DHTAP with Cu(110) as chemisorption due to the small N-Cu distances, high adsorption energies, low adsorption heights, large buckling both of the substrate and the molecule, and large charge transfer from the molecule to the substrate.

Table 32: Adsorption energy ( $E_{\text{ads}}$ ), surface adsorption energy (Surface  $E_{\text{ads}}$ ), adsorption height ( $H_{\text{ads}}$ ), N-Cu distances, buckling of the first layer of the substrate ( $B_s$ ), buckling of the molecule ( $B_m$ ), and charge transfer to the DHTAP molecule ( $\Delta q$ ) for DHTAP adsorbed on Cu(110) in the (7 0 | 1 2), (6 -1 | 1 2), and (6 0 | 1 2) unit cells.

Unit Cell	$E_{\text{ads}}$ (eV)	Surface $E_{\text{ads}}$ (eV/nm <sup>2</sup> )	$H_{\text{ads}}$ (Å)	N-Cu (Å)	$B_s$ (Å)	$B_m$ (eV)	$\Delta q$ (-e)
(7 0   1 2)	3.08	2.39	2.46	2.04	0.10	0.92	-0.8
(6 -1   1 2)	2.93	2.45	2.58	2.05	0.15	0.98	-0.6
(6 0   1 2)	3.04	2.75	2.59	2.02	0.20	1.50	-0.7

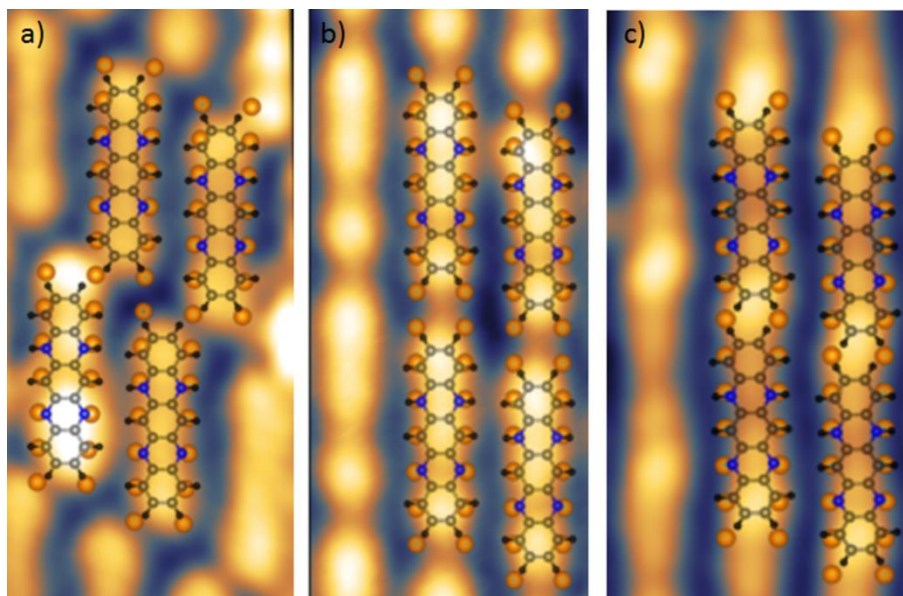


Figure 47: The STM images of DHTAP on Cu(110) in the a)  $(6 -1 | 1 2)$  structure, the  $(7 0 | 1 2)$  structure, and the  $(6 0 | 1 2)$  structure. Overlaid on the STM images are the calculated adsorption configurations. Tunneling parameters:  $I_t = 100$  pA,  $V_{\text{sample}} = +0.5$  V, scale:  $(2.2 \times 4.2)$  nm<sup>2</sup>.

Besides indicating that DHTAP chemisorbs on Cu(110) our results illuminate a number of other important features of the DHTAP/Cu(110) system. For the buckling of the first layer of the substrate along with the buckling of the molecule we note that DHTAP in the  $(7 0 | 1 2)$  unit cell gives the lowest values. This small buckling may be explained by the fact that  $(7 0 | 1 2)$  unit cell is the least compact structure yielding the smallest amount of steric hindrance. If we look at the adsorption energy, we note that DHTAP in the  $(7 0 | 1 2)$  and  $(6 0 | 1 2)$  unit cells have roughly the same adsorption energy, and DHTAP in the  $(6 -1 | 1 2)$  unit cell has the smallest adsorption energy. This is a little surprising given DHTAP in the  $(6 -1 | 1 2)$  experiences the most structural deformation. This discrepancy disappears though when we look at the surface adsorption energy, which we define as the adsorption energy per unit surface area and list in table 32 as Surface  $E_{\text{ads}}$ . Using surface adsorption energy we see that the  $(7 0 | 1 2)$  and  $(6 -1 | 1$

2) unit cells are roughly energetically equivalent with values of  $2.39 \text{ eV/nm}^2$  in the  $(7\ 0\ | 1\ 2)$  unit cell and  $2.45 \text{ eV/nm}^2$  in the  $(6\ -1\ | 1\ 2)$  unit cell. This nicely explains the coexistence of these two structures when we deposit DHTAP at 300 K at a coverage 0.8 ML. The surface adsorption energy also informs us that the  $(6\ 0\ | 1\ 2)$  unit cell is the most energetically stable with a surface adsorption energy of  $2.75 \text{ eV/nm}^2$ . The reason we fail to observe this structure at low deposition temperatures could be an activation barrier related to the steric hindrance between the molecules that must be overcome to achieve this dense packing density.

#### 4.3.4 Conclusions

We have studied the adsorption of DHTAP on Cu(110) using STM, LEED, and DFT. Our experimental results indicated the presence of three different superstructures:  $(6\ -1\ | 1\ 2)$ ,  $(7\ 0\ | 1\ 2)$ , and  $(6\ 0\ | 1\ 2)$ . We used this experimental insight to guide our DFT calculations. We ran DFT calculations of DHTAP in each one of the three experimentally observed superstructures. Overall we found great agreement between our DFT calculations and our experimental results. We found, in agreement with experiment, that DHTAP adsorbs flat on Cu(110) with its long molecular axis parallel to the  $(-110)$  direction. Specifically we calculated DHTAP to adsorb over the trenches in between the close-packed Cu rows with its N atoms bonded to the Cu atoms in the first layer of the surface. We also calculated, in agreement with the STM images, the DHTAP molecule to buckle significantly upon adsorption. In light of this large buckling of the molecule in conjunction with the large adsorption energies, the low adsorption heights and N-Cu distances, and the large amount of charge transfer between the DHTAP molecule and the substrate we characterize the interaction of DHTAP with Cu(110) as chemisorption.

Overall, our results demonstrate the power of theory. Our calculations illuminated many of the properties of the DHTAP/Cu(110) system that our STM and LEED experiments could not, and could explain the coexistence of the  $(6 -1 | 1 2)$ , and  $(7 0 | 1 2)$  phases. As with the polythiophene/Au(111) system in the previous section, we were only able to get good results because we were sure of the competence of the optB88-vdW functional, which again illustrates the importance of screening recently developed methods. We need to properly test new methods to ensure they can provide an adequate description of systems of interest to experimentalists.

## CHAPTER FIVE: CONCLUSIONS

In the third chapter of this dissertation we screened several computational methods by exploring the adsorption of pyridine and thiophene on many transition metal surfaces. We found the PBE, vdW-DF, and vdW-DF2 methods provide a poor description of pyridine on Cu, Ag, and Au(111). All the functionals we studied failed to predict thiophene's experimentally determined adsorption site on these coinage metal surfaces. Specifically our chosen functionals predicted thiophene to adsorb with its molecular plane perpendicular to the surface at low coverage while experiment finds thiophene to adsorb with its molecular plane parallel to the surface at low coverage. Our chosen functionals fared a little better on the pyridine/reactive transition metal systems. Explicitly, we found the optB86-vdW and optB88-vdW functionals gives the best description of pyridine on Rh, Pt, Pd, and Ni(111), consistently calculating pyridine to adsorb, in agreement with experiment, with its molecular plane parallel to the surface. The remaining functionals predicted pyridine to prefer to adsorb with its molecular plane perpendicular to at least one of the reactive transition metal surface. Our results further improved when moving to the less coordinated (110) surfaces. When studying pyridine on Cu, Ag, Au, and Pt(110) only the rPW86-vdW functional gave an incorrect description of pyridine on Pt(110), calculating the molecule to prefer to adsorb with its plane perpendicular to the surface when, experimentally, it adsorbs with its molecular plane parallel to the surface. Finally, on each of these transition metal surfaces changing the orientation of the molecule significantly changed the charge distribution of the system probably as a result of the difference in the electronic properties of a flat  $\pi$ -bonded system and a vertical N lone pair electron bonded system. These results suggested that pyridine on transition metal surfaces presents a challenge

for quantum mechanical modeling with the adsorption of pyridine on less reactive transition metal surfaces with a higher coordination number presenting the greatest challenge. It can be difficult for DFT to distinguish between the flat,  $\pi$  bonded phase and the upright, N lone pair bonded phase of pyridine on transition metal surfaces. The reason DFT struggles with the problem of pyridine on transition metal surfaces is unknown and warrants further investigation especially as N containing organic compounds gain more prevalence in the field of organic molecular electronics.

In contrast to pyridine on transition metal surfaces, thiophene on transition metal surface was more easily described by DFT. All of the functionals predicted, in agreement with the available experimental literature, that thiophene adsorbs with its plane parallel to the surface. This result demonstrated the important role the heteroatom plays for these organic molecule/transition metal systems. Making a simple change from N to S in our aromatic molecule drastically affected both the difficulty of our problem and the behavior of the adsorbate on the surface. In contrast to pyridine, for thiophene we never observed a vertical phase at low coverage.

Despite the differences, we did observe some similarities between our results for the adsorption of pyridine on transition metal surfaces and for the adsorption of thiophene on transition metal surfaces. First, PBE's calculated adsorption energy on the coinage metal surfaces, regardless of the molecule, was always the lowest, indicating the vdW interaction is important for these systems, enhancing the overall organic molecule/coinage metal interaction. On the reactive metal surfaces the revPBE-vdW and rPW86-vdW2 functionals yielded the lowest adsorption energies. Only the opt-type functionals provided an enhancement of the adsorption

energy over PBE. This illustrated the importance of one's choice of exchange functional.

Choosing either the revPBE-vdW or rPW86-vdW2 method, with their overly repulsive exchange functionals, led to an underbinding of the molecule to the surface.

In the last part of this chapter we studied the adsorption of thiophene on transition metals surfaces using the popular meta-GGA SCAN+rVV10 functional. For thiophene on Ag(100), SCAN+rVV10 and optB88-vdW gave similar results. In contrast, for thiophene on Ir(100) and Rh(100) SCAN+rVV10 predicted a larger adsorption energy than optB88-vdW. The SCAN+rVV10 functional also predicted a much larger charge transfer to occur from the surface to thiophene than optB88-vdW. This charge transfer, in fact, was many times the amount predicted by optB88-vdW. In light of this data we suggest that SCAN+rVV10 overbinds thiophene to Rh(100) and Ag(100) due to a density driven self-interaction error. The reason we suspected SCAN+rVV10 overbinds thiophene to transition metal surfaces came from a study that utilized SCAN to explore the adsorption of CO on transition metal surfaces. Compared to PBE, they found SCAN to overbind CO to transition metal surfaces, and attributed this error to a density driven self-interaction error. Furthermore, they theorized this error should also be present for the adsorption of other molecules on transition metal surfaces. Our results confirmed the results of this study.

Finally in the last part of this dissertation we switched our focus to more practical systems. First we studied the adsorption of thiophene on transition metal surfaces from the perspective of HDS. We found that thiophene can rupture one or two C-S bonds over many of the group V and VI transition metal surfaces. We found a strong correlation between the breaking of C-S bonds

and the charge transfer to thiophene's S atom. Guided by this observation we tried to map the charge transfer to thiophene's S atom and adsorption energy of thiophene to the experimentally determined HDS rates of thiophene on transition metal sulfides under realistic reaction conditions. With this approach, which is definitely limited by how well thiophene on transition metal sulfides under realistic reaction conditions correlates to thiophene on bare metal single crystal surfaces, we found a modest correlation between the charge transfer to thiophene's S atom, adsorption energy, and the experimentally determined HDS rates. Further research is needed though to confirm this correlation, and then to apply it to the search for more active HDS catalysis.

Next we moved onto the adsorption of polythiophene and DHTAP on Au and Cu(110) respectively. Both systems could be of interest for use in molecular electronic devices. For the polythiophenes on Au(111) and Au grown on mica we compared the calculated CLBEs to the XPS S2P peaks. We found the CLBE of intact thiophene and broken thiophene to overlap, indicating the possible presence of broken thiophene on Au, a popular electrode material. If thiophene and its derivatives are capable of dissociating over Au it could disrupt the electron transport properties of the system, rendering the system less than ideal for use in molecular electronic devices. We also for terthiophene, interestingly, found the CLBE of the interior S atom to differ significantly from the CLBE of the exterior S atoms. For DHTAP on Cu(111) we found excellent agreement with experiment. Both the calculated position of the molecule on the substrate and the large buckling of the molecule could be observed in the STM images. Moreover our calculations could nicely explain the coexistence of two different DHTAP



structures on Cu(110), and give a possible reason why a third DHTAP structure could only be observed at high coverage.

These studies which possess both experimental and theoretical components illustrate the power of theory. Theoretical calculations can be used to examine the properties of systems that may be difficult to explore experimentally, or they may be used to explain why one obtains a particular experimental result. Regardless, before one investigates a system of interest to experimentalists one must first thoroughly test one's proposed method, especially in an age where the number of methods available to researchers is ever expanding. To effectively screen a method one must test their method, as we have done here, using systems with a large benchmark of both experimental and high-level computational data.

**APPENDIX A:  
COPYRIGHT PERMISSION LETTERS**

## Permission for using article adapted from JCP for which I am an author (Section 3.3)

RightsLink Printable License

### AIP PUBLISHING LICENSE TERMS AND CONDITIONS

Mar 06, 2019

This Agreement between Walter Malone ("You") and AIP Publishing ("AIP Publishing") consists of your license details and the terms and conditions provided by AIP Publishing and Copyright Clearance Center.

License Number	4543250903178
License date	Mar 06, 2019
Licensed Content Publisher	AIP Publishing
Licensed Content Publication	Journal of Chemical Physics
Licensed Content Title	Competing adsorption mechanisms of pyridine on Cu, Ag, Au, and Pt(110) surfaces
Licensed Content Author	Walter Malone, Johnathan von der Heyde, Abdelkader Kara
Licensed Content Date	Dec 7, 2018
Licensed Content Volume	149
Licensed Content Issue	21
Type of Use	Thesis/Dissertation
Requestor type	Author (original article)
Format	Electronic
Portion	Excerpt (> 800 words)
Will you be translating?	No
Title of your thesis / dissertation	A THEORETICAL INVESTIGATION OF SMALL ORGANIC MOLECULES ON TRANSITION METAL SURFACES
Expected completion date	May 2019
Estimated size (number of pages)	275
Requestor Location	Walter Malone 3770 Aristotle Ave.  ORLANDO, FL 32826 United States Attn: Walter Malone
Billing Type	Invoice
Billing Address	Walter Malone 3770 Aristotle Ave.  ORLANDO, FL 32826 United States Attn: Walter Malone
Total	0.00 USD

Terms and Conditions

AIP Publishing -- Terms and Conditions: Permissions Uses

AIP Publishing hereby grants to you the non-exclusive right and license to use and/or distribute

RightsLink Printable License

the Material according to the use specified in your order, on a one-time basis, for the specified term, with a maximum distribution equal to the number that you have ordered. Any links or other content accompanying the Material are not the subject of this license.

1. You agree to include the following copyright and permission notice with the reproduction of the Material: "Reprinted from [FULL CITATION], with the permission of AIP Publishing." For an article, the credit line and permission notice must be printed on the first page of the article or book chapter. For photographs, covers, or tables, the notice may appear with the Material, in a footnote, or in the reference list.
2. If you have licensed reuse of a figure, photograph, cover, or table, it is your responsibility to ensure that the material is original to AIP Publishing and does not contain the copyright of another entity, and that the copyright notice of the figure, photograph, cover, or table does not indicate that it was reprinted by AIP Publishing, with permission, from another source. Under no circumstances does AIP Publishing purport or intend to grant permission to reuse material to which it does not hold appropriate rights.  
You may not alter or modify the Material in any manner. You may translate the Material into another language only if you have licensed translation rights. You may not use the Material for promotional purposes.
3. The foregoing license shall not take effect unless and until AIP Publishing or its agent, Copyright Clearance Center, receives the Payment in accordance with Copyright Clearance Center Billing and Payment Terms and Conditions, which are incorporated herein by reference.
4. AIP Publishing or Copyright Clearance Center may, within two business days of granting this license, revoke the license for any reason whatsoever, with a full refund payable to you. Should you violate the terms of this license at any time, AIP Publishing, or Copyright Clearance Center may revoke the license with no refund to you. Notice of such revocation will be made using the contact information provided by you. Failure to receive such notice will not nullify the revocation.
5. AIP Publishing makes no representations or warranties with respect to the Material. You agree to indemnify and hold harmless AIP Publishing, and their officers, directors, employees or agents from and against any and all claims arising out of your use of the Material other than as specifically authorized herein.
6. The permission granted herein is personal to you and is not transferable or assignable without the prior written permission of AIP Publishing. This license may not be amended except in a writing signed by the party to be charged.
7. If purchase orders, acknowledgments or check endorsements are issued on any forms containing terms and conditions which are inconsistent with these provisions, such inconsistent terms and conditions shall be of no force and effect. This document, including the CCC Billing and Payment Terms and Conditions, shall be the entire agreement between the parties relating to the subject matter hereof.

This Agreement shall be governed by and construed in accordance with the laws of the State of New York. Both parties hereby submit to the jurisdiction of the courts of New York County for purposes of resolving any disputes that may arise hereunder.

V1.2

Questions? [customercare@copyright.com](mailto:customercare@copyright.com) or +1-855-239-3415 (toll free in the US) or +1-978-646-2777.

---

---

## Permission for using article adapted from JPCC for which I am an author (Section 3.4)

Rightslink® by Copyright Clearance Center



RightsLink®



**Title:** A van der Waals Inclusive Density Functional Theory Study of the Nature of Bonding for Thiophene Adsorption on Ni(100) and Cu(100) Surfaces  
**Author:** Walter Malone, Handan Yildirim, Jeronimo Matos, et al  
**Publication:** The Journal of Physical Chemistry C  
**Publisher:** American Chemical Society  
**Date:** Mar 1, 2017  
Copyright © 2017, American Chemical Society

### PERMISSION/LICENSE IS GRANTED FOR YOUR ORDER AT NO CHARGE

This type of permission/license, instead of the standard Terms & Conditions, is sent to you because no fee is being charged for your order. Please note the following:

- Permission is granted for your request in both print and electronic formats, and translations.
- If figures and/or tables were requested, they may be adapted or used in part.
- Please print this page for your records and send a copy of it to your publisher/graduate school.
- Appropriate credit for the requested material should be given as follows: "Reprinted (adapted) with permission from (COMPLETE REFERENCE CITATION). Copyright (YEAR) American Chemical Society." Insert appropriate information in place of the capitalized words.
- One-time permission is granted only for the use specified in your request. No additional uses are granted (such as derivative works or other editions). For any other uses, please submit a new request.

Copyright © 2019 Copyright Clearance Center, Inc. All Rights Reserved. [Privacy statement](#). [Terms and Conditions](#).  
Comments? We would like to hear from you. E-mail us at [customercare@copyright.com](mailto:customercare@copyright.com)

## Permission for using article adapted from Surface Science for which I am an author (Section 3.5)

Rightslink® by Copyright Clearance Center



# RightsLink®



**Title:** Adsorption of thiophene on transition metal surfaces with the inclusion of van der Waals effects

**Author:** Walter Malone, Jeronimo Matos, Abdelkader Kara

**Publication:** Surface Science

**Publisher:** Elsevier

**Date:** March 2018

© 2017 Elsevier B.V. All rights reserved.

Please note that, as the author of this Elsevier article, you retain the right to include it in a thesis or dissertation, provided it is not published commercially. Permission is not required, but please ensure that you reference the journal as the original source. For more information on this and on your other retained rights, please visit: <https://www.elsevier.com/about/our-business/policies/copyright#Author-rights>

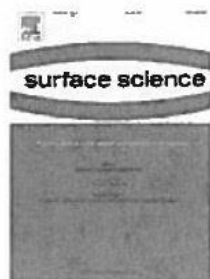
Copyright © 2019 Copyright Clearance Center, Inc. All Rights Reserved. [Privacy statement](#). [Terms and Conditions](#). Comments? We would like to hear from you. E-mail us at [customercare@copyright.com](mailto:customercare@copyright.com)

**Permission for using article adapted from Surface Science for which I am an author  
(Section 4.1)**

Rightslink® by Copyright Clearance Center



RightsLink®



**Title:** Exploring thiophene desulfurization: The adsorption of thiophene on transition metal surfaces

**Author:** Walter Malone, William Kaden, Abdelkader Kara

**Publication:** Surface Science

**Publisher:** Elsevier

**Date:** August 2019

© 2019 Published by Elsevier B.V.

Please note that, as the author of this Elsevier article, you retain the right to include it in a thesis or dissertation, provided it is not published commercially. Permission is not required, but please ensure that you reference the journal as the original source. For more information on this and on your other retained rights, please visit: <https://www.elsevier.com/about/our-business/policies/copyright#Author-rights>

## Permission for using article adapted from JPCC for which I am an author (Section 4.2)

Rightslink® by Copyright Clearance Center



RightsLink®



**Title:** Thiophene Derivatives on Gold and Molecular Dissociation Processes  
**Author:** Tingming Jiang, Walter Malone, Yongfeng Tong, et al  
**Publication:** The Journal of Physical Chemistry C  
**Publisher:** American Chemical Society  
**Date:** Dec 1, 2017  
Copyright © 2017, American Chemical Society

### PERMISSION/LICENSE IS GRANTED FOR YOUR ORDER AT NO CHARGE

This type of permission/license, instead of the standard Terms & Conditions, is sent to you because no fee is being charged for your order. Please note the following:

- Permission is granted for your request in both print and electronic formats, and translations.
- If figures and/or tables were requested, they may be adapted or used in part.
- Please print this page for your records and send a copy of it to your publisher/graduate school.
- Appropriate credit for the requested material should be given as follows: "Reprinted (adapted) with permission from (COMPLETE REFERENCE CITATION). Copyright (YEAR) American Chemical Society." Insert appropriate information in place of the capitalized words.
- One-time permission is granted only for the use specified in your request. No additional uses are granted (such as derivative works or other editions). For any other uses, please submit a new request.

Copyright © 2019 Copyright Clearance Center, Inc. All Rights Reserved. [Privacy statement](#). [Terms and Conditions](#).  
Comments? We would like to hear from you. E-mail us at [customercare@copyright.com](mailto:customercare@copyright.com)



## Permission for using article adapted from JPCC for which I am an author (Section 4.3)

Rightslink® by Copyright Clearance Center



RightsLink®



**Title:** Growth of  
Dihydroetraazapentacene  
Layers on Cu(110)  
**Author:** Anthony Thomas, Walter  
Malone, Thomas Leoni, et al  
**Publication:** The Journal of Physical  
Chemistry C  
**Publisher:** American Chemical Society  
**Date:** May 1, 2018  
Copyright © 2018, American Chemical Society

### PERMISSION/LICENSE IS GRANTED FOR YOUR ORDER AT NO CHARGE

This type of permission/license, instead of the standard Terms & Conditions, is sent to you because no fee is being charged for your order. Please note the following:

- Permission is granted for your request in both print and electronic formats, and translations.
- If figures and/or tables were requested, they may be adapted or used in part.
- Please print this page for your records and send a copy of it to your publisher/graduate school.
- Appropriate credit for the requested material should be given as follows: "Reprinted (adapted) with permission from (COMPLETE REFERENCE CITATION). Copyright (YEAR) American Chemical Society." Insert appropriate information in place of the capitalized words.
- One-time permission is granted only for the use specified in your request. No additional uses are granted (such as derivative works or other editions). For any other uses, please submit a new request.

Copyright © 2019 Copyright Clearance Center, Inc. All Rights Reserved. [Privacy statement](#). [Terms and Conditions](#).  
Comments? We would like to hear from you. E-mail us at [customercare@copyright.com](mailto:customercare@copyright.com)

**APPENDIX B:  
LIST OF PUBLICATIONS**

W. Malone, W. Kaden, A. Kara, Exploring thiophene desulfurization: The adsorption of thiophene on transition metal surfaces, *Surf. Sci.*, 686 (2019) 30.

W. Malone, J. von der Heyde, A. Kara, Competing adsorption mechanisms of pyridine on Cu, Ag, Au, and Pt(110) surfaces, *J. Chem. Phys.* 149 (2018) 214703.

A. Thomas, W. Malone, T. Leoni, A. Ranguis, Z. Chen, O. Siri, A. Kara, P. Zeppenfeld, and C. Becker, Growth of Dihydropyridazine Layers on Cu(110), *J. Phys. Chem. C*, 122 (2018) 10828.

W. Malone, J. Matos and A. Kara, Adsorption of thiophene on transition metal surfaces with the inclusion of van der Waals effects, *Surf. Sci.*, 669 (2018) 121.

T. Jiang, W. Malone, Y. Tong, D. Dragoe, A. Bendounan, A. Kara, V.A. Esaulov, Thiophene Derivatives on Gold and Molecular Dissociation Processes, *J. Phys. Chem. C*, 121 (2017) 27923.

W. Malone, H. Yildirim, J. Matos and A. Kara, A van der Waals Inclusive Density Functional Theory Study of the Nature of Bonding for Thiophene Adsorption on Ni(100) and Cu(100) Surfaces, *J. Phys. Chem. C*, 121 (2017) 6090.

## LIST OF REFERENCES

- [1] R. M. Dreizler, E. K. U. Gross, Density Functional Theory. An Approach to the Quantum Many-Body Problem, Springer-Verlag, Berlin, 1990.
- [2] J. Klimeš, D. R. Bowler, A. Michaelides, Van Der Waals Density Functionals Applied to Solids, Phys. Rev. B, 83 (2011) 195131.
- [3] J. Carrasco, J. Klimeš, A. Michaelides, The Role of Van Der Waals Forces in Water Adsorption on Metals, J. Chem. Phys., 138 (2013) 024708.
- [4] J. Carrasco, B. Santra, J. Klimeš, A. Michaelides, To Wet or Not to Wet? Dispersion Forces Tip the Balance for Water Ice on Metals, Phys. Rev. Lett., 106 (2011) 026101.
- [5] J. Klimeš, A. Michaelides, Perspective: Advances and Challenges in Treating Van Der Waals Dispersion Forces in Density Functional Theory, J. Chem. Phys., 137 (2012) 120901.
- [6] W. Liu, J. Carrasco, B. Santra, A. Michaelides, M. Scheffler, A. Tkatchenko, Benzene Adsorbed on Metals: Concerted Effect of Covalency and Van Der Waals Bonding, Phys. Rev. B, 86 (2012) 245405.
- [7] A. Tkatchenko, L. Romaner, O. T. Hofmann, E. Zojer, C. Ambrosch-Draxl, M. Scheffler, Van Der Waals Interactions Between Organic Adsorbates and at Organic/Inorganic Interfaces, MRS Bull., 35 (2010), 435–442.

- [8] W. Heckel, T. Würger, S. Müller, G. Feldbauer, Van Der Waals Interaction Really Matters: Energetics of Benzoic Acid on TiO<sub>2</sub> Rutile Surfaces, *J. Phys. Chem. C*, 121 (2017) 17207–17214.
- [9] G. Graziano, J. Klimeš, F. Fernandez-Alonso, A. Michaelides, Improved Description of Soft Layered Materials with Van Der Waals Density Functional Theory, *J. Phys. Condens. Matter*, 24 (2012) 424216.
- [10] P. O. Bedolla, G. Feldbauer, M. Wolloch, C. Gruber, S. J. Eder, N. Dörr, P. Mohn, J. Redinger, A. Vernes, Density Functional Investigation of the Adsorption of Isooctane, Ethanol, and Acetic Acid on a Water-Covered Fe(100) Surface, *J. Phys. Chem. C*, 118 (2014) 21428–21437.
- [11] F. Mittendorfer, A. Garhofer, J. Redinger, J. Klimeš, J. Harl, G. Kresse, Graphene on Ni(111): Strong Interaction and Weak Adsorption, *Phys. Rev. B*, 84 (2011) 201401(R).
- [12] R. Sabatini, T. Gorni, S. D. Gironcoli, Nonlocal van der Waals density functional made simple and efficient, *Phys. Rev. B*, 87 (2013) 041108(R).
- [13] S. Grimme, Semiempirical GGA-Type Density Functional Constructed with a Long-Range Dispersion Correction, *J. Comput. Chem*, 27 (2006) 1787–1799.
- [14] S. Grimme, J. Antony, S. Ehrlich, H. Krieg, A Consistent and Accurate Ab Initio Parametrization of Density Functional Dispersion Correction (DFT-D) for the 94 Elements H-Pu, *J. Chem. Phys*, 132 (2010) 154104.

- [15] A. D. Becke, E. R. Johnson, A Density-Functional Model of the Dispersion Interaction. *J. Chem. Phys.*, 123 (2005) 154101.
- [16] A. Tkatchenko, M. Scheffler, Accurate Molecular Van Der Waals Interactions from Ground-State Electron Density and Free-Atom Reference Data, *Phys. Rev. Lett.*, 102 (2009) 073005.
- [17] J. Klimeš, D. R. Bowler, A. Michaelides, Chemical Accuracy for the Van Der Waals Density Functional, *J. Phys. Condens. Matter*, 22 (2009) 022201.
- [18] M. Dion, H. Rydberg, E. Schröder, D. C. Langreth, B. I. Lundqvist, Van Der Waals Density Functional for General Geometries, *Phys. Rev. Lett.*, 92 (2004) 246401.
- [19] K. Lee, É. D Murray, L. Kong, B. I. Lundqvist, D. C. Langreth, Higher-Accuracy Van Der Waals Density Functional, *Phys. Rev. B*, 82 (2010) 081101.
- [20] O. A. Vydrov, T. Van Voorhis, Nonlocal van der Waals Density Functional: The Simpler the Better, *J. Chem. Phys.*, 133 (2010) 244103.
- [21] A. D. Becke, Density-Functional Exchange-Energy Approximation with Correct Asymptotic Behavior, *Phys. Rev. A*, 38 (1988) 3098–3100.
- [22] D. C. Langreth, M. J. Mehl, Beyond the Local-Density Approximation in Calculations of Ground-State Electronic Properties, *Phys. Rev. B*, 28 (1983) 1809–1834.

- [23] J. P. Perdew, J. A. Chevary, S. H. Vosko, K. A. Jackson, M. R. Pederson, D. J. Singh, C. Fiolhais, Atoms, Molecules, Solids, and Surfaces: Applications of the Generalized Gradient Approximation for Exchange and Correlation, *Phys. Rev. B*, 46 (1992) 6671–6687.
- [24] J. Tao, J. P. Perdew, V. N. Staroverov, G. E. Scuseria, Climbing the Density Functional Ladder: Nonempirical Meta–Generalized Gradient Approximation Designed for Molecules and Solids, *Phys. Rev. Lett.*, 9 (2003) 146401.
- [25] J. P. Perdew, A. Ruzsinszky, G. I. Csonka, L. A. Constantin, J. Sun, Workhorse Semilocal Density Functional for Condensed Matter Physics and Quantum Chemistry, *Phys. Rev. Lett.*, 103 (2009) 026403.
- [26] J. Sun, B. Xiao, A. Ruzsinszky, Communication: Effect of the Orbital-Overlap Dependence in the Meta Generalized Gradient Approximation, *J. Chem. Phys.*, 137 (2012) 051101.
- [27] Y. Zhao, D. G. Truhlar, A New Local Density Functional for Main-Group Thermochemistry, Transition Metal Bonding, Thermochemical Kinetics, and Noncovalent Interactions, *J. Chem. Phys.*, 125 (2006) 194101.
- [28] J. M. del Campo, J. L. Gázquez, S. B. Trickey, A. Vela, A New Meta-GGA Exchange Functional Based on an Improved Constraint-Based GGA, *Chem. Phys. Lett.*, 543 (2012) 179–183.
- [29] H. Peng, Z.-H. Yang, J. P. Perdew, J. Sun, Versatile Van Der Waals Density Functional Based on a Meta-Generalized Gradient Approximation, *Phys. Rev. X*, 6 (2016) 041005.

- [30] J. Sun, A. Ruzsinszky, J. P. Perdew, Strongly Constrained and Appropriately Normed Semilocal Density Functional, *Phys. Rev. Lett.*, 115 (2015) 036402.
- [31] N. T. Kalyani, S. Dhoble, Organic light emitting diodes: Energy saving lighting technology—A review, *Renew. Sust. Energ. Rev.*, 16 (2012) 2696–2723.
- [32] A. Buckley, Organic light-Emitting diodes (OLEDs): materials, devices and applications, Woodhead Publishing, Oxford, 2013.
- [33] M. Muccini, A bright future for organic field-Effect transistors, *Nat. Mater.*, 5 (2006) 605–613.
- [34] H. Sirringhaus, 25th Anniversary Article: Organic Field-Effect Transistors: The Path Beyond Amorphous Silicon, *Adv. Mater.*, 26 (2014) 1319–1335.
- [35] H. Klauk, Organic thin-Film transistors, *Chem. Soc. Rev.*, 39 (2010) 2643.
- [36] D. D. Whitehurst, T. Isoda, I. Mochida, Present State of the Art and Future Challenges in the Hydrodesulfurization of Polyaromatic Sulfur Compounds, *Adv. Catal.*, 42 (1998) 345-471.
- [37] B. C. Wiegand, C. M. Friend, Model studies of the desulfurization reactions on metal surfaces and in organometallic complexes, *Chem. Rev.*, 92 (1992) 491-504.
- [38] K. Burke, L. O. Wagner, DFT in a nutshell, *Int. J. Quantum Chem.*, 113 (2013) 96-101.
- [39] E. Engel, R. M. Dreizler, Density functional theory: an Advanced Course, Springer Science & Business Media, 2011.



- [40] K. Wolfram, M. C. Holthausen, *A Chemist's Guide to Density Functional Theory*, Wiley-VCH, Weinheim, 2001.
- [41] K. Burke, *Perspectives on Density Functional Theory*, *J. Chem. Phys.*, 136 (2012) 150901.
- [42] P. Hohenberg, W. Kohn, *Inhomogeneous Electron Gas*, *Phys. Rev.*, 136 (1964) 864-871.
- [43] W. Kohn, L. J. Sham, *Self-Consistent Equations Including Exchange and Correlation Effects*, *Phys. Rev.*, 140 (1965) 1133-1138.
- [44] J. Sun, J. P. Perdew, M. Seidl, *Correlation energy of the uniform electron gas from an interpolation between high- and low-density limits*, *Phys. Rev. B*, 81 (2010) 085123.
- [45] U. von Barth, L. Hedin, *A local exchange-correlation potential for the spin polarized case: I*, *J. Phys. C*, 5 (1972) 1629.
- [46] J. P. Perdew, A. Zunger, *Self-interaction correction to density-functional approximations for many-electron systems*, *Phys. Rev. B*, 23 (1981) 5048.
- [47] J. P. Perdew, Y. Wang, *Accurate and simple analytic representation of the electron-gas correlation energy*, *Phys. Rev. B*, 45 (1992) 13244.
- [48] S. K. Ma, K. A. Brueckner, *Correlation Energy of an Electron Gas with a Slowly Varying High Density*, *Phys. Rev.*, 165 (1968) 18.
- [49] D. M. Ceperley, B. J. Alder, *Ground State of the Electron Gas by a Stochastic Method*, *Phys. Rev. Lett.*, 45 (1980) 566-569.

- [50] L. A. Constantin, E. Fabiano, S. Laricchia, F. Della Sala, Semiclassical Neutral Atom as a Reference System in Density Functional Theory, *Phys. Rev. Lett.*, 106 (2011) 186406.
- [51] J. P. Perdew, K. Burke, M. Ernzerhof, Generalized Gradient Approximation Made Simple, *Phys. Rev. Lett.*, 77 (1996) 3865–3868.
- [52] J. P. Perdew, A. Ruzsinszky, G. I. Csonka, O. A. Vydrov, G. E. Scuseria, L. A. Constantin, X. Zhou, K. Burke, Restoring the Density-Gradient Expansion for Exchange in Solids and Surfaces, *Phys. Rev. Lett.*, 100 (2008) 136406.
- [53] A. Vela, J. C. Pacheco-Kato, J. L. Gázquez, J. M. del Campo, S. B. Trickey, Improved constraint satisfaction in a simple generalized gradient approximation exchange functional, *J. Chem. Phys.*, 136 (2012) 144115.
- [54] Langreth, D.; Perdew, J. The exchange-Correlation energy of a metallic surface. *Solid State Communications* 1975, 17 (11), 1425–1429.
- [55] Gunnarsson, O.; Lundqvist, B. I. Exchange and correlation in atoms, molecules, and solids by the spin-Density-Functional formalism. *Physical Review B* 1976, 13 (10), 4274–4298.
- [56] Langreth, D. C.; Perdew, J. P. Exchange-Correlation energy of a metallic surface: Wave-Vector analysis. *Physical Review B* 1977, 15 (6), 2884–2901.
- [57] T. Thonhauser, V. R. Cooper, S. Li, A. Puzder, P. Hyldgaard, D. C. Langreth, Van Der Waals Density Functional: Self-Consistent Potential and the Nature of the Van Der Waals Bond, *Phys. Rev. B*, 76 (2007) 125112.

- [58 ] E. D. Murray, K. Lee, D. C. Langreth, Investigation of Exchange Energy Density Functional Accuracy for Interacting Molecules, *J. Chem. Theory Comput*, 5 (2009) 2754–2762.
- [59] G. D. Mahan, *Condensed Matter in a Nutshell*, Princeton University Press, Princeton, 2011.
- [60] H. J. Monkhorst, J. D. Pack, Special points for Brillouin-zone integrations, *Phys. Rev. B*, 13 (1976) 5188.
- [61] G. Kresse, D. Joubert, From ultrasoft pseudopotentials to the projector augmented-wave method, *Phys. Rev. B*, 59 (1999) 1758-1775.
- [62] J. C. Phillips, Energy-band interpolation scheme based on a pseudopotential, *Phys. Rev.*, 112 (1958) 685.
- [63] P. E. Blöchl, Projector augmented-wave method, *Phys. Rev. B*, 50 (1994) 17953.
- [64] M. R. Hestenes, and E. Stiefel, Methods of Conjugated Gradients for Solving Linear Systems, *J. Res. Natl. Bur. Stand*, 49 (1952) 409.
- [65] M. P. Teter, M. C. Payne, and D. C. Allan, Solution of Schrödinger's equation for large systems, *Phys. Rev. B*, 40 (1989) 12255.
- [66] P. Pulay, Convergence acceleration of iterative sequences. the case of scf iteration, *Chem. Phys. Lett.*, 73 (1980) 393-398.
- [67] M. Bader, J. Haase, K.-H. Frank, A. Puschmann, A. Otto, Orientational Phase Transition in the System Pyridine/Ag(111): A Near-Edge X-Ray-Absorption Fine-Structure Study, *Phys. Rev. Lett.*, 56 (1986) 1921–1924.

- [68] J. Demuth, K. Christmann, P. Sanda, The vibrations and structure of pyridine chemisorbed on Ag(111): the occurrence of a compressional phase transformation, *Chem. Phys. Lett.*, 76 (1980) 201–206.
- [69] P. Avouris, J. E. Demuth, Electronic excitations of benzene, pyridine, and pyrazine adsorbed on Ag(111), *J. Chem. Phys.*, 75 (1981) 4783–4794.
- [70] Q. Zhong, C. Gahl, M. Wolf, Two-Photon photoemission spectroscopy of pyridine adsorbed on Cu(111), *Surf. Sci.*, 496 (2002) 21–32.
- [71] W.-B. Cai, L.-J. Wan, H. Noda, Y. Hibino, K. Ataka, M. Osawa, Orientational Phase Transition in a Pyridine Adlayer on Gold(111) in Aqueous Solution Studied by in Situ Infrared Spectroscopy and Scanning Tunneling Microscopy, *Langmuir*, 14 (1998) 6992–6998.
- [72] A. Otto, K. Frank, B. Reihl, Inverse photoemission of pyridine on silver (111), *Surf. Sci.*, 163 (1985) 140–152.
- [73] P. N. Sanda, J. M. Warlaumont, J. E. Demuth, J. C. Tsang, K. Christmann, J. A. Bradley, Surface-Enhanced Raman Scattering from Pyridine on Ag(111), *Phys. Rev. Lett.*, 45 (1980) 1519–1523.

- [74] J. E. Demuth, P. N. Sanda, Observation of Charge-Transfer States for Pyridine Chemisorbed on Ag(111), *Phys. Rev. Lett.*, 47 (1981) 57–60.
- [75] R. Dudde, E. Koch, N. Ueno, R. Engelhardt, Comparative study of angle resolved photoemission spectra from pyridine adsorbed on Ag(111) and on Ag polycrystalline substrates, *Surf. Sci.*, 178 (1986) 646–656.
- [76] A. Campion, Surface Raman spectroscopy without enhancement: Pyridine on Ag(111), *J. Electron Spectrosc. Relat. Phenom.*, 29 (1983) 397–400.
- [77] J. E. Rowe, C. V. Shank, D. A. Zwemer, C. A. Murray, Ultrahigh-Vacuum Studies of Enhanced Raman Scattering from Pyridine on Ag Surfaces, *Phys. Rev. Lett.*, 44 (1980) 1770–1773.
- [78] P. Avouris, J. E. Demuth, Vibrational overtone spectroscopy of benzene and pyridine on Ag(111), *J. Chem. Phys.*, 75 (1981) 5953–5954.
- [79] G. Zylka, A. Otto, Search for dynamical charge transfer excitations of CO and pyridine on copper by EELS, *Surf. Sci.*, 475 (2001) 118–130.
- [80] P. Davies, N. Shukla, The adsorption of pyridine at clean, oxidised and hydroxylated Cu(111) surfaces, *Surf. Sci.*, 322 (1995) 8–20.
- [81] K. Tonigold, A. Groß, Adsorption of small aromatic molecules on the (111) surfaces of noble metals: A density functional theory study with semiempirical corrections for dispersion effects, *J. Chem. Phys.*, 132 (2010) 224701.

- [82] A. Bilić, J. R. Reimers, N. S. Hush, Adsorption of Pyridine on the Gold(111) Surface: Implications for “Alligator Clips” for Molecular Wires, *J. Phys. Chem. B*, 106 (2002) 6740–6747.
- [83] D. Mollenhauer, N. Gaston, E. Voloshina, B. Paulus, Interaction of Pyridine Derivatives with a Gold (111) Surface as a Model for Adsorption to Large Nanoparticles, *J. Phys. Chem. C*, 117 (2013) 4470–4479.
- [84] L. Buimaga-Iarinca, C. Morari, Adsorption of small aromatic molecules on gold: a DFT localized basis set study including van der Waals effects, *Theor. Chem. Acc.*, 133 (2014) 1502.
- [85] L. Ferrighi, G. K. H. Madsen, B. Hammer, Self-Consistent meta-Generalized gradient approximation study of adsorption of aromatic molecules on noble metal surfaces, *J. Chem. Phys.*, 135 (2011) 084704.
- [86] G. Kresse, J. Furthmüller, Efficient Iterative Schemes for Ab Initio Total-Energy Calculations Using a Plane-Wave Basis Set, *Phys. Rev. B*, 54 (1996) 11169–11186.
- [87] G. Kresse, J. Furthmüller, Efficiency of Ab-Initio Total Energy Calculations for Metals and Semiconductors Using a Plane-Wave Basis Set, *Comput. Mater. Sci.*, 6 (1996) 15–50.
- [88] G. Kresse, J. Hafner, Ab Initio Molecular Dynamics for Liquid Metals, *Phys. Rev. B*, 47 (1993) 558–561.
- [89] G. Kresse, J. Hafner, Ab initio molecular-dynamics simulation of the liquid-metal-amorphous-semiconductor transition in germanium, *Phys. Rev. B*, 49 (1994) 14251.

- [90] H. Yildirim, T. Greber, A. Kara, Trends in Adsorption Characteristics of Benzene on Transition Metal Surfaces: Role of Surface Chemistry and Van Der Waals Interactions, *J. Phys. Chem. C*, 177 (2013) 20572-20583.
- [91] P. Hao, Y. Fang, J. Sun, G. I. Csonka, P. H. Philipsen, J. P. Perdew, Lattice Constants from Semilocal Density Functionals with Zero-Point Phonon Correction, *Phys. Rev. B*, 85 (2012) 014111.
- [92] F. Netzer, G. Rangelov, The orientation of pyridine on Rh(111), *Surf. Sci.*, 225 (1990) 260–266.
- [93] C. M. Mate, G. A. Somorjai, H. W. K. Tom, X. D. Zhu, Y. R. Shen, Vibrational and electronic spectroscopy of pyridine and benzene adsorbed on the Rh(111) crystal surface, *J. Chem. Phys.*, 88 (1988) 441–450.
- [94] F. Netzer, J.-U. Mack, Angle-Resolved ultraviolet photoemission of pyridine adsorbed on Pd(111), *Chem. Phys. Lett.*, 94 (1983) 492–496.
- [95] F. P. Netzer, J. U. Mack, The electronic structure of aromatic molecules adsorbed on Pd(111), *J. Chem. Phys.*, 79 (1983) 1017–1025.
- [96] V. H. Grassian, E. L. Muettterties, Vibrational Electron Energy Loss Spectroscopic Study of Benzene, Toluene, and Pyridine Adsorbed on Pd(111) at 180 K, *J. Phys. Chem.*, 91 (1987) 389.
- [97] G. Waddill, L. Kesmodel, Resonance electron scattering investigations of adsorbed hydrocarbons: benzene, pyridine and cyclohexane on Pd(111), *Chem. Phys. Lett.*, 128 (1986) 208.

- [98] S. Aminpirooz, L. Becker, B. Hillert, J. Haase, High resolution NEXAFS studies of aromatic molecules adsorbed and condensed on Ni(111), *Surf. Sci. Lett.*, 244 (1991) L152.
- [99] V. Fritzsche, S. Bao, P. Hofmann, M. Polčik, K.-M. Schindler, A. Bradshaw, R. Davis, D. Woodruff, The adsorption site of pyridine on Ni{111} determined by low-Energy photoelectron diffraction, *Surf. Sci.*, 319 (1994) L1.
- [100] M. R. Cohen, R. P. Merrill, Adsorption of pyridine on nickel(111): a HREELS, ARUPS, and XPS study, *Langmuir*, 6 (1990) 1282–1288.
- [101] S. Haq, D. A. King, Configurational Transitions of Benzene and Pyridine Adsorbed on Pt{111} and Cu{110} Surfaces: An Infrared Study, *J. Phys. Chem.*, 100 (1996) 16957–16965.
- [102] J. A. Horsley, J. Stöhr, A. P. Hitchcock, D. C. Newbury, A. L. Johnson, F. Sette, Resonances in the K Shell Excitation Spectra of Benzene and Pyridine: Gas Phase, Solid, and Chemisorbed States, *J. Chem. Phys.*, 83 (1985) 6099.
- [103] V. H. Grassian, E. L. Muetterties, Electron energy loss and thermal desorption spectroscopy of pyridine adsorbed on platinum(111), *J. Phys. Chem.*, 90 (1986) 5900–5907.
- [104] A. L. Johnson, E. L. Muetterties, J. Stöhr, F. Sette, Chemisorption geometry of pyridine on platinum(111) by NEXAFS, *J. Phys. Chem.*, 89 (1985) 4071–4075.
- [105] J. Gland, G. Somorjai, Low energy electron diffraction and work function studies of benzene, naphthalene and pyridine adsorbed on Pt(111) and Pt(100) single crystal surfaces, *Surf. Sci.*, 38 (1973) 157–186.



- [106] C. Wöckel, A. Eilert, M. Welke, M. Schöppke, H.-P. Steinrück, R. Denecke, Pyridine on flat Pt(111) and stepped Pt(355)—An in situ HRXPS investigation of adsorption and thermal evolution, *J. Chem. Phys.*, 144 (2016) 014702.
- [107] M. Bridge, M. Connolly, D. Lloyd, J. Somers, P. Jakob, D. Menzel, Electron spectroscopic studies of pyridine on metal surfaces, *Spectrochim. Acta A*, 43 (1987) 1473–1478.
- [108] E. L. Kolsbjerg, M. N. Groves, B. Hammer, Pyridine adsorption and diffusion on Pt(111) investigated with density functional theory, *J. Chem. Phys.*, 144 (2016) 164112.
- [109] R. Otero, A. L. Vázquez de Parga, J. M. Gallego, Electronic, structural and chemical effects of charge-transfer at organic/inorganic interfaces, *Surf. Sci. Rep.*, 72 (2017) 105-145.
- [110] J.-G. Lee, J. Ahner, J. T. Yates, The adsorption conformation of chemisorbed pyridine on the Cu(110) surface, *J. Chem. Phys.*, 114 (2001) 1414.
- [111] T. Gießel, O. Schaff, R. Lindsay, P. Baumgärtel, M. Polcik, A. M. Bradshaw, A. Koebbel, T. McCabe, M. Bridge, D. R. Lloyd, D. P. Woodruff, Adsorption site and orientation of pyridine on Cu{110} determined by photoelectron diffraction, *J. Chem. Phys.*, 110 (1999) 9666.
- [112] D. B. Dougherty, J. Lee, J. T. Yates, Role of Conformation in the Electronic Properties of Chemisorbed Pyridine on Cu(110): An STM/STS Study, *J. Phys. Chem. B*, 110 (2006) 11991.
- [113] M. Bader, J. Haase, K.-H. Frank, C. Ocal, A. Puschmann, Near-Edge X-Ray Absorption Fine-Structure Studies Of Ring Molecules Adsorbed On Single Crystal Surfaces, *J. Phys. Colloq.*, 47 (1986) C8-491.

- [114] B. Bandy, D. Lloyd, N. Richardson, Selection rules in photoemission from adsorbates: Pyridine adsorbed on copper, *Surf. Sci.*, 89 (1979) 344.
- [115] N. Atodiresei, V. Caciuc, J.-H. Franke, S. Blügel, Role of the van der Waals interactions on the bonding mechanism of pyridine on Cu(110) and Ag(110) surface: First-Principles study, *Phys. Rev. B*, 78 (2008) 045411.
- [116] N. Atodiresei, V. Caciuc, P. Lazić, S. Blügel, Chemical versus van der Waals Interaction: The Role of the Heteroatom in the Flat Adsorption of Aromatic Molecules C<sub>6</sub>H<sub>6</sub>, C<sub>5</sub>NH<sub>5</sub>, and C<sub>4</sub>N<sub>2</sub>H<sub>4</sub> on the Cu(110) Surface, *Phys. Rev. Lett.*, 102 (2009) 136809.
- [117] J. R. Hahn, W. Ho, Imaging and vibrational spectroscopy of single pyridine molecules on Ag(110) using a low-Temperature scanning tunneling microscope, *J. Chem. Phys.*, 124 (2006) 204708.
- [118] J. Q. Hou, H. S. Kang, K. W. Kim, J. R. Hahn, Binding characteristics of pyridine on Ag(110), *J. Chem. Phys.*, 128 (2008) 134707.
- [119] J. R. Hahn, H. S. Kang, Role of molecular orientation in vibration, hopping, and electronic properties of single pyridine molecules adsorbed on Ag(110) surface: A combined STM and DFT study, *Surf. Sci.*, 604 (2010) 258.
- [120] D. Heskett, K. J. Song, A. Burns, E. W. Plummer, H. L. Dai, Coverage dependent phase transition of pyridine on Ag(110) observed by second harmonic generation, *J. Chem. Phys.*, 85 (1986) 7490.

- [121] I. Lee, S. Son, T. Shin, J. R. Hahn, Direct observation of the conformational transitions of single pyridine molecules on a Ag(110) surface induced by long-range repulsive intermolecular interactions, *J. Chem. Phys.*, 146 (2017) 014706.
- [122] S. Kelemen, A. Kaldor, Pyridine adsorption on Ag(110), *Chem. Phys. Lett.*, 73 (1980) 205.
- [123] D. Heskett, L. Urbach, K. Song, E. Plummer, H. Dai, Oxygen and pyridine on Ag(110) studied by second harmonic generation: Coexistence of two phases within monolayer pyridine coverage, *Surf. Sci.*, 197 (1988) 225.
- [124] A. Hamelin, S. Morin, J. Richer, and J. Lipkowski, Adsorption of pyridine on the (110) face of silver, *J. Electroanal. Chem.*, 272 (1989) 241.
- [125] F. Henglein, J. Lipkowski, D. Kolb, An optical study of pyridine adsorption on gold using synchrotron radiation, *J. Electroanal. Chem.*, 303 (1991) 245.
- [126] C. I. Smith, A. J. Maunder, C. A. Lucas, R. J. Nichols, P. Weightman, Adsorption of Pyridine on Au(110) as Measured by Reflection Anisotropy Spectroscopy, *J. Electrochem. Soc.*, 150 (2003) E233.
- [127] N. Li, V. Zamlynyy, J. Lipkowski, F. Henglein, B. Pettinger, In situ IR reflectance absorption spectroscopy studies of pyridine adsorption at the Au(110) electrode surface, *J. Electroanal. Chem.*, 524-525 (2002) 43.
- [128] J.-F. Li, Y.-J. Zhang, A. V. Rudnev, J. R. Anema, S.-B. Li, W.-J. Hong, P. Rajapandiyan, J. Lipkowski, T. Wandlowski, Z.-Q. Tian, Electrochemical Shell-Isolated Nanoparticle-

Enhanced Raman Spectroscopy: Correlating Structural Information and Adsorption Processes of Pyridine at the Au(Hkl) Single Crystal/Solution Interface, *J. Am. Chem. Soc.*, 137 (2015) 2400.

[129] K.-H. Frank, R. Drudde, E. Koch, Electron affinity levels of benzene and azabenzenes on Cu(111) and Au(110) revealed by inverse photoemission, *Chem. Phys. Lett.*, 132 (1986) 83.

[130] J.-F. Li, S.-Y. Ding, Z.-L. Yang, M.-L. Bai, J. R. Anema, X. Wang, A. Wang, D.-Y. Wu, B. Ren, S.-M. Hou, T. Wandlowski, Z.-Q. Tian, Extraordinary Enhancement of Raman Scattering from Pyridine on Single Crystal Au and Pt Electrodes by Shell-Isolated Au Nanoparticles, *J. Am. Chem. Soc.*, 133 (2011) 15922.

[131] G. Nyberg, S. R. Bare, P. Hofmann, D. A. King, M. Surman, Off-Specular and out-of-Plane vibrational electron energy loss spectra of benzene and pyridine adsorbed on Pt(110), *Appl. Surf. Sci.*, 22-23 (1985) 392-402.

[132] M. Surman, S. R. Bare, P. Hofmann, D. A. King, The influence of orientation on the H-D exchange reactions in chemisorbed aromatics: Benzene and pyridine adsorbed on Pt{110}, *Surf. Sci.*, 179 (1987) 243.

[133] W. Moritz, D. Wolf, Structure determination of the reconstructed Au(110) surface, *Surf. Sci.*, 88 (1979) L29-L34.

[134] J. Möller, H. Niehus, W. Heiland, Direct measurement of Au(110) surface structural parameters by low energy ion backscattering, *Surf. Sci.*, 166 (1986) L111-L114.

[135] K.-M. Ho, K.P. Bohnen, Stability of the missing-row reconstruction on fcc (110) transition-metal surfaces, *Phys. Rev. Lett.*, 59 (1987) 1833.

- [136] M. Copel, T. Gustafsson, Structure of Au(110) Determined with Medium-Energy-Ion scattering, *Phys. Rev. Lett.*, 57 (1986) 723.
- [137] P. Fery, W. Moritz, D. Wolf, Structure determination of the (1×2) and (1×3) reconstructions of Pt(110) by low-energy electron diffraction, *Phys. Rev. B*, 38 (1988) 7275.
- [138] H. Niehus, Analysis of the Pt(110)-(1 × 2) surface reconstruction, *Surf. Sci.*, 145 (1984) 407.
- [139] A. R. Murphy, J. M. J. Frechet, P. Chang, J. Lee, V. Subramanian, Organic thin film transistors from a soluble oligothiophene derivative containing thermally removable solubilizing groups, *J. Am. Chem. Soc.*, 126 (2004) 1596-1597.
- [140] D. Fichou, *Handbook of Oligo- and Polythiophenes*, WileyVCH, New York, 1998.
- [141] H. E. Katz, L. Torsi, A. Dodabalapur, Synthesis, material properties, and transistor performance of highly pure thiophene oligomers, *Chem. Mater.*, 7 (1995) 2235-2237.
- [142] H. E. Katz, Organic molecular solids as thin film transistor semiconductors, *J. Mater. Chem.*, 7 (1997) 369-376.
- [143] S. Mohapatra, B. T. Holmes, C. R. Newman, C. F. Prendergast, C. D. Frisbie, M. D. Ward, Organic thin-film transistors based on tolyl-substituted oligothiophenes, *Adv. Funct. Mater.*, 6 (2004) 605-609.
- [144] G. Gigli, O. Inganäs, M. Anni, M. De Vittorio, R. Cingolani, G. Barbarella, L. Favaretto, Multicolor oligothiophene-based light-emitting diodes, *Appl. Phys. Lett.*, 78 (2001) 1493-1495.

- [145] M. Berggren, O. Inganäs, G. Gustafsson, J. Ramusson, R. Andersson, T. Hjertberg, O. Wennerstrom, Light-emitting diodes with variable colours from polymer blends, *Nature*, 372 (1994) 444 – 446.
- [146] A. Imanishi, S. Yagi, T. Yokoyama, Y. Kitajima, T. Ohta, Structural and Electronic Properties of Adsorbed C<sub>4</sub>H<sub>4</sub>S on Cu(100) and Ni(100) Studied by S K-XAFS and S-1s XPS, *J. Electron Spectrosc. Relat. Phenom.*, 80 (1996) 151–154.
- [147] J. Stöhr, E. B. Kollin, D. A. Fischer, J. B. Hastings, F. Zaera, F. Sette, Surface Extended X-Ray-Absorption Fine Structure of Low- Z Adsorbates Studied with Fluorescence Detection, *Phys. Rev. Lett.*, 55 (1985) 1468–1471.
- [148] F. Zaera, E. B. Kollin, J. L. Gland, Thiophene Chemisorption and Thermal Decomposition on Nickel(100) Single-Crystal Surfaces, *Langmuir*, 3 (1987) 555–557.
- [149] F. Mittendorfer, Initial Steps in the Desulfurization of Thiophene/Ni(100)-A DFT Study, *J. Catal.*, 214 (2003) 234–241.
- [150] H. Orita, N. Itoh, Adsorption of Thiophene on Ni(100), Cu(100), and Pd(100) Surfaces: Ab Initio Periodic Density Functional Study, *Surf. Sci.*, 550 (2004) 177–184.
- [151] Z.-X. Hu, H. Lan, W. Ji, Role of the Dispersion Force in Modeling the Interfacial Properties of Molecule-Metal Interfaces: Adsorption of Thiophene on Copper Surfaces, *Sci. Rep.*, 4 (2014) 5036.
- [152] C. Morin, A. Eichler, R. Hirschl, P. Sautet, J. Hafner, DFT Study of Adsorption and Dissociation of Thiophene Molecules on Ni(110), *Surf. Sci.*, 540 (2003) 474–490.

- [153] F. Mittendorfer, J. Hafner, A DFT Study of the Adsorption of Thiophene on Ni(100), *Surf. Sci.*, 492 (2001) 27–33.
- [154] J. Baumgartner, R. Frety, M. Guenin, Molecular Poisoning of Ni/SiO<sub>2</sub> Catalyst. A Magnetic and Catalytic Study of the Effect of Thiophene, Carbonyl Sulfide and Carbon Disulfide Adsorption, *Stud. Surf. Sci. Catal.*, 72 (1993) 2515–2518.
- [155] Q. Ge, S. Jenkins, D. King, Localisation of Adsorbate-Induced Demagnetisation: CO Chemisorbed on Ni{110}, *Chem. Phys. Lett.*, 327 (2000) 125–130.
- [156] C. S. Feigerle, A. Seiler, J. L. Peña, R. J. Celotta, D. T. Pierce, CO Chemisorption on Ni(110): Effect on Surface Magnetism, *Phys. Rev. Lett.*, 56 (1986) 2207–2210.
- [157] F. Mittendorfer, J. Hafner, Density-Functional Study of the Adsorption of Benzene on the (111), (100) and (110) Surfaces of Nickel, *Surf. Sci.*, 472 (2001) 133–153.
- [158] S. Terada , T. Yokoyama , M. Sakano , A. Imanishi , Y. Kitajima , M. Kiguchi , Y. Okamoto , T. Ohta , Thiophene adsorption on Pd(111) and Pd(100) surfaces studied by total-reflection S K-edge X-ray absorption fine-structure spectroscopy, *Surf. Sci.*, 414 (1998) 107–117 .
- [159] H. Orita , N. Itoh , Adsorption of thiophene on Ni (100), Cu (100), and Pd (100) surfaces: ab initio periodic density functional study, *Surf. Sci.*, 550 (2004) 177–184.
- [160] A. Patra, J. Sun, J. Perdew, Re-thinking CO adsorption on transition-metal surfaces: Density-driven error?, *arXiv:1807.05450* 2018.

- [161] C. Song, An overview of new approaches to deep desulfurization for ultra-clean gasoline, diesel fuel and jet fuel, *Catal. Today*, 86 (2003) 211-263.
- [162] H. M. Wang, E. Iglesia, Thiophene hydrodesulfurization catalysis on supported Ru clusters: Mechanism and site requirements for hydrogenation and desulfurization pathways, *J. Catal.*, 273 (2010) 245-256.
- [163] J. R. Anderson, M. Boudart, *Catalysis: Science and Technology*, Springer, Berlin, 1996.
- [164] R. J. Mikovsky, A. J. Silvestri, H. Heineman, On the mechanism of thiophene desulfurization, *J. Catal.*, 34 (1974) 324-326.
- [165] A. Borgna, E. J. M. Hensen, J. A. R. van Veen, J. W. Niemantsverdriet, Intrinsic kinetics of thiophene hydrodesulfurization on a sulfided NiMo/SiO<sub>2</sub> planar model catalyst, *J. Catal.*, 221 (2004) 541-548.
- [166] M. J. Girgis, B. C. Gates, Reactivities, reaction networks, and kinetics in high-pressure catalytic hydroprocessing, *Ind. Eng. Chem. Res.*, 30 (1991) 2021-2058.
- [167] P. J. Owens, C. H. Amberg, Thiophene Desulfurization by a Microreactor Technique, *Adv. Chem. Ser.*, 33 (1961) 182-198.
- [168] H. C. Lee, J. B. Butt, Kinetics of the desulfurization of thiophene: Reactions of thiophene and butane, *J. Catal.*, 49 (1977) 320-331.



- [169] E. J. M. Hensen, M. J. Vissenberg, V. H. J. deBeer, J. A. R. van Veen, R. A. van Santen, Kinetics and Mechanism of Thiophene Hydrodesulfurization over Carbon-Supported Transition Metal Sulfides, *J. Catal.*, 163 (1996) 429-435.
- [170] E. J. M. Hensen, H. J. A. Brans, G. Lardinois, V. H. J. de Beer, J. A. R. van Veen, R. A. van Santen, Periodic Trends in Hydrotreating Catalysis: Thiophene Hydrodesulfurization over Carbon-Supported 4d Transition Metal Sulfides, *J. Catal.*, 192 (2000) 98-107.
- [171] M. J. Ledoux, O. Michaux, G. Agostini, P. Panissod, The influence of sulfide structures on the hydrodesulfurization activity of carbon-supported catalysts, *J. Catal.*, 102 (1986) 275-288.
- [172] T. A. Pecoraro, R. R. Chianelli, Hydrodesulfurization catalysis by transition metal sulfides, *J. Catal.*, 67 (1981) 430-445.
- [173] P. G. Moses, B. Hinnemann, H. Topsoe, J. K. Nørskov, The hydrogenation and direct desulfurization reaction pathway in thiophene hydrodesulfurization over MoS<sub>2</sub> catalysts at realistic conditions: A density functional study, *J. Catal.*, 248 (2007) 188-203.
- [174] A. J. Gellman, M. H. Farias, G. A. Somorjai, The catalytic hydrodesulfurization of thiophene on the Mo(100) crystal surface, *J. Catal.*, 88 (1984) 546-548.
- [175] A. J. Gellman, M. H. Farias, M. Salmeron, G. A. Somorjai, A thermal desorption study of thiophene adsorbed on the clean and sulfided Mo(100) crystal face, *Surf. Sci.*, 136 (1984) 217-228.

- [176] M. E. Bussell, G. A. Somorjai, A radiotracer ( $^{14}\text{C}$ ) and catalytic study of thiophene hydrodesulfurization on the clean and carbided Mo(100) single-crystal surface, *J. Catal.*, 106 (1987) 93-104.
- [177] M. E. Bussell, A. J. Gellman, G. A. Somorjai, Thiophene hydrodesulfurization over transition metal surfaces: Structure insensitive over molybdenum and structure sensitive over rhenium, *J. Catal.*, 110 (1988) 423-426.
- [178] M. E. Bussell, A. J. Gellman, G. A. Somorjai, The role of adsorbate overlayers in thiophene hydrodesulfurization over molybdenum and rhenium single crystals, *Catal. Lett.*, 1 (1988) 195-201.
- [179] D. G. Kelly, M. Salmeron, G. A. Somorjai, *Surf. Sci.*, The adsorption and reactions of hydrocarbons on Molybdenum single crystal surfaces; when clean and in the presence of co-adsorbed sulfur or carbon, 175 (1986) 465-486.
- [180] A. J. Gellman, D. Neiman, G. A. Somorjai, Catalytic hydrodesulfurization over the Mo(100) single crystal surface: I. Kinetics and overall mechanism, *J. Catal.*, 107 (1987) 92-102.
- [181] A. J. Gellman, M. E. Bussell, G. A. Somorjai, Catalytic hydrodesulfurization over the Mo(100) single crystal surface: II. The role of adsorbed sulfur and mechanism of the desulfurization step, *J. Catal.*, 107 (1987) 103-113.
- [182] G. Y. Guo, H. H. Wang, Calculated elastic constants and electronic and magnetic properties of bcc, fcc, and hcp Cr crystals and thin films, *Phys. Rev. B*, 62 (2000) 5136.

- [183] L. Schimka, R. Gaudoin, J. Klimeš, M. Marsman, G. Kresse, Lattice constants and cohesive energies of alkali, alkaline-earth, and transition metals: Random phase approximation and density functional theory results, *Phys. Rev. B*, 87 (2013) 214102.
- [184] J. A. Rodriguez, Bonding and Decomposition of Thiophene, Sulfhydryl, Thiomethoxy and Phenyl Thiolate on Mo Surfaces, *Surf. Sci.*, 278 (1992) 326–338.
- [185] J. Cheng, P. Hu, Utilization of the Three-Dimensional Volcano Surface To Understand the Chemistry of Multiphase Systems in Heterogeneous Catalysis, *J. Am Chem. Soc.*, 130 (2008) 10868.
- [186] A. R. Singh, J. H. Montoya, B. A. Rohr, C. Tsai, A. Vojtyl, J. K. Nørskov, Computational Design of Active Site Structures with Improved Transition-State Scaling for Ammonia Synthesis, *ACS Catal.*, 8 (2018) 4017.
- [187] F. Zhang, D. Q. Wu, Y. Xu, X. L. Feng, Thiophene-based Conjugated Oligomers for Organic Solar Cells, *J. Mater. Chem.*, 21 (2011) 17590–17600.
- [188] R. Meerheim, C. Körner, K. Leo, Highly Efficient Organic Multi-junction Solar Cells with a Thiophene Based Donor Material, *Appl. Phys. Lett.*, 105 (2014) 063306.
- [189] A. Mishra, C. Q. Ma, P. Bäuerle, Functional Oligothiophenes: Molecular Design for Multidimensional Nanoarchitectures and Their Applications, *Chem. Rev.*, 109 (2009) 1141–1276.
- [190] S. K. Swathi, K. Ranjith, P. Kumar, P. C. Ramamurthy, Novel Thiophene Derivative Hybrid Composite Solar Cells, *Sol. Energy Mater. Sol. Cells*, 96 (2012) 101–107.

- [191] D. A. Serban, V. Kilchytska, A. Vlad, A. Martin-Hoyas, B. Nysten, A. M. Jonas, Y. H. Geerts, R. Lazzaroni, V. Bayot, D. Flandre, et al., Low-power Dihexylquaterthiophene-based Thin Film Transistors for Analog Applications, *Appl. Phys. Lett.*, 92 (2008) 143503.
- [192] T. Leydecker, D. Trong Duong, A. Salleo, E. Orgiu, P. Samori, Solution-processed Field-Effect Transistors Based on Dihexylquaterthiophene Films with Performances Exceeding Those of Vacuum-Sublimed Films, *ACS Appl. Mater. Interfaces*, 6 (2014) 21248–21255.
- [193] G. Generali, F. Dinelli, R. Capelli, S. Toffanin, S. Di Maria, M. Gazzano, G. Barbarella, M. Muccini, Correlation among Morphology, Crystallinity, and Charge Mobility in OFETs Made of Quaterthiophene Alkyl Derivatives on a Transparent Substrate Platform, *J. Phys. Chem. C*, 115 (2011) 23164–23169.
- [194] G. Generali, R. Capelli, S. Toffanin, A. Facchetti, M. Muccini, Ambipolar Field-effect Transistor Based on  $\alpha,\omega$ -Dihexylquaterthiophene and  $\alpha,\omega$ -Diperfluoroquaterthiophene Vertical Heterojunction, *Microelectron. Microelectron. Reliab.*, 50 (2010) 1861–1865.
- [195] E. M. Mannebach, J. M. Spalenka, P. S. Johnson, Z. H. Cai, F. J. Himpsel, P. G. Evans, High Hole Mobility and Thickness-Dependent Crystal Structure in  $\alpha,\omega$ -Dihexylsexithiophene Singlemonolayer Field-effect Transistors, *Adv. Funct. Mater.*, 23 (2013) 554–564.
- [196] R. Capelli, F. Dinelli, M. Gazzano, R. D’Alpaos, A. Stefani, G. Generali, M. Riva, M. Montecchi, A. Giglia, L. Pasquali, Interface Functionalities in Multilayer Stack Organic Light Emitting Transistors (OLETs), *Adv. Funct. Mater.*, 24 (2014) 5603–5613.

- [197] B. Reeja-Jayan, A. Manthiram, Influence of Polymer–metal Interface on the Photovoltaic Properties and Long-term Stability of nc-TiO<sub>2</sub>-P3HT Hybrid Solar Cells, *Sol. Energy Mater. Sol. Cells*, 94 (2010) 907–914.
- [198] F. Garnier, R. Hajlaoui, A. El Kassmi, G. Horowitz, L. Laigre, W. Porzio, M. Armanini, F. Provasoli, Dihexylquaterthiophene, a Two-Dimensional Liquid Crystal-like Organic Semiconductor with High Transport Properties, *Chem. Mater.*, 10 (1998) 3334–3339.
- [199] A. Guarnaccio, M. D’Auria, R. Racioppi, G. Mattioli, A. A. Bonapasta, A. De Bonis, R. Teghil, K. C. Prince, R. G. Acres, A. Santagata, Thiophene-based Oligomers Interacting with Silver Surfaces and the Role of a Condensed Benzene Ring, *J. Phys. Chem. C*, 120 (2016) 252–264.
- [200] F. Elfeninat, C. Fredriksson, E. Sacher, A. Selmani, A Theoretical Investigation of the Interactions between Thiophene and Vanadium, Chromium, Copper, and Gold, *J. Chem. Phys.*, 102 (1995) 6153–6158.
- [201] E. Ito, M. Hara, K. Kanai, Y. Ouchi, K. Seki, J. Noh, Comparative Study of Tetrahydrothiophene and Thiophene Selfassembled Monolayers on Au(111): Structure and Molecular Orientation, *Bull. Korean Chem. Soc.*, 30 (2009) 1755–1759.
- [202] E. O. Sako, H. Kondoh, I. Nakai, A. Nambu, T. Nakamura, T. Ohta, Reactive Adsorption of Thiophene on Au(111) from Solution, *Chem. Phys. Lett.*, 413 (2005) 267–271.
- [203] M. H. Dishner, J. C. Hemminger, F. J. Feher, Formation of a Self-assembled Monolayer by Adsorption of Thiophene on Au(111) and its Photooxidation, *Langmuir*, 12 (1996) 6176–6178.

- [204] J. Noh, E. Ito, T. Araki, M. Hara, Adsorption of Thiophene and 2,5-Dimethylthiophene on Au (111) from Ethanol Solutions, *Surf. Sci.*, 532-535 (2003) 1116–1120.
- [205] E. Ito, J. Noh, M. Hara, Different Adsorption States between Thiophene and  $\alpha$ -Bithiophene Thin Films Prepared by Self-assembly Method, *Jpn. J. Appl. Phys.*, 42 (2003) L852–L855.
- [206] F. Terzi, R. Seeber, L. Pigani, C. Zanardi, L. Pasquali, S. Nannarone, M. Fabrizio, S. J. Daolio, 3-Methylthiophene Self-Assembled Monolayers on Planar and Nanoparticle Au Surfaces, *Phys. Chem. B*, 109 (2005) 19397–19402.
- [207] T. W. Kelley, P. F. Baude, C. Gerlach, D. E. Ender, D. Muyres, M. A. Haase, D. E. Vogel, S. D. Theiss, Recent Progress in Organic Electronics: Materials, Devices, and Processes, *Chem. Mater.*, 16 (2004) 4413–4423.
- [208] A. Maliakal, K. Raghavachari, H. Katz, E. Chandross, T. Siegrist, Photochemical Stability of Pentacene and a Substituted Pentacene in Solution and in Thin Films, *Chem. Mater.*, 16 (2004) 4980–4986.
- [209] B. Gao, M. Wang, Y. Cheng, L. Wang, X. Jing, F. Wang, Pyrazine-Containing Acene-Type Molecular Ribbons with up to 16 Rectilinearly Arranged Fused Aromatic Rings, *J. Am. Chem. Soc.*, 130 (2008) 8297–8306.
- [210] U. H. F. Bunz, J. U. Engelhart, B. D. Lindner, M. Schaffroth, Large N-Heteroacenes: New Tricks for Very Old Dogs?, *Angew. Chem. Int. Ed.*, 52 (2013) 3810–3821.
- (11) [211] L. Zhang, C. Y. Liu, X. Fu, L. D. Sun, P. Zeppenfeld, Pentacene/Cu(110) Interface Formation Monitored by in Situ Optical Spectroscopy, *Phys. Rev. B*, 89 (2014) 035428.

- [212] S. Söhnchen, S. Lukas, G. Witte, Epitaxial Growth of Pentacene Films on Cu(110), *J. Chem. Phys.*, 121 (2004) 525–534.
- [213] K. Müller, A. P. Seitsonen, T. Brugger, J. Westover, T. Greber, T. Jung, A. Kara, Electronic Structure of an Organic/Metal Interface: Pentacene/Cu(110), *J. Phys. Chem.*, 116 (2012) 23465–23471.
- [214] K. Müller, A. Kara, T. K. Kim, R. Bertschinger, A. Scheybal, J. Osterwalder, T. A. Jung, Multimorphism in Molecular Monolayers: Pentacene on Cu(110), *Phys. Rev. B*, 79 (2009) 245421.
- [215] J. Lagoute, K. Kanisawa, S. Fölsch, Manipulation and Adsorption-Site Mapping of Single Pentacene Molecules on Cu(111), *Phys. Rev. B*, 70 (2004) 245415.
- [216] A. Baby, G. Fratesi, S. R. Vaidya, L. L. Patera, C. Africh, L. Floreano, G. P. Brivio, Anchoring and Bending of Pentacene on Aluminum (001), *J. Phys. Chem. C*, 119 (2015) 3624–3633.